Technische Universität München
TUM School of Engineering and Design

Deflagration-to-Detonation Transition in H_2-CO-Air Mixtures

Daniel Heilbronn

Vollständiger Abdruck der von der TUM School of Engineering and Design der Technischen Universität München zur Erlangung eines
DOKTORS DER INGENIEURWISSENSCHAFTEN (DR.-ING.)
genehmigten Dissertation.

Vorsitz:
Prof. Rafael Macián-Juan, Ph.D.
Prüfer der Dissertation:
1. Prof. Dr.-Ing. Thomas Sattelmayer
2. Prof. Dr. rer. nat. Hans-Josef Allelein

Die Dissertation wurde am 28.04.2023 bei der Technischen Universität München eingereicht und durch die TUM School of Engineering and Design am 14.12.2023 angenommen.

Vorwort

Die vorliegende Arbeit entstand am Lehrstuhl für Thermodynamik der Technischen Universität München während meiner Tätigkeit als wissenschaftlicher Mitarbeiter von 2017 bis 2022. Sie wurde durch das Bundesministerium für Wirtschaft und Energie über die Gesellschaft für Reaktorsicherheit (GRS) gefördert.

Mein besonderer Dank gilt meinem Doktorvater Herrn Prof. Dr.-Ing. Thomas Sattelmayer für das in mich gesetzte Vertrauen und die Möglichkeit diese Arbeit unter seiner Betreuung durchführen zu können. Seine Beiträge haben maßgeblich zum Erfolg dieser Arbeit beigetragen. Weiterhin möchte ich mich für die Freiheiten und Möglichkeiten im Rahmen der Lehre bedanken, die mir viel Spaßbereitet hat und lange in guter Erinnerung bleiben wird.

Herr Prof. rer. nat. Hans-Josef Allelein danke ich für die freundliche Übernahme des Korefereats und Herrn Prof. Dr. Rafael Macián-Juan für den Vorsitz bei der mündlichen Prüfung.

Ich möchte ich den Projektpartnern von ProScience insbesondere Dr. Andreas Friedrich, Dr. Mike Kuznetsov, Anke Veser, Prof. Dr.-Ing. Thomas Jordan für die fachliche und praktische Unterstützung und die vielen inhaltlichen Diskussion danken. Auf Seiten der GRS danke ich Herrn Dr. Weinriefer für die organisatorische und Herrn Harms für die finanzielle Betreuung des Projekts.

Oberingenieur Dr. Christoph Hirsch danke ich für die fachliche Hilfe beim Aufbau und die praktischen Ratschläge im Umgang mit den Gefahrstoffen H_2 und CO, sowie dem sicheren Betrieb des Labors. Weiterhin gilt mein Dank der mechanischen Werkstatt um Jens Hümmer, sowie dem Team der elektrischen Werkstatt, die meine Defizite in der Elektrizitätslehre ausgleichen mussten. Gerhard Giel für danke ich für praktische Tipps von unschlagbarem Wert. Mein Dank gilt dem Sekretariat um Helga Basset, Sigrid Schulz-Reichwald und Brigitte Hirsch für ihre Unterstützung bei allen organisatorischen, administrativen und finanziellen Angelegenheiten.

Meinen Korrekturlesern Jan Kaufmann, Sascha Filimon, Simon Tartsch, Christoph Wieland und Christoph Barfuß danke ich für ihre Anregung und

Korrekturen.

Ebenso möchte ich mich bei den Studierenden bedanken, die mich während meiner Promotion unterstützt haben. Hierbei sind besonders Nikolas Wein, Dariush Hosseini und Kajetan Planötscher hervorzuheben.

Ich danke allen aktuellen und ehemaligen Mitarbeitern:innen des Lehrstuhls für Thermodynamik für die tolle Zeit. Ich bin sehr dankbar für all die anregenden Diskussionen, vielseitigen Nebenaktivitäten, Mittagspausen, Feierabende und nicht zuletzt die Freundschaften, die sich während der gemeinsamen Arbeit am Lehrstuhl entwickelt haben. Inbesondere gilt mein Dank meinem Büro- und Projektkollegen Christoph Barfuß für den leichten Start am Lehrstuhl, die angenehme Zusammenarbeit und Arbeitsatmosphäre, die Geselligkeit sowie die wertvollen fachlichen Diskussionen. Ich danke Jan Kaufmann für die enge und produktive Zusammenarbeit in der Lehre, die dabei entwickelten Ideen, viele anregende Diskussionen und die unzähligen Aktivitäten in- und außerhalb des Lehrstuhls.

Abschließend möchte ich meiner Familie danken. Ohne euere bedingungslose Unterstützung in Schule, Studium und während der Promotion wäre alles nicht möglich. Euch habe ich alles zu verdanken!

Liebe Sophie, vielen Dank für deine Unterstützung und deine Nachsicht mit mir während des Verfassens der Dissertation. Du warst und bist mir eine große Stütze. Ich danke dir von Herzen dafür!

Tórshavn, März 2024 Daniel Heilbronn

Abstract

Mixtures of hydrogen (H_2) and carbon monoxide (CO), often known as syngas, are found in the chemical industry and in severe accident scenarios in nuclear power plants. An explosive mixture with ambient air might be formed due to leakage. The scenario of ignition, flame acceleration, and the onset of detonation, known as the deflagration-to-detonation transition (DDT), poses a worst-case scenario due to the high pressure load on the surrounding structure. A precise risk assessment is therefore needed. Experiments to provide fundamental knowledge on flame propagation in H_2-CO-air mixtures and validation data are rare.

This thesis aims to provide fundamental knowledge on flame propagation in H_2-CO-air mixtures by an experimental investigation in a small-scale channel. The used GraVent-channel has a rectangular cross-section and a length of 6 m. Flame propagation was investigated by pressure sensors and flame trajectory tracking by photodiodes in four partially obstructed and one unobstructed configuration. In order to determine the impact of CO on flame propagation, three fuel compositions of 100/0, 75/25, and 50/50 H_2/CO were investigated in a range from 15 vol.-% to 40 vol.-% fuel in air. In addition to homogeneous fuel distributions, inhomogeneous mixtures involving transverse concentration gradients were investigated. The experiments were analyzed with respect to run-up distances to the speed of sound of the products, onset of detonation, and peak pressures.

In obstructed configurations, the onset of detonation is not altered by the CO-content in the case of fuel-lean compositions. In the case of fuel-rich conditions, however, the detonation regime is extended to higher fuel contents by higher CO-contents. A decelerating effect was found in the unobstructed channel. For inhomogeneous mixtures, no accelerating effect was found in obstructed configurations. In the unobstructed channel, the accelerating effect of concentration gradients is decreased if the CO-content of the fuel is increased.

Kurzfassung

Gemische aus Wasserstoff (H_2) und Kohlenmonoxid (CO), oft als Synthesegas bezeichnet, kommen in der chemischen Industrie und bei schweren Unfällen in Kernkraftwerken vor. Durch eine Leckage kann sich durch Mischung mit der Umgebungsluft ein explosives Gemisch bilden. Das Szenario von Zündung, Flammenbeschleunigung und Eintritt einer Detonation, das als Deflagrations-Detonations Transition (DDT) bezeichnet wird, stellt aufgrund der hohen Drucklasten auf die umgebenden Struktur ein Worst-Case-Szenario dar. Daher ist eine genaue Risikobewertung erforderlich. Experimente zur Flammenausbreitung in H_2-CO-Luft-Gemischen sind selten.

Ziel dieser Arbeit ist es, grundlegende Erkenntnisse über die Flammenausbreitung in H_2-CO-Luft-Gemischen mittels einer experimentellen Untersuchung in einem kleinskaligen Kanal zu erlangen. Die verwendete GraVent-Anlage hat einen rechteckigen Querschnitt und ist 6 m lang. Die Flammenausbreitung wird mittels Drucksensoren sowie Photodioden zur Bestimmung der Flammentrajektorie in vier teilblockierten Konfigurationen sowie einer unblockierten Konfiguration untersucht. Zur Bestimmung des Einflusses von CO werden drei Brennstoffzusammensetzungen von 100/0, 75/25 und 50/50 H_2/CO in einem Bereich von 15 vol.-% bis 40 vol.-% von Brennstoff in Luft gezündet. Neben homogenen Mischungen werden auch Mischungen mit transversalen Konzentrationsgradienten untersucht. Die Experimente werden hinsichtlich der Anlaufstrecken zur Schallgeschwindigkeit der Produkte, des Einsetzens der Detonation sowie der Spitzendrücke ausgewertet.

In teilblockierten Konfigurationen wird das Einsetzen der Detonation bei unterstöchiometrischen Gemischen nicht durch den CO-Gehalt beeinflusst. Bei überstöchiometrischen Gemischen wird das Detonationsregime durch höhere CO-Gehalte auf höhere Brennstoffgehalte ausgedehnt. Im unblockierten Kanal wurde ein verzögernder Effekt von CO festgestellt. Infolge inhomogener Gemische ist in teilversperrten Konfigurationen kein beschleunigender Effekt feststellbar. Im unblockierten Kanal wird die beschleunigende Wirkung von Konzentrationsgradienten verringert, wenn der CO-Gehalt des Brennstoffs erhöht wird.

Contents

List of Figures

List of Tables

Nomenclature

Roman letters

A	Area	m^2
A	Pre exponential factor	s^{-1}
a	Speed of sound	$\mathrm{m\,s}^{-1}$
a	Thermal diffusivity	$\mathrm{m}^2\,\mathrm{s}^{-1}$
c_p	Isobaric heat capacity	$\mathrm{J\,kg}^{-1}\,\mathrm{K}^{-1}$
D	Detonation velocity	$\mathrm{m\,s}^{-1}$
D	Mass Diffusivity	$\mathrm{m}^2\,\mathrm{s}^{-1}$
d	Diameter	m
E_A	Activation energy	J
H	Height	m
h	Specific enthalpy	$\mathrm{J\,kg}^{-1}$
K	Correction factor	
k	Rate coefficient	s^{-1}
k	Turbulent kinetic energy	$\mathrm{m}^2\,\mathrm{s}^{-2}$
L	Characteristic geometric length	m
l	Characteristic chemical/flow length	m
m	Mass	kg
n	Temperature exponent	
p	Pressure	$\mathrm{N\,m}^{-2}$

q	Specific heat	$\mathrm{J\,kg^{-1}}$
R	Specific gas constant	$\mathrm{J\,kg^{-1}\,K^{-1}}$
s	Flame velocity	$\mathrm{m\,s^{-1}}$
S	Spacing	m
t	Time	s
T	Temperature	K
u	Velocity	$\mathrm{m\,s^{-1}}$
X	Volume fraction	vol.-%
x	Distance	m
x, y, z	Carthesian Coordinates	m

Greek letters

δ	Thickness	m
Δ	Deviation/Step width	
ϵ	Dissipation rate of turbulent kinetic energy	$\mathrm{J\,kg^{-1}\,s^{-1}}$
Γ	Stretch rate	$\mathrm{s^{-1}}$
γ	Heat capacity ratio	
Θ	Thermicity	$\mathrm{s^{-1}}$
σ	Expansion ratio	
ρ	Density	$\mathrm{kg/m^3}$
λ	Detonation cell width	m
Φ	Equivalence ratio	
ν	Kinematic viscosity	$\mathrm{m^2\,s^{-1}}$

Superscripts

$(\ )'$	Fluctuation (Reynolds decomposition)
$\overline{(\ )}$	Mean of variable
$(\ )^f$	Formation
$(\ )^s$	Sensible

Subscripts

$(\ )_{\mathrm{amb}}$	Ambient
$(\ )_{\mathrm{b}}$	Burnt
$(\ )_{\mathrm{CJ}}$	Chapman-Jouguet
$(\ )_{\mathrm{crit}}$	Critical
$(\ )_{\mathrm{D}}$	Diffusion
$(\ )_{\mathrm{dyn}}$	Dynamic
$(\ )_{\mathrm{eff}}$	Effective
$(\ )_{\mathrm{F}}$	Fuel
$(\ )_{\mathrm{f}}$	Flame
$(\ )_{\mathrm{i}}$	State i
$(\ )_{\mathrm{ij}}$	Transition from state i to j
$(\ )_{\mathrm{ind}}$	Induction
$(\ )_{\mathrm{init}}$	Initial
$(\ )_{\mathrm{inj}}$	Injection
$(\ )_{\mathrm{L}}$	Laminar
$(\ )_{\mathrm{M}}$	Markstein
$(\ )_{\mathrm{max}}$	Maximum

$(\ )_{\mathrm{mes}}$	Measurement
$(\ )_{\mathrm{obs}}$	Obstructed
$(\ )_{\mathrm{p}}$	Preheat zone
$(\ )_{\mathrm{post}}$	Post
$(\ )_{\mathrm{pr}}$	Products
$(\ )_{\mathrm{pre}}$	Prior
$(\ )_{\mathrm{vN}}$	Von Neumann
$(\ )_{\mathrm{re}}$	Reactants
$(\ )_{\mathrm{ref}}$	Reference
$(\ )_{\mathrm{s}}$	Supply
$(\ )_{\mathrm{t}}$	Turbulent
$(\ )_{\mathrm{term}}$	Terminal
$(\ )_{\delta}$	Reaction zone
$(\ )_{\eta}$	Kolmogorov

Dimensionless numbers

Le	Lewis number	a/D
Ka	Karlovitz number	$\left(l_{\mathrm{L}}/l_{\eta}\right)^2$
Ka_{δ}	Second Karlovitz number	$\left(l_{\delta}/l_{\eta}\right)^2$
M	Mach number	u/a
Ma	Markstein number	$L_{\mathrm{M}}/l_{\mathrm{L}}$
Re	Reynolds number	uL/ν
$\tilde{u}$	Dimensionless velocity	u/D
β	Zeldovich number	$E_{\mathrm{A}}(T_{\mathrm{b}} - T_{\mathrm{init}})/RT_{\mathrm{b}}^2$

Abbreviations

1D	One-dimensional
2D	Two-dimensional
3D	Three-dimensional
BR	Blockage Ratio
CFD	Computational fluid dynamics
CJ	Chapman-Jouguet
DDT	Deflagration-to-detonation transition
DNS	Direct numerical simulation
FA	Flame acceleration
KH	Kelvin-Helmholz instability
LD	Landau-Darrieus instability
LOCA	Loss of Coolant Accident
LS	Leading shock
MCCI	Molten Core-Concrete Interaction
MS	Mach stem
PAR	Passive autocatalytic recombiner
RM	Richtmyer-Meshkov instability
RT	Rayleigh-Taylor instability
SWACER	Shock wave amplification by coherent energy release
TD	Thermo-diffusive instability
TP	Triple point
TS	Transverse shock
URANS	Unsteady Reynolds-averaged Navier-Stokes Equations
UV	Ultraviolet
VN	Von Neumann
ZND	Zeldovich-von Neumann-Döring

Chemical formulas

CO	Carbon monoxide
CO_2	Carbon dioxide
H_2	Hydrogen
H	Hydrogen radical
H_2O	Water
HO_2	Hydroperoxyl radical
H_2O_2	Hydrogen peroxide
M	Non-reacting species
N_2	Nitrogen
O_2	Oxygen
O	Oxygen radical
OH	Hydroxyl radical

1 Introduction

1.1 Motivation

Countries worldwide face the severe consequences of the anthropogenic greenhouse effect [1]. Reducing greenhouse gas emissions is becoming increasingly urgent, while a reliable energy supply must be ensured [2]. The use of syngas[‡], which consists mainly of hydrogen (H_2) and carbon monoxide (CO), can contribute to a future energy supply [3]. Syngas gas can be produced by coal gasification [4] or biomass [5], offering opportunities to reduce greenhouse gas emissions for a sustainable energy supply. It can be used as an energy carrier for power-to-gas concepts [3]. In addition, syngas is already an essential raw gas used for many production processes in chemical plants, e.g., for the production of ammonia [6]. However, as the production and storage of large quantities of syngas increase, so does the risk of leakage and subsequent explosion accidents [7], involving equipment damage, injuries, and loss of life. Therefore, an accurate risk assessment is required.

Mixtures of H_2 and CO also play a crucial role in severe accident scenarios such as loss of coolant accidents (LOCA) in nuclear power plants [8]. Simulations of the accident at the Fukushima-Daichii nuclear power plant in 2011 showed that large amounts of H_2 and CO were produced during the accident due to the oxidation of the fuel rod cladding and molten core-concrete interactions (MCCI) [9]. The subsequent explosion in reactors 1, 3, and 4 of the Fukushima nuclear power plant resulted in additional emission of radioactive gases [10] and severe structural damage to the reactor buildings and technical inventory [11]. In European nuclear power plants, passive autocatalytic recombiners (PARs) were installed to reduce combustible gas accumulation

---

[‡] In this thesis, syngas is referred to as a mixture of H_2 and CO only. In real-world applications, syngas comprises a variety of other combustible and non-combustible components depending on its origin and usage.

in the reactor building. However, their efficiency in recombining CO is lower than for H_2. The decomposition of the total fuel content is thus slowed down [12].

In both scenarios, the risk assessment must consider the formation of a flammable cloud as the leaking gases mix with the ambient air. In industrial applications, the explosive mixture often forms in a confined and partially obstructed space. The low molecular weight of H_2-CO-mixtures, high temperatures, and possible jet release of the gases can lead to stratification under the ceiling of the confining structure [13]. Due to the low ignition energy and wide flammability limits of H_2-CO-air mixtures, ignition by a spark or by contact with a hot surface is likely in accident scenarios [8]. The subsequent explosion is characterized by the propagation of a flame through a premixed fuel-air mixture. The term explosion incorporates the different flame propagation mechanisms of deflagration and detonation [14].

After ignition, a laminar deflagration with low flame velocities will initially propagate. Obstacles in the flame propagation path (e.g., pipes or other fixtures) will create turbulence, leading to flame acceleration (FA) and, eventually, the onset of detonation. The entire process is referred to as deflagration-to-detonation transition (DDT) [15]. The pressure load on the surrounding structure increases with increasing flame speed [14]. In particular, the onset of detonation and the propagation of a self-sustaining detonation can be considered a worst-case scenario, as pressures up to 20 times the initial pressure can be expected [15]. The exact development of the explosion depends on many factors, such as the surrounding geometry, the geometry of the obstacles, the fuel gas composition, and the fuel content in the air [14]. FA can further be amplified if the flame propagates through a stratified fuel-air mixture [16].

For a detailed prediction of mixture formation, as well as flame propagation and explosion-induced pressure loads in real-world scenarios, computational fluid dynamics (CFD) are used. One approach is directly solving all relevant transport equations based on first principles using direct numerical simulation (DNS). Chemical and flow time and length scales must be resolved from the largest to the smallest scale. Hence, the DNS approach requires a high grid resolution. Due to the large scale of the industrial plants and the limited computational power, DNS is not applicable for the risk assessment of entire plants with appropriate resources. In the case of the unsteady Reynolds-averaged Navier-Stokes (URANS) models, highly resolved grids are not required. Only large-scale flow motions are resolved in these under-resolved approaches, and sub-grid models must be included [17, 18]. In order to validate the models, validation data covering the entire process over a wide range of parameters, such as gas mixtures and obstacle configurations, is needed [19].

Despite the increasing availability of computing power and efficient under-resolved solvers, individual computations on industrial scales can take up to several days [20]. However, the composition of the gas cloud changes as the accident progresses, while an exact ignition timing and location cannot always be predicted [9]. Thus, many individual simulations may be required. Therefore, predictions based on empirical criteria and basic experimental knowledge about the flame dynamics in different gas mixtures can considerably shorten and simplify a risk assessment.

Due to the widespread industrial application of H_2, much research on FA and DDT in H_2-air mixtures is available. This includes experimental data in unobstructed and partially obstructed geometries for small and large scales [15]. The influence of mixture inhomogeneities was investigated in the case of transverse [16, 21–29] as well as in case of lateral concentration gradients [30–35].

Studies covering the entire process of DDT in H_2-CO-air mixtures are rare. Experimental data is available for very lean mixtures at one small scale, unvented [36] and one large scale, vented geometry [37]. In both cases, the channel was obstructed over the total length. A widespread variation of fuel content, obstacle geometry, and experimental data for an unobstructed channel is not available. Due to the transient evolution of real-world accident scenarios, a wide spread of equivalence ratios within the flammable cloud can be expected [38].

In practice, it is often assumed H_2-CO-air mixtures pose a less significant risk for FA and DDT due to inhibiting effects of CO. Therefore, and due to the lack of data, additional CO is replaced by H_2 in conservative risk assessments [39].

However, it is not clear whether this assumption is valid over a wide range of geometrical configurations, fuel contents, and fuel mixtures. Consequently, this thesis aims to provide insight into FA and DDT in H_2-CO-air mixtures based on experimental investigations. The data collected covers a wide range of fuel contents in homogeneous and inhomogeneous cases.

1.2 Aim of this thesis

Based on the knowledge about FA and DDT in H_2-air mixtures, this work aims to extend the understanding towards H_2-CO-air mixtures. Therefore, a total of 6.000 experiments have been conducted. The experimental matrix includes fuel mixtures of 75/25 H_2/CO and 50/50 H_2/CO, as well as 100/0 H_2/CO mixtures as reference cases. Experiments were conducted at the small-scale GraVent facility, featuring unobstructed and partially obstructed geometries. The rear third of the channel always remained unobstructed. The influence of mixture inhomogeneities is compared to the results in H_2-air mixtures reported in previous works at the test rig from Vollmer [23] and Boeck [16]. Based on the thermodynamic properties of the CO-containing mixtures, similarities and differences are investigated, and approaches to compare different fuels are presented.

This work starts by providing fundamentals on flame dynamics in closed channels in Ch. 2. First, the reaction pathways of syngas oxidation are presented. The chapter further discusses flame propagation regimes from laminar flame propagation, flame acceleration to the onset, and the propagation of detonations. Special attention is paid to comparing H_2-air and H_2-CO-air mixtures. Finally, the state of knowledge on flame acceleration and deflagration-to-detonation transition in H_2-CO-air mixtures is presented.

The experimental setup is described in Ch. 3. This includes a precise description of the channel, the investigated obstacle configurations, and the applied experimental procedures. Flame propagation in an inhomogeneous mixture is likely in accident scenarios. Therefore special attention is paid to the generation of transverse concentration gradients in the three-component H_2-CO-air mixture. The applied measurement techniques are explained at the end of the chapter.

Results are presented in Ch. 4. For a better understanding, the data evaluation based on actual experimental results is presented first, beginning with the homogeneous case. Experiments are evaluated concerning the run-up distances to the speed of sound of the products, the onset of detonation, and measured peak pressures. Furthermore, the investigation differentiates between the onset of detonation in obstructed and unobstructed channel configurations. The investigation of inhomogeneous mixtures extends the analysis.

In Ch. 5, a summary followed by an outlook highlighting the most important aspects of the presented results and possible future research close this work.

2 Fundamentals

This thesis focuses on the process of FA and DDT after a weak ignition of a H_2-CO-air mixture in a closed channel. Therefore, the structure of this chapter follows the sequence of flame dynamics as shown in Fig. 2.1 with a focus on the comparison between H_2-air and H_2-CO-air mixtures. First, an overview of the explosion process is given. Sec. 2.2 explains the fundamentals of reactive compressible flows and outlines the most important equations. Basic chemical reactions of the combustion of H_2-CO-mixtures are presented in Sec. 2.3. The process of flame acceleration and the onset of detonation are discussed in Sec. 2.5 and 2.6. In Sec. 2.7, the detonation phenomenon is described. Finally, available experiments on FA and DDT in H_2-CO-air mixtures are reviewed in Sec. 2.8

2.1 Flame dynamics in accident scenarios

Depending on multiple boundaries and initial conditions such as confining geometry, mixture composition, and thermodynamic state, explosion phenomena can result in different flame propagation regimes: deflagration and detonation. The resulting peak pressures and loads on the confining structure are related to the flame speed. In case of a deflagration, flames can reach velocities in the order of $100\,\mathrm{m\,s^{-1}}$, while the overpressure is about $0.1\,\mathrm{MPa}$. In case of a detonation, the flame can reach supersonic velocities up to $2000\,\mathrm{m\,s^{-1}}$ and an overpressure of more than $2\,\mathrm{MPa}$. Even higher peak pressures are reached during the onset of detonation.

Since highly energetic ignition sources such as explosives are typically not found in accident scenarios, direct detonation initiation is highly unlikely.

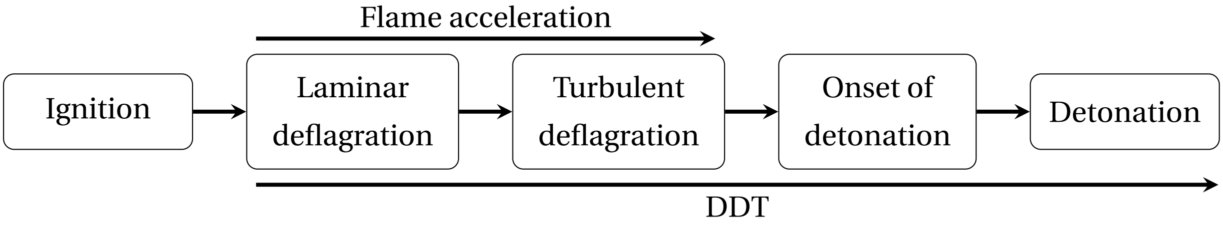

Figure 2.1: Flame evolution in accident scenarios (adapted from [40]).

Flame propagation starts with a mild ignition by a spark or a hot surface, followed by flame propagation in the deflagration flame regime. In order to transit to a detonation, several steps in flame evolution are required, as depicted in Fig. 2.1.

In the deflagration regime, flame propagation is caused by molecular diffusion of heat and species. A deflagration can further be classified in a laminar and turbulent regime. After ignition, the flame spreads in the laminar regime. A smooth, undistorted flame surface characterizes the laminar regime. Instabilities at the flame front distort the smooth surface and lead to a wrinkled flame front. The accompanying enlargement of the flame front surface increases the overall reaction rate and marks the onset of the flame acceleration process. In the case of a closed channel, the expanding hot products act as a piston, pushing the reactants in the direction of flame propagation and generating a flow in the channel. Turbulent flow regions are formed ahead of the flame, especially at wall layer boundaries and in the wake of geometry changes, such as obstacles. A turbulent flow is composed of eddies of different sizes. The eddies enhance the transfer of heat and species at the flame front. The overall reaction rate is further increased, and the flame front surface is enlarged. The flame is accelerated, and the flame propagation speed rises.

Additionally, acoustic waves are emitted by the flame each time the heat release within the flame changes [41]. These waves coalesce and might form a shock ahead of the flame. Adiabatic shock heating increases the pressure and temperature of the reactants. The interaction of reflected shocks and the flame further increases the reaction rate. As a result of strong flame acceleration, flame speeds up to 1000 m s^{-1} are reached, and the conditions necessary for the onset of detonation can be met. Due to a local explosion, the onset of detonation may follow. The detonation complex consists of a coupled shock and reaction front. In a detonation, the ignition of the reactants is achieved by autoignition due to heating by a shock. A detonation is accompanied by high overpressure and propagates at supersonic velocities into the fresh mixture.

2.2 1D compressible reactive flow

The following description of the basic equations for a one-dimensional (1D) reactive compressible flow is taken from [42]. Shock and flame front are treated as an infinitesimally thin discontinuity. The notation follows the one given in Fig. 2.2 with 1 being the state upstream and 2 being the state downstream of the flame.

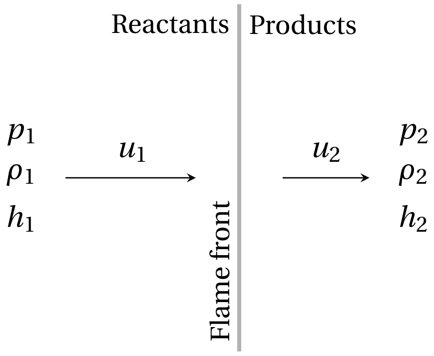

Figure 2.2: States upstream and downstream of a combustion wave with a fixed coordinate system.

A given steady-state, adiabatic, inviscid combustion wave in a perfect gas can be treated by the application of the equations of

$$\text{mass}: \quad \rho_1 u_1 = \rho_2 u_2, \tag{2.1}$$

$$\text{momentum}: \quad p_1 + \rho_1 u_1^2 = p_2 + \rho_2 u_2^2 \tag{2.2}$$

$$\text{and energy:} \quad h_1^s + q_{12} + \frac{u_1^2}{2} = h_2^s + \frac{u_2^2}{2}. \tag{2.3}$$

In Eqn. 2.1 to 2.3, ρ is the density, u the flow velocity, p the pressure, and h the sensible enthalpy at the given state. The enthalpy h_i at each state i is the sum of the sensible enthalpy h_i^s and the enthalpy of formation h_i^f

$$h_\mathrm{i} = h_\mathrm{i}^s + h_\mathrm{i}^f = c_\mathrm{p}(T_\mathrm{i} - T_\mathrm{ref}) + h_\mathrm{i}^f. \tag{2.4}$$

In Eqn. 2.4, the temperature at state i is given by T_i. T_ref is the temperature at reference conditions. The isobaric heat capacity c_p is given by

$$c_\mathrm{p} = \frac{R\gamma}{\gamma - 1}. \tag{2.5}$$

In Eqn. 2.5, R is the specific gas constant, and γ is the heat capacity ratio. The specific heat of the reaction q_{12} in equation 2.3 is given by the difference between the enthalpies of formation of the reactants h_1^f and the products h_2^f

$$q_{12} = h_1^f - h_2^f. \tag{2.6}$$

For H_2-CO mixtures, the specific heat at isobaric, stoichiometric conditions varies between $q_{12} = 10.4\,\mathrm{MJ\,m^{-3}}$ for 100/0 H_2/CO and $q_{12} = 11.1\,\mathrm{MJ\,m^{-3}}$ for 50/50 H_2/CO.

The speed of sound a at state 1 is given by $a_1 = \sqrt{\gamma R T_1}$. The Mach number M_1 can be defined by

$$M_1 = \frac{u_1}{a_1}. \tag{2.7}$$

The Rayleigh line can be derived from Eqn. 2.1 and 2.2. By doing so, a relation between the change in pressure p_2/p_1 in terms of the change in density ρ_1/ρ_2 and the initial Mach number M_1 is given by

$$\frac{p_2}{p_1} = 1 + \gamma M_1^2 \left(1 - \frac{\rho_1}{\rho_2}\right). \tag{2.8}$$

Additionally, combining the conservation equations for momentum 2.2 and energy 2.3, as well as 2.4 and 2.6 and introducing the Hugoniot equation can be obtained

$$\frac{p_2}{p_1} = \frac{\dfrac{\gamma+1}{\gamma-1} - \dfrac{\rho_1}{\rho_2} + \dfrac{2\gamma}{\gamma-1}\dfrac{q_{12}}{c_\mathrm{p} T_1}}{\dfrac{\gamma+1}{\gamma-1}\dfrac{\rho_1}{\rho_2} - 1}. \tag{2.9}$$

In an adiabatic shock wave, the general Hugoniot equation given in 2.9 can be rewritten and combined with 2.8, representing the normal shock relations. A transition from reactants to products must follow the Rayleigh line, while the final state lies on the Hugoniot curve.

2.3 Chemical kinetics

The global reaction of H_2 and CO with oxygen (O_2) can be subdivided into elementary reactions. A kinetic model of the global reaction is based on a set of elementary reactions. The kinetic model allows the determination of the individual reaction paths of the global reaction. Highly reactive radicals are the most important species for the reaction progress. Concerning the number of radicals consumed and produced by elementary reactions, each elementary reaction can be attributed to chain initiation reactions, chain branching reactions, and chain termination reactions [43].

The rate of each reaction can be estimated by the rate coefficient k. If Arrhenius-type reactions are assumed, k is given by

$$k = AT^n e^{\frac{-E_\mathrm{A}}{RT}}. \tag{2.10}$$

According to Eqn. 2.10, the rate coefficient k depends on a pre-exponential constant A, the thermodynamic temperature T, the temperature exponent n, the activation energy E_A and the gas constant R. Within reaction mechanisms, the activation energy E_A, the pre-exponential constant A, and the temperature exponent n are tabulated for each elementary reaction.

Comparative studies of recent syngas oxidation mechanisms can be found in [4,44,45]. For the scope of this thesis, the Davis-mechanism [46] is used. Kinetic models of the H_2-CO-O_2-system are crucial as these form fundamental systems of any hydrocarbon combustion chemistry [45]. The most important reactions in the oxidation of H_2-CO-mixtures are:

$$\mathrm{H + O_2 \rightleftharpoons O + OH} \tag{R 1}$$

$$\mathrm{O + H_2 \rightleftharpoons H + OH} \tag{R 2}$$

$$\mathrm{H_2 + OH \rightleftharpoons H_2O + H} \tag{R 3}$$

$$\mathrm{O + H_2O \rightleftharpoons OH + OH} \tag{R 4}$$

$$\mathrm{H + O_2 + M \rightleftharpoons HO_2 + M} \tag{R 5}$$

$$\mathrm{H_2O_2 + M \rightleftharpoons OH + OH + M} \tag{R 6}$$

$$\mathrm{H_2 + HO_2 \rightleftharpoons H_2O_2 + H} \tag{R 7}$$

$$\mathrm{HO_2 + HO_2 \rightleftharpoons H_2O_2 + O_2} \tag{R 8}$$

$$\mathrm{OH + H_2 \rightleftharpoons H + H_2O} \tag{R 9}$$

$$\mathrm{HO_2 + H \rightleftharpoons OH + OH} \tag{R 10}$$

$$HO_2 + OH \rightleftharpoons H_2O + O_2 \qquad \text{R 11}$$

$$H + OH + M \rightleftharpoons H_2O + M \qquad \text{R 12}$$

$$HO_2 + O \rightleftharpoons O_2 + OH \qquad \text{R 13}$$

Four reactions involving CO are of major importance [44]:

$$CO + O + M \rightleftharpoons CO_2 + M \qquad \text{R 14}$$

$$CO + O_2 \rightleftharpoons CO_2 + O \qquad \text{R 15}$$

$$CO + OH \rightleftharpoons CO_2 + H \qquad \text{R 16}$$

$$CO + HO_2 \rightleftharpoons CO_2 + OH \qquad \text{R 17}$$

If no moisture or H_2 is present, CO oxidation proceeds through R 14 and R 15. As the reaction rates of R 14 and R 15 are low, the oxidation rate of CO is slow. However, if small amounts of H radicals are present, reactions R 16 and R 17 dominate the CO oxidation [43].

The main path for CO oxidation and a major heat source is given by R 16 [44]. As OH radicals are needed for R 16, the production of OH by other reactions is essential for CO oxidation. Production of OH can be achieved by adding moist or H_2 [45], which explains why the oxidation of H_2-CO fuels is dominated by H_2 chemistry. Furthermore, R 16 is a chain-propagating step, providing H radicals needed for the production of further OH radicals via R 1. Therefore, understanding the explosion behavior of the H_2-O_2 system is crucial for understanding the more complex H_2-CO-O_2 system.

Three characteristic explosion limits can be determined for a stoichiometric H_2-O_2 mixture, as shown in the p-T-diagram in Fig. 2.3. The blue line in the diagram can be interpreted as the explosion limit of a given mixture at a given temperature and pressure in a closed vessel. The explosion limit is crossed three times when increasing the pressure at a constant temperature, as indicated by the grey line in Fig. 2.3. If the pressure is sufficiently low, no explosion is found as radicals diffuse to the wall of the vessel and are not available for reactions below the first explosion limit. As soon as the first explosion limit is exceeded, production of radicals exceeds deactivation by diffusion to the walls, and the mixture explodes following the OH chain involving R 1 - R 4. The second explosion limit is reached by further increasing the pressure. In this state, R 1 and R 5 compete for H radicals. The less reactive HO_2 diffuses to the wall and is deactivated. In experiments, an extension of the second explosion limit towards higher pressure and temperature is observed. Autoignition is found on both sides of the extended second explosion limit. However, for states on the left side, a faster reaction than for initial states on the right side is observed. This behavior is particularly relevant for H_2-air mixtures as temperature and pressure are close to the extended second explosion limit downstream of shocks of $M > 2$. The onset of detonation is more likely if the downstream state is located on the left side of the extended second explosion limit due to the faster reaction [16]. The third explosion limit is reached when the pressure is further increased as the H_2O_2 cycle becomes more important [43]. Since these reactions are also part of H_2-CO-O_2 mechanism, the explosion limits of syngas show a similar behavior [47–51]. In [52], Liang et al. showed that the typical Z-shaped explosion behavior shown in Fig. 2.3 can also be found for syngas mixtures containing little amounts of H_2. A comparison of explosion limits of 50/50 and 100/0 H_2/CO mixtures showed almost no differences.

The inhibiting effect of CO on syngas ignition delay times was demonstrated using a rapid compression machine (RCM) by Keromnes et al. [53]. However, the effect of CO inhibition is more prominent for mixtures containing more than 50 % CO. In addition, it was shown that H_2 dominates the ignition behavior of syngas mixtures. Even the addition of 50 % CO showed only a minor influence on the ignition delay time for stoichiometric mixtures at about 400 kPa. Compared with mixtures of the same H_2 content, mixtures of 5/95 H_2/CO showed a much longer ignition delay time. In these cases, H_2 consumption is fast, while the slower CO oxidation is initialized by the OH providing H_2 reactions. For the 50/50 H_2/CO mixture, the quick consumption of H_2 increases temperature and much higher radical concentration. Therefore, CO is consumed faster. For 5/95 H_2/CO, the lower H_2 content leads to a significantly increased ignition delay time. The H_2 consumption is further ampli-

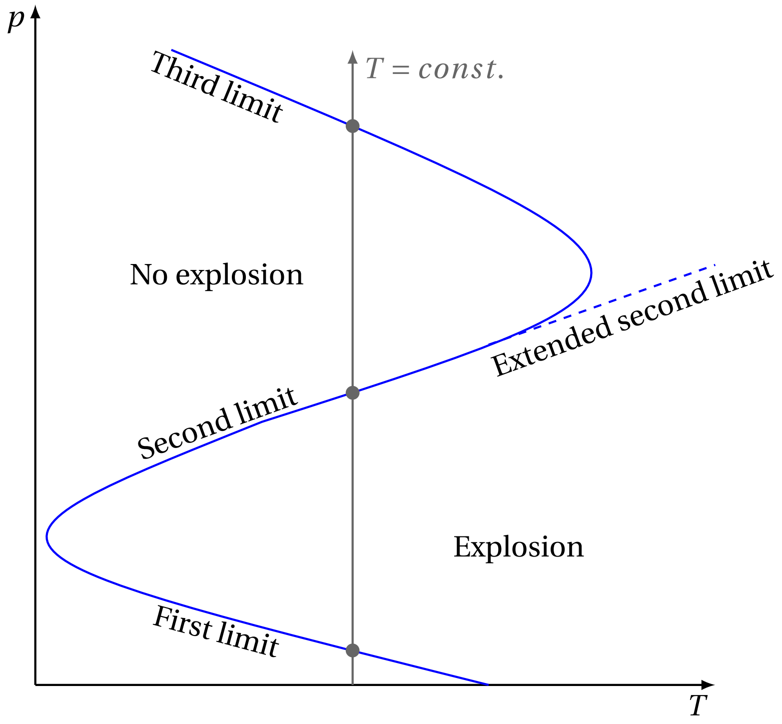

Figure 2.3: Schematic explosion limits of H_2-O_2 systems (adapted from [43]).

fied by reaction R 17, which consumes the less reactive HO_2 and produces the more reactive OH radical, leading to a quick increase of OH concentration.

Overall, the inhibiting effect of CO on ignition delay times is most noticeable for CO contents of more than 50 %. While 50 % CO leads to an increase by a factor of 2 in ignition delay time, concentrations of 90 % lead to an increase by a factor of 10. However, regarding laminar flame speeds, the inhibiting effect of CO occurs already at lower CO contents.

2.4 Laminar and turbulent deflagration

2.4.1 Laminar flame propagation

Although flame propagation in ducts can be considered turbulent in the case of even small flow velocities, laminar flames provide essential insights into characteristic flame properties.

A schematic of the structure of a laminar flame is shown in Fig. 2.4. The flame consists of a preheat zone l_P and a reaction zone l_δ. In the preheat zone, heat conduction and diffusion lead to an increase in mixture temperature starting from the temperature of the reactants T_{re}. As the temperature strongly affects the reaction rate, exothermic reactions occur in the smaller reaction zone l_δ. Reactants are consumed, and their fraction drops while the reaction product fraction rises. The temperature rises until the final temperature of the burnt mixture T_{pr} is reached.

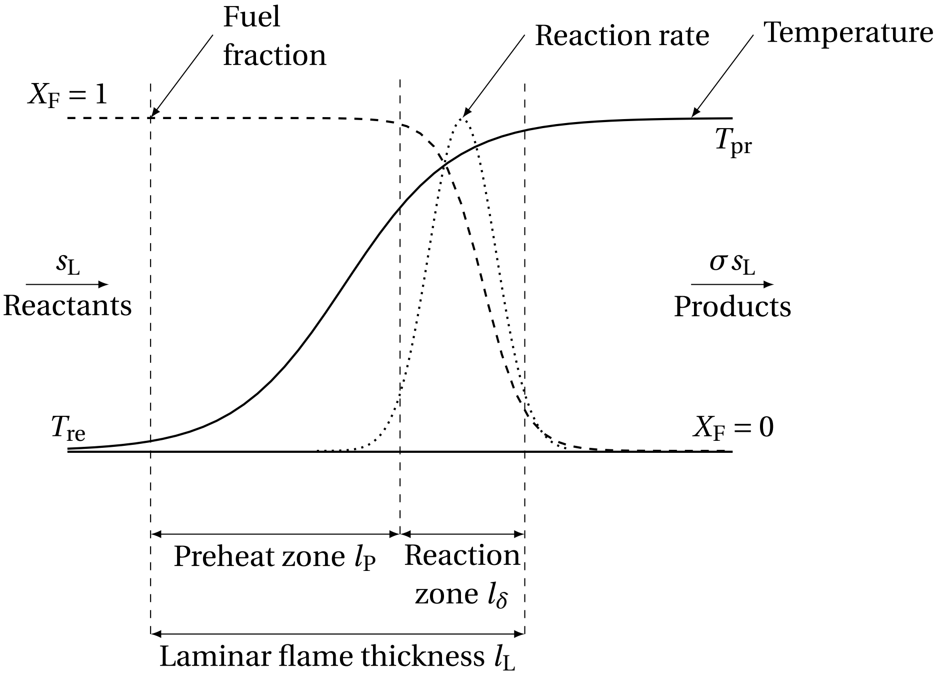

Figure 2.4: Schematic of laminar flame structure (adapted from [15]).

The propagation speed of the flame with respect to the unburnt mixture equals the laminar flame speed s_L. The laminar flame speed is one of the most important flame parameters [54] and is a fundamental property of fuel-air mixtures. Besides the temperature and pressure of the unburnt mixture, the equivalence ratio Φ and the fraction of H_2 and CO in the fuel have an important impact on s_L. The equivalence ratio Φ is defined as the ratio of the actual fuel fraction, compared to the stoichiometric composition at $X_F = 29.6\,\text{vol.-\%}$ in air for H_2/CO mixtures. The CO content in the fuel does not alter the stoichiometric composition. Due to the increasing interest in the use of syngas, various measurements of s_L can be found in literature [55–68]. Based on literature and calculations of counterflow flames in CANTERA using the Davis reaction mechanism [46], an interpolation table was created by Barfuss et al. [69]. The table allows for the calculation of laminar flame speeds between the flammability limits of H_2 (4.85-75 vol.-%) and CO (12.5-74.5 vol.-% [4]). Mixtures of H_2 and CO are provided in steps of 10 %. The laminar flame speeds s_L for the relevant fuel mixtures are plotted in Fig. 2.5.

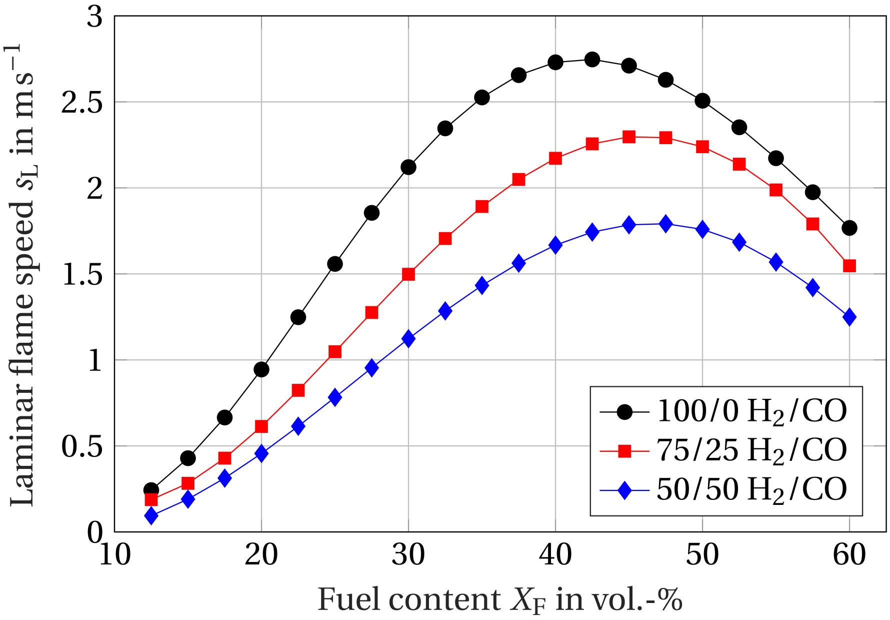

Figure 2.5: Laminar flame speed s_L of 100/0, 75/25 and 50/50 H_2/CO mixtures over fuel content X_F [69].

As shown in Fig. 2.5, the maximum laminar flame speed increases with increasing H_2 content. The fuel content at which the maximum laminar flame speed is found decreases with increasing H_2-content in the fuel. The maximum occurs at X_F = 42.5 vol.-% for 100/0, at 45 vol.-% for 75/25 and at 47.5 vol.-% for 50/50 H_2/CO. As shown in Fig. 2.5, the difference in s_L between the fuels is non-linear. When comparing 100/0 and 50/50 H_2/CO, the increase of laminar flame speed with the fuel content is stronger for 100/0 H_2/CO. The difference in s_L between the fuel compositions increases with X_F. This behavior further outlines the impact of H_2 on the overall reaction rate of the fuel-air mixture.

The reactants approach the steady flame front with laminar flame speed s_L, as indicated in Fig. 2.4. Since mass conservation must be satisfied, the downstream velocity of the flame is given by $s_L\sigma$. The expansion ratio σ is defined by the ratio of the densities of the unburned ρ_{re} to the burned mixture ρ_{pr}

$$\sigma = \frac{\rho_{re}}{\rho_{pr}}. \tag{2.11}$$

By replacing H_2 with CO in the fuel composition at a fixed equivalence ratio, the expansion ratio σ increases slightly for isobaric combustion, as shown in Fig. 2.6. The highest expansion ratio is found near stoichiometric mixtures and coincides with the highest adiabatic flame temperature. As the CO content increases, the maximum expansion ratio shifts to slightly higher fuel content. For fuel-rich mixtures of 100/0 and 75/25 H_2/CO σ almost coincides. This behavior can also be observed in the evolution of the adiabatic flame temperature [4]. In contrast to the laminar flame speed s_L, the impact of the H_2-content on the expansion ratio σ is less pronounced.

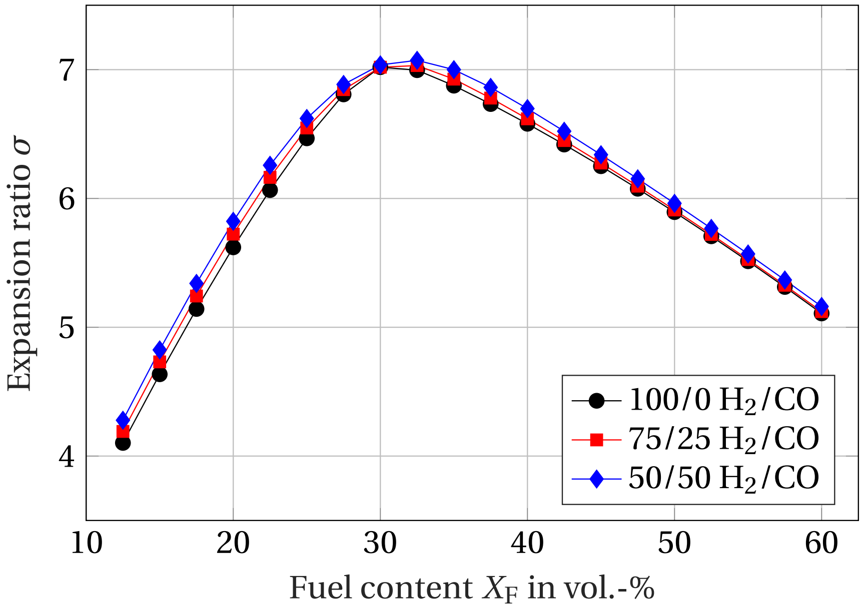

Figure 2.6: Expansion ratio σ for isobaric combustion of 100/0, 75/25 and 50/50 H_2/CO mixtures over fuel content X_F (calculated using CANTERA [70] and material properties from Davis [46]).

In addition to the laminar flame speed, CO also affects the flame structure, as shown in Fig. 2.7 for 50/50 and in Fig. 2.8 for 5/95 H_2/CO at $\Phi = 0.6$. Both figures show the heat released by the respective reactions, the total heat release, and the temperature in the flame. The peak temperatures are very similar for both flames. However, due to the higher reactivity of H_2, the total heat release is higher for 50/50 than for 5/95 H_2/CO. The increased reactivity and the faster diffusion of H_2 lead to higher laminar flame speed with increasing H_2 content, as shown in Fig. 2.5. For 50/50 H_2/CO, heat release starts as soon as the temperature increases, resulting in a very thin preheat zone. The main heat release is due to R 5, which also causes the early rise in the total heat release. H radicals are mainly formed by R 3 and R 16. The H radicals diffuse upstream and form a radical pool for R 7. OH radicals are produced and attack H_2 and CO. The structure of H_2-CO-air flames with high H_2 content is similar to that of H_2-air flames. Unlike the nearly inert preheating zone of CH_4-air flames, the reactions occur over the entire flame front.

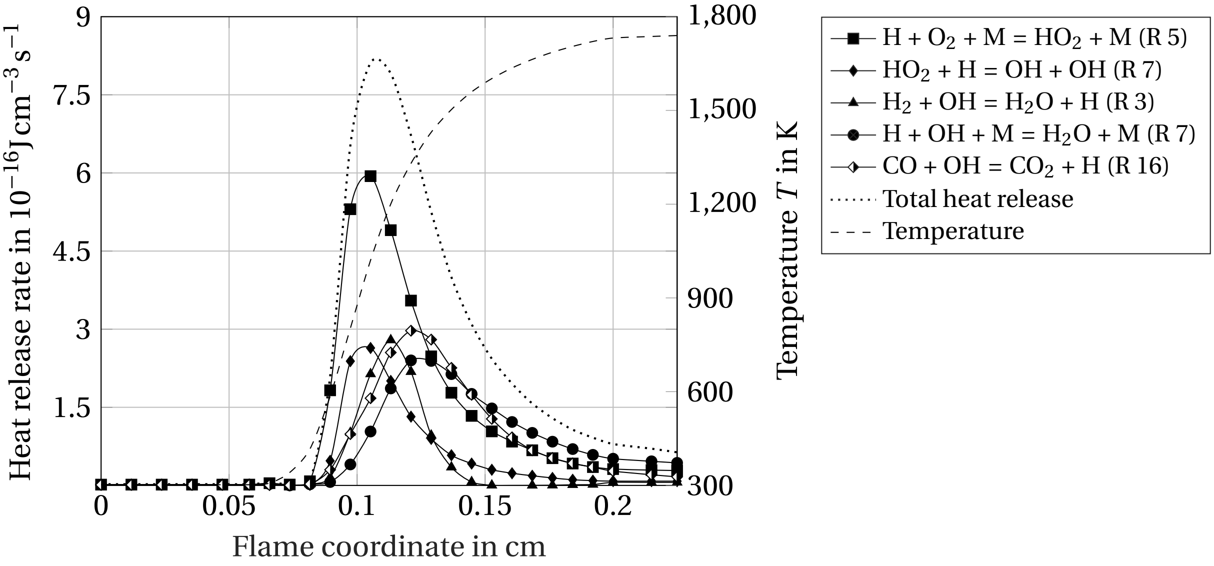

Figure 2.7: Heat release rates of the most important reactions over flame coordinate for $X_F = 20.1$ vol.-% for 50/50 H_2/CO (adapted from [4]).

In contrast to 50/50 H_2/CO at Fig. 2.7, the total heat release for 5/95 H_2/CO in Fig. 2.8 sets in at a higher temperature. The total heat release shows a broader distribution and peaks lower than 50/50 H_2/CO. The main heat-releasing reaction is R 16, which is also the main source of H. Similar to the 50/50 H_2/CO case, the H diffuse upstream, forming HO_2 with incoming O_2 by R 5. Via R 7 and R 8, OH is formed and oxidzes CO by releasing additional H. The contribution to the total heat release of R 14 is small and decreases quickly as the H_2 content is raised. The main path for H_2 oxidation via R 3 competes for OH radicals with R 16 and has little influence on the total heat release.

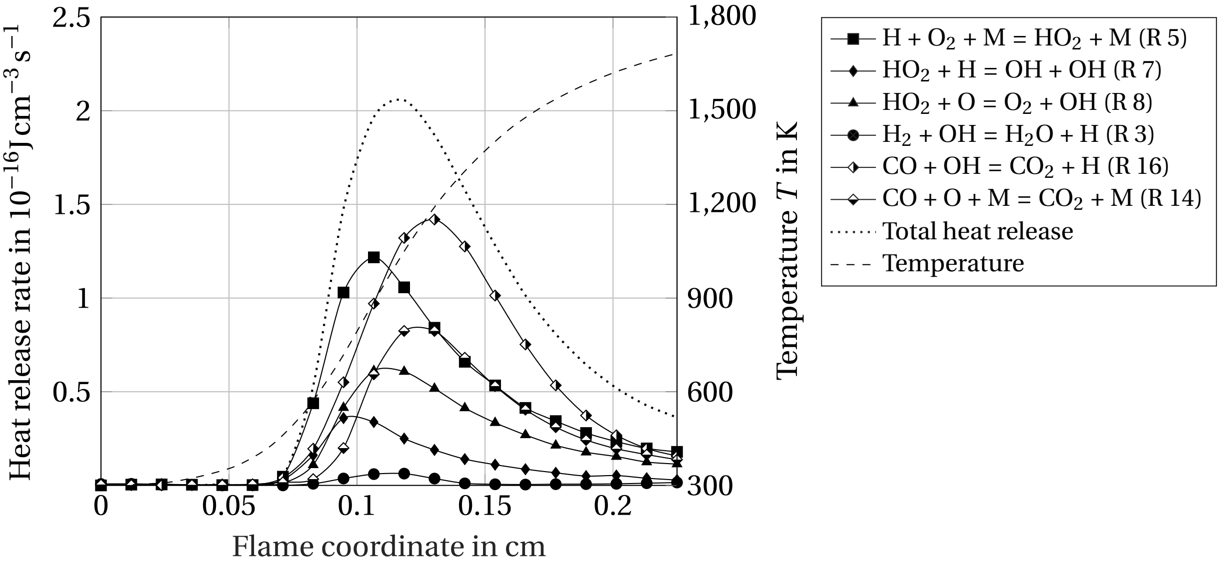

Figure 2.8: Heat release rates of the most important reactions over flame coordinate for $X_F = 20.1$ vol.-% for 5/95 H_2/CO (adapted from [4]).

A comparison of the laminar flame structure for 50/50 and 5/95 H_2/CO shows that the laminar flame thickness δ_L decreases with increasing H_2 content. The additional reactivity of H_2 outweighs the diffusivity of H_2. Furthermore, the relative thickness of the preheat in comparison to the reaction zone decreases.

In addition to the fuel composition, the equivalence ratio also affects the laminar flame structure. Comparing flames of a 50/50 H_2/CO mixture at equivalence ratios of 0.6, 1.0, and 2.08, the influence of the equivalence ratio becomes clear. For lean fuel mixtures, H_2 and CO are completely consumed. In fuel-rich mixtures, large amounts of CO remain unreacted. The characteristic flame thickness decreases as the equivalence ratio is increased. A minimum is reached at $\Phi = 2.08$ when the velocity of the laminar flame reaches its maximum.

2.4.2 Flame and flow instabilities

After the initial laminar flame propagation, various instabilities occur. The smooth laminar flame surface becomes wrinkled, which leads to an increase in the overall reaction rate [15]. Instabilities can be due to hydrodynamic or flame front effects. Flow instabilities are:

- **Kelvin-Helmholtz (KH) instability**: If fluids of different densities are in relative motion, the KH instability might lead to the distortion of the interface [71]. For FA and DDT in channels, KH instabilities are found when the flame passes through the narrow gap of an obstacle, creating a shear layer downstream of the obstacle [72].
- **Rayleigh-Taylor (RT) instability**: RT instabilities are found at an interface between two fluids of different densities. If the fluids are accelerated by gravity or other external forces, disturbances at the interface of the fluids are amplified [71]. RT instabilities are found as the flame passes obstacles in case of an accelerated flow [72].
- **Richtmyer-Meshkov (RM) instability**: The RM instability can be considered a special case of RT instability, as the acceleration of the different fluids is accomplished by the interaction with a shock. The growth of this instability is first linear in time, but finally, both fluids mix chaotically [73, 74]. RM instabilities arise from shocks reflected by side walls or obstacles interacting with the flame [72].

In particular, the KH and RT instabilities are found for flames propagating through partially blocked channels, leading to a dramatic increase in flame surface area and the generation of turbulence that accelerates the flame [15].

Apart from hydrodynamic instabilities, Landau-Darrieus (LD) and thermal-diffusive instabilities (TD) are found directly at the flame front. The occurrence of these instabilities depends on the initial conditions and the mixture composition. Especially in the early phase of flame propagation, the LD and TD instabilities increase the flame surface.

The influence of the LD instability on a flame front is depicted in Fig. 2.9. The expansion of the hot combustion products leads to the formation of a curved flame front. Due to the curvature, the streamlines converge downstream of convex sections and diverge behind concave sections of the flame front. The flame is locally accelerated in convex and decelerated in concave regions. The curvature increases with time from t_1 to t_2. However, an exponential development is not observed as the LD instability is damped due to diffusive effects [75].

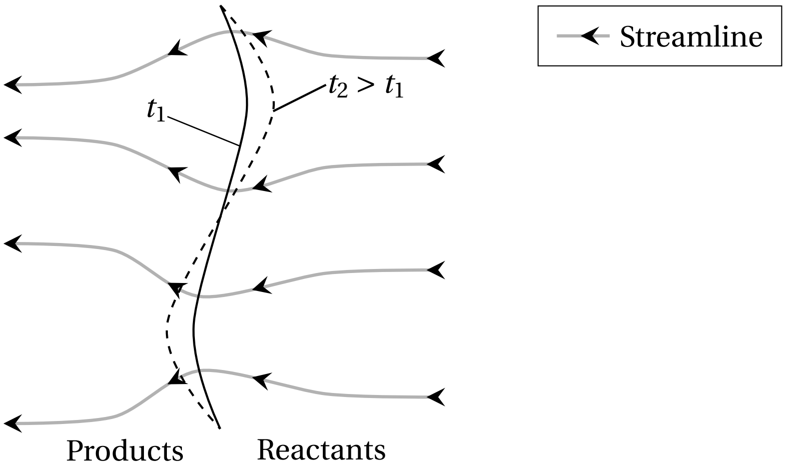

Figure 2.9: Schematic of Landau-Darrieus (LD) instability [15].

The TD instability results from an imbalance of diffusive fluxes of heat and species. The imbalance can be described using the Lewis number

$$\mathrm{Le} = \frac{a}{D}. \tag{2.12}$$

Le compares the thermal diffusivity a and the diffusivity D of the deficient species of the unburnt mixture. As a and D vary with the mixture composition, two different scenarios can be distinguished, as shown in Fig. 2.10. If $\mathrm{Le} < 1$ as shown on the left of Fig. 2.10, the thermal diffusivity a is lower than the species diffusivity D. Reactants (blue arrows) diffuse towards convex parts of the flame. At the same time, the heat loss (red arrows) is decreased in these flame regions, leading to a local increase in temperature and burning velocity. The opposite process appears in the concave parts of the flame. Therefore, small perturbations of the flame front are amplified over time.

If Le > 1, as shown on the right in Fig. 2.10, the thermal diffusivity is higher than species diffusion. Perturbations in the flame front are smoothened, and the flame is stabilized.

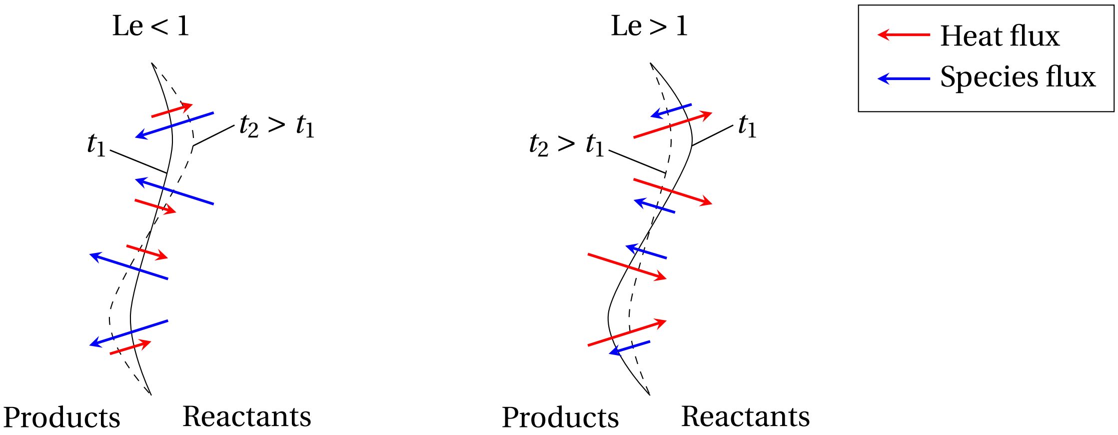

Figure 2.10: Schematic of thermal-diffusive (TD) instability [15].

For H_2-air mixtures, Le is found below unity for lean mixtures. TD instabilities are therefore found at lean conditions and promote flame acceleration during early stages of flame acceleration [76]. In the case of H_2-CO-air mixtures, Le follows a similar trend. The addition of CO leads to an increase in Le in lean conditions. The same accounts for an increase in fuel content toward the stoichiometric composition. However, Le is found below unity for all mixtures considered in this thesis for $\Phi < 1$. The transition to Le> 1 occurs close to the stoichiometric composition, as the deficient species is switched from H_2 and CO to O_2 [77].

2.4.3 Turbulent deflagration

A deflagration can be considered turbulent as soon as the flow velocity ahead of the flame is sufficiently high. A criterion for the transition to a turbulent flow is the Reynolds number, defined by

$$\mathrm{Re} = \frac{uL}{\nu}. \tag{2.13}$$

In Eqn. 2.13 L is the characteristic length, u is the flow velocity, and ν is the kinematic viscosity [78]. A flow can be considered turbulent as soon as Re is above a given value, depending on the confining structure [15]. In this case, flow instabilities lead to random fluctuations in the flow. The flow velocity u is a superposition of the mean flow velocity $\bar{u}$ and the random velocity fluctuation u' [78]. If isotropic turbulence is assumed, the velocity fluctuation can be linked to the turbulent kinetic energy k by

$$u' = \sqrt{\frac{2}{3}k}. \tag{2.14}$$

Random vortices arise, which differ in size. The size of the largest vortices is in order of the confining structure [78]. The mean size of the largest vortices is given by

$$l_\mathrm{t} = \frac{u'^3}{\epsilon}, \tag{2.15}$$

with ϵ being the turbulent dissipation rate [78]. The timescale of the largest vortices is given by

$$t_\mathrm{t} = \frac{l_\mathrm{t}}{u'}. \tag{2.16}$$

The kinetic energy is transferred from the largest vortices of size l_t to smaller vortices [78]. On the microscopic scale of the turbulent flow, the Kolmogorov length scale l_η, viscous forces lead to the dissipation of the turbulent kinetic energy k [79, 80]. The Kolmogorov length scale can be estimated by

$$l_\eta = \left(\frac{\nu^3}{\epsilon}\right)^4. \tag{2.17}$$

Analog to the integral time scale t_t, the time scale of the smallest vortices is given by:

$$t_\eta = \frac{l_\eta}{u'}. \tag{2.18}$$

The turbulent dissipation rate ϵ is linked to the flow velocity u. Hence, the dissipation rate ϵ increases for higher flow velocities while the Kolmogorov length scale l_η decreases.

Turbulent flow and turbulent length scales affect premixed combustion. In order to distinguish different regimes of turbulence-chemistry-interaction, the characteristic length scales of combustion and turbulent flow are compared by using non-dimensional numbers: the turbulent Reynolds number $\mathrm{Re_t}$, the Karlovitz number Ka and the second Karlovitz number Ka_δ.

The turbulent Reynolds number $\mathrm{Re_t}$ is defined by

$$\mathrm{Re_t} = \frac{u' l_\mathrm{t}}{\nu}. \tag{2.19}$$

In contrast to the definition of the Reynolds number, the flow velocity u is replaced by the fluctuation velocity u', while the characteristic length scale of the flow L is replaced by the turbulent length scale l_t in Eqn. 2.19.

The laminar flame thickness l_L and the turbulent microscopic length scale l_η are compared by the Karlovitz number

$$\mathrm{Ka} = \left(\frac{l_\mathrm{L}}{l_\eta}\right)^2. \tag{2.20}$$

On a smaller scale the second Karlovitz number Ka_δ compares the reaction zone thickness l_δ with the Kolmogorov length scale l_η by

$$\mathrm{Ka}_\delta = \left(\frac{l_\delta}{l_\eta}\right)^2 \approx 0.01\mathrm{Ka}. \tag{2.21}$$

For H_2 and other hydrocarbon mixtures, the thickness of the reaction zone can be estimated by $l_\delta \approx 0.1 l_L$.

Based on the Karlovitz number, turbulent combustion can be categorized into different regimes. The regimes defined by Borghi [81] and modified by Peters [82] are depicted in Fig. 2.11.

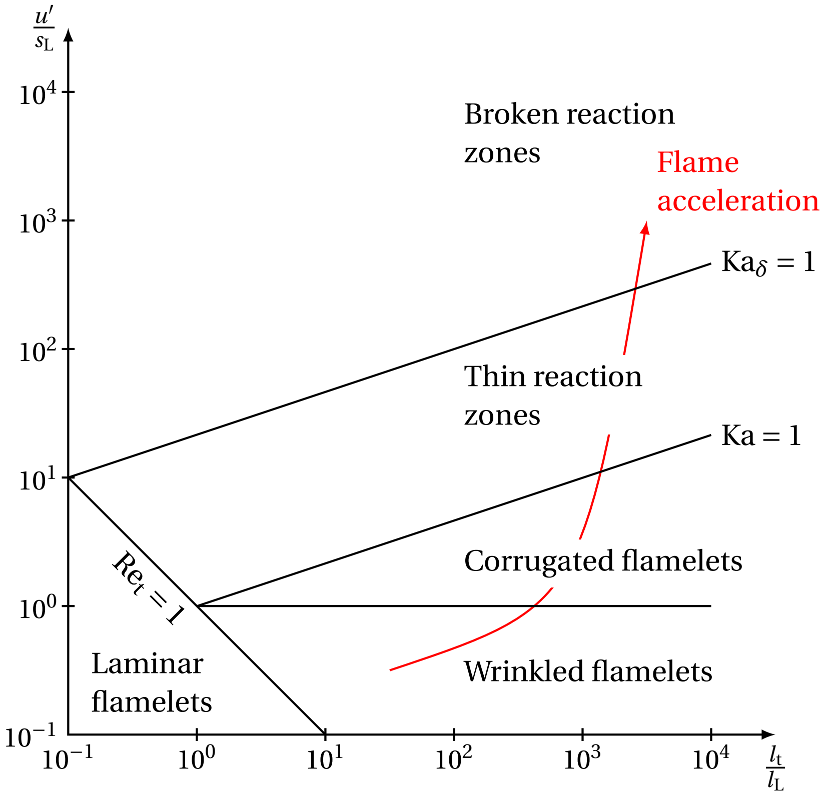

Figure 2.11: Turbulent premixed combustion regimes according to Borghi [81] and Peters [82].

Based on Fig. 2.11 the following combustion regimes can be identified:

- **Laminar flames**: As $Re_t < 1$ the flow is laminar. Flame front distortion is attributed to intrinsic instabilities.
- **Wrinkled flamelets**: The largest vortices are larger than the laminar flame thickness ($l_t > l_L$). The vortices cause a macroscopic enlargement of the flame surface.

- **Corrugated flamelets**: The flame front is wrinkled by the turbulent vortices, while the smallest scales of the turbulent flow are still larger than the laminar flame thickness $l_{\mathrm{L}} > l_{\eta}$. Therefore, the chemistry within the flame remains unaffected.

Within the flamelet regime, the turbulent burning velocity can be defined by

$$s_{\mathrm{t}} = s_{\mathrm{L}} \frac{A_{\mathrm{f,t}}}{A_{\mathrm{f,L}}}. \tag{2.22}$$

In Eqn. 2.22, the laminar flame speed s_{L} is amplified by the ratio of the turbulent flame surface $A_{\mathrm{f,t}}$ and the laminar flame surface $A_{\mathrm{f,L}}$. Hence, the turbulent burning velocity s_{t} can be much larger than the laminar burning velocity s_{L}, allowing for a higher overall reaction rate. The macroscopic enlargement of the turbulent flame surface is caused by the interaction of large vortices with the flame surface. If the turbulent velocity fluctuation u' is further increased, the flamelet regime is left:

- **Thin reaction zones**: As Ka < 1, the smallest turbulent scales are of the size of the laminar flame thickness. The smallest vortices alter the laminar flame structure, resulting in a thickening of the flame front. Due to the interaction, mixing, and consequently, the turbulent burning velocity is increased.

- **Broken reaction zones**: As the size of the smallest vortices becomes smaller than the reaction zone thickness l_{δ}, the vortices can penetrate the reaction zone. The chemical reactions are affected by turbulence, and the flow alters the radical pool in the reaction zone. Local extinction effects might occur, and multiple burning pockets form.

2.5 Flame acceleration

Flame acceleration is the mechanism of flame speed increase during flame propagation. Starting from an initially laminar flame spreading at s_L FA can lead to flames traveling at supersonic speeds. A distinction can be made between weak and strong flame acceleration. In case of weak flame acceleration, the velocity of the flame remains below the speed of sound of the reactants through which the flame is propagating ($M_\mathrm{F} < 1$). The conditions for the onset of detonation are not met, and the flame is referred to as a slow flame. In the case of strong flame acceleration, the supersonic combustion regimes are reached ($M_\mathrm{F} > 1$). The combustion regime is called fast flame or choked flame, and the onset of detonation is possible [15].

The physical mechanism of FA can be described as a feedback loop of gas dynamic and fluid dynamic mechanisms as shown in Fig. 2.12. During the initial phase of flame acceleration, the gas dynamic feedback loop is the dominating mechanism. Pressure waves are emitted each time the heat release within the flame changes. The fresh gas ahead of the flame is preconditioned as temperature and pressure rise. Furthermore, intrinsic instabilities such as the RT-instability are amplified by the interaction with pressure waves in a curved flame front. Hence, the overall surface area of the flame is increased. A misalignment of the pressure and density gradient can enhance flame wrinkling, providing a better mixing of hot products and cold reactants [83].

The pressure waves induce a flow ahead of the flame. In addition, the expansion of the hot combustion products acts as a piston. An accelerated flow ahead of the flame is created. As soon as a flow field ahead of the flame is established, the fluid dynamic feedback loop dominates over the gas dynamic loop. With increasing flow velocities, the turbulent intensity ahead of the flame is increased, leading to enhanced flame wrinkling.

In the case of an unobstructed channel, the formation of the boundary layer and its interaction with the flame and the shock system becomes the dominating mechanism for the increase in the overall reaction rate. The boundary layer thickens over time and interacts with the flame. The interaction of the flame with the turbulent boundary layer leads to an increase in the local burning rate close to the channel walls, forming a characteristic tulip-shaped flame [84]. As the flame spreads through the channel, turbulence is also generated in the core flow. If the tube is sufficiently long, flame speeds up to $600 - 1000\,\mathrm{m\,s^{-1}}$ are reached, and the conditions necessary for the onset of detonation are satisfied.

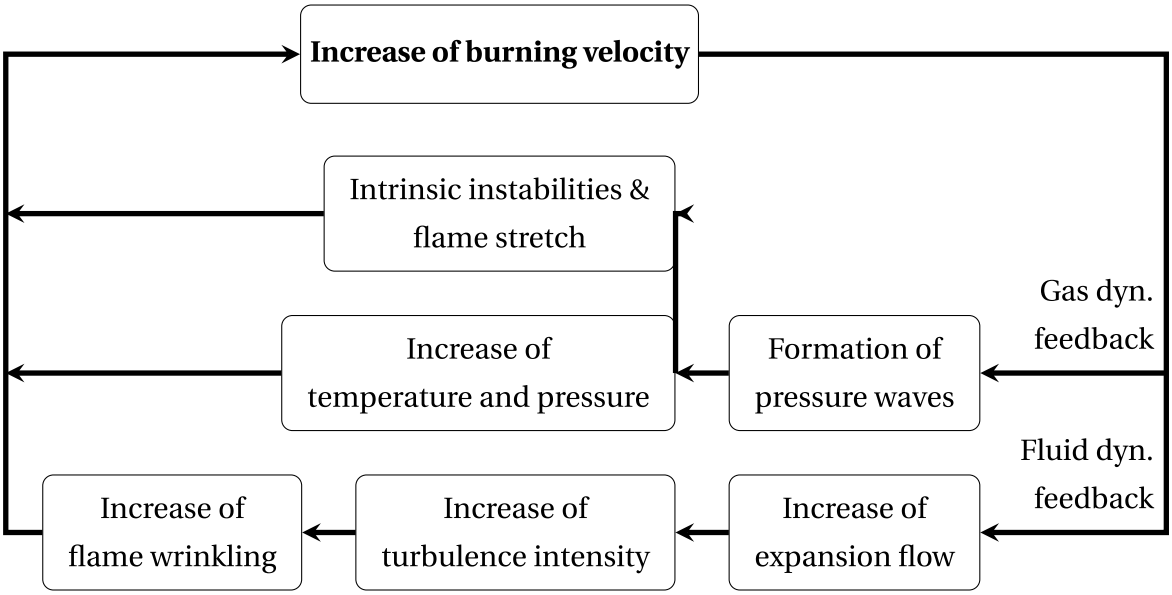

Figure 2.12: Fluid and gas dynamic feedback loop of flame acceleration (adapted from [85]).

In obstructed channels, the process of FA is enhanced by the rapid increase of the flame surface. The flow generated by the expansion of the combustion products creates vortices downstream of the obstacles. Depending on the size and velocity of the flow, these vortices may grow into large recirculation zones, occupying the volume between the obstacles. During the early stages of flame propagation along an obstructed channel, the flame might be entrained and subsequently burns in the formed vortices. If a turbulent shear layer between the core flow and the vortices is already formed, the flame will propagate in the core flow and burn into the recirculation zone afterward [86]. Turbulence produced by the interaction of the flow with the obstacles will increase the total burning rate. This results in a higher flow velocity, establishing the fluid dynamic feedback loop. In the case of strong FA, a lead shock or a system of shocks followed by a turbulent flame will evolve. Flame velocities can be as high as the speed of the sound of the products (often referred to as choking regime) [15].

Strong FA occurs in obstructed channels with sufficient length-to-height ratio when the expansion ratio σ of the fuel-air mixture is larger than a fuel-specific critical expansion ratio σ^*. Comparison with experimental data for other fuels, as well as theoretical considerations, show that σ^* is a function of the Zeldovich number β as well as the ratio of the turbulent length scale l_T to the laminar flame thickness δ_L [87]. The Zeldovich number β is defined by

$$\beta = \frac{E_\mathrm{a}(T_\mathrm{b} - T_\mathrm{U})}{RT_\mathrm{b}^2}. \tag{2.23}$$

The Zeldovich number can be interpreted as a dimensionless indicator for the global activation energy of the combustion process. The global activation energy is defined with respect to the global reaction. In an approach to provide a simplified correlation for the ignition delay time for H_2-CO-air mixtures, the global activation energy was calculated for various conditions by Donato and Petersen in [88]. It was shown that the global activation energy can be estimated to $E_\mathrm{a} = 59\,\mathrm{kcal\,mol^{-1}}$. While the temperature and the pressure have a large impact on E_a due to the second explosion limit of the H_2-O_2-system, the impact of the CO content and the fuel content X_F on E_A is of minor importance. Therefore the global activation energy E_A is assumed to remain constant for the mixtures investigated. As shown in Fig. 2.13, the Zeldovich number decreases slightly with increasing CO-content for a fixed fuel content. The temperature of the burnt mixture T_b changes only slightly with increasing CO-content at a fixed fuel content. Hence the variation of β at a fixed fuel content between H_2-air and H_2-CO-air mixtures is small. If the fuel content is increased, the Zeldovich number is decreased. This is caused by increased adiabatic flame temperature T_ad. Close to the stoichiometric composition, β is the same for all fuels. For fuel-rich mixtures, β increases, while slightly lower values are obtained for higher CO-contents in the mixture.

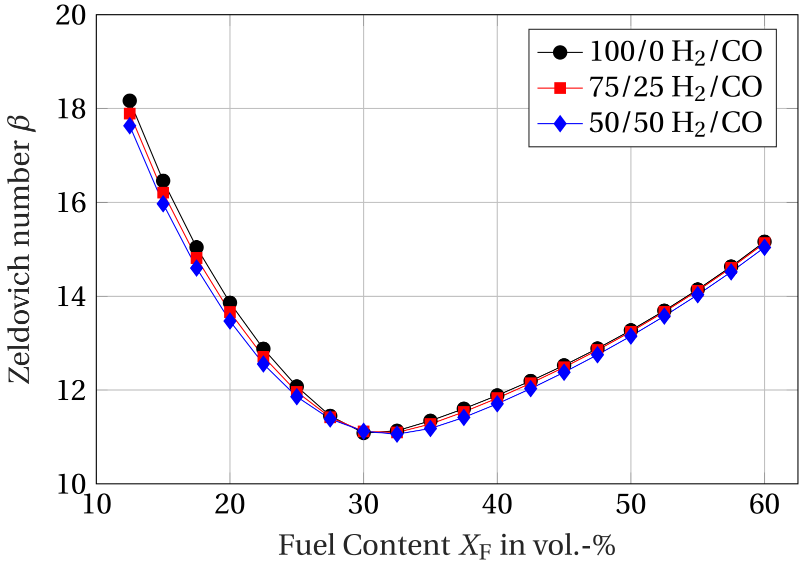

Figure 2.13: Zeldovich number β of 100/0, 75/25 and 50/50 H_2/CO mixtures over fuel content X_F.

A decrease in β decreases the ability of turbulent motions to quench the flame locally. This effect is influenced by the local behavior of the flame as the turbulent motion of the flow result in shear stresses and flame stretch [87]. The effect of the stretch rate Γ on the local burning velocity s_U is expressed by the Markstein length L_M [89] by

$$s_U = s_L + L_M \Gamma. \tag{2.24}$$

As shown in Eqn. 2.24, the local stretch rate Γ can increase or decrease the burning velocity s_U with respect to the laminar burning velocity s_L. The local stretch rate Γ is defined by $\Gamma = (1/A_f)(dA_f/dt)$. The Markstein length is a mixture property. Measurements of L_M in H_2-CO-air mixtures were conducted by Brown et al. in [89], Hassan et al. [60], Bouvet et al. [90], and Prathap et al. [65]. In Fig. 2.14, the measured Markstein length L_M is plotted over the fuel content. For comparison, measurements of 100/0 H_2/CO are added. For fuel-lean mixtures, L_M is below zero for 100/0 and 50/50 H_2/CO. A transition to positive L_M is found close to the stoichiometric composition.

Due to the similar behavior of L_M over the fuel content of 100/0 and 50/50, it can be assumed that flames in H_2-CO-air-mixtures up to a CO-content of 50 vol.-% in the fuel behave similarly to H_2-air-mixtures when subjected to flame stretch: for $L_\mathrm{M} < 0$, flame stretch leads to an increase of the local burning velocity. For $L_\mathrm{M} > 0$, stretch decreases the local burning velocity, which might result in local extinction [87].

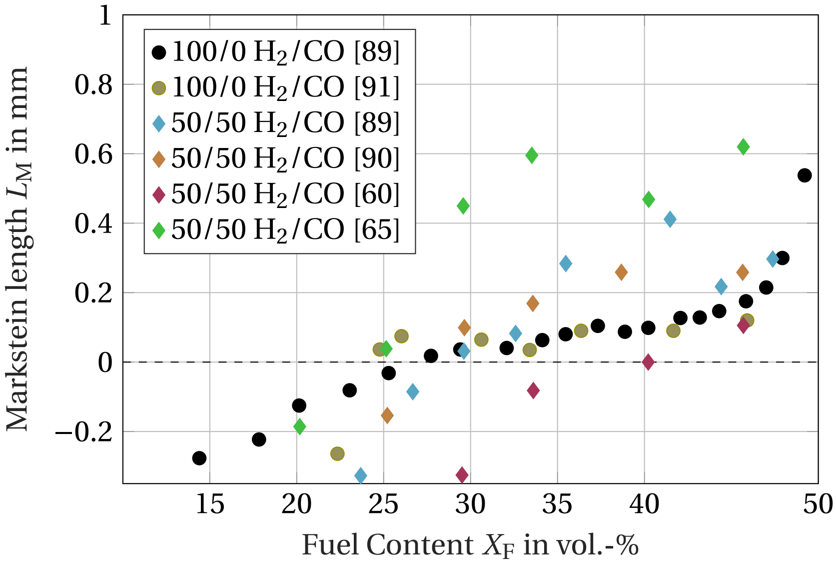

Figure 2.14: Markstein length L_M of 100/0 and 50/50 H_2/CO mixtures over fuel content X_F.

For H_2-air mixtures, the critical expansion ratio is given by $\sigma^* = 3.75$. Based on the similarity of β as well as the Markstein length L_M, it could be assumed that the critical expansion ratio of H_2-air and H_2-CO-air mixtures is quite similar. However, as shown above, the laminar flame speed s_L depends highly on the H_2 content of the mixture. Hence, differences in the critical expansion ratio for H_2-CO-air mixtures can be expected. Kuznetsov et al. showed in [37], that the critical expansion ratio σ^* for a given fuel of H_2 and CO can be approximated by

$$\sigma^* = 3.75 + 1.3 X_{\mathrm{CO},f} - 0.4 X_{\mathrm{CO},f}^2 \tag{2.25}$$

In Eqn. 2.25, $X_{\mathrm{CO},f}$ is the share of CO in a H_2/CO mixture. By extrapolation, the critical expansion ratio of CO in air can be estimated to $\sigma^*_{\mathrm{CO}} = 4.65$. However, ignition of and flame propagation in CO-air mixtures are challenging. Therefore FA in dry CO-air mixtures without moisture and small amounts of H_2 can be considered unlikely.

In addition to the influence of the channel's internal geometry and the material properties of the fuel-air mixture, FA is influenced by fuel concentration gradients. The effect of transverse concentration gradients was investigated by Vollmer et al. [21–23], and Boeck et al. [16, 24–29]. Transverse fuel concentration gradients were generated in H_2-air mixtures in the test rig, also used in this work. Depending on the obstacle geometry, concentration gradients' amplifying or attenuating influence on flame acceleration was found. A reinforcing effect was found in the unblocked channel. Flame stretching and the variation of the effective burning velocity σs_{L} was identified as the main driver. In partially blocked geometries, flame stretching is suppressed by obstacles. An amplifying effect of concentration gradients was found only up to a global concentration of 24 vol.-%. At higher fuel concentrations, flames propagating in transverse concentration gradients require a longer distance to reach supersonic speeds. This trend reversal at 24 vol.-% could be reproduced using the effective burning rate $(s_{\mathrm{L}}\sigma)_{\mathrm{eff}}$ by Boeck in [16]. The effective burning rate can be calculated by integrating the local laminar flame speed and expansion ratio over the channel height. As shown in [16], $(s_{\mathrm{L}}\sigma)_{\mathrm{eff}}$ is larger for inhomogeneous H_2-air mixtures up to 24 vol.-%.

2.6 Onset of detonation

As soon as the flame speed is around the speed of sound of the products a_{pr}, the critical conditions for the onset of detonation are satisfied. The transition to a detonation wave is accomplished by a localized explosion in the mixture due to preconditioning by compression and/or turbulent mixing [92]. Two mechanisms can cause localized explosions:

- Reflection and/or focusing of shocks or

- local instabilities and mixing processes due to flame-shock interactions, pockets of a quenched mixture, temperature and pressure fluctuations in the flow or the boundary layer.

The first mechanism is termed *strong solution* and is often found in obstructed channels when shocks interact with obstacles. This process often involves Mach stems [15]. An example of the onset of detonation in an obstructed channel is given in Fig. 2.15. The figure shows shadowgraphs of a H_2-air mixture at a fuel content of 29.6 vol.-% in a channel equipped with obstacles of 30 % blockage ratio. The flame propagates from left to right. A strong shock propagates ahead of the turbulent flame brush in the first image. The shock is reflected at the second obstacle. A circular blast wave is formed in image 3. The blast wave interacts with the leading shock triggering the onset of detonation. In the last image, the flame brush is directly coupled to the shock wave [93].

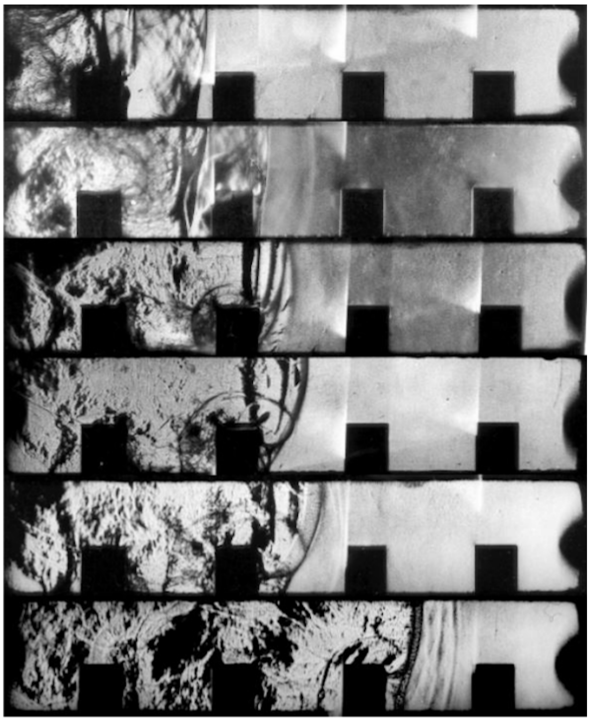

Figure 2.15: Shadowgraphy of the onset of detonation in an obstructed channel (adapted from [93]).

The latter can be found in smooth tubes and is termed *weak solution*. In this case, the onset of detonation can occur ahead of the turbulent flame brush near the leading shock in the boundary layer or due to an interaction of the flame front with a reflected shock.

The basic mechanism is believed to be the same for both cases and is generalized as shock wave amplification by coherent energy release (SWACER) for the onset of detonation. The first experimental observation of this mechanism was made by Lee [94]. According to Lee, the onset of detonation is achieved by a spontaneous flame traveling through a local induction time gradient. The origin is found in a sensitized region (hot spot) with a low induction time concerning the surrounding mixture. High gradients of induction time can be achieved as the induction time is a highly non-linear function of local temperature and pressure. The reaction will be initiated in the mixture with the lowest induction time. Due to thermal expansion, a shock is created. The shock in front of the flame will be amplified if the energy released by the flame is in coherence with a compression wave. Thereby, the mixture in regions with longer induction times can also be ignited. If the sensitized region is sufficiently large, this process can lead to the onset of detonation [15]. The onset of detonation leads to a jump in velocity and high-pressure peaks due to the localized explosion.

As the hot spot formation and shock amplification depend strongly on local mixture parameters, the onset of detonation is subjected to stochastic fluctuations [72]. Empirical criteria are used to determine whether an onset of detonation is possible. Dorofeev et al. [93] state that the onset of detonation is possible if

$$L \geq 7\lambda. \tag{2.26}$$

In Eqn. 2.26 λ is the detonation cell size, the characteristic chemical size of the detonation (see Sec. 2.7). L is the characteristic size of the confining geometry. The detonation cell size is a function of the mixture composition and the initial thermodynamic state of the mixture. Depending on the geometrical configuration, various definitions of the characteristic length need to be applied. Furthermore, the limits for the onset of detonation depend on the total geometrical size of the investigated geometry. In a series of experiments in a large-scale test rig and a downscale version, Dorofeev et al. showed in [93] that the critical detonation cell size for the onset of variation was in the order of the scaling factor between the test rigs. As detonations often feature irregular detonation cells, measurements of λ often include uncertainties. Therefore, the correlation incorporates an uncertainty of $\approx 30\,\%$ [15].

2.7 Detonation

A detonation complex is formed by coupling a shock wave and a flame front. The energy released in the flame front sustains the shock strength. Ignition of the reactants is achieved by adiabatic shock compression. Although detonations are known to be a three-dimensional (3D) phenomenon, the 1D theory provided by Chapman [95] and Jouguet [96] can predict important aspects of this phenomenon. The model does not consider detailed chemical reactions but assumes direct heat release due to the reaction behind the shock wave. The detonation is treated like a discontinuity.

Based on the Rayleigh-line Eqn. 2.8 and Hugoniot-curve Eqn. 2.9, an infinite number of solutions can be obtained by the intersection of the curves. As the slope of the Rayleigh-line given by $-\gamma M_1^2$ is negative only, the grey shaded regions in Fig. 2.16 can be excluded. If the Rayleigh-line is tangential to the Hugoniot-curve, two solutions are obtained. Starting from the initial state at (1,1), the lower solution corresponds to the maximum deflagration velocity (CJ-deflagration). This solution is not observed in experiments. The discussion focuses on the upper CJ-solution (CJ-detonation). The CJ-detonation corresponds to the minimum detonation velocity at which an intersection between the Rayleigh-line and a Hugoniot-curve for the corresponding specific heat release q is possible. An extension of the Rayleigh-line towards the adiabatic Hugoniot-curve yields the detonation complex's post-shock state. At the same time, the Rayleigh-line intersection with the Hugoniot-curve gives the state downstream of the flame front. The flow velocity behind the detonation complex is sonic. Therefore, perturbations downstream of the complex can not reach the detonation complex. As the specific entropy reaches a local minimum, the CJ-detonation is considered stable.

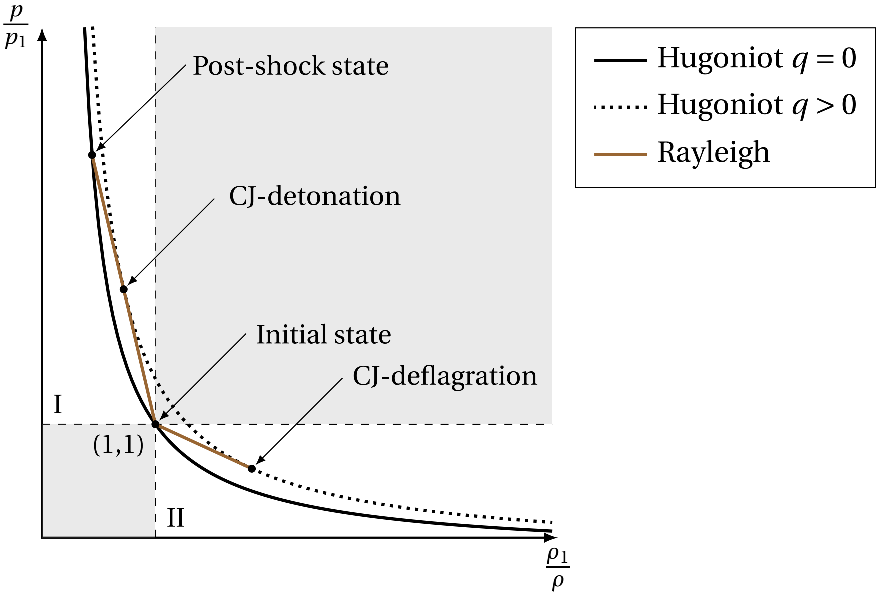

Figure 2.16: Rayleigh-line, Hugoniot-curve, and lower and upper CJ-states (adapted from [42]).

The velocities of the CJ-solutions for a perfect gas are given by

$$D_{\mathrm{CJ}} = \sqrt{\gamma R T_1 + \frac{\gamma^2 - 1}{2} q} \pm \sqrt{\frac{\gamma^2 - 1}{2} q}. \tag{2.27}$$

The solution in Eqn. 2.27 with the negative sign denotes the speed of a CJ-deflagration. The solution with the positive sign marks the velocity of a stable detonation at the CJ-detonation state. If the shock speed exceeds D_{CJ}, an overdriven detonation is found. In this case, expansion waves emitted by the flame front can reach the detonation complex and relax the unstable overdriven detonation into a stable CJ-detonation.

Zeldovich, von Neumann, and Döring extended the CJ-theory [97–99]. The ZND-model splits the single discontinuity of the CJ-model into an infinitesimal thin shock (leading shock) and a reaction zone as depicted in Fig. 2.17.

The post-shock state is termed the von-Neumann state and can be calculated by an intersection of the Rayleigh line and the adiabatic Hugoniot curve. Due to the shock relations, the velocity behind the leading shock is subsonic.

The reaction zone is split into an induction and a reaction zone. The induction zone is characterized by an induction time τ_{ind} during which the concentrations of free radicals increase. It can be assumed that the thermodynamic state of the shocked gas remains constant. The induction time is related to the activation energy of the chemical reactions E_{A}. In the case of high activation energy, the induction time increases while the reaction is completed rapidly, while the reaction proceeds gradually for lower activation energy. High activation energies reduce the stability of the ZND detonation [42]. Downstream of the induction zone, the exothermic reaction zone is found. The reaction zone is characterized by the thermicity Θ, representing energy transformation from chemical bonds to heat and motion [100]. The expansion of the hot reaction products leads to an acceleration of the flow. According to the CJ-theory, the final state corresponds to the upper CJ-state of stable detonation.

Even though the 1D detonation theory agrees well with experimental data regarding detonation velocity, it can be proven mathematically that a 1D detonation is not stable [102]. Any perturbation of the planar reaction zone will establish a system of transverse and longitudinal shock waves as shown in Fig. 2.18. Transverse shocks (TS) oscillate perpendicular to the propagation direction of the detonation. The intersection of the transverse waves with the leading shock (LS) forms a Mach stem (MS). The shock strength of the MS is higher than that of the leading shock. As the induction time is a function of the temperature, τ_{ind} is lower downstream of the Mach stem. The shock and the flame front are strongly coupled, resulting in an overdriven detonation (up to $1.2D_{\mathrm{CJ}}$). The strength of the shock subsequently decays, and the Mach stem transitions into the incident shock. This results in an increase in induction time. The distance between the shock and the flame front increases while the local propagation velocity decreases down to $0.8D_{\mathrm{CJ}}$ [103]. The cycle is repeated as soon as the inclosing transverse waves collide, leading to a localized explosion forming a Mach stem. If the distance between the shock and the flame front becomes too large, the detonation might fail. The shock de-

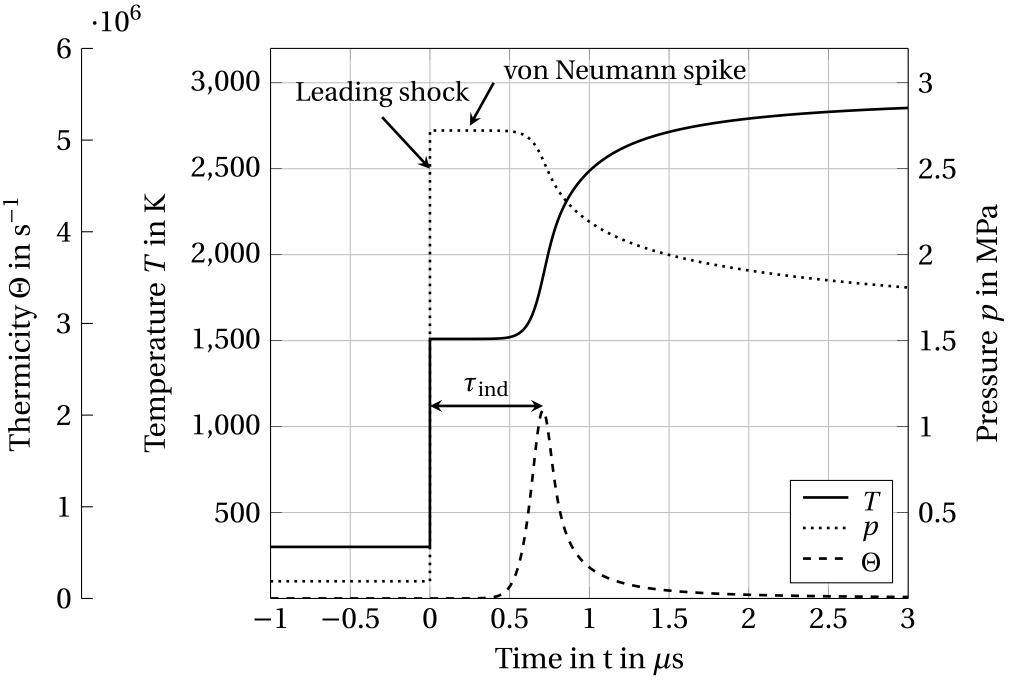

Figure 2.17: Structure of 1D detonation complex according to ZND theory for 50/50 H_2/CO at X_F =29.6 vol.-% at T_{init} = 293 K and p_{init} = 100 kPa from calculations using CANTERA [70] in combination with the shock and detonation toolbox [101] and the Davis reaction mechanism [46].

couples from the flame front traveling through the remaining mixture downstream. Due to the lack of energy transfer from the flame, the shock decays in strength [39].

The intersections of the transverse shocks with the Mach stem or the leading shock are named triple points (TP). The trajectory of the triple points leads to the cellular detonation cell pattern. The characteristic size of the detonation cells λ is the detonation cell width. Predicting the onset and propagation of detonations, λ is essential in semi-empirical models and simple simulation approaches for accident scenarios.

Despite its importance, no theory for predicting the detonation cell size exists [42]. Very few measurements for H_2-CO-air mixtures are available. Therefore, calculations of λ rely on semi-empirical models. Chemical length scales govern the cell size. Calculations of λ are based on the induction time τ_{ign}

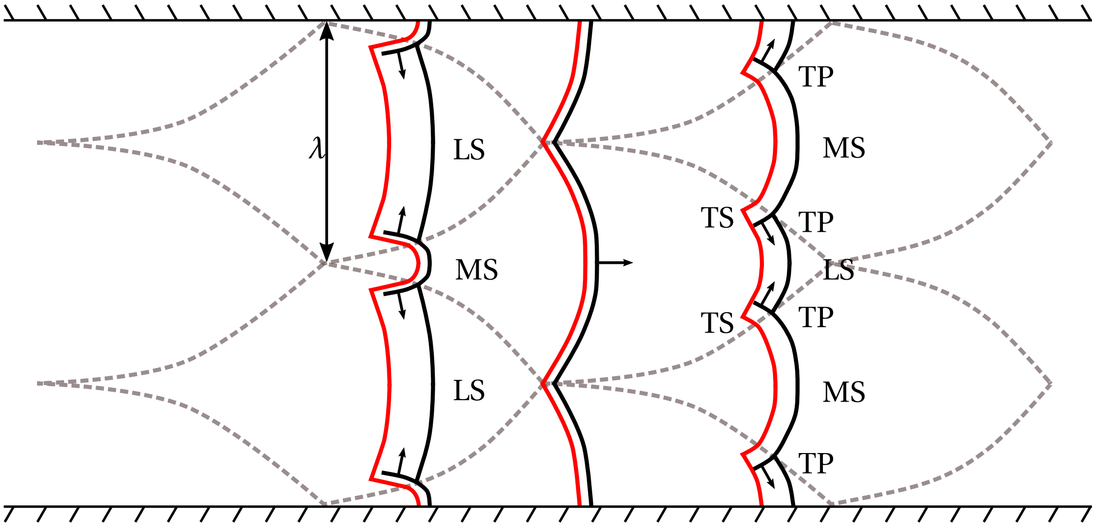

Figure 2.18: 2D shock structure of a detonation (adapted from [39]). Black lines: shocks and transverse waves. Red lines: flame front. Grey dashed lines: cellular pattern.

for a given mixture [104, 105]. Several authors investigated induction time in H_2-CO mixtures as part of the validation of the H_2-CO-O_2 reaction mechanisms [47, 49, 50, 53, 54, 106, 107].

Herzler and Naumann investigated ignition delay times of 50/50 H_2/CO at $\Phi = 0.5$ at pressures around 1.5 MPa and temperatures between 1000 – 1200 K [106]. Results and comparison with pure H_2 showed that τ_{ign} for 50/50 and 100/0 H_2/CO are very similar for the investigated conditions. In [50], Thi et al. investigated τ_{ign} for a mixture of 70/30 and 33/67 H_2/CO at equivalence ratios of 0.3, 1.0 and 1.3 for pressures of 0.3 MPa, 1 MPa and 2 MPa. At high temperatures and high pressure (1 MPa and 2 MPa), the ignition of syngas is inhibited when the equivalence ratio increases. For lower temperatures, τ_{ign} is shorter.

In [49], shock tube measurements were conducted at $\Phi = 0.5$. Mixtures of 100/0, 80/20 and 50/50 H_2/CO were investigated at pressures of 0.1, 1.3 and 3.3 MPa and temperatures between 960 – 1330 K. The results indicate that the addition of CO leads to an increase in τ_{ign}. However, this increase depends on the pressure. For temperatures like the temperatures at the von Neumann state, the increase in τ_{ign} is higher at pressures of 1.2 and 3.2 compared to 0.16 MPa. For a mixture of 80/20 H_2/CO, almost no differences are obtained compared to 100/0 H_2/CO. In the case of higher CO contents, differences in τ_{ign} become evident. The activation energy E_{A} can explain the pressure dependence. For 100/0 an increase from 57 to $378.5\,\text{kJ}\,\text{mol}^{-1}$ is observed when the pressure increases from 0.16 to 3 MPa. For 50/50 H_2/CO, the same pressure rise leads to a smaller increase in E_{A} from 50 to $190\,\text{kJ}\,\text{mol}^{-1}$.

In [53], Keromnes showed that the inhibiting effect of CO on τ_{ign} is found only if the CO content is above 50 vol.-% in the fuel. In [54] a comprehensive review lists current results on τ_{ign} for pressure from 0.16 MPa to 4.9 MPa for mixtures of 100/0 to 10/90 H_2/CO at equivalence ratios of 0.35 to 1. It is concluded that in cases of high H_2 content (> 50 vol.-%) in the fuel, the addition of CO does not lead to a significant increase in τ_{ign}. For higher CO contents, a lack of H radicals leads to an increase in τ_{ign}. Like [49], the authors argue that the activation energy at higher pressures is reduced if CO is added to the mixture. Furthermore, the competition between the chain branching reaction R 1 and the chain propagation reaction R 5, which is favorable at higher pressures, leads to a complex behavior at high pressures: while in the temperature range between 1100 and 1250 K τ_{ign} is shorter at 1.6 than at 3.2 MPa, this trend is reversed if the temperature is increased above 1250 K. Overall, the influence of CO on τ_{ign} is small for CO contents below 50 % in the fuel.

As shown for the variation of τ_{ign} with respect to the CO content in the fuel, λ for H_2-air and H_2-CO-air can be expected to be similar for the investigated mixtures. However, detonation cell size measurements based on soot foils are very limited for H_2-CO-air mixtures. Austin and Shepherd measured detonation cell sizes for stoichiometric fuel-air mixtures [108]. Detonations in mixtures of CO and small amounts of H_2, as well as other hydrocarbons, were initiated by an acetylene-O_2 mixture. They report irregular structure and a strong decrease in λ for increasing H_2-content. In [109], Vasil'ev calculated λ for multi-fuel mixtures. Validation data from [108] includes stoichiometric H_2-CO-air mixtures up to 30/70 H_2/CO. The investigation showed that the variation of λ for H_2 contents above 30 vol.-% in the fuel can be neglected. This observation was confirmed by a more recent approach for the cellular structures in two-fuel mixtures by Trotsyuk and Fomin [110].

In [111], Wang et al. measured detonation cell sizes in H_2-CO-O_2 mixtures at sub-atmospheric pressures in round and square tubes. The study of stoichiometric mixtures at an initial pressure of 4-60 kPa showed only a little variance of λ for the studied mixtures of 50/50, 33/66, and 25/75 H_2/CO. A comparison of λ by Kuznetsov et al. [37] based on the semi-empirical model by Gavrikov et al. [104] showed little variation in λ with a varying H_2 content.

All available measurements and data are summarised in Fig. 2.19. Variation of λ might be related to different reaction mechanisms and models for predicting the detonation cell size. A comparison of the experimental data from [108] with the predictions by the models at stoichiometry reveals that the variation between the models and different fuels is in the order of the scatter of the experimental results caused by the challenging evaluation of the soot foils and the irregularity of the detonation cells.

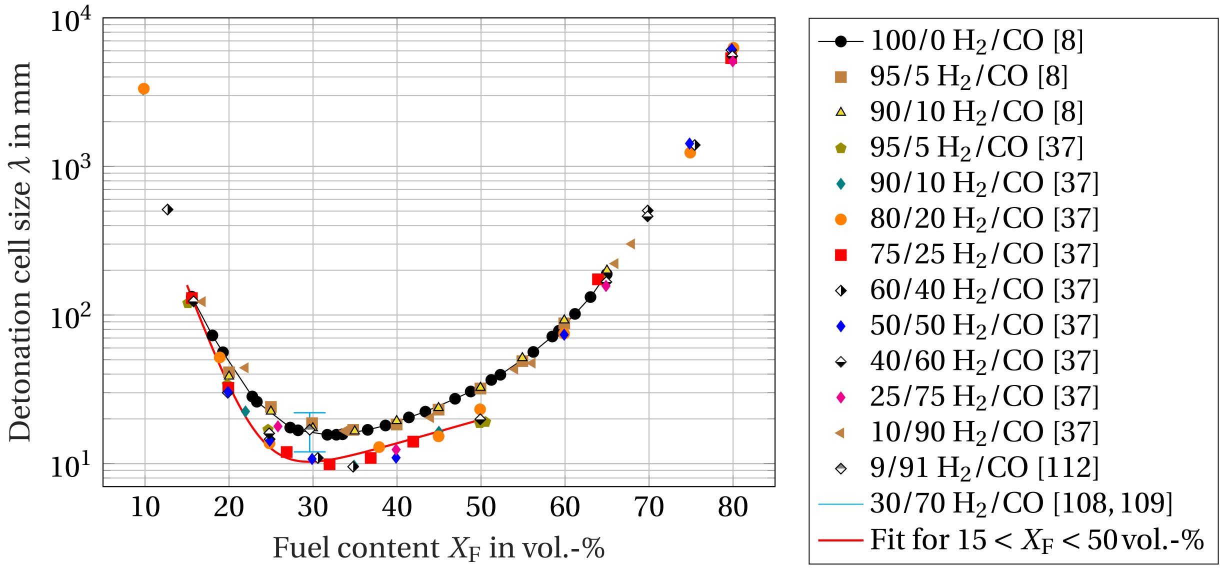

Figure 2.19: Calculations of detonation cell sizes λ in H_2-CO-air mixtures from [8, 37], measurements from [108, 109] over fuel content X_F.

A fit, based on the detonation cell size given in Fig. 2.19, is used in the present work. The fit assumes that λ is independent of the fuel composition. The detonation cell size in mm is given by

$$\lambda = 2.794 \times 10^4\,\mathrm{mm} \cdot \exp(-0.347 \cdot X_F) + 3.12\,\mathrm{mm} \cdot \exp(0.03696 \cdot X_F). \qquad (2.28)$$

2.8 State of knowledge on DDT in H_2-CO-air mixtures

Experiments on flame dynamics involving the complete DDT in H_2-CO-air mixtures are rare. In order to give a broader view of the effects of CO on the flame dynamics in H_2-CO-air mixtures, this section outlines studies on the early stages of FA, detonations, and the complete DDT.

In [77, 113–115], the effect of the H_2-content in the fuel, the equivalence ratio, and the obstacle configuration on the early stages of flame propagation and FA in a closed duct was investigated[‡]. A fully optically accessible 1 m long channel with a square cross section of 100x100 mm was used for the studies. In [113], Yu et al. varied the equivalence ratio from 0.6 to 3, while the fuel was varied between 90/10 and 10/90 H_2/CO. The investigations showed that the flame propagation time from ignition to the discharge valve increased with increasing CO-content in the fuel. For fuels containing more than 50 % H_2, the fastest flames were found at $\Phi = 1.5$, while for fuels of higher CO-content the fastest flames were found at $\Phi = 2.0$. A comparison with analytical models by Yang et al. in [114] showed an underestimation of the experimental flame speeds by the models in the case of the fuel-lean mixtures. The authors explain the differences by thermo-diffusive instabilities in the flame once the H_2-content exceeds 10 %.

In [77], Yang et al. investigated the influence of a single obstacle with a blockage ratio of 30 and 60 % mounted 200 mm downstream of the igniter on flame dynamics in stoichiometric mixtures from 0/100 to 50/50 H_2/CO. It was found that the blockage ratio and the H_2-content greatly influence flame shapes and speeds. The results showed that the influence of the blockage ratio decreases with increasing H_2-content. Varying the blockage ratio from 30 % to 60 % had little effect on the flame speed once the H_2-content exceeded 10 %.

In [115] Han et al. performed experiments in a 2 m long channel with a cross section of 60x60 mm. A set of three obstacles of 50 % blockage ratio and a spacing of 100 mm from each other were placed at distances of 100, 600 and 1100 mm from the igniter. The experiments were conducted in stoichiomet-

---

[‡] The main objective of the studies is the formation of the tulip shaped flame. Since this phenomenon is not discussed further in this work, the summary is limited to flame speed results

ric fuel-air mixtures with fuels ranging from 10/90 to 90/10 H_2/CO. The study observed two mechanisms of FA caused by obstacles: delayed burning as described in [116] and enhanced turbulence. The flame speed and hence the turbulence at the entrance of the obstructed section greatly influenced the effect of the two mechanisms. At low H_2-contents, the flame speed at the entry of the obstacles is low if the obstacles are placed 600 mm downstream of the igniter. In this case, large pockets of unburned gas form in the wake of the obstacles. Delayed burning in these obstacles results in strong FA. At higher H_2-content, the increase in laminar flame speed leads to fast consumption of the unburned pockets, decreasing their effect on FA, while intensified turbulence promotes FA. The results showed that the maximum velocity increases with the H_2-content in the fuel. However, the differences are smaller between 50/50 and 90/10 H_2/CO than between 10/90 and 50/50 H_2/CO.

The complete process of FA was investigated by Veser et al. in [36]. Experiments were conducted using lean H_2-CO-air mixtures in a 7.2 m long channel. The channel was equipped with orifice like obstacles of 30 % blockage ratio and a spacing of 100 mm. It was found that CO-addition hinders FA in very lean mixtures. For a fuel content of more than 13 vol.-%, the influence of CO can be neglected if the CO volume fraction in the fuel is treated like H_2. However, as the channel was obstructed throughout the whole channel length and the fuel content was limited to 15 vol.-%, an onset of detonation did not occur.

Kuznetsov et al. [37] conducted experiments on a larger scale. The semi-confined experiments used a 9 m long channel with rectangular cross section of 3 m in width and 0.6 m in height. The channel was equipped with obstacles of a blockage ratio of 60 % at a spacing of 0.6 m over the whole length. While the channel was closed at the upper side, the lower side was connected to a large venting volume. The fuel content was varied between 13-22 vol.-% with mixtures of 100/0, 75/25, 50/50 and 25/75 H_2/CO. Detonations occurred at the same lean fuel content of 21 vol.-% for 100/0 and 75/25, and 50/50 H_2/CO.

Eder investigated the influence of CO-addition on detonations in smooth pipes for H_2-CO-air mixtures [39]. The test rig consisted of a 6 m long tube, of 66 mm in diameter. The fuel was varied between 100/0 and 93/7 H_2/CO. H_2-CO-air was investigated only for fuel contents that supported detonations in H_2-air mixtures between 19.5-53 vol.-%, based on the detonation cell size criteria for smooth tubes: $D > \lambda$. The addition of CO within the investigated range did not affect the detonation limits. Calculations of the ZND-structure revealed that the reaction zone width of H_2-CO-air mixtures is like those found for H_2-air mixtures.

Detonations at sub-atmospheric pressure in H_2-CO-O_2 mixtures were investigated by Wang et al. in [111]. Stoichiometric mixtures of 25/75, 33/66, and 50/50 H_2/CO were tested in square and round tubes. The initial pressure was varied between 6-30 kPa. The study showed that detonations in the investigated geometry traveled with a small velocity deficit with respect to D_{CJ}. At the limiting pressure the velocity deficit increases to 14-17 %. The detonation cell size was measured using smoke foils.

In [117] Chen et al., investigated the influence of CO and N_2 dilution on detonations in H_2-air mixtures in a tube of 72 mm diameter and 10 m length. H_2-air mixtures of equivalence ratios ranging from 0.5 to 3 were studied. The CO-content in the fuel was set to 10 vol.-%. The experimental setup used a driver section to initiate detonations in the investigated mixtures. Ion probes, pressure sensors, and smoke foils were used to determine flame propagation velocities, pressures, and detonation cell sizes. A linear correlation was used to fit experimental detonation cell sizes to the induction lengths determined by detailed chemistry calculations. The results showed that the lean detonation limit for mixtures of H_2 and CO is approximately constant since the addition of CO does not change the stoichiometry of the mixture. The detonation limit for rich H_2-air mixtures decreased linearly with the addition of CO. If the CO-content in the mixture exceeds 58 vol.-%, detonation becomes impossible.

3 Experimental Setup

Experimental data presented in this thesis was collected at the GraVent test rig. The GraVent was designed and built by Vollmer [23] and used in follow-up projects by Boeck [16]. Katzy [76] used a short version of the channel. In the following chapter, the geometry of the test rig is explained first. The experimental procedure and the generation of transverse concentration gradients in the ternary mixture are outlined in Sec. 3.2 and 3.3. This chapter concludes with a description of the measurement system in Sec. 3.4.

3.1 Geometry

As shown in Fig. 3.1, the GraVent test rig has a total length of 6 m. The channel consists of a total of seven segments. Six are standard segments, each of 0.9 m, while one is an optical segment of 0.6 m length. The channel is closed at both sides by solid plates, termed ignition, and end plate. The coordinate system used throughout this thesis is also introduced in Fig. 3.1: x is the axial, y is the lateral, and z is the vertical direction. The origin is centered at the inward-facing surface of the channel at the ignition plate. The z-axis is anchored at the floor of the explosion channel (see Fig. 3.2).

The channel has a rectangular cross section of 60 mm in height and 300 mm in width. An additional venting volume is located under the explosion channel [23]. Plates separate the venting volume from the explosion channel. In order to minimize the influence of the additional volume on the generation of transverse concentrations gradients and FA, the venting volume was filled with wax. The venting volume was not filled in former investigations by Vollmer [23] and Boeck [16]. However, the influence of the venting volume on FA and DDT was neglected.

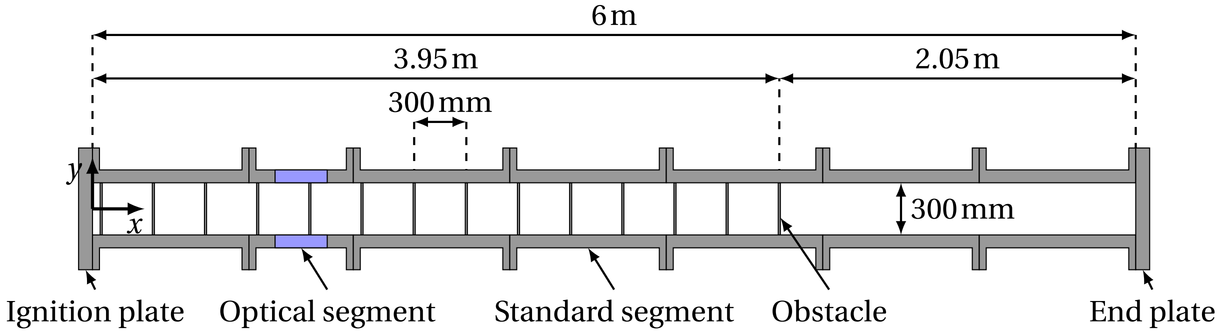

Figure 3.1: Schematic of the GraVent test rig for an obstacle spacing of 300 mm (top view).

The channel allows for the installation of obstacles at the floor and ceiling by using notches equally spaced at a distance of 100 mm. As shown in Fig. 3.2, the obstacles are mounted so that the blockage ratio BR is defined by the obstacle height h in the channel by $\mathrm{BR} = 2h/H$. The obstacle and deflection plate width in y-direction is 12 mm.

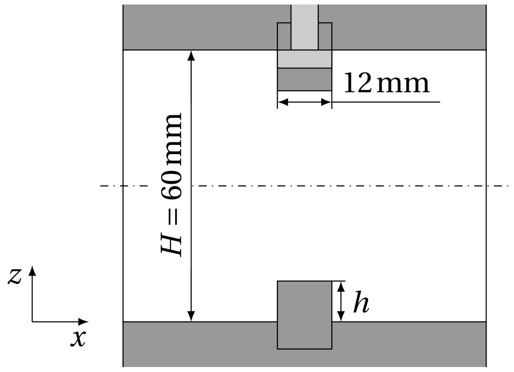

Figure 3.2: Lateral cross-sectional view of the GraVent for a blockage ratio of 30 %.

In order to investigate the influence of the obstacle configuration on DDT, two obstacle geometries were used. One of $h = 18$ mm (BR60) and one of $h = 9$ mm (BR30) as shown in Fig. 3.3. Each obstacle incorporates deflection plates to generate transverse concentration gradients (see Sec. 3.3). When mounted, the outlets of the injection ports in the obstacles close flush with the channel ceiling (see Fig. 3.2). At the channel floor, obstacles of the same geometry but without injection ports and deflection plates are installed. In the case of the unobstructed channel (BR00), deflection plates are mounted at the ceiling notches, while flat inlays are mounted on the floor. The deflection plates induce a blockage ratio of 2 %.

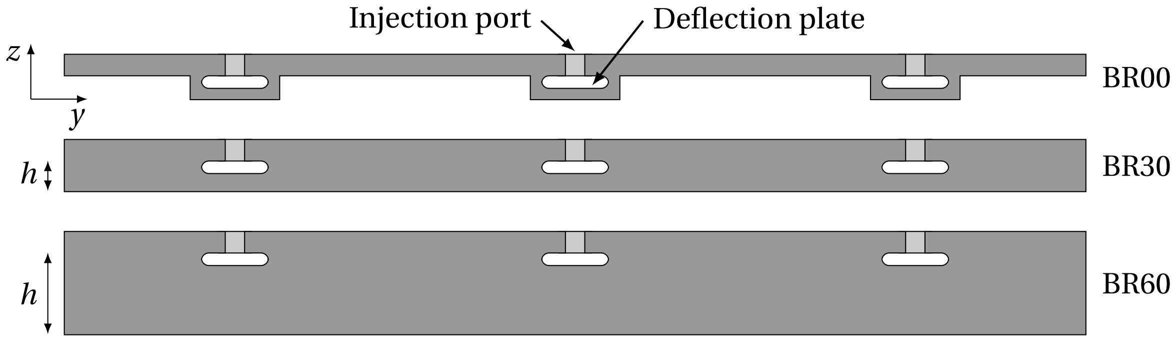

Figure 3.3: Cross section of the obstacles mounted at the channel's ceiling.

The first obstacle was mounted at a distance of 50 mm from the ignition plate. Further obstacles were mounted at a spacing of $S = 100$ and $S = 300$ mm from each other. Compared to former investigations on the channel, a total length of 3.95 m was partially obstructed to trigger DDT in H_2-CO-air mixtures. The unobstructed section at the back of the channel has a length of 2.05 m. The length of the channel, the obstructed section, the distance of the first obstacle from the ignition plate, and the position of the optical segment were not changed during the investigation. Investigated configurations are listed in Table 3.1. The naming convention for each configuration is the same way as in Vollmer [23] and Boeck [16].

Table 3.1: Obstacle configurations.

Blockage ratio BR in %	Spacing S in mm	Obstructed length L_{obs} in m	Term
30	100	3.95	BR30S100L
	300	3.95	BR30S300L
60	100	3.95	BR60S100L
	300	3.95	BR60S300L
0	-	-	BR00

3.2 Experimental procedure

Before each set of experiments, the fuel gas is prepared in a separate gas mixing unit. H_2 (purity: 3.0) and CO (purity: 2.3) are mixed in an external gas cylinder using the method of partial pressures. The mixtures used are 100/0, 75/25, and 50/50 H_2/CO. The accuracy of the mixture generation is determined by gas chromatography to be ±1 %. In order to achieve homogeneity, the higher specific impulse of CO was used to enforce mixing in the gas cylinder by injecting CO after H_2. The mixture was set to rest for at least 12 h to ensure a homogeneous mixture [118]. The pressure in the mixing unit (up to 5 MPa) is reduced by a two-stage pressure-reducing valve. The fuel supply system of the channel is operated at a pressure of $p_s = 0.6\,\mathrm{MPa}$. The fuel supply system consists of pipes and reservoirs made of stainless steel. The formation of iron pentacarbonyl $Fe(CO)_5$ cannot be neglected [119]. Studies on the influence of $Fe(CO)_5$ on flame propagation in H_2-CO-air mixtures revealed a significant reduction in laminar flame speed [120]. The inhibition decreases with increasing H_2 content in the fuel. Recent studies found that the inhibition is most prominent at fuel-rich conditions of $\Phi > 1.5$ if a fuel mixture of 50/50 H_2/CO is used [90]. As fuel-rich mixtures are not the focus of this study, the inhibiting effect of $Fe(CO)_5$ is neglected in the discussion of the results.

The test rig is controlled by LabView-based software. The procedure of each experiment is depicted in Fig. 3.4. Before the initiation of the automated measurement sequence, the injection time t_{inj}, the diffusion time t_{D}, and the measurement time t_{mes} are specified by the operator. The injection time t_{inj} is the duration of the fuel injection into the channel. The diffusion time t_{D} allows for adjustment of the fuel distribution over the channel height (see Sec. 3.3). The measurement time t_{mes} corresponds to the duration of data logging by the measurement system.

Each experiment starts with the preparation of the fuel-air mixture in the channel. A vacuum pump is used to reach a partial vacuum in the initially air-filled channel. An automated sequence is started as soon as the desired partial vacuum is reached. The fuel is injected into the channel. The injection valves are opened for the time t_{inj}. Diffusion distributes the fuel over the channel height during the user-defined diffusion time t_D. At the end of the diffusion time, the measuring sequence starts, and the data loggers are activated. After 1.5 ms, ignition is triggered using a spark plug centered in the ignition plate (see Fig. 3.13). The automated and the measurement sequence end at the same time. In order to clear the channel from the exhaust gases, the channel is flushed with pressurized air for 5 min. After flushing, a follow-up experiment can be started. Due to the flushing of the channel with air at ambient temperature and the large mass of the test rig, temperature variations between each experiment are neglected. It is assumed that the standard ambient conditions of $p_\mathrm{amb} = 101.325\,\mathrm{kPa}$ and $T_\mathrm{amb} = 293\,\mathrm{K}$ correspond to the conditions of the gas mixture at ignition. The assumption of standard ambient conditions is also used to determine specific properties of the fuel-air mixture (such as D_CJ, a_Re, etc.) for further evaluation of the measurement data.

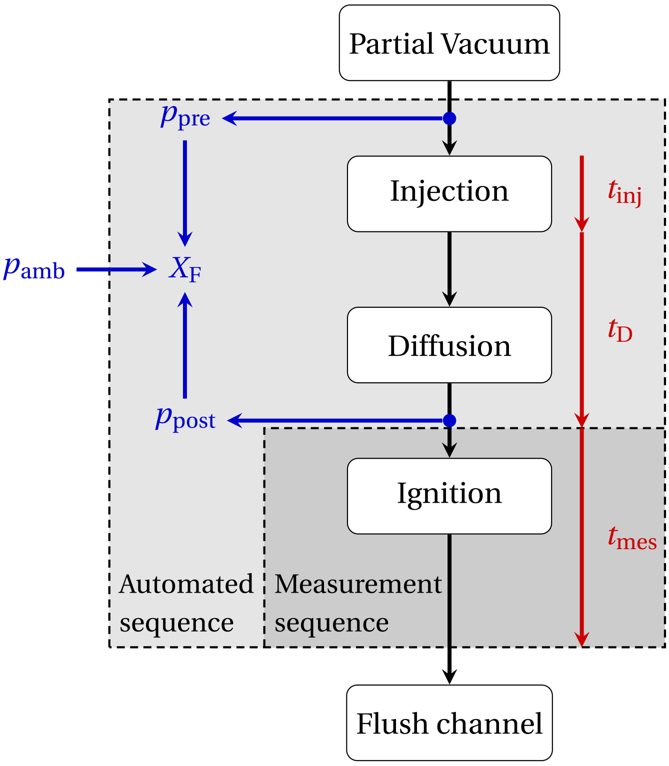

Figure 3.4: Schematic of the experimental procedure.

From the start of the automated sequence to the start of the measurement sequence, the relative pressure p in the channel is measured by two static pressure sensors (type WIKA S20 and SWA09). One is mounted at the ignition plate, the other at the end plate. Based on the data provided by the sensors, the pressure before ignition p_{pre} and at the end of the diffusion time p_{post} is determined by averaging 100 samples from each sensor. The pressures p_{pre} and p_{post} are used to determine the fuel content X_{F} for each sensor by the partial pressure method by

$$X_{\text{F}} = \frac{\Delta p}{p_{\text{amb}}} = \frac{p_{\text{post}} - p_{\text{pre}}}{p_{\text{amb}}}. \tag{3.1}$$

The ambient pressure p_{amb} is obtained at the time of each experiment from a nearby weather station [121]. The fuel content is determined at both pressure sensors and afterward averaged. As the influence of pressure on flame propagation is not part of this study and since Eqn. 3.1 is valid only for slight deviation of p_{post} with respect to the ambient pressure p_{amb} only experiments ignited at relative pressures of ±1 kPa to the ambient are regarded.

In order to investigate DDT in H_2-CO-air mixture for different geometries, an experimental matrix containing desired fuel contents is established. As listed in Table 3.2, the fuel content varies between 15 and 40 vol.-%, including fuel lean and fuel rich mixtures. Several experiments are performed for each desired fuel content (at least three per fuel, fuel content, diffusion time, and obstacle configuration). The experimental procedure allows for a high repetition rate. However, the global fuel content in the channel cannot be accurately adjusted due to fluctuations in gas supply pressure. Experiments at measured fuel contents of ±0.5 vol.-% with respect to the fuel contents listed in Table 3.2 are attributed to the desired fuel content. Experiments with higher deviations are discarded.

Table 3.2: Desired fuel contents.

X_{F} in vol.-%	15	17.5	20	22.5	25	27.5	30	35	40
Φ	0.42	0.55	0.59	0.69	0.79	0.90	1.02	1.28	1.59

3.3 Generation of transverse concentration gradients in H_2-CO-air mixtures

Fuel is injected into the channel via injection ports in the channel ceiling. The distribution of the ports for a standard segment is shown in Fig. 3.5. The ports are aligned with the notches in the ceiling of the channel. Each port matches with either an injection port of an obstacle or a deflection plate as displayed in Fig. 3.3. Fuel distributors supply the injection ports. Upstream of each distributor, a valve controls the time of fuel injection t_{inj}. The flow through each valve is controlled by a choked nozzle of 0.9 mm diameter at each distributor. Thereby, a homogeneous fuel distribution along the x-axis is maintained.

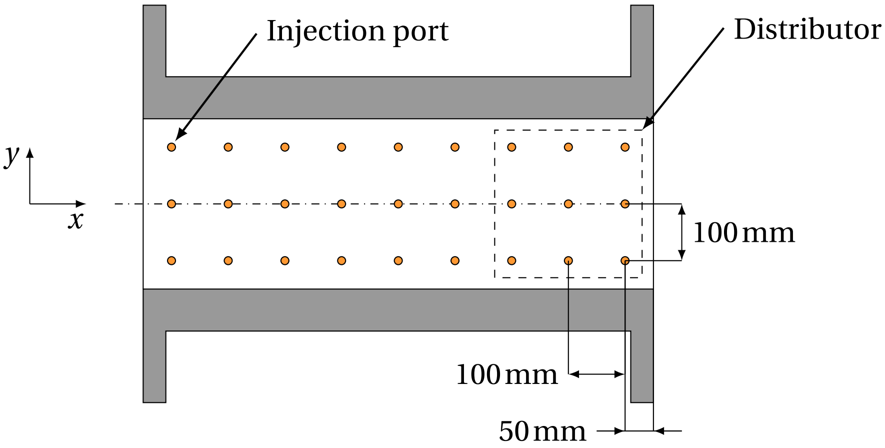

Figure 3.5: Fuel ports at the ceiling of a standard segment (adapted from [16]).

The injection process and the mechanism to generate vertical concentration gradients are shown in Fig. 3.6. After passing the injection port, the notches or obstacles mounted at the channel ceiling deflect the gas flow in the x-direction (I in Fig. 3.6). Due to interaction with the flow from other injection ports, the flow is reversed, and a stratified layer is formed (II in Fig. 3.6). Diffusion sets in, and the fuel spreads over the channel height. Depending on the diffusion time t_{D}, the fuel concentration gradient can be varied (III in Fig. 3.6). Short diffusion times lead to steep concentration gradients, while homogeneous mixtures are achieved by diffusion times of 30 s and more. For diffusion times of 3 s and 5 s, the pressure data obtained by the static pressure sensors tend to overshoot. An accurate determination of the fuel content based on the pressure data is thus not possible. Comparisons of the pressure profile from the static pressure sensors at short and long diffusion times show good agreement when the injection time and pressure before injection are kept constant. Hence, the injection time and pressure before injection was kept constant for inhomogeneous and homogeneous mixtures. The corresponding fuel contents are thus very similar and within the allowed variation range of ±0.5 vol.-%.

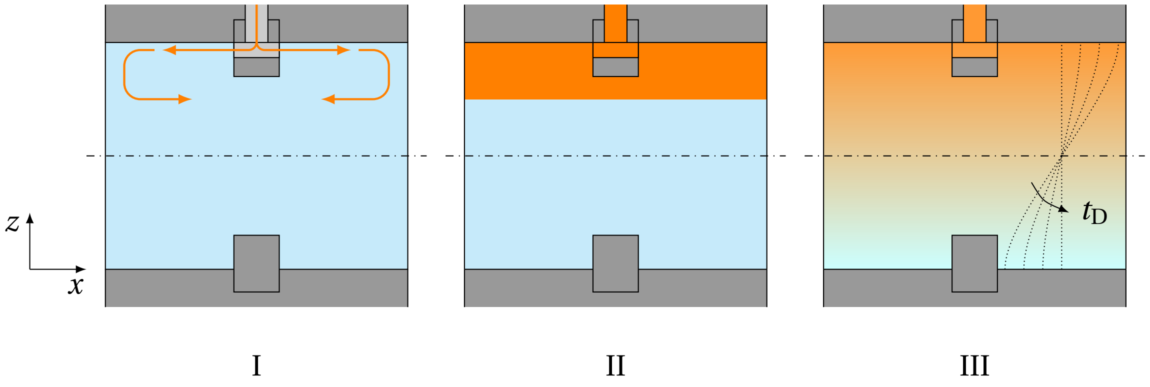

Figure 3.6: Fuel injection and generation of transverse concentration gradients for BR30.

The method for the generation of transverse concentration gradients was designed for H_2-air mixtures by Vollmer [22] and Ettner [122] and was used additionally by Boeck [16]. During the design process, experiments have been used to validate a CFD model of the injection process using Ansys FLUENT. Experiments to study the formation of concentration gradients were conducted at a model of the test rig shortened in length to 300 mm. The model's length and width correspond to the test rig's dimensions. Gas samples were taken at various heights of the model. A gas chromatograph analyzed the samples. A similar approach was used for the validation of H_2-CO-air mixtures in the present thesis. The content of H_2 and CO was determined at different heights and various diffusion times. Due to the complex experimental approach, measurements were conducted only at $\Phi = 1$. The measurement uncertainty is estimated to be ±0.5 vol.-%. The model uses the same fuel supply system and experimental procedure shown for the GraVent in Fig. 3.4. Hence, the fuel content in the model cannot be adjusted accurately. Therefore, the experimental results include variations in global fuel content X_F. A more detailed description of the experimental procedure is given in Appendix A. The CFD model in Ansys FLUENT provided by Vollmer [22], and Ettner [122] was extended to consider the ternary mixture of H_2, CO, and air in the context of this work. The CFD model is applied to all desired fuel contents (see Table 3.2) except for 40 vol.-%. The diffusion time of the CFD model is limited to $t_D = 45\,s$.

Preliminary fuel injection simulations showed undesired recirculation zones in fuels containing CO. Hence, establishing a stratified mixture becomes more challenging due to the higher molecular weight of H_2/CO mixtures than pure H_2. The pressure in the fuel supply system was identified as an appropriate tuning parameter to reduce the momentum of the injected fuel mass flow. The pressure in the fuel supply system was reduced from 0.8 MPa as used by Vollmer and Boeck to $p_s = 0.6\,MPa$ for the present study. Consequently, undesired recirculations can be avoided, as shown in the CFD simulations and the experimental investigation of the fuel injection. However, the reduction in p_s also leads to an increase in injection time, which affects the generation of the concentration gradients.

The results of the CFD simulation for a fuel content of $X_F = 22.5\,vol.-\%$ for 50/50 H_2/CO are plotted for H_2 (left) and CO (right)in Fig. 3.7. The distribution of H_2 and CO is plotted for each diffusion time t_D. As shown in Fig. 3.7, a gradient is found for H_2 and CO. For both gases, the gradient vanishes over the diffusion time. In contrast to the expectation for 50/50 H_2/CO, the gradients for H_2 and CO at each diffusion time reveal that the gases are not distributed equally across the vertical coordinate. The gradients for CO are higher than for H_2. The higher diffusivity of H_2 leads to a quicker diffusion compared to CO [123]. Hence the mixtures contain more H_2 than CO in the lower part of the channel and less H_2 than CO in the upper part than one would assume for a homogeneous distribution. For diffusion times of $t_D \geq 30\,s$, the CFD model only shows minor variations of the fuel content over the channel height at long diffusion times. A homogeneous distribution for H_2 is reached after a diffusion time of 30 s as the shape of the concentration gradient does not change between 30 s and 45 s. Slight differences in the CO-content are observed at $t_D = 30\,s$. However, as the concentration difference is below 0.6 vol.-%, it can be assumed that further diffusion effects are of minor importance. Homogeneous fuel distribution is assumed after a diffusion time of 30 s.

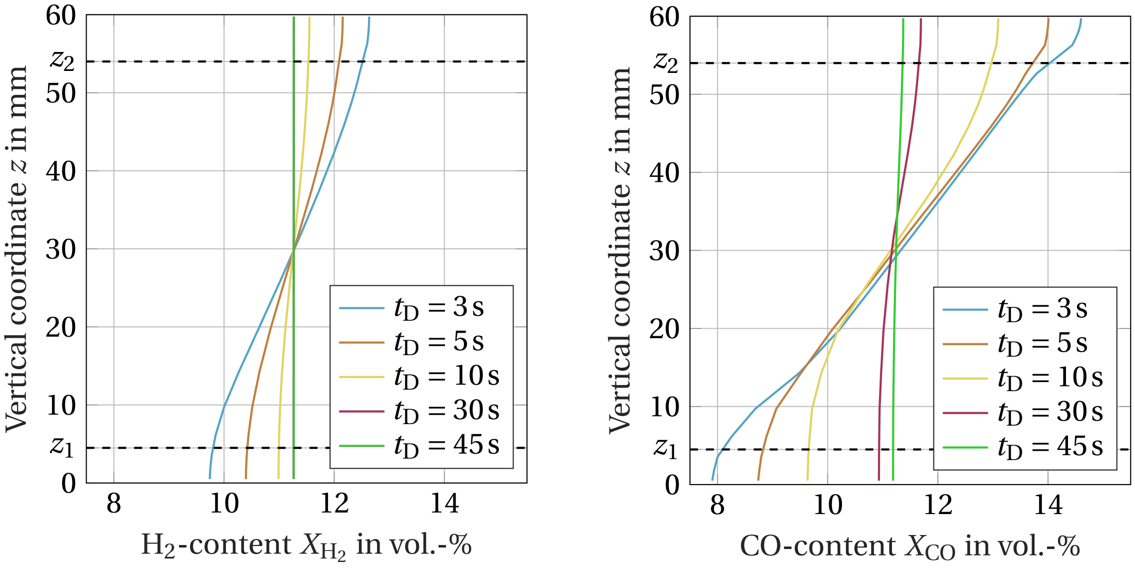

Figure 3.7: H_2-content X_{H_2} (left) and CO-content X_{CO} (right) over vertical coordinate z for $X_F = 22.5\,\text{vol.-\%}$ and 50/50 H_2/CO.

The fuel distribution over the channel axis leads to a more complex distribution of flame properties compared to H_2-air mixtures, as these depend on the overall fuel content and the H_2/CO-ratio. In Fig. 3.8 the local hydrogen fraction X_{H_2} of the fuel, the density of the reactants ρ_{Re}, the speed of sound of the reactants a_{Re}, the expansion ratio σ, the laminar flame speed s_L and the effective burning velocity $s_L\sigma$ are plotted over the vertical coordiante z for different diffusion times based on the calculated fuel distribution for $X_F = 22.5\,\text{vol.-\%}$ and 50/50 H_2/CO. As shown in the first plot of the left side, the H_2-content in the fuel varies between ±5 vol.-% with respect to the total H_2-content of the fuel. H_2-rich regions are found in the lower part of the channel, while lower H_2-contents are found in the upper part. The H_2-content in the upper part remains lower until $t_D = 30\,s$. In the lower part of the channel, the H_2-content decreases considerably for each time step in t_D. The density of the fuel-air mixture is similar to air at standard conditions ($\rho = 1.2\,kg\,m^{-3}$). The variation of ρ_{Re} over z is less than 3 %. Similar behavior can be observed for the speed of the sound of the reactants a_{Re}. For concentration gradients in H_2-air mixtures, a high variation of a_{Re} is observed in [16]. This is due to the molar mass of H_2 being a factor of 7.5 less than 50/50 H_2/CO. Furthermore, the variation of a for 50/50 H_2/CO with respect to the surrounding air is small ($a_{50/50} = 476\,m\,s^{-1}$

vs. $a_{\mathrm{air}} = 342\,\mathrm{m\,s^{-1}}$). The expansion ratio σ is highest at the upper part of the channel and is found to depend mainly on the total fuel content. The same applies to the laminar flame speed s_{L} and the effective burning velocity $s_{\mathrm{L}}\sigma$.

In order to compare the results of the CFD model and the experiment, the concentration difference for the fuel gases H_2 and CO is used. The concentration difference is defined based on the gas concentration between the top at $z_2 = 54\,\mathrm{mm}$ and the lowest measurement position of the channel at $z_1 = 4.5\,\mathrm{mm}$ at each desired fuel content X_{F} and diffusion time t_{D}. The dashed lines in Fig. 3.7 indicate the probe heights.

The concentration difference based on the CFD and the experimental results for H_2 is plotted in Fig. 3.9 and for CO in Fig. 3.10 for 75/25 H_2/CO. The concentration difference of H_2 is higher than for CO, as the total H_2 content is higher. More H_2 is present under the channel's ceiling, while the H_2 concentration at the floor is independent of the H_2 content. The highest concentration difference is reached at the lowest fuel content of $X_{\mathrm{F}} = 15\,\mathrm{vol.\text{-}\%}$, followed by a local minimum at 17.5 vol.-%. If the fuel content increases, H_2 and CO show a similar trend, as the concentration difference increases with increasing fuel content. The concentration difference can be assumed independent of X_{F} at high fuel contents of $X_{\mathrm{F}} \geq 30\,\mathrm{vol.\text{-}\%}$. As injection time becomes longer, the initial diffusion of the fuel is increased before the first probe after $t_{\mathrm{D}} = 3\,\mathrm{s}$ is taken. The measured concentration difference further confirms that the spread of H_2 and CO becomes small if $t_{\mathrm{D}} \geq 30\,\mathrm{s}$. Slight differences in the concentration difference of CO in order of 1 vol.-% are visible, while H_2 has already distributed over the total channel height.

For 50/50 H_2/CO, the concentration difference of H_2 at Fig. 3.11 is lower than for CO at Fig. 3.12. The higher diffusivity of H_2 compared to CO seems to become more important as the CO content increases. This might be related to the longer injection times. As preliminary calculations[‡] show, the injection time at a fuel content of 20 vol.-% is increased from 0.14 at 75/25 to 0.24 s by a factor of 1.84 for 50/50 H_2/CO (see Appendix B). The increase in t_{inj} for 50/50 with respect to 75/25 H_2/CO is larger at higher fuel contents. Hence the in-

---

[‡] It should be mentioned that the injection times for the test rig and the model are longer by a factor of 2 with respect to the preliminary calculation.

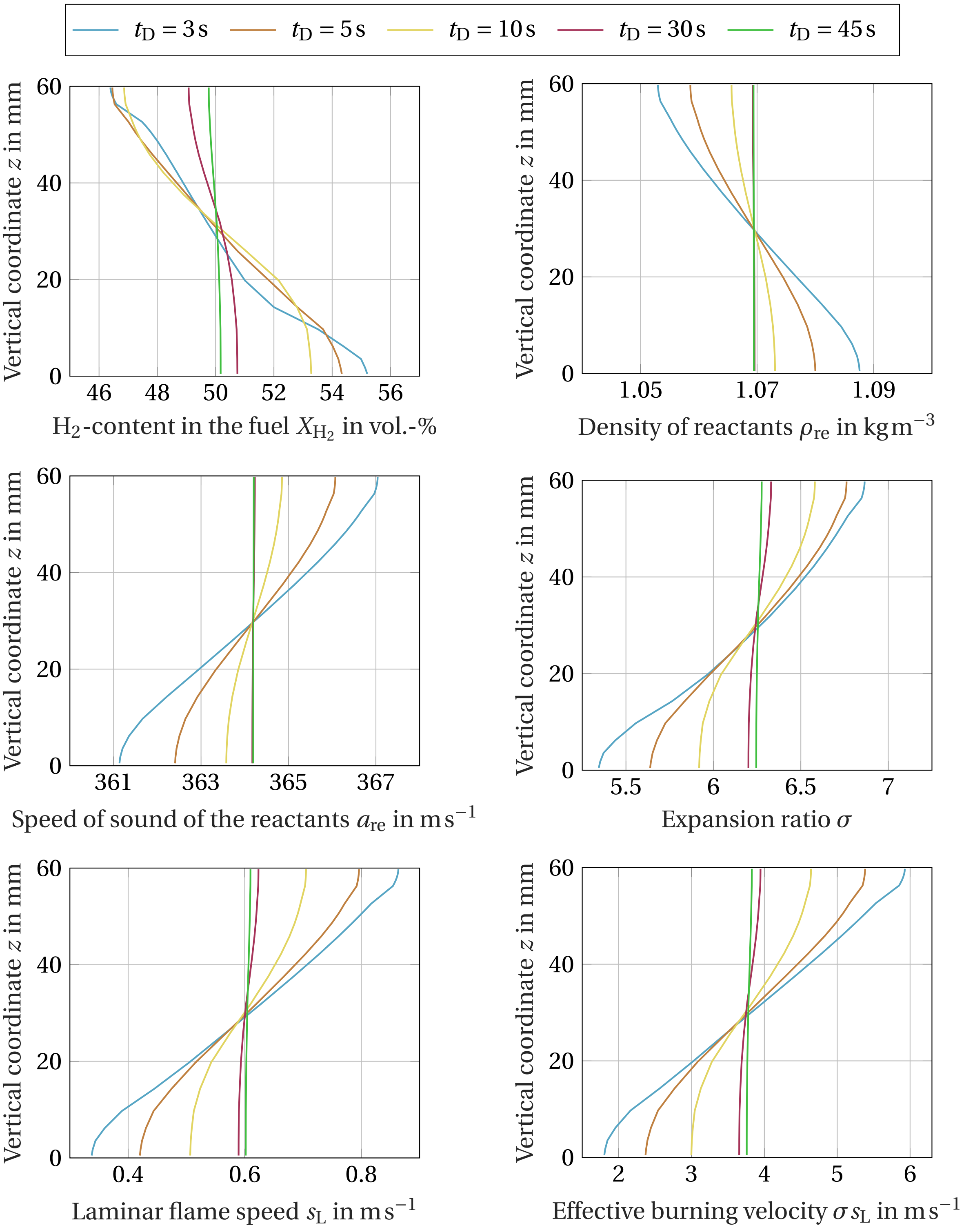

Figure 3.8: Mixture properties X_{H_2}, ρ_{re}, a_{re}, σ, s_L, σs_L over vertical coordinate z for $X_F = 22.5$ vol.-% and 50/50 H_2/CO.

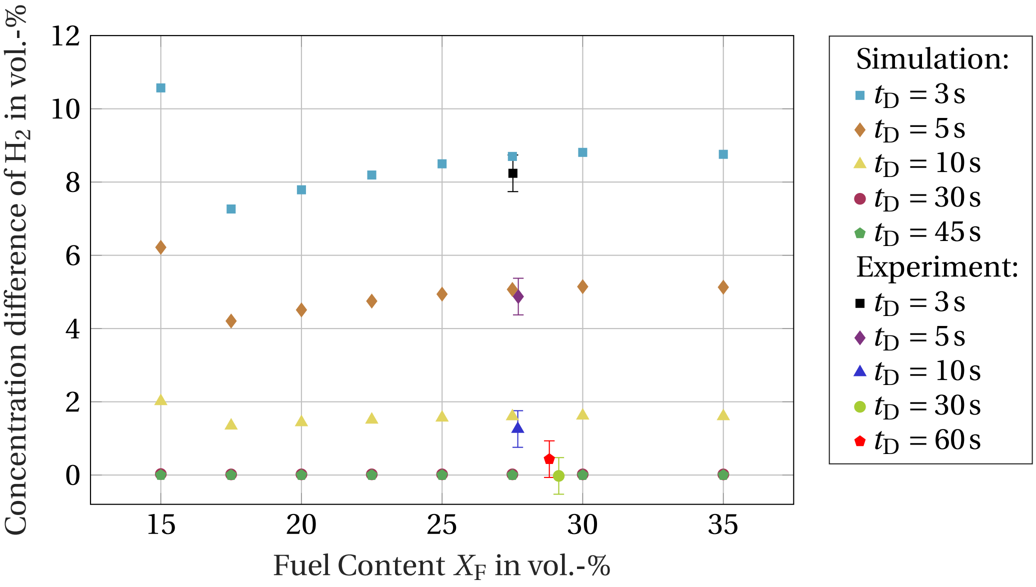

Figure 3.9: Concentration difference of the H_2-content X_{H_2} between the top and bottom of the channel over fuel content X_F for 75/25 H_2/CO.

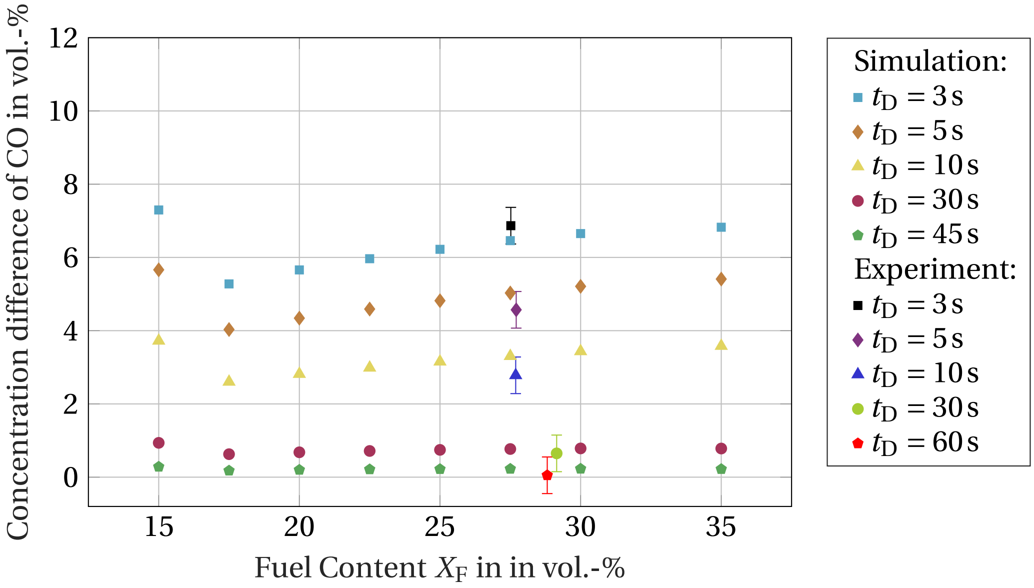

Figure 3.10: Concentration difference of the CO-content X_{CO} between the top and bottom of the channel over fuel content X_F for 75/25 H_2/CO.

fluence of diffusion during injection is increased with increasing fuel content, too. In contrast to 75/25, the concentration difference in H_2 and CO is not increasing with fuel content for 50/50 H_2/CO. A localized maximum is reached at $X_F = 17.5$ vol.-%. The concentration difference of H_2 and CO decrease for higher fuel contents.

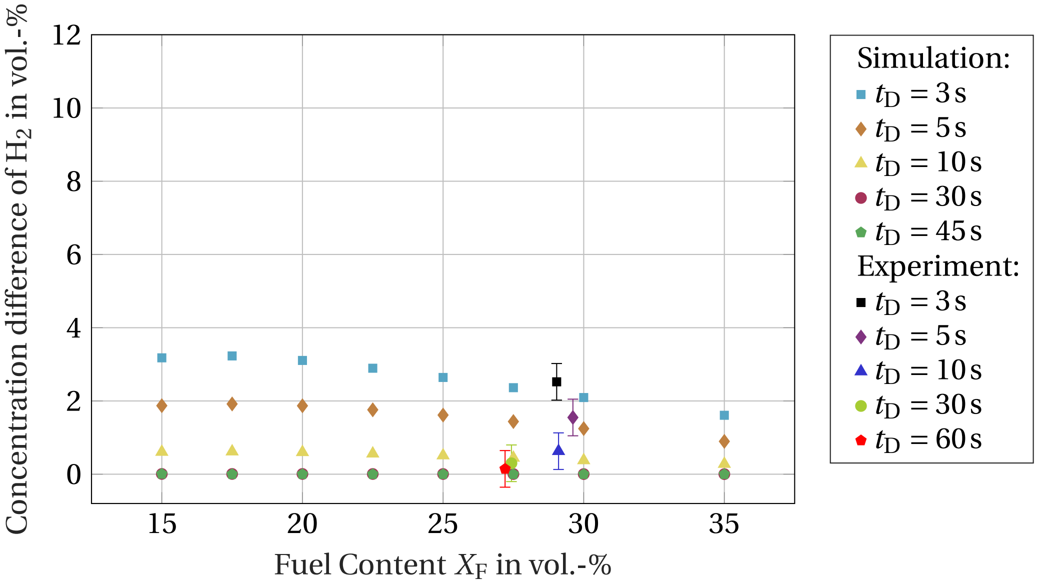

Figure 3.11: Concentration difference of the H_2-content X_{H_2} between the top and bottom of the channel over fuel content X_F for 50/50 H_2/CO.

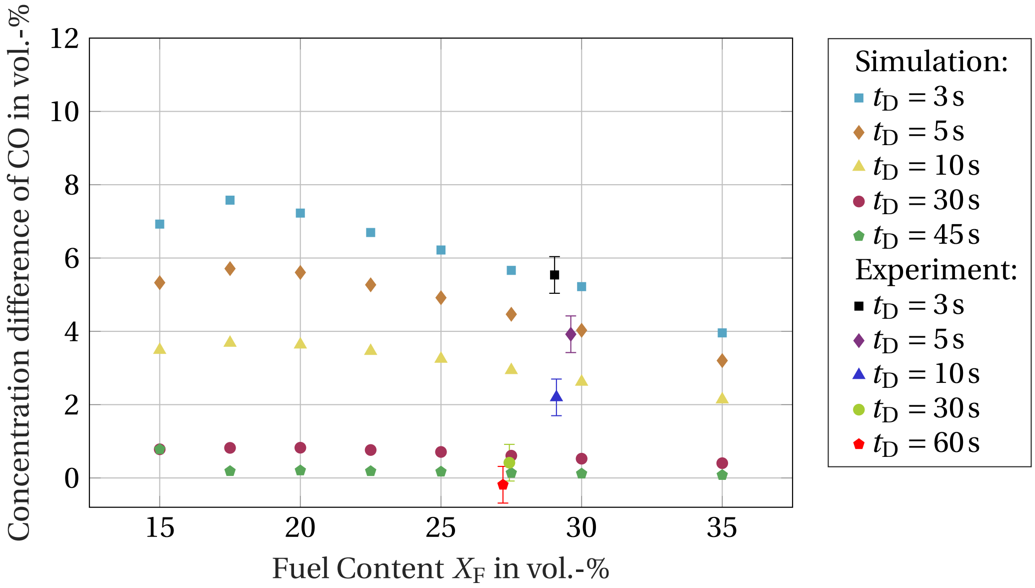

Figure 3.12: Concentration difference of the CO-content X_{CO} between the top and bottom of the channel over fuel content X_F for 50/50 H_2/CO.

Compared to the generation of transverse concentration gradients in H_2-air, as used by Vollmer and Boeck, the gas distribution for the ternary mixture of H_2, CO, and air becomes more complex. The lower diffusivity of CO compared to H_2 and the longer injection times t_{inj} lead to lower transverse concentration gradients. An evaluation of the fuel distribution function given in [16] reveals, that the spread in H_2 at $X_F = 20$ vol.-% is 31 vol.-% for $t_D = 3$ s. In comparison the sum of H_2 and CO spread is calculated to be 13.5 vol.-% for 75/25 and 10 vol.-% for 50/50 H_2/CO. The complex behavior of the gas mixture influences the local distribution of flame propagation properties such as the expansion ratio σ and the laminar flame speed s_L, which Boeck identified [16] as one of the main drivers of stronger FA in inhomogeneous mixtures and partially obstructed geometries. The local gas composition, as well as the local fuel content, must be considered.

3.4 Measurement system

The GraVent test rig is equipped with optical and conventional measurement systems. The conventional measurement systems are used for the presented investigation of DDT in H_2-CO-air mixtures, consisting of photodiodes and pressure sensors. Photodiodes and pressure sensors are mounted in the channel ceiling as depicted in Fig. 3.13.

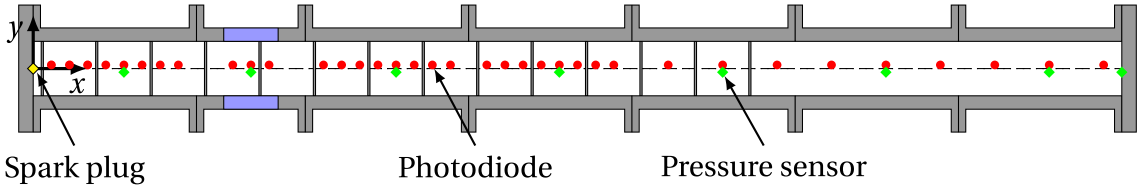

Figure 3.13: Photodiodes (red circles) and pressure sensors (green squares) in the GraVent test rig (top view).

Overall, 36 photodiodes and seven pressure sensors are mounted perpendicular to the main direction of flame propagation. One pressure sensor is mounted in the end plate, contrary to the direction of flame propagation. The photodiodes are shifted slightly upwards regarding the center axis of the channel ceiling (15 mm).The positions of the diodes are listed in Table 3.3. The pressure sensors are mounted slightly below (−15 mm). The positions of the sensors are listed in Table 3.4. The data of the photodiode, as well as of the pressure sensors, are recorded using four synchronized USB-controlled measurement cards (type DT-9836) operated at a frequency of 225 kHz.

Table 3.3: Position of photodiodes in the channel.

Nr.	1	2	3	4	5	6	7	8	9	10	11	12	13	14	15
x in m	0.1	0.2	0.3	0.4	0.5	0.6	0.7	0.8	1.1	1.2	1.3	1.6	1.7	1.8	1.9
Nr.	16	17	18	19	20	21	22	23	24	25	26	27	28	29	30
x in m	2	2.1	2.2	2.3	2.5	2.6	2.7	2.8	2.9	3	3.1	3.2	3.5	3.8	4.1
Nr.	31	32	33	34	35	36									
x in m	4.4	4.7	5	5.3	5.6	5.9									

Table 3.4: Position of dynamic pressure sensors in the channel.

Nr.	PDyn 1	PDyn 2	Pdyn 3	Pdyn 4	Pdyn 5	Pdyn 6	Pdyn 7	Pdyn 8
x in m	0.5	1.2	2	2.9	3.8	4.7	5.6	6

The photodiodes are of type Hamamatsu S1336-18BQ. The ultraviolet (UV)-sensitive diodes register the luminescence of the passing flame and allow to determine the arrival time of the flame at the position of each photodiode in the channel. The diodes are mounted in the channel's ceiling as shown in Fig. 3.14. The diode is protected from the pressure and heat of the flame by a UV-transmissive quartz glass window. Holes in the screw-in adapter and a plastic cap reduce the viewing angle to 10° allowing for a precise determination of the time of arrival.

The signals of the diodes are transmitted to transistor-based amplifiers. The amplification factor was kept constant during all experiments. If the amplification factor is chosen sufficiently high, the flame's arrival at one of the photodiodes will result in a step-signal. The arrival time can be determined based on the signal of each photodiode exceeding a certain threshold. For low fuel contents, the signal of the photodiodes does not exceed the threshold. Therefore, the lowest fuel content investigated in the present thesis is 15 vol.-% as only flames of $X_F \geq 15$ vol.-% resulted in sufficient signal peaks of the photodiodes.

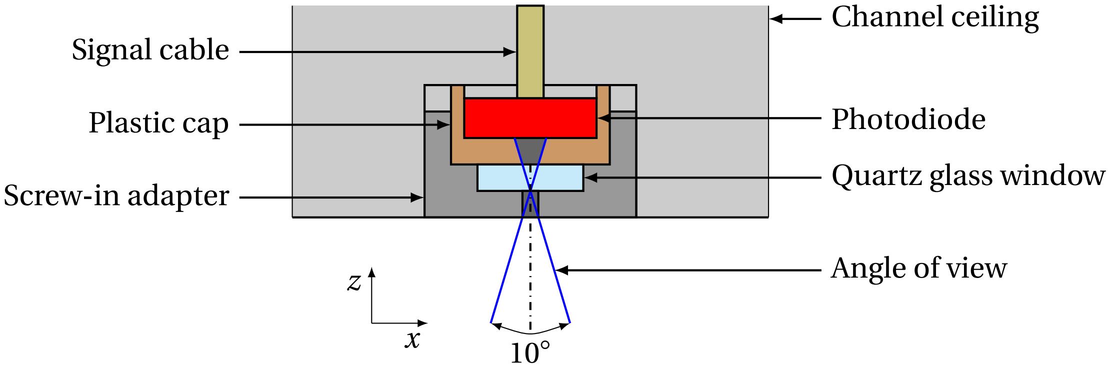

Figure 3.14: Photodiode in the channels ceiling (adapted from [23]).

The signals of the photodiodes are used to determine the flame speed u_f along the channel axis x. This is done based on the arrival time at two photodiodes t_i and t_{i+1}. The positions along the channel axis x_i and x_{i+1} are known, with x_{i+1} being downstream of x_i. The flame speed u_f at the intermediate position x_{mid} can be calculated by

$$u_f\Big|_{x_{mid}} = \frac{\Delta x_{i,i+1}}{\Delta t_{i,i+1}} = \frac{x_{i+1} - x_i}{t_{i+1} - t_i}. \tag{3.2}$$

The dynamic[‡] pressure transducers are piezoelectric pressure sensors of type Kistler 601A. A type Kistler 5011B charge amplifier amplifies the output signal and converts the charge output to a voltage signal. The sensors can measure peak pressures up to 250 bar. In order to prevent thermal shocking of the sensors by the flame, each sensor was covered with a thin layer of high-temperature silicone each time the channel was revised. As shown in [124], the influence of thin layers on the pressure signal can be neglected. Further information on the post-processing of the pressure sensor data can be found in Boeck [16].

[‡] Dynamic, in this case, refers to a short response time of the sensor to a pressure jump and not to the dynamic pressure fraction ρu^2 of the total pressure.

4 Results

Many single-shot experiments have been conducted in the framework of this thesis. A shot-by-shot analysis is not possible. In order to be able to classify the presented results, this chapter starts with the data evaluation in Sec. 4.1. In Sec. 4.2, the results of experiments with a homogeneous fuel distribution over the channel height are presented. The investigation is grouped according to FA, the onset of detonation, and the resulting peak pressures. The influence of fuel composition, fuel content, and obstacle geometry is investigated. The chapter is closed with the findings on the influence of concentration gradients on flame propagation in Sec. 4.3.

4.1 Data evaluation

Based on velocity data provided by the photodiodes, velocity-position (u_{F}-x)-diagrams are obtained. Based on the u_{f}-x-diagrams and the pressure data from the pressure sensors, characteristic quantities of the DDT process are evaluated. These are:

- The run-up distance x_{apr}, defined as the distance at which the flame velocity exceeds 95% of the speed of sound of the products of isobaric combustion $a_{\mathrm{pr}}{}^{\ddagger}$ [125].
- The relative terminal velocity $\tilde{u}_{\mathrm{term}}$, defined as the ratio of the mean terminal velocity in the unblocked part of the channel and the Chapman-Jouguet velocity $D_{\mathrm{CJ}}^{\ddagger}$ for the given fuel-air mixture.

[‡] Calculated using CANTERA [70] and the Shock-and-Detonation Toolbox [101]. Material properties are taken from [46].

- The maximum dynamic pressure $p_{\mathrm{dyn,max}}$, defined as the peak pressure measured at the pressure sensors in the ceiling of the channel.

The determination of the aforementioned quantities is explained using a velocity-distance diagram.

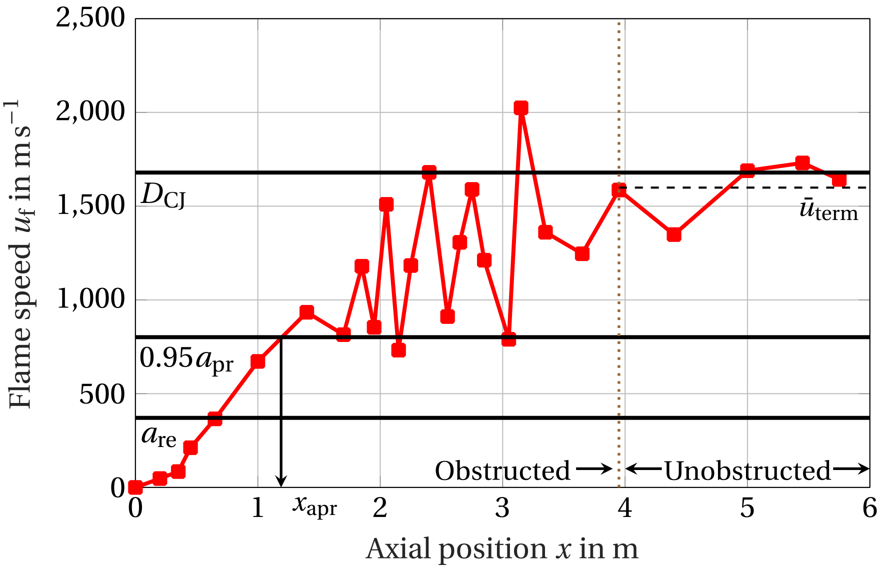

Figure 4.1: Flame speed u_f over axial position x for X_F =20.2 vol.-% and 75/25 H_2/CO at BR60S300.

In Fig. 4.1, a typical velocity profile of the flame speed u_f over the axial position x in 75/25 H_2/CO for a fuel content of X_F =20.2 vol.-% in a partially blocked channel (BR60S300) can be seen. Besides the flame speed u_f, the speed of the sound of the reactants a_{re}, the speed of sound of the products a_{pr}, and the Chapman-Jouguet velocity D_{CJ} for the given mixture are included in the figure. The transition between the obstructed and the unobstructed section is marked by a dotted, vertical line. After a slow initial acceleration phase, the slope of the curve becomes steeper at about $x = 0.45$ m. Then, the flame accelerates approximately linearly to a velocity above $0.95a_{Pr}$. The run-up distance is evaluated to $x_{apr} = 1.19$ m. After exceeding a_{pr}, strong velocity fluctuations are observed in the partially blocked section of the channel. The flame velocity varies between a_{Pr} and D_{CJ}. As soon as the flame leaves the obstructed section, it accelerates again to a mean terminal velocity of $\overline{u}_{term} = 1599\,\mathrm{m\,s^{-1}}$. The relative terminal velocity is $\tilde{u}_{term} = 0.95$.

The relative terminal velocity can be used to distinguish the regimes of flame propagation found in obstructed channels [126]: for $\tilde{u}_{\mathrm{term}} = 1$ the flame is in the detonation regime. Relative terminal velocities above unity can be caused by two different effects: First, an onset of detonation at the end of the obstructed section, and second, the expansion of a detonation from the obstructed to the unobstructed section. Both effects result in overdriven detonations. The short length of the unobstructed section does not allow for a relaxation of the detonation to the CJ-state as described in Sec. 2.7. Furthermore, overdriven detonations could be the result of a variation of the fuel content between the obstructed and unobstructed section due to the volume of the obstacles [‡]. In this case, fuel leaner mixtures are expected in the unobstructed section. In the obstructed section, a higher fuel content is found with respect to the measured fuel content. The fuel content is measured by the method of partial pressures, representing an averaged value of the fuel content. The flame is found in the choked flame regime for $\tilde{u}_{\mathrm{term}} \approx 0.5$. In this case, the flame velocity is similar to the isobaric speed of sound of the combustion products a_{pr}. For $\tilde{u}_{\mathrm{term}} \approx 0.3$, the flame propagates at the speed of sound of the reactants a_{re}. In between $0.3 < \tilde{u}_{\mathrm{term}} < 0.5$, the flame is specified as fast deflagration (or fast flame). A slow flame is identified for $\tilde{u}_{\mathrm{term}} \ll 0.3$.

Besides the relative terminal velocity, additional information about the flame propagation regime is delivered by the peak pressure $p_{\mathrm{dyn,max}}$. The higher the flame speed, the higher the pressure generated by the flame. For fast deflagrations, shock waves are formed by the coalescence of pressure waves in front of the flame. Shocks are characterized by a steep pressure rise. The higher the Mach number of the shock, the higher the pressure peak downstream of the shock. If detonations occur in a given mixture, the dynamic peak pressure $p_{\mathrm{dyn,max}}$ can be used as an additional indicator. Furthermore, $p_{\mathrm{dyn,max}}$ serves as an estimate of the load on the surrounding structure.

In order to determine the maximum dynamic pressure $p_{\mathrm{dyn,max}}$, the data provided by the pressure sensors PDyn 1 - PDyn 7 is analyzed. In Fig. 4.2, the pressure data from four selected pressure sensors are plotted over time for

---

[‡] The highest deviation is found at BR60S100 at a difference in the volume of $\approx 7\,\%$. For configurations in which detonations are observed, the volume change is $< 4\,\%$.

single-shot experiment of 75/25 H_2/CO at X_F = 20.2 vol.-% at BR60S300. In addition, the von-Neumann pressure p_{vN} and the Chapman-Jouguet pressure p_{CJ} for the mixture are shown. Ignition occurs at time $t = 0$ ms. The signals from the sensors show qualitatively different profiles.

At PDyn 1, a slow pressure increase can be seen, typical for the slow flame regime [127]. The flame passes the position of PDyn 1 at $t = 11.61$ ms. At about 12.5 ms, a jump occurs. A pressure wave reflection inside the obstructed section could have caused this. Between PDyn 1 and PDyn 3, the transition to the fast flame regime occurs. The coalescence of the pressure waves emitted during FA has led to the formation of a shock. This can be seen at PDyn 3 at 13.76 ms, as the pressure rises abruptly without any previous slow pressure rise as in the PDyn 1 data. Immediately after the passing of the leading shock, additional pressure waves can be seen. These are due to the interaction of the leading shock with the obstacles. The interaction between shock reflections and the flame leads to the velocity variations shown in Fig. 4.1. Comparing the data from PDyn 3 with those from PDyn 4 and 5 reveals a similar pattern (see Fig. 4.4). The peak pressures registered are similar to PDyn 3. The pressure signals obtained for sensors PDyn 3-5 are typical for supersonic flames in partially obstructed channels. Compared to detonation, pressure data of fast flames involve a steep increase in pressure combined with high pressure over a longer time. However, the peak pressure is lower than for a detonation [128]. A significant increase in peak pressure is observed in the unblocked section of the channel.

The pressure sensor closest to the end of the obstructed section is PDyn 6. The peak pressure measured there corresponds to the maximum peak pressure $p_{dyn,max} = 2.17$ MPa for the given single-shot experiment. The level of the first peak in the pressure profile determines the peak pressure. Reflections of shocks might lead to higher pressure levels afterward. However, these peaks are not considered in the determination of $p_{dyn,max}$. The pressure level and the flame velocity in this channel section indicate that the detonation regime is reached. The measured peak pressure $p_{dyn,max}$ is between the Chapman-Jouguet pressure p_{CJ} and the von Neumann pressure p_{vN} of the fuel-air mixture. A pressure jump is observed at 18 ms, which is related to reflection from

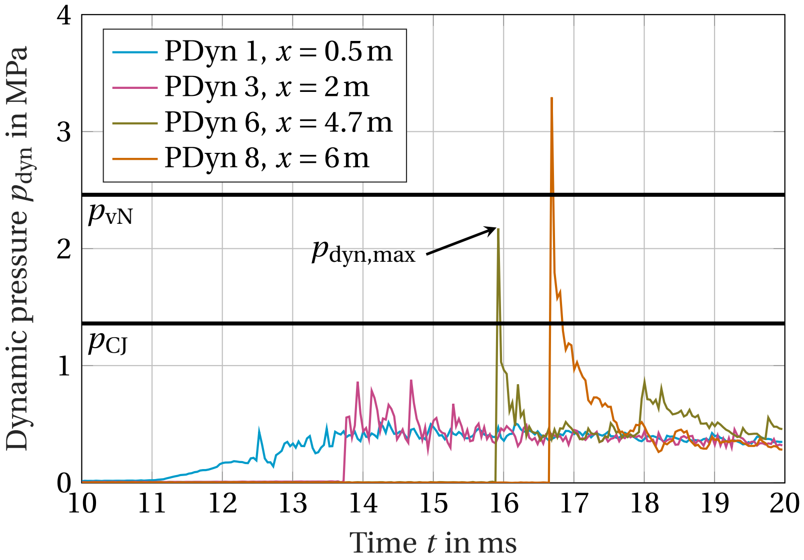

Figure 4.2: Dynamic pressure p_{dyn} over time t for X_{F} =20.2 vol.-% and 75/25 H_2/CO at BR60S300.

the detonation at the end plate. Compared to PDyn 6, the pressure jump at PDyn 8 is even higher. This is due to the reflection of the detonation at the end plate. Furthermore, PDyn 8 is mounted parallel to the flow direction in the channel. Hence, in addition to the static pressure, the dynamic pressure component of the flow acts directly on the sensor. As a result, the peak pressures are higher than for the sensors mounted perpendicular to the flame propagation direction [128]. Therefore, $p_{\mathrm{dyn,max}}$ is determined using the data from PDyn 1-7.

In order to reduce stochastical effects on the results, each experiment is repeated at least three times. As described in 3.2, variations in the fuel content of ±0.5 vol.-% with regards to the desired fuel content are accepted. The following compares three single-shot experiments (Exp) with fuel contents within the valid range of fuel content variation. In Fig. 4.3 u_{F}-x-diagrams for X_{F} =20.2 vol.-%, X_{F} =19.9 vol.-%, and X_{F} =19.7 vol.-% at 75/25 H_2/CO are shown. The mean speed of sound of the products $\bar{a}_{\mathrm{pr}}$ and Chapman-Jouguet velocity $\bar{D}_{\mathrm{CJ}}$ with respect to the fuel content X_{F} of each experiment are added. Due to the accepted variation in X_{F}, a_{pr} and D_{CJ} vary at $\approx \pm 1\,\%$ with respect to their average values. As indicated by Fig. 4.3, the results of the experiments are in good agreement with each other. A qualitative comparison shows that all flame speed profiles show the same behavior: a fast acceleration to a_{pr}, velocity fluctuations in the obstructed section, and slight acceleration in the unobstructed part of the channel. Differences between the experiments are observed in the fluctuations in the partially blocked section of the test rig. However, since this section is not part of the evaluated parameters of the experiments, the relevance of these fluctuations is limited. For the run-up distance to a_{Pr} and the relative terminal velocity $\tilde{u}_{\mathrm{term}}$ the standard deviation is $SD = 0.018\,\mathrm{m}$ for x_{apr} and $SD = 0.006$ for $\tilde{u}_{\mathrm{term}}$.

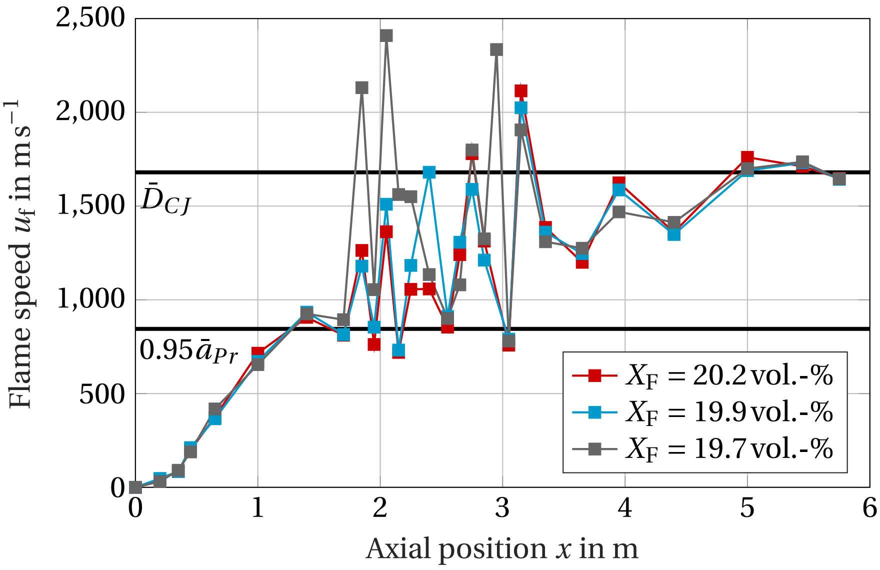

Figure 4.3: Flame speed u_{F} over axial position x for a desired fuel content of X_{F} =20 vol.-% and 75/25 H_2/CO at BR60S300.

Analogous to the velocity in Fig. 4.3, Fig. 4.4 shows the peak pressures $p_{\mathrm{dyn\,max,i}}$ of the respective pressure sensors i for experiments of X_{F} =20.2 vol.-%, X_{F} =19.9 vol.-% and X_{F} =19.7 vol.-%. For better classification of the peak pressure, the respective mean values of the Chapman-Jouguet pressure $\bar{p}_{\mathrm{CJ}}$ and of the von-Neumann pressure $\bar{p}_{\mathrm{vN}}$ with respect to each experiment are added. Similar to Fig. 4.3, the variation of X_{F} between each experiment leads to deviations from the means of $\bar{p}_{\mathrm{CJ}}$ and $\bar{p}_{\mathrm{vN}}$ by ±2 %. The plot shows a larger variation of $p_{\mathrm{dyn\,max,i}}$ compared to u_{F}. The development of $p_{\mathrm{dyn\,max,i}}$ along the axial position in the channel x is similar. At $x = 0.6\,\mathrm{m}$, $p_{\mathrm{dyn\,max,1}}$ agrees well among the displayed experiments. Downstream, the pressure rises above p_{CJ} at X_{F}

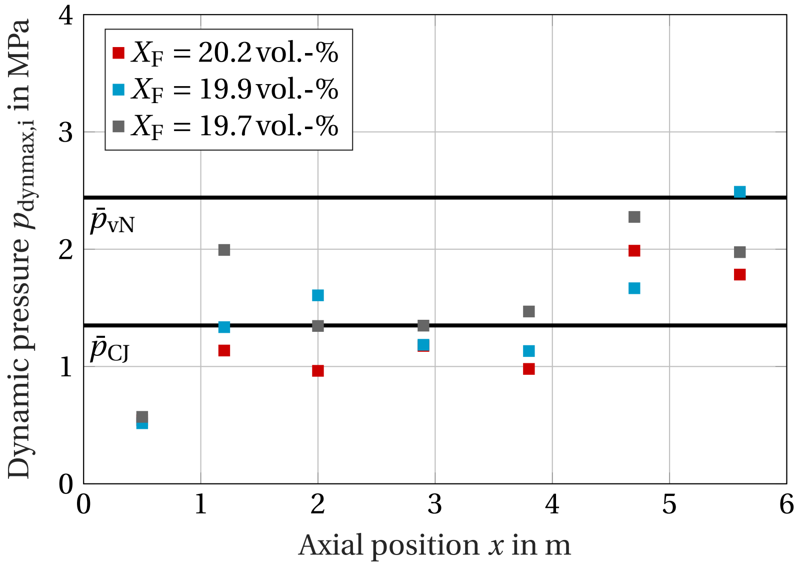

Figure 4.4: Maximum dynamic pressure $p_{\mathrm{dyn\,max,i}}$ for pessure sensors PDyn 1-7 over axial position x for a desired fuel content of X_F =20 vol.-% and 75/25 H_2/CO at BR60S300.

=19.7 vol.-%. This could be due to a localized explosion. From PDyn 3 on, the respective peak pressures converge again. Like the flame velocity data, the peak pressures indicate that the flames are in the same propagation regime in all experiments. This assumption is supported by the small scatter of $p_{\mathrm{dyn,max}}$ around p_{CJ} in the remaining part of the obstacle section. As the obstacle section ends, the measured peak pressure increases. The maximum dynamic pressure $p_{\mathrm{dyn,max}}$ is reached at 4.7 m for experiments for X_F =20.2 vol.-% and for X_F =19.7 vol.-% and at 5.6 m for experiment for X_F =19.9 vol.-%. This results in a mean value at the desired fuel content of X_F = 20 vol.-% of $p_{\mathrm{dyn,max}}$ = 2.3 MPa and a variance of SD = 0.18 MPa.

4.2 Homogeneous mixtures

In order to investigate FA and DDT in homogeneous H_2-CO-air mixtures, the parameters $\tilde{u}_{\mathrm{term}}$, x_{apr}, and $p_{\mathrm{dyn,max}}$ explained in Sec. 4.1 are determined for each single-shot experiment. The data presented in the following section is based on the average of all experiments performed for each fuel and at a desired fuel content. Single-shot experiments with a variation of ±0.5 vol.-% with respect to the desired fuel content were assigned to the desired fuel content. At least three tests are combined into one data point at each desired fuel content. The diffusion time for the homogeneous case is $t_\mathrm{D} = 60\,\mathrm{s}$. This results in a uniform distribution of the fuel over the channel height z and a reduction of the initial turbulence at the ignition of the mixture. The section is structured according to the flame propagation mode. Sec. 4.2.1 discusses FA in terms of x_apr in all investigated configurations. Sec. 4.2.2 presents the onset of detonations based on $\tilde{u}_\mathrm{term}$ in the obstructed configurations. The onset of detonations in the unobstructed configuration is discussed in Sec. 4.2.3. The resulting pressures $p_\mathrm{dyn,max}$ are analyzed in Sec. 4.2.4.

4.2.1 Flame acceleration to fast flames

The run-up distances to the speed of sound of the products x_apr are plotted over the fuel content X_F in Fig. 4.5 to Fig. 4.8 for the obstructed and in Fig. 4.9 for the unobstructed configuration. The run-up distance changes with the fuel content, the fuel composition, and the obstacle configuration. Except for BR60S100, x_apr decreases with increasing fuel content. A local minimum is typically found around 25 vol.-%. If the fuel content further increases, the run-up distance increases. The following section discusses the influence of the fuel composition and the fuel content in detail for each obstacle configuration.

For BR30S100, the mean run-up distance is 1.08 m for 100/0, 1.20 m for 75/25 and 1.49 m for 50/50 H_2/CO. The run-up distance x_apr is plotted over the fuel content X_F in Fig. 4.5. The figure shows that the difference between 100/0 and 75/25 H_2/CO is small for fuel contents up to 25 vol.-%. In contrast, the difference to 50/50 H_2/CO in this region ranges between 0.2-0.5 m. Furthermore, the dependence of x_apr on the fuel content is larger at 50/50 than at 100/0 and 75/25 H_2/CO. For 100/0 and 75/25 H_2/CO, the minimum run-up distance is reached at 25 vol.-%. For 50/50 H_2/CO, the minimum is shifted to a higher fuel content at 27.5 vol.-%. Differences in x_apr for 50/50 H_2/CO are small in the region between 22.5-35 vol.-%. Increasing the fuel content from 15 vol.-% on leads to a decrease in the standard deviation. The run-up distance is very similar for all fuels and fuel contents in the fuel-rich region. A slight increase is observed at a fuel content of 40 vol.-% for 50/50 H_2/CO. All in all, it seems to be reasonable to assume an almost constant run-up distance for fuel-rich mixtures. It should be noted that TD-instabilities, which are important for early FA in the case of lean H_2-air mixtures [15], are not present at fuel-rich conditions. Hence, flame surface enlargement due to flame wrinkling by TD instabilities is not found. However, the laminar flame speed and expansion ratio increase in fuel-rich mixtures, balancing the reduced effects of flame wrinkling.

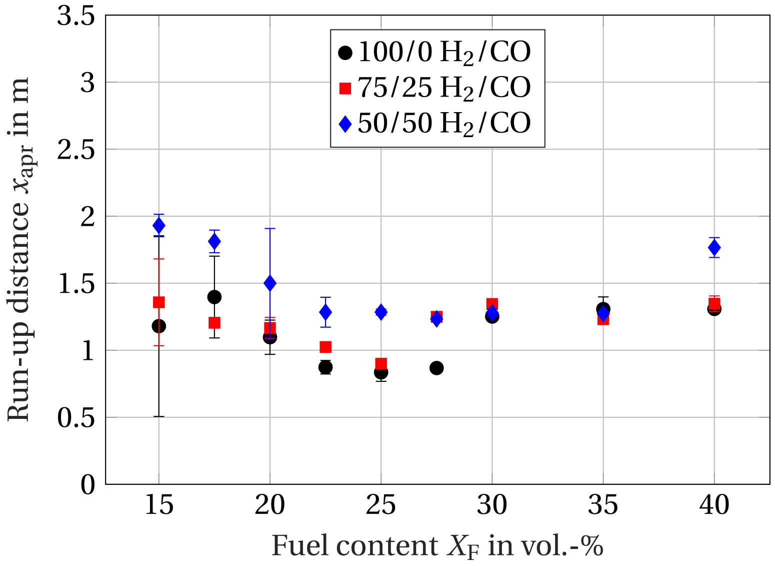

Figure 4.5: Run-up distance to speed of sound of the isobaric products x_{apr} over fuel content X_F at BR30S100.

For BR30S300, the run-up distance increases compared to BR30S100 as indicated in Fig. 4.6. This results from larger obstacle spacing and a smaller number of obstacles. Average run-up distances are 1.47 m for 100/0, 1.70 m for 75/25 and 1.77 m for 50/50 H_2/CO. In contrast to BR30S100, the differences between 100/0 and 75/25 H_2/CO are larger. Like BR30S100, x_{apr} decreases for an increasing fuel content. A minimum is reached at 22.5 vol.-% for 100/0 and 75/25 H_2/CO. For 50/50 H_2/CO, a minimum is found at 25 vol.-%. For fuel-rich mixtures, the trend in x_{apr} is unambiguous. From 30 vol.-% on for 100/0 and 50/50 as well as from 25 vol.-% for 75/25 H_2/CO on, no clear trend is shown for the run-up distances. Generally, the trend in x_{apr} over X_F is similar to BR30S100.

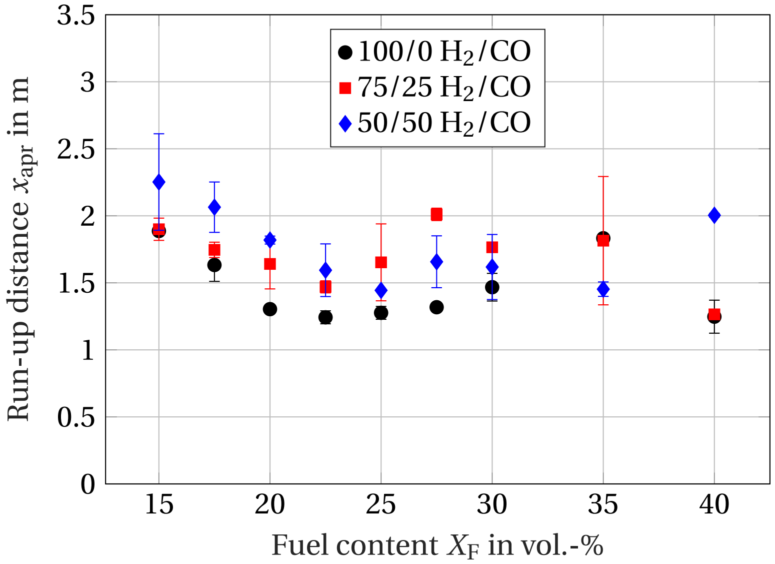

Figure 4.6: Run-up distance to speed of sound of the isobaric products x_{apr} over fuel content X_F at BR30S300.

In Fig. 4.7, the run-up distances for BR60S300 are plotted over the fuel content. In comparison to BR30S300, the run-up distances at 1.26 m for 100/0, 1.29 m for 75/25 and 1.35 m for 50/50 H_2/CO are shorter, but longer than for BR30S100. In the case of BR60S300, a u-shaped curve of x_{apr} over the fuel content X_F is most prominent for 100/0 and 75/25 H_2/CO. Between all investigated configurations the impact of the fuel content on x_{apr} is the strongest in BR60S300. For 100/0 H_2/CO the difference in x_{apr} between 15 vol.-% and the minimum at 25 vol.-% is about 0.5 m. Increasing the fuel content from 25 vol.-% on leads to a monotonic increase in x_{apr} for 100/0 H_2/CO. A similar behavior is obtained at 75/25 H_2/CO. The difference between 100/0 and 75/25 H_2/CO is small for fuel contents up to 30 vol.-%. 50/50 H_2/CO follows the trend of 100/0 and 75/25 closely, up to a fuel content of 22.5 vol.-%. Larger discrepancies are given in the range of 22.5-27.5 vol.-% for 50/50 H_2/CO.

For BR60S100, the run-up distance x_{apr} is shown in Fig. 4.8. The impact of fuel composition and fuel content differs from those observed for the other obstructed configurations investigated. While x_{apr} decreased with increasing fuel content at BR30 and BR60S300, an opposite behavior is observed for BR60S100. The shortest run-up distances are found at the lean limit of the

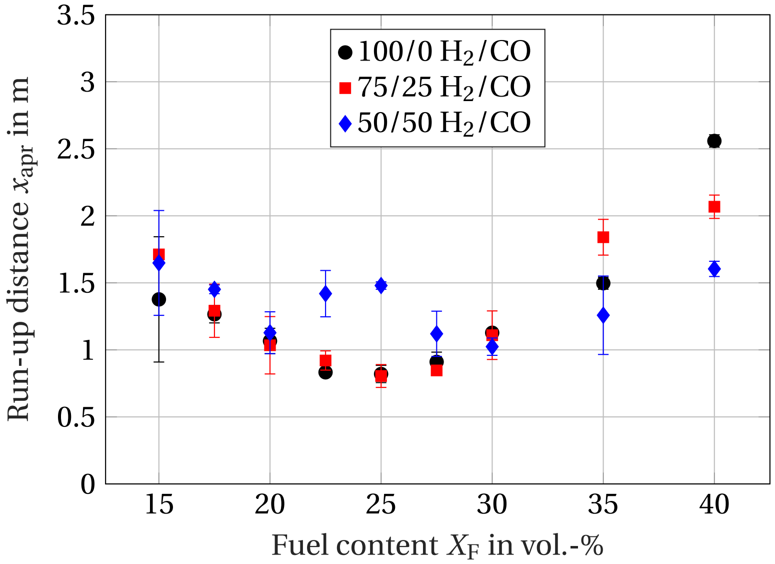

Figure 4.7: Run-up distance to speed of sound of the isobaric products x_{apr} over fuel content X_{F} at BR60S300.

investigated fuel contents at 15 vol.-% for 100/0 and 75/25 and at 17.5 vol.-% for 50/50 H_2/CO. By increasing the fuel content, the run-up distance increases as well. Up to a fuel content of 27.5 vol.-%, the shortest run-up distances are found for 50/50 H_2/CO. In this obstacle configuration, the differences between the fuels investigated are the smallest. Furthermore, the impact of the fuel content on the run-up distance is smaller than for BR30 and BR60S300.

The run-up distance to the isobaric speed of sound of the combustion products x_{apr} over the fuel content X_{F} for BR00 is shown in Fig. 4.9. Experiments at 15 vol.-% were not evaluated due to the low signal amplitude in the photodiode data. In contrast to the partially blocked channel, a_{pr} is not exceeded for all fuels and fuel contents. An unambiguous dependence of x_{apr} on the fuel composition is observed. At 100/0 H_2/CO, a_{pr} is exceed for fuel contents between 20 and 30 vol.-%. For 75/25 mixtures from 22.5-30 vol.-% reach $0.95a_{\mathrm{pr}}$, while the range is further reduced for 50/50 H_2/CO from 25-30 vol.-%. For flames reaching flame speeds above $0.95a_{\mathrm{pr}}$, a dependence of x_{apr} on the fuel content is observed for 100/0 H_2/CO only. A minimum in x_{apr} is reached at a fuel content of 25 vol.-%. The run-up distance increases in leaner mixtures. The change in x_{apr} becomes smaller for fuel-rich mixtures than fuel-lean mix-

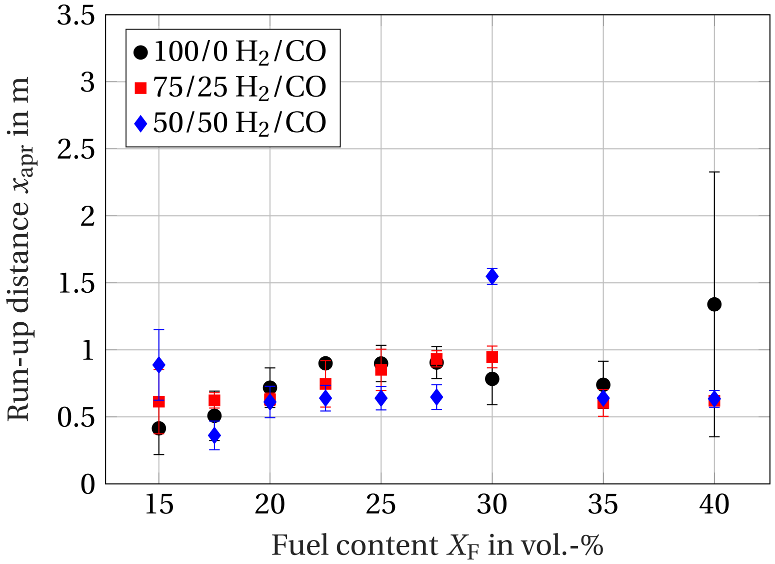

Figure 4.8: Run-up distance to speed of sound of the isobaric products x_{apr} over fuel content X_F at BR60S100.

tures. The dependence of x_{apr} on X_F is weaker at 75/25 than at 100/0 H_2/CO. A minimum is observed at 25 vol.-%. However, the decrease in x_{apr} compared to the mean run-up distance over all fuel contents becomes negligible. A similar observation can be made for 50/50 H_2/CO. A clear trend cannot be observed due to the little number of mixtures reaching flame speeds above $0.95a_{pr}$.

Summarizing the discussion of the run-up distance for the obstructed configuration, different influences of the configuration, fuel composition, and fuel content can be identified. The shortest run-up distances are found for BR60S100. In this configuration, the influence of fuel composition and content is minimal. A more specific behavior concerning fuel content is obtained for less obstructed configurations, such as BR30 and BR60S300. For these configurations, the shortest run-up distance is obtained for BR30S100 and BR60S300. For BR30S300, the minimum x_{apr} is increased by almost 50 % with respect to BR30S100 and BR60S300. Furthermore, the impact of the fuel composition is more prominent at the BR30 configurations than at BR60. For BR00, the decelerating effect of H_2-CO-air mixtures compared to H_2-air becomes most evident.

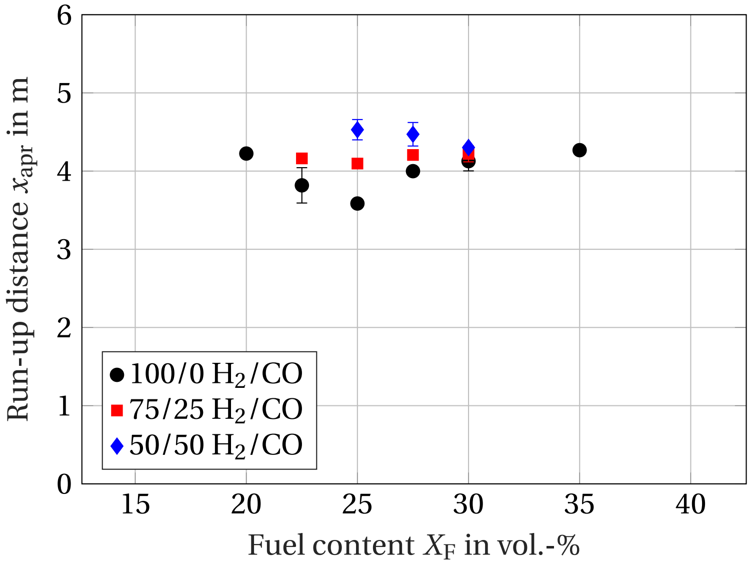

Figure 4.9: Run-up distance to speed of sound of the isobaric products x_{apr} over fuel content X_F at BR00.

The differences in x_{apr} concerning the different configurations are linked to different mechanisms of FA. For BR00, the expansion of the combustion product is the main driver for FA. The flow induced by the expansion leads to the formation of a boundary layer. Thereby the turbulence necessary to increase the overall consumption of the fuel to trigger FA is generated. This process is influenced by the effective burning velocity σs_L, intrinsic instabilities at the flame front, and the wall roughness. The Markstein-length and the Lewis number Le are similar for fuel-lean conditions. It can be assumed that the effect of stretch and intrinsic flame instabilities is similar for the fuels investigated. Hence, the effective burning velocity has the strongest impact on FA. As shown in Sec. 2.4, s_L is highly influenced by the H_2 content, while the expansion ratio σ is similar for all fuel compositions. Overall, the effective burning velocity σs_L is lower for an increased CO-content at the same fuel content.

This explains why higher CO-contents require higher fuel contents to exceed a_{Pr} at BR00. For the investigated geometry, a threshold in the effective burning velocity $s_L\sigma$ can be estimated for fuel-lean mixtures of the fuel compositions investigated. For effective burning velocities below $(s_L\sigma)_{crit}$ FA up to a_{Pr} is not observed. For mixtures in which $s_L\sigma$ is larger than $(s_L\sigma)_{crit}$, FA up to a_{Pr} in the given geometry is possible. The threshold of $(s_\mathrm{L}\sigma) = 5.24$ poses a limit to FA up to a_pr for all fuel compositions. It should be emphasized that the threshold is limited to the given configuration of a 6 m long channel length with a rectangular cross-section, as strong FA might be found for lower fuel contents in a longer channel. The threshold should not be treated similarly to the σ-criterion for FA in obstructed configurations. The effect of the obstacles in the case of BR30 is similar to a rough wall. Turbulence production is increased by the expansion of the combustion products causing stronger FA. This leads to a shorter run-up distance and a wider range of fuel contents exceeding a_Pr compared to BR00. The impact of the effective burning velocity σs_L is decreased.

FA at higher blockage ratios (such as BR60) is caused by jet flows through the opening of the obstacles. Turbulence is produced in the shear layer between the jet and the gas pockets enclosed by the obstacles [128]. The delayed burning of the pockets leads to strong FA [129]. A possible limit of FA can be caused by flame quenching in the highly turbulent shear layer between the jets and the pockets. As shown by Barfuss in a DNS simulation in [130] of a flame propagating at a_Re through repeated obstacles of BR60, quenching is of minor importance for mixtures of H_2-CO-air for CO-contents up to 50 % in the fuel. This becomes evident at BR60S100. Fuel composition and fuel content are of minor importance for x_apr.

For BR60S300 X_F becomes more important, as the expansion of the combustion products in the early stages of flame propagation takes longer until the pockets between the obstacle are completely burnt. Hence, the build-up of shear layers takes more time, and FA becomes weaker. However, the impact of the jet flows still governs the later stages of FA, which is why the influence of the fuel composition is weaker at BR60S300 than at BR30.

In terms of practical applications, the following can be summarized:

- The influence of CO becomes more evident in the case of smaller turbulence generation by the interaction of the expansion flow with the obstacles. Especially for flame propagation in an unobstructed channel, weaker FA is observed for an increased CO content. The fuel content at which flame speeds exceed a_Pr needs to be significantly higher than for 100/0 H_2/CO. In practical applications, CO in a fuel mixture is often replaced with additional H_2 based on volume fractions. This approach leads to an overprediction of the tendency of FA, especially at BR00.

- For obstacle configurations featuring a low blockage ratio, the influence of lower laminar flame speed is lower due to CO addition. Longer run-up distances are obtained for CO addition. For shorter obstacle spacings at the same blockage ratio, the influence of CO-contents up to 25 vol.-% is small, and run-up distances similar to 100/0 H_2/CO can be expected.
- For obstacle configurations featuring higher blockage ratios, the influence of turbulence production in the wake of the obstacle dominates over the influence of the fuel composition up to a CO-content of 50 vol.-% in the fuel. This effect is most evident at BR60S300.

4.2.2 Detonations in obstructed configurations

Once the flame speed exceeds the speed of sound of products a_{Pr}, the onset of detonation is possible. Hence, the onset of detonation is possible for all fuel-air mixtures investigated in obstructed configurations. Therefore, the following section compares the impact of fuel content, fuel composition, and obstacle configuration on the onset of detonation in the obstructed configurations. In order to investigate the flame propagation regime of a given mixture, the relative terminal velocity $\tilde{u}_{\mathrm{term}}$ is presented in the following.

In Fig. 4.10 to 4.13, the relative terminal velocity $\tilde{u}_{\mathrm{term}}$ is plotted over the fuel content X_{F} for the investigated fuels of 100/0, 75/25, and 50/50 H_2/CO for the partially obstructed configurations BR30S100, BR30S300, and BR60S300. For fuel contents of 15 vol.-%, $\tilde{u}_{\mathrm{term}}$ is found between 0.4 – 0.6. All mixtures are in the fast flame regime. If the fuel content is increased to 17.5 vol.-%, $\tilde{u}_{\mathrm{term}}$ increases. However, the increase depends on the obstacle configuration. Small increases in $\tilde{u}_{\mathrm{term}}$ are found at BR30S100 and BR60S300. While the standard deviation at 17.5 vol.-% for BR60S300 is similar to $X_{\mathrm{F}} = 15$ vol.-%, this is not the case for BR30S100. High standard deviations are found for 100/0 and 75/25 H_2/CO. Large fluctuations in $\tilde{u}_{\mathrm{term}}$ are associated with a transition between the regime of fast flames and detonations. It can be concluded that a transition to detonation is imminent for 100/0 and 75/25 at BR30S100, while 50/50 H_2/CO remains in the fast flame regime. At BR60S300, the fluctuations and the mean of $\tilde{u}_{\mathrm{term}}$ at 17.5 vol.-% are lower. A transition is not observed. For BR30S300 a jump in $\tilde{u}_{\mathrm{term}}$ is shown between 15 vol.-% and 17.5 vol.-%. This is still accompanied by high fluctuations in $\tilde{u}_{\mathrm{term}}$ at 75/25 H_2/CO. A similar fluctuation of the lean detonation limit was observed for H_2-air mixtures in tubes with repeated obstacles by Eder in [39]. In the tube configuration, the transition from a slow flame to a fast flame to detonation was found in equivalence ratio from $\Phi = 0.46$ to 0.58. All flame propagation regimes were found for different shots within this range of equivalence ratios.

If the fuel content increases further, $\tilde{u}_{\mathrm{term}}$ is found in the detonation regime for BR30S100, BR30S300, and BR60S300. Within the detonation regime, the fluctuation of $\tilde{u}_{\mathrm{term}}$ is smaller than in the transition region. A stable detonation seems to be reached by all fuels. In case of BR60S300 $\tilde{u}_{\mathrm{term}}$ is very similar for all fuels investigated between $20-25$ vol.-%. For BR30S100, a similar trend can be observed. As shown in Fig. 4.10 there are small differences in $\tilde{u}_{\mathrm{term}}$ between the different fuels for 20-30 vol.-%. The highest $\tilde{u}_{\mathrm{term}}$ is observed at almost all fuel contents for 100/0 H_2/CO. For 75/25, $\tilde{u}_{\mathrm{term}}$ is very similar to 100/0 H_2/CO. For 50/50, a shift from the values obtained for 100/0 and 75/25 H_2/CO is observed. This trend is stronger in BR30S300 for 20-30 vol.-%. In this configuration, fuels of 100/0 and 75/25 H_2/CO are found at terminal velocities of $\tilde{u}_{\mathrm{term}} \approx 1.2$. For 50/50 H_2/CO, $\tilde{u}_{\mathrm{term}}$ is varying close to unity. In the detonation regime, $\tilde{u}_{\mathrm{term}}$ is mostly above unity. This likely relates to the quasi-detonation's expansion into the channel's unobstructed section. As shown in Sec. 4.1, the transition from the obstructed to the unobstructed section is accompanied by an increase in u_{F}, likely to result in an overdriven detonation. Similar behavior was observed by Beauvais et al. in [128], Vollmer in [23], and Boeck in [16]. However, as the length of the obstructed section in [16, 23] was 2.05 m, the overdriven detonation was able to relax to a propagation speed closer to D_{CJ}.

The flames remain in the detonation regime up to a fuel content of 30 vol.-% for the obstacle configurations BR30S100, BR30S300, and BR60S300. Differences between the obstacle configurations and fuels are observed if the fuel content increases. At BR30S100 $\tilde{u}_{\text{term}}$ is decreased to 0.9 for 100/0 H_2/CO at 35 vol.-%. The decrease in $\tilde{u}_{\text{term}}$ from $X_F = 30$ vol.-% is accompanied by an increase in the standard deviations, similar to the transition from the fast flame regime to the detonation regime at $X_F = 17.5$ vol.-%. In contrast, 75/25 and 50/50 H_2/CO remain in the detonation regime, featuring low variations in $\tilde{u}_{\text{term}}$. At $X_F = 40$ vol.-%, detonations are observed for 50/50 H_2/CO only. In the case of 100/0 and 75/25 H_2/CO, the terminal velocity is close to the value obtained at 15 vol.-%.

For BR30S300, all fuels stay in the detonation regime at $X_F = 30$ vol.-%. In contrast to leaner mixtures in the detonation regime, a larger velocity deficit with respect to D_{CJ} is obtained for 75/25 H_2/CO. The flame might still be attributed to the detonation regime as the standard deviation is small. For $X_F = 40$ vol.-%, only 50/50 H_2/CO is found in the detonation regime. Similar to BR30S100, $\tilde{u}_{\text{term}}$ of 100/0 and 75/25 H_2/CO are similar for 15 and 40 vol.-%. A stable detonation is observed for 50/50 H_2/CO at 40 vol.-%, since the standard deviation is small compared to the transition at 17.5 vol.-%. At BR60S300 a transition is displayed for 100/0 and 75/25 H_2/CO between 30 vol.-% and 35 vol.-%. While $\tilde{u}_{\text{term}}$ for 50/50 H_2/CO is still around unity, the standard deviation is already increased. At $X_F = 40$ vol.-% $\tilde{u}_{\text{term}}$ is decreased to 0.55 indicating a transition to the fast flame regime. However, $\tilde{u}_{\text{term}}$ and the standard deviation are still higher than for 100/0 and 75/25 H_2/CO, suggesting that the transition is not completed.

The behavior at BR60S100 differs from BR30 and BR60S300, as no detonations are observed. The relative terminal velocity varies between 0.14 and 0.33 for all fuel contents investigated. Furthermore, the variation of $\tilde{u}_{\text{term}}$ is smaller than at other obstacle configurations. At the leanest fuel content, $\tilde{u}_{\text{term}}$ is found at 0.2. In contrast to BR30 and BR60S300, this corresponds to terminal velocities close to the speed of sound of the reactants. Following the terminology in [127], these flames are considered slow flames. If the fuel content is increased, $\tilde{u}_{\text{term}}$ increases slightly. The relative terminal velocity is similar for all fuels. The standard deviation for all fuel contents and fuels is low. No sudden jumps in $\tilde{u}_{\text{term}}$ as shown in Fig. 4.10 to 4.12 are observed. The maximum $\tilde{u}_{\text{term}}$ is reached at a fuel content of 25 vol.-% for all fuels. If the fuel content is

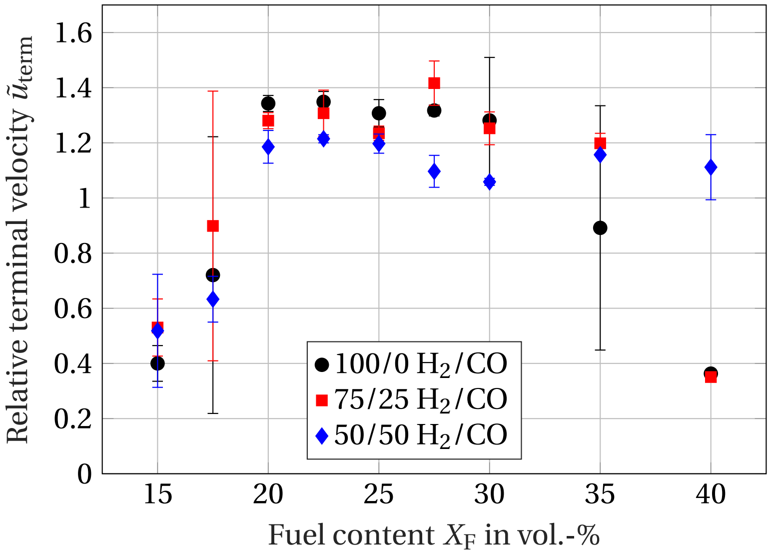

Figure 4.10: Relative terminal velocity $\tilde{u}_{\text{term}}$ over fuel content X_F at BR30S100.

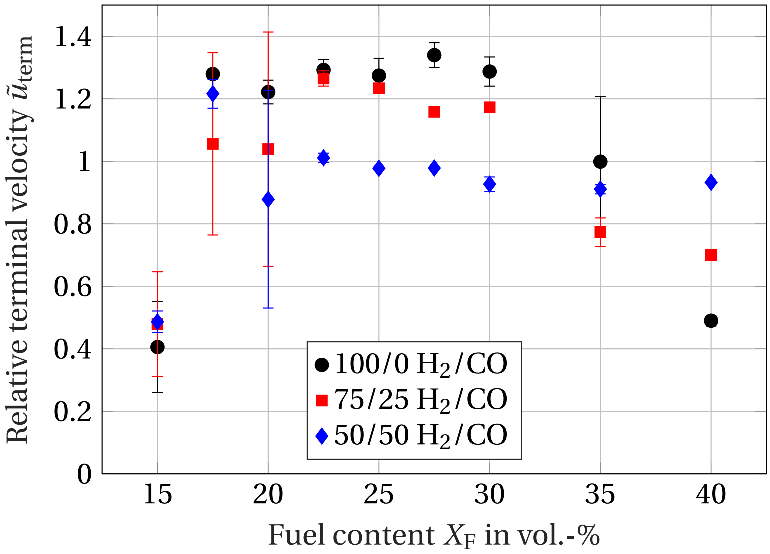

Figure 4.11: Relative terminal velocity $\tilde{u}_{\text{term}}$ over fuel content X_F at BR30S300.

further increased, $\tilde{u}_{\text{term}}$ drops. Although the velocities in the obstructed part of the channel are found above a_{pr}, $\tilde{u}_{\text{term}}$ is found between 0.14 to 0.33 for BR60S100. Hence, flames decelerate at the transition between the obstructed and the unobstructed section. In contrast to BR30 and BR60S300, no apparent differences are observed for fuel-rich mixtures.

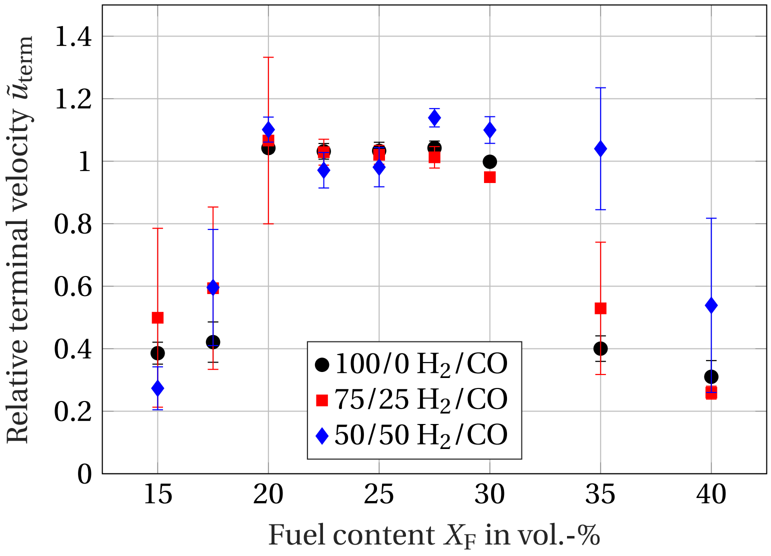

Figure 4.12: Relative terminal velocity $\tilde{u}_{\text{term}}$ over fuel content X_F at BR60S300.

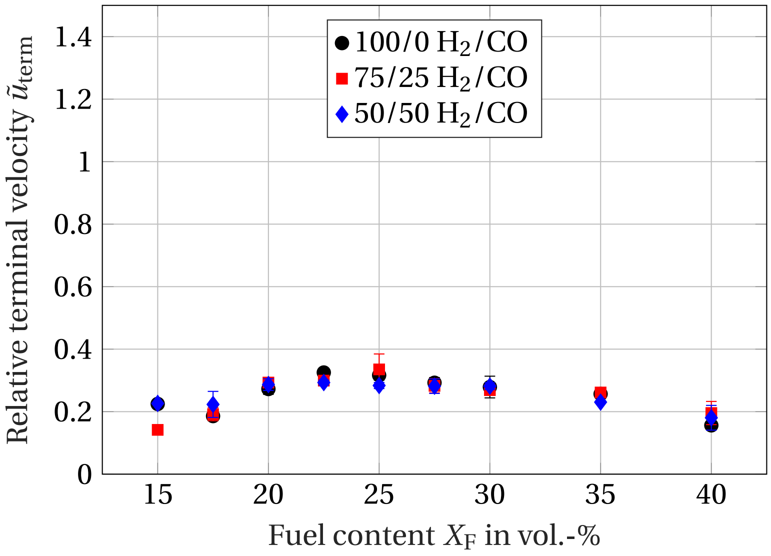

Figure 4.13: Relative terminal velocity $\tilde{u}_{\text{term}}$ over fuel content X_F at BR60S100.

A comparison of the flame speeds for BR60S100 and BR60S300 in Fig. 4.14 reveals the qualitatively different behavior. In the case of BR60S300, exceeding $0.95a_{\text{pr}}$ is followed by strong velocity fluctuations. The velocity fluctuates between D_{CJ} and a_{pr}. Between first exceeding $0.95a_{\text{pr}}$ and the end of the obstructed section, the mean velocity is found at $\bar{u} = 1207\,\text{m}\,\text{s}^{-1}$, corresponding to a velocity deficit of 29 % with respect to D_{CJ}. In the literature, this is referred to as a quasi-detonation [131]. In contrast, for BR60S100, the flame velocity does exceed $1000\,\mathrm{m\,s^{-1}}$ only once. The fluctuations are found mainly around a_{pr}. The mean velocity in this part of the channel is $\bar{u} = 746\,\mathrm{m\,s^{-1}}$, corresponding to a velocity deficit of 55 % with respect to D_{CJ}. According to [131], the velocity in the quasi-detonation regime ranges from $0.5D_{\mathrm{CJ}}$ to D_{CJ}. The velocity deficit depends on the obstacle configuration. The propagation of the flame in the quasi-detonation regime is governed by decoupling and re-initiation of the detonation due to the interaction with the obstacles.

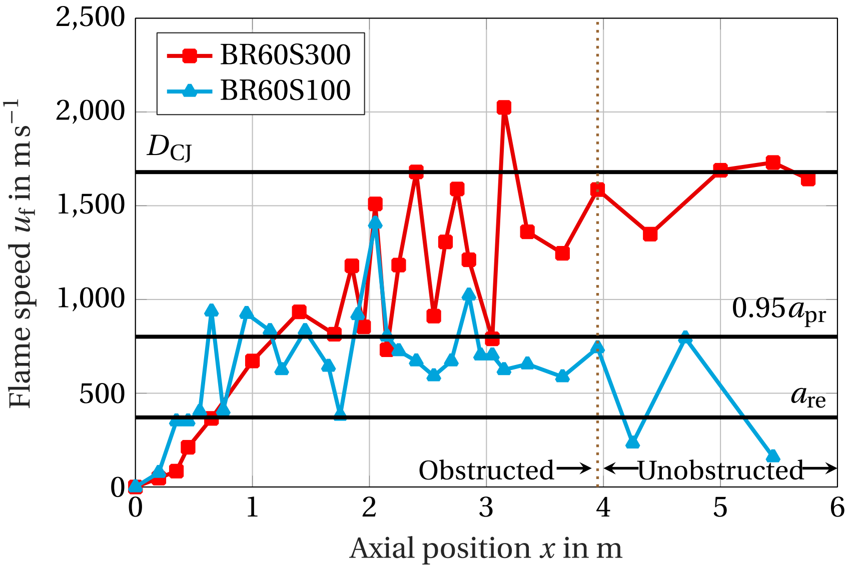

Figure 4.14: Flame speed u_{f} over axial position x at BR60S300 and BR60S100 for 75/25 H_2/CO at $X_{\mathrm{F}} = 20$ vol.-%.

The main difference in the flame propagation behavior is observed at the rear part of the obstructed section. At $x = 3.1$ m, the flame speeds are similar and close to $0.95a_{\mathrm{pr}}$. For BR60S300, an acceleration is found downstream of this position. A jump in the flame speed results in a velocity above D_{CJ}. When leaving the obstructed section, the flame accelerates to $\tilde{u}_{\mathrm{term}} = 0.95$. For BR60S100, the flame speed remains below a_{pr} in the rear part of the obstructed section. In the unobstructed section, the flame is decelerated, leading to the low terminal velocities as plotted in Fig. 4.13. Beauvais et al. have shown in [128], that high BR combined with short spacing can suppress flame speeds beyond a_{pr}. Obstacles with BR$\geq$ 30 lead to the formation of a jet due to the flow passing through the obstacle opening. Strong FA is thus possible within very short distances. However, if the obstacle distance is too small, the shear layers formed when the flow passes through the orifice can no longer attach to the channel wall. The reinforced FA is no longer fully effective, and the maximum flame velocities do not exceed a_{pr}.

For all obstructed configurations investigated, the flame speed at the end of the obstructed section determines the final combustion regime. Detonations are observed in the rear part of the channel only if quasi-detonations propagate through the obstructed part of the channel. The velocity at the end of the obstructed section at $x = 3.95\,\mathrm{m}$ is plotted over the fuel content for both BR60 configurations in Fig. 4.15. The flame speed for BR60S100L is considerably lower than for BR60S300L. The rear part of the channel is too short for the onset of detonation in the vicinity of the turbulent flame brush, as often found in unobstructed channels [15]. Even for higher flame speeds, as found at 15-17.5 vol.-%, no onset of detonation is observed. Hence, the onset of detonation is accomplished in the obstructed section by the reflection of shocks from obstacles, as already shown by Boeck in [16] using optical measurement techniques. Comparing Fig. 4.12 and Fig. 4.15 reveals that detonations formed in the obstructed part also propagate in the unobstructed section. Failures of detonations in the unobstructed section are not observed.

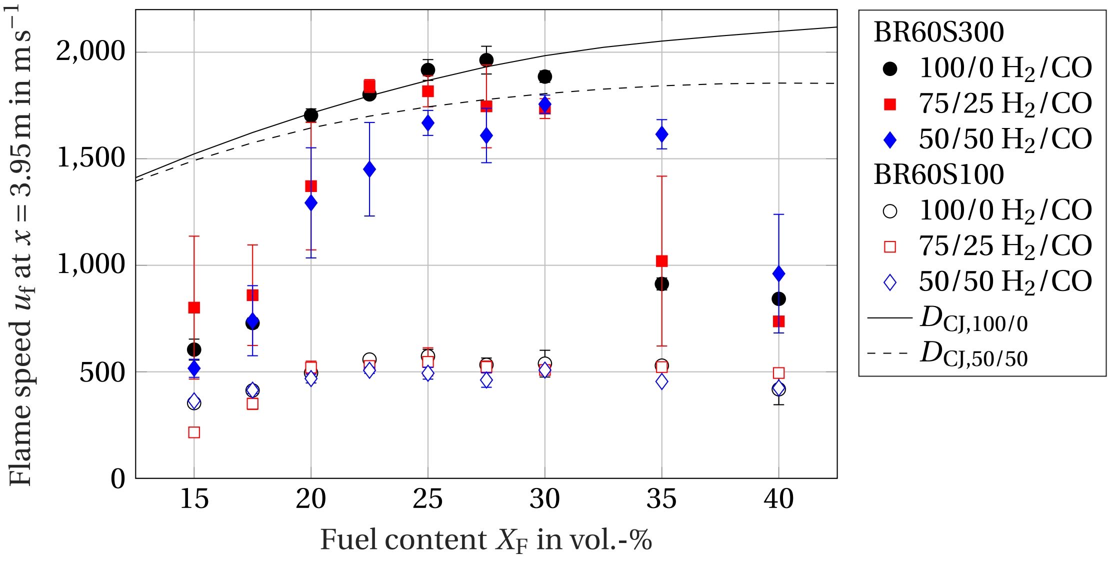

Figure 4.15: Flame speed u_f at the end of the obstructed section at axial position $x = 3.95\,\mathrm{m}$ over fuel content X_F at BR60S300 and BR60S100.

Table 4.1: Detonation limits for homogeneous mixtures of H_2-CO-air in the partially obstructed channel, characteristic length of the obstructed section, and maximum cell size λ for the detonable fuel-air mixtures.

Fuel	BR30S100L	BR30S300L	BR60S100L	BR60S300L
100/0 H_2/CO	20-30	17.5-35	-	20-30 vol.-%
75/25 H_2/CO	20-35	17.5-35	-	20-30 vol.-%
50/50 H_2/CO	20-40	17.5-40	-	20-35 vol.-%
Char. length L	646 mm	980 mm	323 mm	490 mm
Max. cell size λ	33 mm	70 mm	-	33 mm

The detonation limits for the partially obstructed channels with regard to the fuel are listed in Table 4.1. In order to compare the results, the characteristic length L of the obstacle configuration is added. L is calculated based on the definition given in [93]. For the unobstructed section in the rear part of the channel, the third root of the total volume (332 mm) is considered to be the characteristic length scale [132]. The maximum detonation cell size[‡] λ within the given detonation limit is listed in the last row. The largest cell size always corresponds to the lean limit of the detonation regime. The obstacle configuration determines the lean and fuel-rich limit of the detonation regime. The fuel content of the lean limit of detonations is the same for all fuel compositions investigated.

As shown in Sec. 2.7, the detonation cell size is very similar for all mixtures investigated. The characteristic length of the unobstructed channel does not change between the various obstacle configurations. Considering the unobstructed part of the channel solely, a self-sustained detonation should be able to propagate at the same fuel contents for all fuels in all configurations. However, this is observed only for the transition to the detonation regime of fuel-lean mixtures. As shown in Sec. 2.7, the detonation limit for fuel-lean mixtures is unaffected by CO. A similar behavior was observed by Kuznetsov et al.

[‡] Calculation based on the fit given by Eqn. 2.28.

in [37]. Only mixtures containing more than 50 vol.-% CO do not transition to the detonation regime. In addition, the presented results show that a variation of the obstacle geometry has a higher impact on the onset of detonation than the variation of the fuel up to a CO-content of 50 vol.-%. Furthermore, detonations in H_2-CO-air mixture have proven stable when leaving the obstructed section.

In contrast to fuel-lean mixtures, the detonation limit for fuel-rich mixtures depends on the fuel and the obstacle configuration. Higher CO-contents lead to fuel-richer detonation limits. However, the reason for this trend is not apparent. As shown for the flame speed at the end of the obstructed section, the 50/50 H_2/CO flame already propagates in the quasi-detonation regime. Hence, the onset of detonation must take place in the obstructed section. In contrast, for 100/0 H_2/CO, strong FA leads to flame velocities up to a_{pr} but no onset of detonation.

Calculations of the ZND structure revealed that the relative consumption of H_2 is higher than the relative CO-consumption in fuel-rich flames. The thermicity of the flame front becomes wider for fuel-rich H_2-air mixtures when compared to H_2-CO-air mixtures. This would decrease detonation stability, leading to an increased tendency for decoupling of shock and flame front [42]. It should be expected that the influence of the chemistry is similar for all investigated obstacle configurations. However, the obstacle configuration also influences the fuel-rich detonation limit. Therefore, this cannot be related to altered combustion chemistry only.

In terms of practical applications, the following can be summarized:

- The influence of CO is similar for all obstacle configurations investigated. The obstacle configuration governs the lean detonation limit. Within the investigated range, the CO-content of the fuel does not influence the lean detonation limit. If the obstacle configuration allows for the formation of a quasi-detonation within the obstructed section, the detonation will also propagate in the unobstructed part. The CO-content does not decrease the stability of detonations.

- Based on the data for H_2-air mixtures and calculations using the theory by Gavrikov [104], Kuznetsov et al. showed [37] that the detonation cell size for H_2-CO-air mixtures is similar to that of H_2-air mixtures. Hence the lean detonation limit obtained by the 7λ-criterion is also valid for the investigated H_2-CO-air mixtures. For the GraVent test rig, the limit is very conservative, which can be related to the small scale of the test rig.

- The higher the CO-content of the fuel, the higher the fuel-rich limit of the detonation. The obstacle configuration also influences the fuel-rich detonation limit. Hence the extension of the fuel-rich detonation limit for increasing CO-content is not only related to the changed combustion chemistry.

- For highly obstructed configurations, no detonations are observed. Quasi-detonations are not formed within the obstructed section, although strong FA is found and the 7λ-criterion is fulfilled.

4.2.3 Detonations in the unobstructed configuration

The relative terminal velocity $\tilde{u}_{\text{term}}$ for the unobstructed configuration BR00 is plotted over the fuel content X_{F} in Fig. 4.16. Besides the run-up distance, the lack of turbulence-promoting obstacles influences the terminal velocity, as the onset of detonation due to shock reflection from obstacles is not possible.

At 17.5 vol.-% the terminal velocity is found between 0.03 to 0.07. All flames propagate in the slow flame regime at velocities below the speed of sound of the reactants. If the fuel content is increased to 20 vol.-%, major differences in $\tilde{u}_{\text{term}}$ occur. 100/0 H_2/CO is found in the fast flame regime at $\tilde{u}_{\text{term}} = 0.65$. As this regime is not stable in unobstructed channels, an onset of detonation might occur if the channel length is sufficiently long. In contrast, 75/25 and 50/50 H_2/CO show terminal velocities below a_{re}. A second jump in $\tilde{u}_{\text{term}}$ is observed at 22.5 vol.-%. While the transition to the detonation regime is obvious for 100/0 H_2/CO, an increase to $\tilde{u}_{\text{term}} = 0.75$ appears for 75/25 H_2/CO. An analysis of the u-x diagrams for fuel contents of 22.5-30 vol.-% reveals that

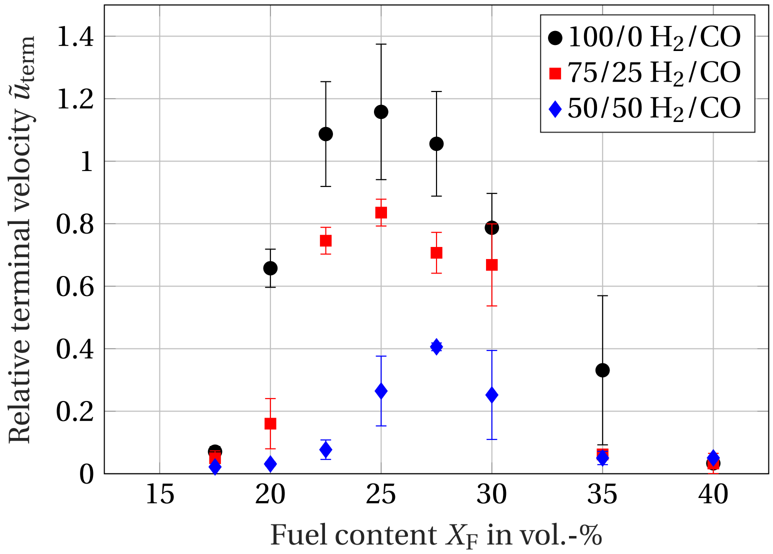

Figure 4.16: Relative terminal velocity $\tilde{u}_{\mathrm{term}}$ over fuel content X_{F} at BR00.

the flame speed exceeds D_{CJ} in most cases. A deceleration at the end of the channel leads to terminal velocities below unity.

While $\tilde{u}_{\mathrm{term}}$ for 100/0 and 75/25 H_2/CO remain in the regime between 22.5 and 27.5 vol.-%, an increase with increasing fuel content is observed for 50/50 H_2/CO. At 25 vol.-%, $\tilde{u}_{\mathrm{term}}$ is close to the speed of sound of the reactants but does not exceed a_{re}. The peak velocity is reached at a fuel content of 27.5 vol.-% at $\tilde{u}_{\mathrm{term}} = 0.4$, marking the transition from a slow to a fast flame. A decline in $\tilde{u}_{\mathrm{term}}$ is found for all fuels at 30 vol.-%. While it can be assumed that 100/0 and 75/25 H_2/CO remain in the detonation regime, a transition from the fast to the slow flame regime is found for 50/50 H_2/CO. If the fuel content is further increased, $\tilde{u}_{\mathrm{term}}$ for 75/25 and 50/50 H_2/CO are found in the slow flame regime. For 100/0 H_2/CO $\tilde{u}_{\mathrm{term}}$ is found above a_{re} at 35 vol.-%. At 40 vol.-%, $\tilde{u}_{\mathrm{term}}$ is similar to the values obtained at 17.5 vol.-% for all fuels.

Compared to former studies with unobstructed configurations at the GraVent test rig [16], peak flame velocities and pressures are higher in the present study. This might be related to the optional venting volume beneath the explosion channel. While the venting volume was filled with wax for this work, it was empty during former studies. An influence of the additional volume was neglected due to sealed joints between the floor plates of the segments. The presented results suggest that the venting volume had a decelerating effect on the flame propagation. A larger leakage might result from an unsealed connection between the explosion channel and the venting volume in the optical section, leading to an undesired venting effect. This is most evident in the unobstructed channel, as the additional acceleration by obstacle-induced turbulence production is missing.

A closer interpretation of the flame propagation for 75/25 H_2/CO can be obtained if the pressure signals are included. An analysis is presented at a fuel content of 22.5 vol.-%. The maximum peak pressure is always found at the pressure sensor closest to the end plate. The peak dynamic pressure at the end plate sensor is similar for 75/25 and 100/0 H_2/CO and exceeds $p_{\mathrm{dyn,max}}$ by a factor of 10, as shown in Fig. 4.17. The pressure signal at $x = 5.6\,\mathrm{m}$ is still typical for a fast flame. However, the steep pressure rise at $x = 6\,\mathrm{m}$ suggests a localized explosion occurred in the preconditioned gas, trapped between the propagating flame and the end plate. The leading shock wave created by FA enters this region and is reflected at the end plate.

In contrast to the pressure profile of a detonation in the partially obstructed channel, as shown in Fig. 4.2, the pressure profile does not show a single pressure spike like in Fig. 4.2. The second pressure spike indicates a local explosion in the mixture, leading to a higher pressure peak than the interaction of the leading shock with the end plate. The delay between the pressure peak caused by the reflection of the leading shock and the localized explosion is $\Delta t = 0.03\,\mathrm{ms}$. This behavior is observed at 75/25 H_2/CO in the unblocked channel between 22.5 to 27.5 vol.-%. At 100/0 H_2/CO, similar cases are observed at $X_{\mathrm{F}} = 20$ vol.-% for 100/0 H_2/CO. Eder reported a similar behavior in H_2-air mixtures in [39]. Detonations were initiated at the end of a tube for mixtures between 16.5-19.5 vol.-%. In all cases, fast deflagrations with flame speeds between a_{pr} and D_{CJ} were measured before the onset of detonation at the end plate.

In experiments with 50/50 H_2/CO, the leading shock cannot sufficiently precondition the mixture close to the end plate. A local explosion cannot occur, and the peak pressure at the end plate is given by shock reflection. For 100/0 H_2/CO, the pressure data at the endplate shows pressure peaks like those ob-

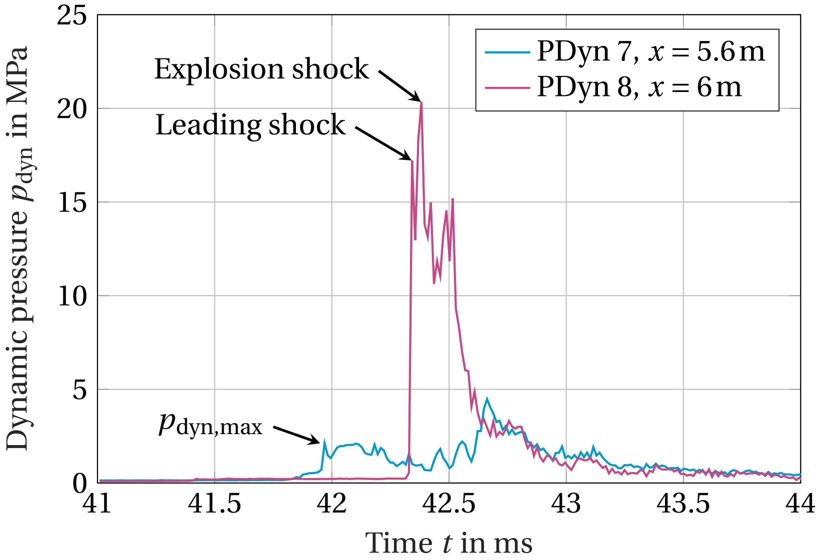

Figure 4.17: Dynamic pressure p_{dyn} at axial positions $x = 5.6$ m and $x = 6$ m over time t for 75/25 H_2/CO and $X_F = 22.2$ vol.-% at BR00.

tained at partially blocked configurations. Therefore, the onset of detonation occurs upstream of the end plate.

The behavior of the flame at 75/25 H_2/CO allows for further insight into the onset of detonation by shock reflection. Conclusions can also be used for the onset of detonation in the unobstructed channel, as the reflection of the leading shock is the primary cause of the onset of detonation. Therefore, the Mach number M_S of the leading shock is calculated. The Mach number can be obtained by the time difference between of arrival of the shock at the pressure sensor closest to the endplate (at $x = 5.4$ m) and the endplate at $x = 6$ m. The shock is assumed to travel through an undisturbed fuel-air mixture at ambient conditions. No Mach number was obtained at the lean and fuel-rich limit of the test matrix. In these cases, no pressure peaks were measured but a continuous pressure rise. As shown in Fig. 4.18, the Mach number M_S is influenced by the fuel and the fuel content. Note that in Fig. 4.18, each data point marks the results of a single experiment in contrast to the plots shown before.

For 100/0 H_2/CO fast flames are observed for $X_F = 20$ vol.-%. This results in shock a of $2 < M_S < 3$ as shown in Fig. 4.18. Detonations are observed for 100/0 H_2/CO based on $\tilde{u}_{term}$ in the fuel range of 22.5-27.5 vol.-%. The corresponding Mach number is found between 5-6. The variation of M_S in this range of fuel contents is small. This can be expected as the Mach-number of CJ-detonations in this range only change slightly. However, it should be mentioned that calculated Mach-numbers of CJ-detonations in the fuel range of 22.5-27.5 vol.-% are range from 4.6 to 4.85. The difference in the measured shock velocities might arise from an overdriven detonation or preconditioning of the fuel-air mixture. At the rich limit of the detonation regime of 100/0 H_2/CO at 30 vol.-%, some flames propagate in the detonation regime while others propagate in the fast flame regime as well as in between. This behavior is also indicated in Fig. 4.18, as the M_S varies between 2.7 and 5.5. For 35 vol.-%, M_S is below 2. For 75/25 H_2/CO the field of interest is found between 22.5-30 vol.-%. In this range, M_S is between 2-3. For a fuel content of $X_F = 22.2$ vol.-% as shown in Fig. 4.17, the Mach number of the leading shock is 2.81. For 50/50 H_2/CO, an increasing flame velocity and the establishment of shock fronts are observed for 25-30 vol.-%. Still, the shock Mach-number is below 2.

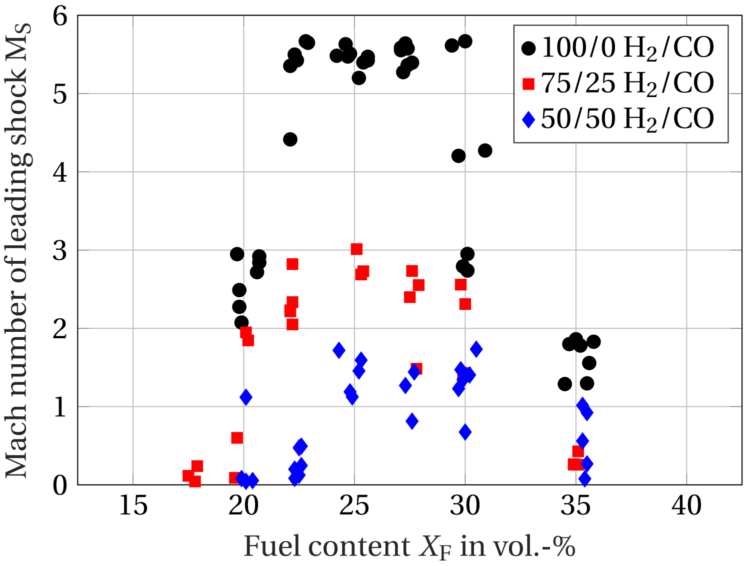

Figure 4.18: Mach number of the leading shock M_S over fuel content X_F at BR00.

In order to distinguish experiments in which the onset of detonation is due to a reflection of the leading shock at the back plate from the onset of detonation further upstream, the peak pressure at the back plate is plotted over the

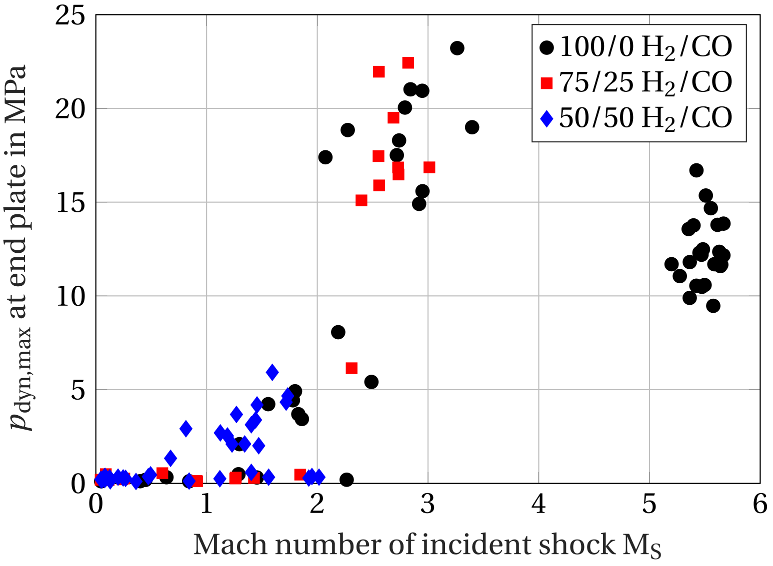

Figure 4.19: Maximum dynamic pressure $p_{\mathrm{dyn\,max,\,8}}$ at $x = 6\,\mathrm{m}$ over Mach number of the leading shock $\mathrm{M_S}$ at BR00.

Mach number of the incident shock in Fig. 4.19. The reflection of detonations formed further upstream in the channel, such as in 100/0 H_2/CO for fuel contents of 22.5-30 vol.-% leads to lower peak pressures at the end plate as shown on the right of Fig. 4.19. The Mach number of the leading shock is higher than for 75/25 H_2/CO. According to Fig. 4.19, the lower limit for the Mach number of the incident shock is found in the fast flame regime for 75/25 H_2/CO.

As outlined in Sec. 2.3, the ignition delay time of H_2-CO-air mixtures is significantly altered from those for H_2-air mixtures only if the CO-content surpasses 50 vol.-% in the fuel. The Mach number of the shock for the investigated mixtures determines the temperature and pressure of the fuel-air mixture downstream of a shock. Therefore, establishing a shock of similar strength will lead to similar ignition delay times in all fuels. This can be observed in Fig. 4.19. When interpreting pressures above the pressure of a reflected CJ-detonation, as shown in the center of the plot, the lower limit for a shock to cause an onset of detonation is $M_s = 2.5$.

This value is close to the critical Mach number for the onset of detonation reported by Boeck in [16] for H_2-air mixtures. He concluded that the thermodynamic state related to a shock reflection of a leading shock at $M_S = 2.5$

is needed to create a strong ignition. The second explosion limit, as defined in Sec. 2.3, is crossed, and the onset of detonation can take place. Since the chemistry of H_2-CO-air mixtures is governed by the H_2-O_2-system, it seems reasonable to assume similar thermodynamic states for the onset of detonation.

Hence, all fuels investigated need to generate shocks of similar strength for the onset of detonation. This hypothesis is further supported by the fact that a shock in 100/0 H_2/CO traveling at the same shock Mach number leads to similar peak pressures at the end plate as for 75/25 H_2/CO. An onset of detonation is triggered in 100/0 H_2/CO, too. The weaker FA caused by a reduction of σs_L for an increasing CO-content in the fuel leads to lower shock velocities. Hence, sufficient preconditioning of the fresh mixture between the flame and the endplate is not achieved. The onset of detonation cannot be observed at 50/50 H_2/CO. It can be assumed that the onset of detonation is possible in longer channels. Regarding the obstructed configuration, the FA-enhancing effect by obstacles promotes the required shock formation.

In summary, the following can be concluded:

- The onset of detonation without interaction of the leading shock with the end plate is observed at 100/0 H_2/CO only. The detonation range is shifted to lower fuel contents with respect to former investigations at the GraVent test rig.
- For 75/25 H_2/CO, the onset of detonation can occur at the rear end of the channel. Terminal velocities are lower than D_CJ. Examining the peak pressure and the shock Mach number at the end of the channel revealed high-pressure peaks at the end plate, which can only be explained by the onset of detonation due to shock reflection.
- The critical Mach number for the onset of detonation for 75/25 H_2/CO can be estimated by tracking the onset of detonation in the rear part of the channel. The Mach number of the required shock is similar to H_2-air mixtures. This might be due to the importance of the H_2-O_2-system for the combustion of H_2-CO-mixtures.

- The weaker FA in the case of 50/50 H_2/CO does not lead to shocks strong enough to cause the onset of detonation. For unobstructed configurations, longer channels might be needed to generate stronger shocks.

4.2.4 Peak pressure evolution

The pressure levels associated with flame propagation pose a significant threat to the surrounding structure. Therefore, the following section compares the peak pressures obtained for the investigated obstacle configurations. Various phenomena influence the pressure peaks. In the following section, the peak pressure of stable detonations propagating in the unobstructed part of the channel is reviewed first. Afterward, the reflection on the end plate is discussed. Finally, the pressure peaks due to the onset of detonation are described.

Stable detonation propagation in the channel's unobstructed section leads to higher dynamic pressures than fast flame propagation. Within the same flame propagation regime, the pressure obtained in the rear part of the channel is a function of the fuel composition and content. As shown in Fig. 4.20 for BR30S300, the impact of the fuel in the detonation regime can be seen. As discussed above, the detonation regime is found for $17.5 \leq X_{\mathrm{F}} \leq 35$ vol.-% for 100/0 and 75/25 and for $17.5 \leq X_{\mathrm{F}} \leq 40$ vol.-% for 50/50 H_2/CO at BR30S300. The detonation limits are also evident from the peak pressure at $x = 5.4\,\mathrm{m}$ at 15 and particularly 40 vol.-%. Although $\tilde{u}_{\mathrm{term}}$ is higher for 100/0 and 75/25 within the detonation regime than for 50/50, the peak pressures are the highest for 50/50 H_2/CO. In the detonation regime, the peak pressure increases with the CO content in the fuel. The average peak pressure is 13 % higher for 50/50 H_2/CO than for 100/0 H_2/CO. This observation is in accordance with the predictions made by the ZND model. A similar observation is made for BR30S100 and BR60S300.

Similar to the pressure in the unobstructed section, the flame propagation regime impacts the peak pressure at the end plate sensor. Fig. 4.21 shows the pressure $p_{\mathrm{dyn,max}}$ at the end plate sensor PDyn 8 over the fuel content X_{F} for BR30S300. The peak pressures are generally higher compared to other

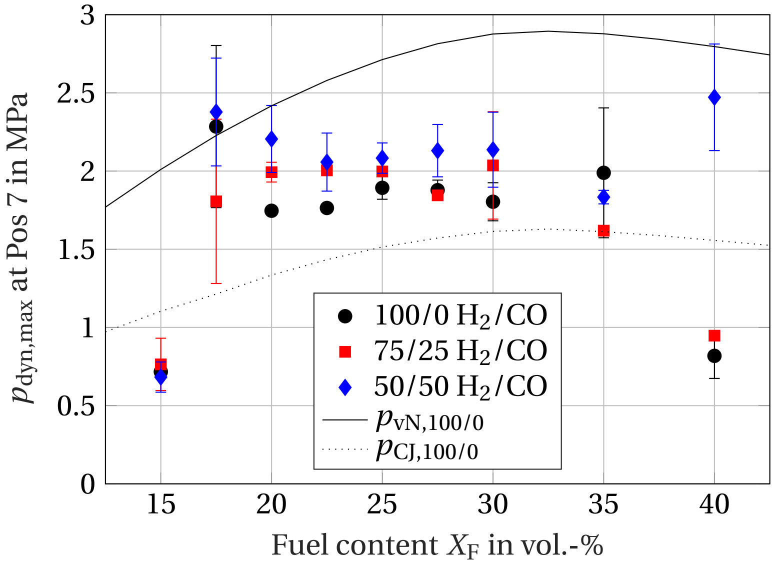

Figure 4.20: Maximum dynamic pressure $p_{\mathrm{dyn\,max},\,7}$ at $x = 5.4\,\mathrm{m}$ over fuel content X_{F} at BR30S300.

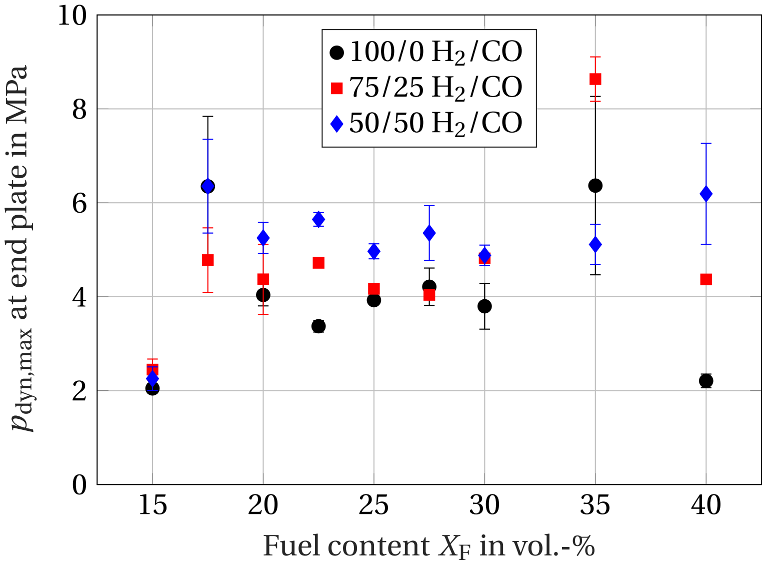

Figure 4.21: Maximum dynamic pressure $p_{\mathrm{dyn\,max},\,8}$ at $x = 6\,\mathrm{m}$ over fuel content X_{F} at BR30S300.

sensors due to the orientation of the pressure sensor. Compared to Fig. 4.20 $p_{\mathrm{dyn,max}}$ is higher at each respective fuel content. An increase in the peak pressure at the detonation limits is still shown. Within the range of 20-35 vol.-%, the peak pressure oscillates closely to its average for all fuel investigated. For

20 vol.-% $X_F \leq$ 30 vol.-% the average peak pressure is given by 3.87 MPa for 100/0, 4.42 MPa for 75/25 and 5.52 MPa for 50/50 H_2/CO. The peak pressure increases with increasing CO content in the fuel. This effect can be attributed to the increase in the detonation pressure and in the specific impulse due to the higher density of the reactants and products. Although D_{CJ} is decreasing with increasing CO content in the fuel, the effect is outweighed by the increase in pressure and density. The increased peak pressure at the detonation limits might be related to localized explosions when the flame leaves the obstructed section at the onset of detonation.

The maximum dynamic pressures $p_{dyn,max}$ for partially obstructed configurations are plotted over the fuel content X_F in Fig. 4.22 to 4.24. The von Neumann pressure p_{vN} and the Chapman-Jouguet pressure p_{CJ} for 100/0 H_2/CO are added for comparison[‡]. It should be noted that the maximum dynamic pressure is often connected to pressure waves associated with FA or the onset of detonation and not the propagation of a stable detonation. It is observed that $p_{dyn,max}$ changes with the fuel content, the fuel, and the obstacle configuration. The mean peak dynamic pressure is calculated to 2.39 MPa for 100/0, 2.56 MPa for 75/25 and 2.84 MPa for 50/50 H_2/CO. Independent of the fuel and the fuel content, $p_{dyn,max}$ for 15 vol.-% is close to p_{CJ}, as all mixtures remain in the fast flame regime. For BR30S100, the flame propagation regime for all fuels changes at X_F = 20 vol.-% from fast flames to detonations. For 100/0 H_2/CO this change is accompanied by a doubling in $p_{dyn,max}$ between 17.5 and 20 vol.-%. While at the former, $p_{dyn,max}$ is close to p_{CJ}, the latter exceeds p_{vN}. For 75/25 H_2/CO $p_{dyn,max}$ is similar to X_F = 15 vol.-%. As shown in Fig. 4.12, $\tilde{u}_{term}$ is found in the fast flame as well as the detonation regime at X_F = 17.5 vol.-%. The mean peak pressure, as well as the standard variation, is influenced by an onset of detonation. Therefore the completed transition to the detonation regime at 20 vol.-% results in a smaller increase in $p_{dyn,max}$ compared to 100/0 H_2/CO. For 50/50 H_2/CO a jump in $p_{dyn,max}$ is observed at 17.5 vol.-%. As $\tilde{u}_{term}$ is not found within the detonation regime for X_F = 17.5 vol.-%, localized explosions could cause this peak. However, no self-sustained, stable detonation is formed. The peak pressure also supports this

---

[‡] The v. N. pressure and the C.-J. pressure change with the CO content in the fuel. However, changes are minor compared to the influence of the fuel content. For the v. N. and C.-J. pressure data, see Appendix C.

interpretation in the unobstructed section, similar to the one obtained for X_F = 15 vol.-%. The relative terminal velocity remains below unity.

Within the detonation regime for 20-30 vol.-%, $p_{dyn,max}$ follows p_{CJ} and increases slightly with the fuel content. The maximum $p_{dyn,max}$ is observed at 27.5 vol.-% for all fuels. The maximum in $p_{dyn,max}$ does not coincide with the maximum p_{CJ} and p_{vN}, which are reached at 32.5 vol.-% for each fuel. Large differences with respect to the fuels are not observed, while pressure fluctuations are generally low. As the mixtures become fuel rich at 30 vol.-%, fluctuations in $p_{dyn,max}$ increase, while $p_{dyn,max}$ remains close to p_{vN}. At 35 vol.-%, the change in the flame propagation regime for 100/0 H_2/CO is reflected in $p_{dyn,max}$, too. As indicated in Fig. 4.10, major fluctuations at $\tilde{u}_{term}$ at 35 vol.-% for 100/0 H_2/CO indicate that detonations are still found in some experiments. This can also be seen in $p_{dyn,max}$. For 75/25 and 50/50 H_2/CO, stable detonations are observed at 35 vol.-%. The peak pressure remains above p_{vN}, while the fluctuations are low. At 40 vol.-% the peak pressure for 100/0 as well as for 75/25 H_2/CO decreases below p_{CJ}, reaching a similar level as shown at 17.5 vol.-%. For 50/50 H_2/CO, $p_{dyn,max}$ is close to p_{vN}.

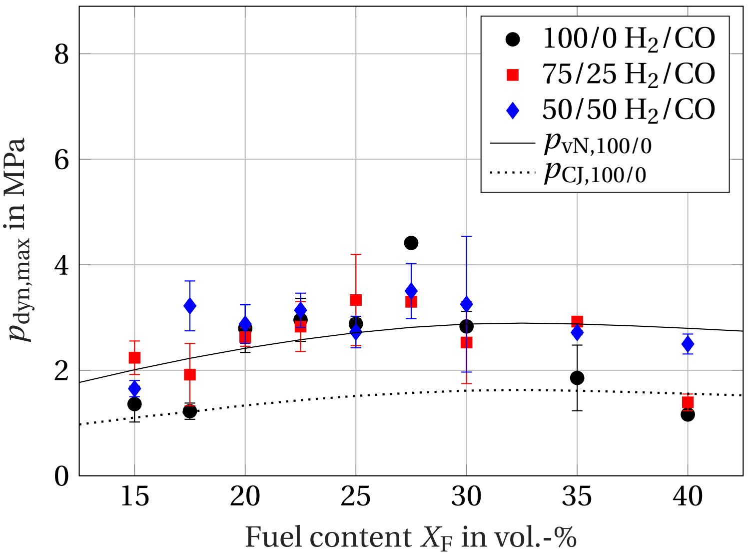

Figure 4.22: Maximum dynamic pressure $p_{dyn,max}$ over fuel content X_F at BR30S100.

For BR30S300, the maximum dynamic pressure $p_{dyn,max}$ is plotted over the fuel content X_F in Fig. 4.23. The mean dynamic peak pressure for the configuration is 2.39 for 100/0, 2.21 for 75/25 and 2.75 MPa for 50/50 H_2/CO. The change in the flame propagation regime at 17.5 vol.-% leads to a jump in $p_{\mathrm{dyn,max}}$. Within the detonation regime, large pressure variations are observed at 20 vol.-% for 50/50 and at 27.5 vol.-% for 100/0 and 75/25 H_2/CO. Compared to BR30S100, $p_{\mathrm{dyn,max}}$ is lower. However, a clear dependence on fuel is not evident. In most cases, $p_{\mathrm{dyn,max}}$ shows the highest values for 50/50 H_2/CO. High fluctuations at 35 vol.-% coincide with a decrease in $\tilde{u}_{\mathrm{term}}$ at 100/0 and 75/25 H_2/CO. At 40 vol.-%, the peak pressures of all fuels but 50/50 H_2/CO are found below p_{CJ}. As $\tilde{u}_{\mathrm{term}}$ is found in the detonation regime at 50/50 H_2/CO for 40 vol.-%, the peak pressure is above p_{vN}.

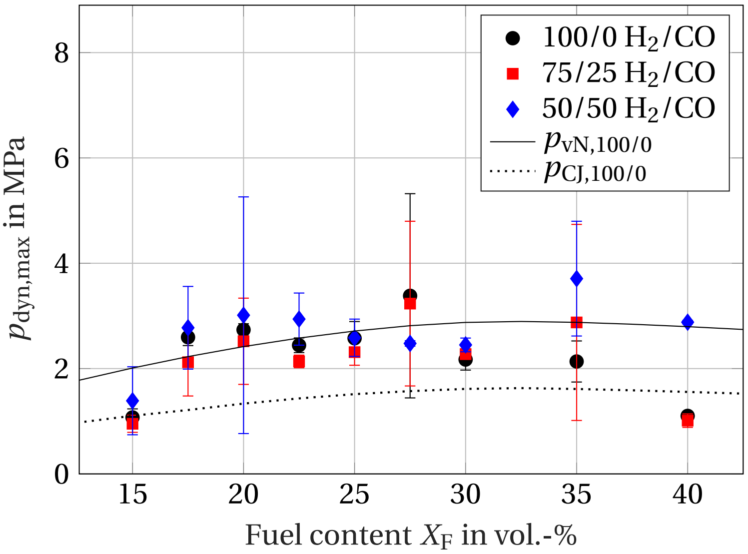

Figure 4.23: Maximum dynamic pressure $p_{\mathrm{dyn,max}}$ over fuel content X_F at BR30S300.

The peak pressure for BR60S300 is plotted in Fig. 4.24. The average peak pressure is 2.49 MPa for 100/0, 2.41 MPa for 75/25 and 2.61 MPa for 50/50 H_2/CO. In contrast to BR30S100 and BR30S300, the peak pressure increases in the fast flame region between 15 and 17.5 vol.-%. Only 50/50 H_2/CO $p_{\mathrm{dyn,max}}$ remains close to p_{CJ}. Higher pressures and higher pressure fluctuations are indicated within the detonation regime compared to the other obstacle configurations. The peak pressures are higher than p_{vN} in most cases. The highest pressures are found at a fuel content of 27.5 vol.-% for all fuels. In fuel-rich mixtures with 30 vol.-%, $p_{\mathrm{dyn,max}}$ decreases at 100/0 and 75/25 H_2/CO, while the pressure drop is small at 27.5 vol.-% for 50/50 H_2/CO. At 35 vol.-%, the peak dynamic pressures for 100/0 and 75/25 are below p_{CJ}. At 50/50 H_2/CO, detonation is accompanied by peak pressures between p_{vN} and p_{CJ}. The transition from detonations to fast flames for 50/50 H_2/CO between 35 and 40 vol.-% leads to a drop in peak pressure to a level of p_{CJ}.

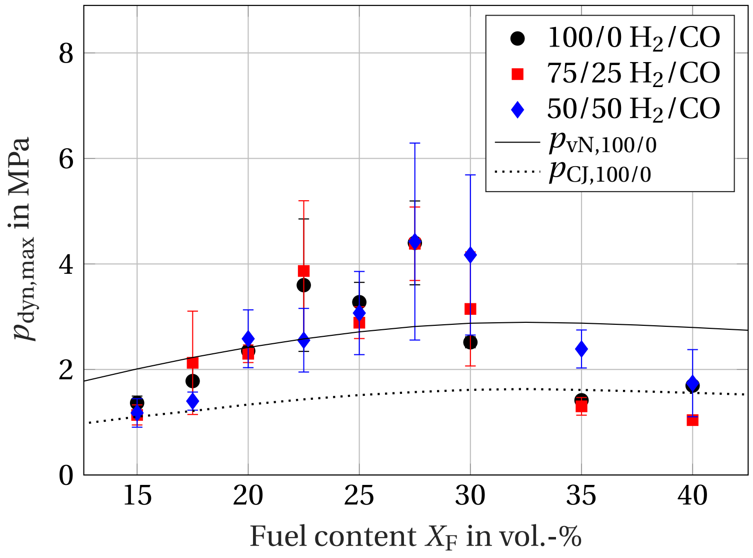

Figure 4.24: Maximum dynamic pressure $p_{dyn,max}$ over fuel content X_F at BR60S300.

The unchanged flame propagation characteristics over the entire fuel range for BR60S100 are also reflected in the measured dynamic peak pressures as shown in Fig. 4.25. The mean peak pressures are 1.0 MPa for 100/0, 1.1 MPa for 75/25 and 1.0 MPa for 50/50 H_2/CO. While major jumps at the transition between the regimes are observed at BR30 and BR60S300, $p_{dyn,max}$ remains almost constant over all fuel contents investigated. Similar to the relative terminal velocity, a slight increase from 15 vol.-% to 25 vol.-% is observed. The maximum dynamic pressure follows the trend of p_{CJ}. However, the peak pressure, even in the most reactive mixtures of 100/0 H_2/CO, does not exceed p_{CJ}. The maximum dynamic pressure is 1.15 MPa.

The maximum dynamic pressure for BR00 is plotted in Fig. 4.26. The mean peak pressures at the unobstructed channel are 2.43 MPa for 100/0, 1.19 MPa for 75/25 and 0.58 MPa for 50/50 H_2/CO. Like in the partially obstructed configurations, the flame propagation regimes greatly impact the dynamic peak

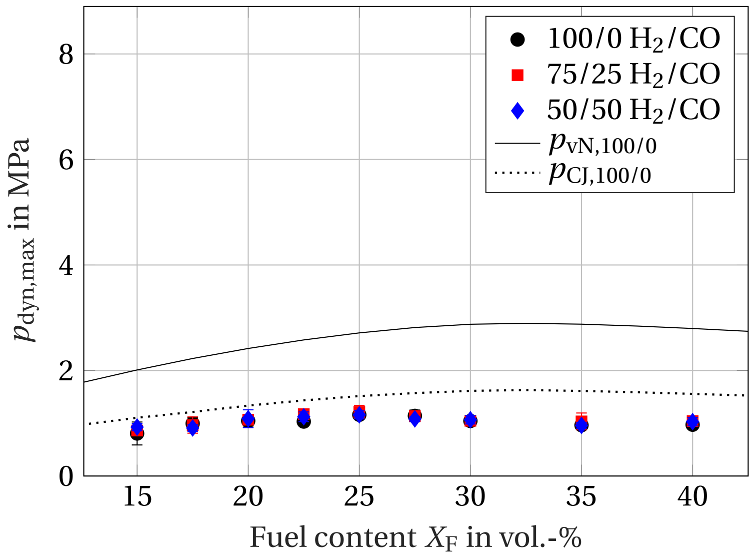

Figure 4.25: Maximum dynamic pressure $p_{\mathrm{dyn,max}}$ over fuel content X_{F} at BR60S100.

pressures. The slow flames at $X_{\mathrm{F}} = 15$ and 40 vol.-% lead to low overpressure of 0.1-0.3 MPa at low pressure fluctuations. Similar peak pressures are found at 75/25 and 50/50 H_2/CO at 20 and 35 vol.-%. The peak pressure rises as soon as the flame propagation regime changes from a slow to a fast flame. This can be observed at 20 vol.-% for 100/0, at 22.5 vol.-% for 75/25 and at 25 vol.-% for 50/50 H_2/CO. As shown in Fig. 4.16, the flame propagation regime is similar for 100/0 at 20 vol.-% and for 75/25 at 22.5-30 vol.-%. This trend is also visible in the peak pressures. The peak pressures obtained in this regime are similar to the fast flames found in the partially obstructed configurations[‡].

However, the onset of detonation in the unblocked channel at 100/0 H_2/CO leads to higher peak pressures compared to the obstructed configurations, as shown at 22.5-27.5 vol.-%. Peak pressures associated with the onset of detonation are commonly higher than the pressures at the corresponding von Neumann state for the given mixture. At partially obstructed configurations such as BR30 and BR60S300, the onset of detonation is mainly found within the obstructed section. Shock reflection and focusing on obstacles play an essential role. Shocks emitted by the onset of detonation diffract at obstacles. Hence, the pressure sensors might be subjected to direct impacts by shock waves

---

[‡] See BR60S300 at 17.5 vol.-%.

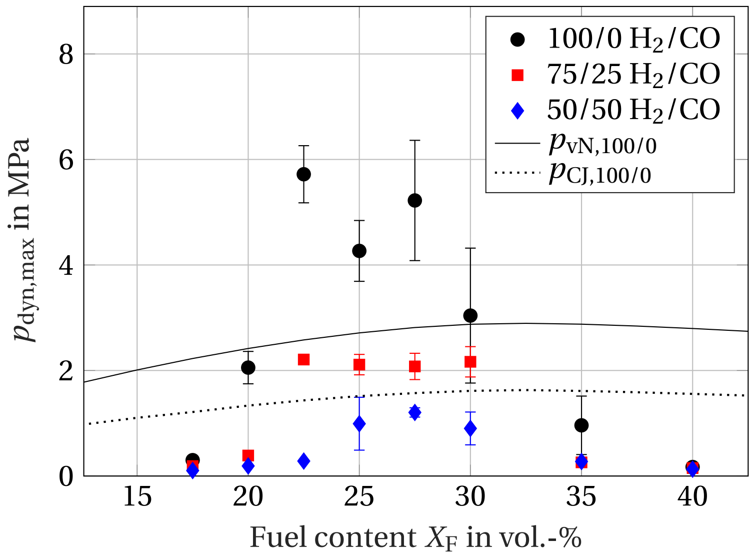

Figure 4.26: Maximum dynamic pressure $p_{dyn,max}$ over fuel content X_F at BR00.

and diffracted shock waves, leading to lower peak pressures. In comparison, shock waves emitted by the onset of detonation in the unblocked channel can propagate freely. No diffraction and thereby weakening of the shocks is possible [122]. Compared to the peak pressures at 75/25 at 22.5-27.5 vol.-%, the pressure at 100/0 H_2/CO fluctuates stronger, although the flame propagation regime remains the same for each fuel. This might be related to the location of the onset of detonation in the case of 100/0 H_2/CO. The closer the local explosion to the position of the pressure sensor occurs, the higher the measured peak pressure. For 100/0 H_2/CO, the onset of detonation is observed without shock reflection at the endplate.

For 75/25 H_2/CO, the peak pressure is around 2.1 MPa, for fuel content of 22.5-30 vol.-%. The peak pressure corresponds to the measurement at Pos 6 at $x = 5.4$ m. The peak pressures in this range are very similar. This further supports the assumption that the flames at 75/25 H_2/CO propagate in the same regime close to the onset of detonation. The reflection of the leading shock at the end plate leads to the onset of detonation. As the peak pressure corresponds to the first pressure spike of the signal, reflections of pressure waves are not considered in this evaluation. However, as shown in Fig. 4.17, the reflections can cause higher pressure peaks than the leading shock. For 50/50

H_2/CO $p_{\mathrm{dyn,max}}$ increases only for fuel contents of 25-30 vol.-%. Due to the lower flame speed, the peak pressure is around 1 MPa.

- The peak pressures are similar for the same combustion regime for all fuels. For obstructed configurations, the peak pressure is influenced by the obstacle configuration. A clear distinction with respect to the fuel is not possible, as the distance between localized explosions influences the pressure peaks.
- The dynamic pressures in case of a propagating detonation in the unobstructed part of the channel increase with increasing CO-content. The dynamic pressure exerted on surfaces adverse to the direction of flame propagation is also higher for CO containing mixtures. This behavior cannot be captured by replacing CO with H_2 due to the lower molecular weight of H_2 and the lower von Neumann pressure.
- In the unobstructed channel, large differences with respect to the combustion regime are obtained, as pressure waves can propagate without interaction with obstacles. In particular, for 100/0 H_2/CO, the peak pressures are higher than in the obstructed configurations due to the onset of detonation. As the onset of detonation is not accomplished at the turbulent flame brush for 75/25 and 50/50 H_2/CO, the corresponding peak pressures are lower. Due to lower terminal velocities and weaker FA, the peak pressure drops with higher CO contents in the fuel.

4.3 Inhomogeneous mixtures

After discussing the results in homogeneous fuel-air mixtures, this section is extended by discussing experimental findings in inhomogeneous fuel-air mixtures. Transverse concentration gradients were established by diffusion as described in Sec. 3.3. The results presented in the following section are compared with CFD-based fuel distributions. The distribution of H_2 and CO over time for the global fuel contents investigated can be found in Appendix D for 75/25 and in Appendix E for 50/50 H_2/CO. A precise measurement of the fuel content by the method of partial pressures is not possible for short diffusion times (see Sec. 3.3). It is assumed that the same injection settings (p_{inj}, t_{inj}) for short and long diffusion times ($t_{\mathrm{D}} \geq 30\,\mathrm{s}$) lead to similar fuel contents within the accepted range of the desired fuel content. The characteristic properties for evaluating the inhomogeneous experiments, such as a_{re}, a_{pr}, and D_{CJ}, are evaluated based on the desired fuel content.

The obstacle configurations investigated were limited to configurations that supported the onset of detonation in the homogeneous case. Furthermore, the investigated fuel content was limited to the lean transition limit of fast flames to detonations. For BR30S100, this included 15-25 vol.-%, for BR30S300 15-20 vol.-%, and for BR00 17.5-35 vol.-%. The results presented in the following section are structured analog to the homogeneous results. First, FA in inhomogeneous mixtures is discussed in Sec. 4.3.1. Sec. 4.3.2 presents the impact of concentration gradients on the onset of detonation in the obstructed configurations. The onset of detonation in the unobstructed channel in the case of concentration gradients is analyzed in Sec. 4.3.3. Finally, the peak pressures obtained are shown in Sec. 4.3.4. For ease of comparison, the results of the homogenous mixtures, indicated by a diffusion time of 60 s, are added to each plot presented.

4.3.1 Flame acceleration to fast flames

In Fig. 4.27, the run-up distance to the speed of sound of the products x_{apr} is plotted over the fuel content for 75/25 H_2/CO at BR30S100. The respective standard deviations are only plotted for homogeneous mixtures to maintain easier readability of the plots. In the case of a fuel content of 15 vol.-%, the run-up distances are shorter for steep concentration gradients. However, the variation of x_{apr} due to the standard deviation in the homogeneous mixture is similar to the effect of the concentration gradients. If the fuel content increases, the run-up distances of homogeneous and inhomogeneous mixtures become similar. For fuel contents of more than 17.5 vol.-%, homogeneous mixtures have shorter run-up distances than inhomogeneous mixtures. This applies to all fuel contents up to 25 vol.-%. For longer diffusion times of 10

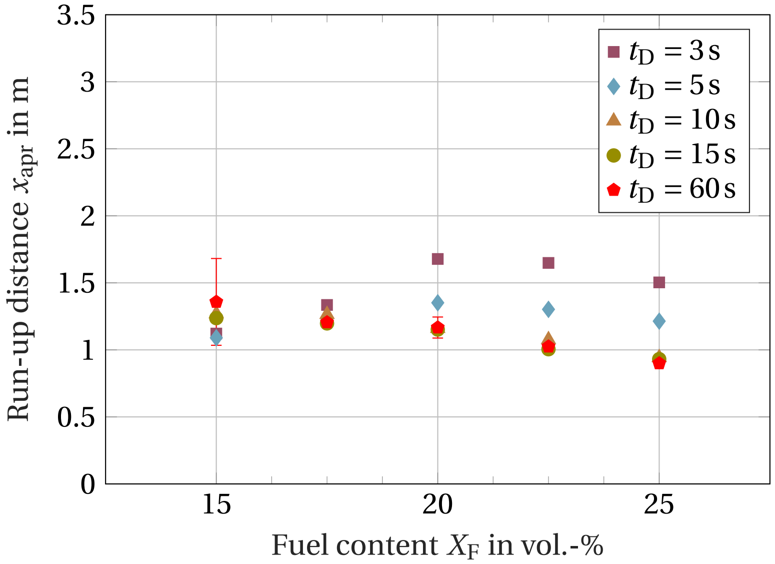

Figure 4.27: Run-up distance to the speed of sound of the isobaric products x_{apr} over fuel content X_F at BR30S100 for inhomogeneous mixtures of 75/25 H_2/CO.

and 15 s, no differences to the homogeneous case are observed. For diffusion times of 3 s and 5 s, the run-up distance becomes longer if the transverse concentration gradients become steeper. While at 5 s the run-up distance at 17.5 and 20 vol.-% are very similar, a retarding effect is observed for 3 s. This effect leads to an increase in x_{apr} between 17.5 and 20 vol.-%. While the difference in x_{apr} between 3 s and 5 s remains constant at ≈ 0.31 m, the difference between the homogeneous case and 5 s increases. The decrease in x_{apr} with increasing fuel content, as observed for homogeneous mixtures from 20 to 27.5 vol.-%, is weaker at inhomogeneous mixtures.

In Fig. 4.28 x_{apr} is plotted over the fuel content for 50/50 H_2/CO at BR30S100. Similar to 75/25 H_2/CO, an accelerating effect of concentration gradients is observed at a global fuel content of 15 vol.-%. With an exception at 10 s the run-distances become similar at 17.5 vol.-%. If the fuel content increases further, x_{apr} is shorter for homogeneous mixtures. In contrast to 75/25 H_2/CO, the run-up distance at very steep gradients of $t_D = 3$ s increases with increasing fuel content at $X_F \geq 20$ vol.-%. However, the increase is small and insignificant with respect to the standard deviation of x_{apr} at $t_D = 3$ s. A similar trend is observed at a waiting time of 5 s from 22.5 vol.-%. However, it should be mentioned that x_{apr} is very similar for fuel contents between 22.5-30 vol.-% for homogeneous mixtures. In contrast, a decrease in x_{apr} is observed in homogeneous mixtures at 75/25 H_2/CO in the same range of fuel content.

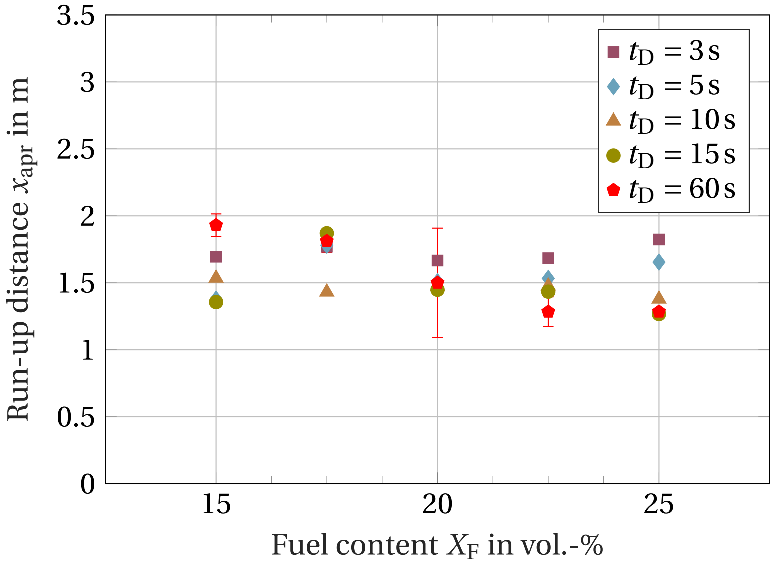

Figure 4.28: Run-up distance to the speed of sound of the isobaric products x_{apr} over fuel content X_F at BR30S100 for inhomogeneous mixtures of 50/50 H_2/CO.

The run-up distances for BR30S300 are plotted over the fuel content in Fig. 4.29. An accelerating effect of concentration gradients, as observed at BR30S100, is not visible at 15 vol.-%. For 75/25 H_2/CO, the run-up distances for inhomogeneous mixtures at 15 vol.-% match the homogeneous case. A similar behavior is observed at 17.5 vol.-%. For 20 vol.-% x_{apr} for the homogeneous case is shorter than for inhomogeneous cases. A distinct influence of diffusion time is not observed. For 50/50 H_2/CO, the scatter in x_{apr} is wider at 15 vol.-% than at 75/25 H_2/CO. Stronger concentration gradients lead to a longer run-up distance. All diffusion times except 3 s are found within the homogeneous case's standard deviation of x_{apr}. No effect of concentration gradients on the run-up distance is visible for higher fuel contents. For BR60S300, similar results are obtained. Therefore, the impact of concentration gradients on x_{apr} in BR60S300 is not further discussed but can be found in Appendix F.

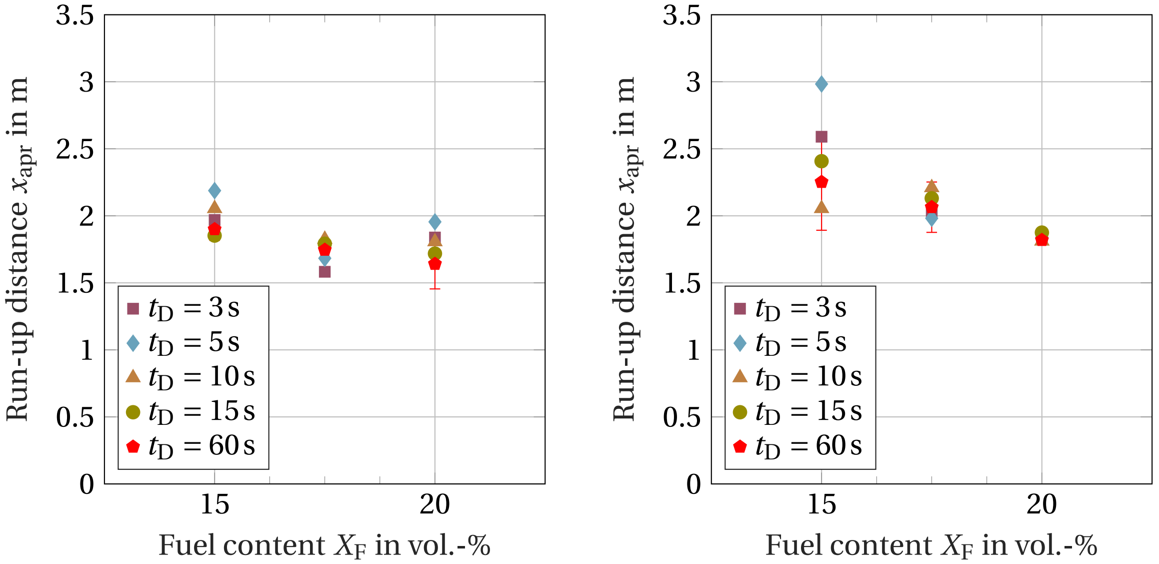

Figure 4.29: Run-up distance to the speed of sound of the isobaric products x_{apr} over fuel content X_F at BR30S300 for inhomogeneous mixtures of 75/25 (left) and 50/50 H_2/CO (right).

In general, it can be concluded that strong FA to flame speeds above a_{pr} is promoted only in the cases of very lean mixtures of $X_F = 15$ vol.-% and steep concentration gradients at BR30S100. This contrasts Boeck [16], who described a promotion of FA at BR30S300 and BR60S300 due to concentration gradients in H_2-air mixtures. A reason for this behavior is the variation of mixture properties such as the laminar flame speed s_L and the expansion ratio σ over the vertical coordinate. Like Boeck in [16], the effective burning velocity is obtained for flame propagation in mixture gradients by

$$(\sigma s_L)_{eff} = \frac{1}{H}\int_0^H \sigma(z)\, s_L(z)\, dz. \tag{4.1}$$

The higher $(\sigma s_L)_{eff}$, the stronger the flame acceleration in the given mixture. Besides the global fuel content, $(\sigma s_L)_{eff}$ is influenced by concentration gradients. In [16], the switch from an accelerating to a decelerating effect of concentration gradients on FA in the case of BR60S300 and BR30S300 could be predicted based on the global fuel content. For mixtures up to a global fuel content of 22.4 vol.-% $(\sigma s_L)_{eff}$ is higher in the case of concentration gradients. Hence, stronger FA is observed in inhomogeneous mixtures for X_F < 22.4 vol.-%. For higher fuel contents, $(\sigma s_L)_{eff}$ is higher in homogeneous mixtures, FA is stronger for homogeneous mixtures.

For mixtures of H_2-CO-air, the distributions of the mixture properties are more complicated, as discussed in Sec. 3.3. An evaluation of the effective burning velocity $(\sigma s_L)_{eff}$ is shown in Fig. 4.30 for 75/25 (left) and 50/50 H_2/CO (right). For the sake of simplicity, the effective burning velocity is plotted for $t_D = 3, 5$ and 45 s. For other diffusion times, $(\sigma s_L)_{eff}$ is between the boundaries of the plotted curves.

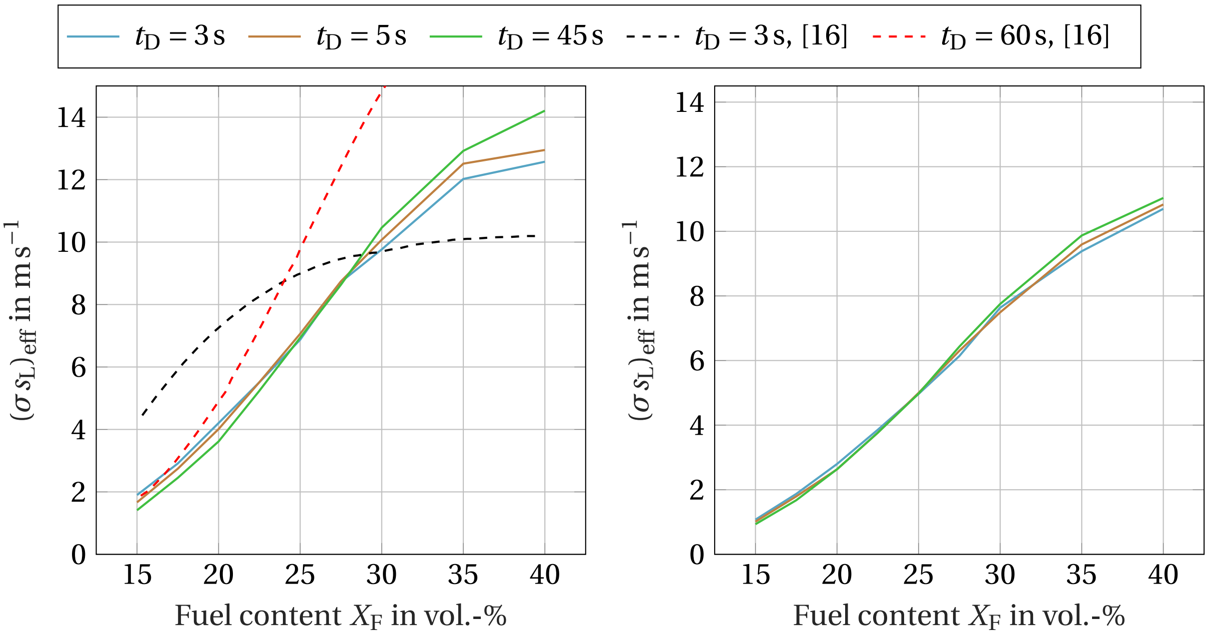

Figure 4.30: Effective burning velocity $(\sigma s_L)_{eff}$ over fuel content X_F for 75/25 (left) and 50/50 H_2/CO (right).

The effective burning velocity is higher for fuel-lean mixtures in the case of concentration gradients than for homogeneous mixtures. As shown in Fig. 4.30, the effective burning velocity $(\sigma s_L)_{eff}$ is higher in inhomogeneous mixtures up to a global fuel content of 27.5 vol.-% for 75/25 and 24.5 vol.-% for 50/50 H_2/CO. If the fuel content increases further, $(\sigma s_L)_{eff}$ is larger for homogenous mixtures. The difference in $(\sigma s_L)_{eff}$ for fuel-lean compositions is larger at 75/25 than for 50/50 H_2/CO. For comparison, the dashed lines include the effective burning velocities of H_2-air mixtures, as investigated by Boeck [16].

For all fuel contents up to the switch-over, the difference between $(\sigma s_L)_{\mathrm{eff}}$ for $t_D = 3\,\mathrm{s}$ and homogeneous mixtures of $t_D = 60\,\mathrm{s}$ is higher in H_2-air than in H_2-CO-air mixtures. Therefore, concentration gradients promote FA in H_2-air mixtures, while a similar effect cannot be observed in H_2-CO-air mixtures in partially obstructed configurations.

In Fig. 4.31, x_{apr} is plotted over the global fuel content for 75/25 H_2/CO in the unobstructed channel. When comparing inhomogeneous and homogeneous mixtures, two effects can be observed. First, the range of fuel contents at which the flame speed exceeds the speed of sound of the isobaric combustion product is extended on the fuel-lean and the fuel-rich side. In the case of fuel-lean mixtures, flames at a global fuel content of 17.5 and 20 vol.-% reach a_{pr}. For these mixtures, the influence of diffusion time is of minor importance. Especially for 20 vol.-% as x_{apr} is very similar for different diffusion times. On the fuel-rich side at 35 vol.-%, only mixtures involving steep concentration gradients at short diffusion times of 3-5 s allow for strong FA. The second effect caused by concentration gradients is a slight decrease in the run-up distance for fuel contents of 22.5-30 vol.-% for inhomogeneous mixtures. At 22.5, 27.5 and 30 vol.-%, steep concentration gradients lead to a decrease in the run-up distance.

For 50/50 H_2/CO, the influence of transverse concentration gradients over the global fuel content is plotted in Fig. 4.32. In contrast to 75/25 H_2/CO, the extension of the global fuel content at which flame speeds exceed a_{pr} is smaller. Only very steep gradients at 22.5 vol.-% allow for strong FA, while at homogeneous mixtures, strong FA is observed for mixtures of $X_F \geq 25$ vol.-%. For fuel contents of 25 vol.-%, concentration gradients have almost no effect on FA. At 30 vol.-%, homogeneous mixtures and steep concentration gradients cause strong FA. Less steep concentration gradients at diffusion times of 10-15 s do not cause strong FA.

In conclusion, the influence of concentration gradients in the unobstructed configuration is highly influenced by the fuel composition. For 75/25 H_2/CO, concentration gradients promote FA up the speed of sound of the products at leaner global fuel contents than in homogeneous mixtures. A similar effect is observed in fuel-rich mixtures. At global fuel contents at which flame

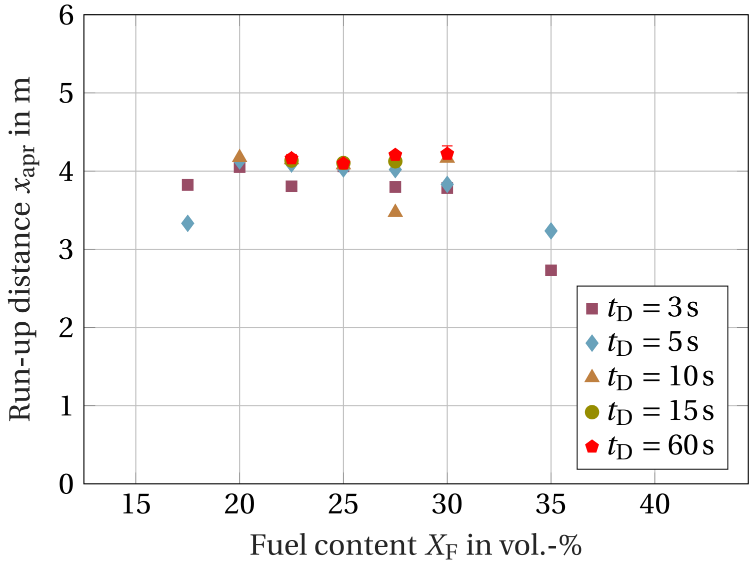

Figure 4.31: Run-up distance to speed of sound of the isobaric products x_{apr} over fuel content X_F at BR00 for inhomogeneous mixtures of 75/25 H_2/CO.

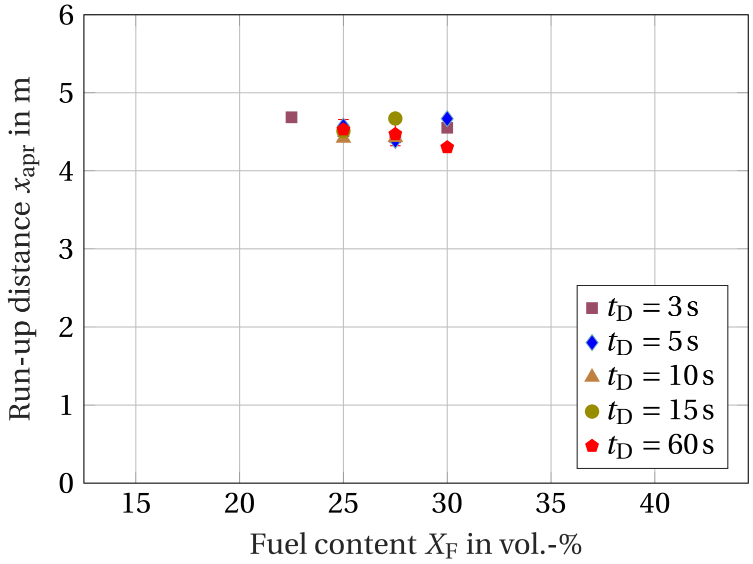

Figure 4.32: Run-up distance to speed of sound of the isobaric products x_{apr} over fuel content X_F at BR00 for inhomogeneous mixtures of 50/50 H_2/CO.

speeds in homogeneous mixtures exceeded a_{pr}, a reduction in x_{apr} for inhomogeneous mixtures is observed. For 50/50 H_2/CO, the accelerating effect of concentration gradients on FA is much weaker. An extension of the global fuel content at which flame speeds exceed $0.95 a_{\mathrm{pr}}$ is only observed at 22.5 vol.-% in the case of inhomogeneous mixtures. A comparison with homogeneous mixtures shows that x_{apr} is similar in homogeneous and inhomogeneous mixtures if a_{pr} is exceeded in both mixtures.

In contrast to the impact of concentration gradients in H_2-air mixtures, as investigated by Boeck [16], the impact in H_2-CO-air mixtures is weaker. In [16], the run-up distance to $0.95 a_{\mathrm{pr}}$ in H_2-air mixture is reduced from 4.2 m in homogeneous mixtures to 2.9 m for steep concentration gradients at 3 s diffusion time at a global fuel content of 30 vol.-%. For 75/25 H_2/CO, x_{apr} decreases from 4.2 m in the homogeneous case to 3.8 m at the same global fuel content and diffusion time. For 50/50 H_2/CO, x_{apr} increases from 4.3 m in the homogeneous case to 4.6 m for $t_{\mathrm{D}} = 3\,\mathrm{s}$. The global fuel content is above the switch-over in the effective burning velocity $(\sigma s_{\mathrm{L}})_{\mathrm{eff}}$ for H_2-air mixtures at 24 vol.-%. Therefore, $(\sigma s_{\mathrm{L}})_{\mathrm{eff}}$ in the homogeneous mixture is higher than for the inhomogeneous mixture. The same holds for the mixtures of 75/25 and 50/50 H_2/CO. Furthermore, FA is also observed in mixtures of effective burning velocities $(\sigma s_{\mathrm{L}})_{\mathrm{eff}}$ lower than the threshold given in Sec. 4.2.1, which reproduced the lean limit for FA in homogeneous mixtures in all fuel compositions.

Besides the effective burning velocity variation, Boeck [16] argued that flame elongation increases the overall fuel consumption in inhomogeneous mixtures. Since FA is weaker in inhomogeneous mixtures in the unobstructed channel without an increase in effective burning velocity, it can be assumed that flame elongation plays a crucial role in FA in these cases. The results further indicate that flame elongation is more important at 75/25 than at 50/50 H_2/CO since FA is weaker in inhomogeneous mixtures of 50/50 than at 75/25 H_2/CO. Optical measurement techniques are not part of this work. Therefore experimental evidence cannot be provided at this stage.

In the case of FA in inhomogeneous mixtures in the unobstructed channel presented above, a prediction can be made using the approach by Grune et al. [133]. The authors argue that in fuel-lean mixtures, the area of maximum reactivity governs the flame propagation in inhomogeneous mixtures. By referring to the maximum reactivity of inhomogeneous mixtures, a comparison regarding FA between inhomogeneous and homogeneous mixtures at different global fuel contents is possible. Supposing that the maximum reactivity in an inhomogeneous mixture is equal to a homogeneous mixture at a given higher fuel content, FA can be expected at a lower global fuel content in the inhomogeneous mixture. Since flame propagation properties such as laminar flame speed and expansion ratio increase with fuel content for fuel-lean mixtures (see Sec. 2.4), the fuel content can be used as an indicator for the reactivity of the mixture. If this approach is used in the present case, a conservative prediction based on a comparison with the results of FA in homogeneous mixtures is possible. For 75/25 H_2/CO, the limit for FA for homogeneous mixtures is 22.5 vol.-%. In the case of concentration gradients, this limit is exceeded by mixtures at a global fuel content of 17.5 vol.-% at diffusion times of 3 and 5 s. For global fuel contents of $X_F > 20$ vol.-%, the maximum reactivity in inhomogeneous mixtures exceeds the threshold for FA given by a global fuel content in a homogeneous mixture of 22.5 vol.-% at all diffusion times of $t_D \leq 10$ s. As shown in Fig. 4.31, FA is stronger in these mixtures if concentration gradients are present. For 50/50 H_2/CO, diffusion times of 3 and 5 s lead to maximum fuel contents higher than the threshold for FA in the case of homogeneous mixtures at 25 vol.-%. FA up to a_{pr} is only found for $t_D = 3$ s. The method remains conservative without a high deviation. It seems reasonable to use the approach of maximum reactivity for predicting FA in a practical application in the first place.

In summary, the following can be concluded:

- An accelerating effect of concentration gradients can be observed only for a global fuel content of 15 vol.-% at BR30S100. For higher fuel contents and other obstacle configurations, the run-up distance to a_{pr} in inhomogeneous mixtures is similar to or weaker than for homogeneous mixtures. The behavior in FA is similar for 75/25 and 50/50 H_2/CO.

- The difference in effective burning velocity between the homogeneous and the inhomogeneous mixtures is small. This results from the impact of H_2 on the laminar flame speed and the lower concentration differences over the channel height.

- In contrast to partially obstructed configurations, the impact of concentration gradients in the unobstructed channel on FA is evident. In fuel-lean mixtures, the fuel content at which the flame speed exceeds the speed of sound of the combustion products is decreased in the case of concentration gradients. Strong FA is also found in fuel-rich mixtures with higher global fuel content than homogeneous mixtures.

- When compared to homogeneous mixtures, the run-up distance to the speed of sound of the products in inhomogeneous mixtures decreases. Compared to the differences in x_{apr} for H_2-air mixtures, as reported by Boeck [16], the differences in x_{apr} between the homogeneous and inhomogeneous mixtures are lower.

- The impact of concentration gradients is stronger at 75/25 than at 50/50 H_2/CO. The range of global fuel contents at which inhomogeneous mixtures exceed a_{pr} is broader at 75/25 than at 50/50 H_2/CO. Furthermore, the reduction in x_{apr} is stronger at 75/25 than at 50/50 H_2/CO.

4.3.2 Detonations in partially obstructed configurations

In Fig. 4.33, the relative terminal velocity $\tilde{u}_{\mathrm{term}}$ is plotted over the fuel content X_{F} for 75/25 H_2/CO at BR30S100 in case of transverse concentration gradients. For $X_{\mathrm{F}} = 15\,\mathrm{vol.\text{-}\%}$, an accelerating effect of transverse concentration gradients on the relative terminal velocity is observed. At the leanest fuel content investigated, all mixtures involving diffusion times of 15 s or less lead to higher terminal velocities. However, a clear change in the flame propagation regime is not visible. As shown in Fig. 4.33, $\tilde{u}_{\mathrm{term}}$ is 0.71. In this case, shorter waiting times do not lead to higher terminal velocities, as all mixtures involving transverse concentration gradients are close to 0.71.

If the fuel content increases, the lean detonation limit is reached for the BR30S100 configuration in the homogeneous case. A high standard deviation accompanies this limit. A similar spread is found for inhomogeneous cases. While a diffusion time of 15 s leads to higher terminal velocities, other diffusion times result in lower $\tilde{u}_{\mathrm{term}}$ with respect to the homogeneous case. Hence

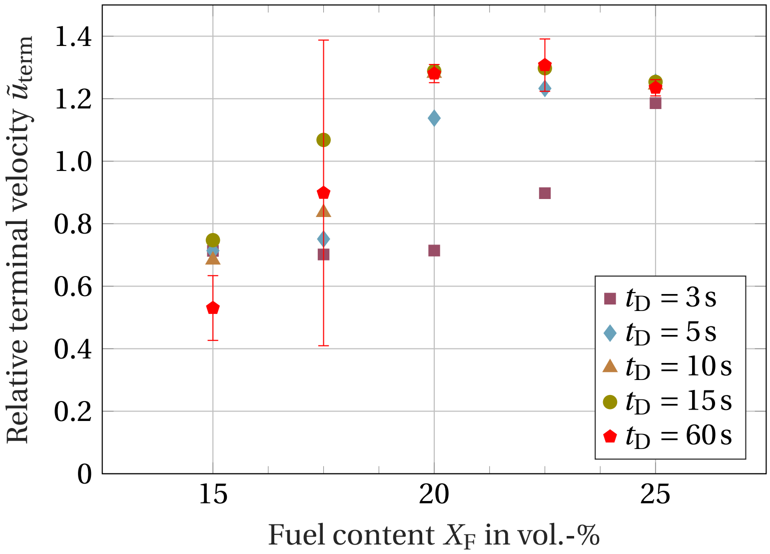

Figure 4.33: Relative terminal velocity $\tilde{u}_{\mathrm{term}}$ over fuel content X_{F} at BR30S100 for inhomogeneous mixtures of 75/25 H_2/CO.

concentration gradients at the lean limit of the detonation regime do not promote the onset of detonation. A different trend can be observed if the fuel content increases to 20 vol.-%. Steep concentration gradients lead to reduction in $\tilde{u}_{\mathrm{term}}$, mostly prominent at $t_{\mathrm{D}} = 3\,\mathrm{s}$. This can also be observed at 5 s. The largest difference between the homogeneous case and the steepest gradient occurs at 20 vol.-%. The difference in $\tilde{u}_{\mathrm{term}}$ decreases for further increased fuel contents. At 22.5 vol.-% almost no difference in $\tilde{u}_{\mathrm{term}}$ is observed for all diffusion times except for 3 s. The difference in $\tilde{u}_{\mathrm{term}}$ between homogeneous mixtures and steep concentration gradients drops, and the transition between the fast flame regime and the detonation regime is observed for $t_{\mathrm{d}} = 3\,\mathrm{s}$. The difference vanishes at a fuel content of 25 vol.-%.

The influence of transverse concentration gradients on the relative terminal velocity for 50/50 H_2/CO in BR30S100 is shown in Fig. 4.34. Like 75/25 H_2/CO, an increase in $\tilde{u}_{\mathrm{term}}$ is depicted for short diffusion times at a fuel content of 15 vol.-%. However, a change in the combustion regime is not observed, although $\tilde{u}_{\mathrm{term}}$ is higher than at 75/25 H_2/CO. For an increased fuel content, similar behavior is observed. With respect to homogeneous mixtures, a slight increase in $\tilde{u}_{\mathrm{term}}$ is depicted at 17.5 vol.-% for inhomogeneous mixtures. For $X_{\mathrm{F}} \geq 20$ vol.-%, the relative terminal velocity for homogeneous mixtures is higher than for inhomogeneous mixtures. However, the propagation regime is not altered by transverse concentration gradients. In contrast to the results of 75/25 H_2/CO, a shift of the transition limit to the detonation regime in the case of steep concentration gradients is not visible. All mixtures are found in the detonation regime. However, the terminal velocities for inhomogeneous mixtures at short diffusion times are lower than in the homogeneous case. This is valid for $t_D = 3\,s$ for all cases of $X_F \geq 20$ vol.-% and for $t_D = 5\,s$ for $X_F = 20$ vol.-%.

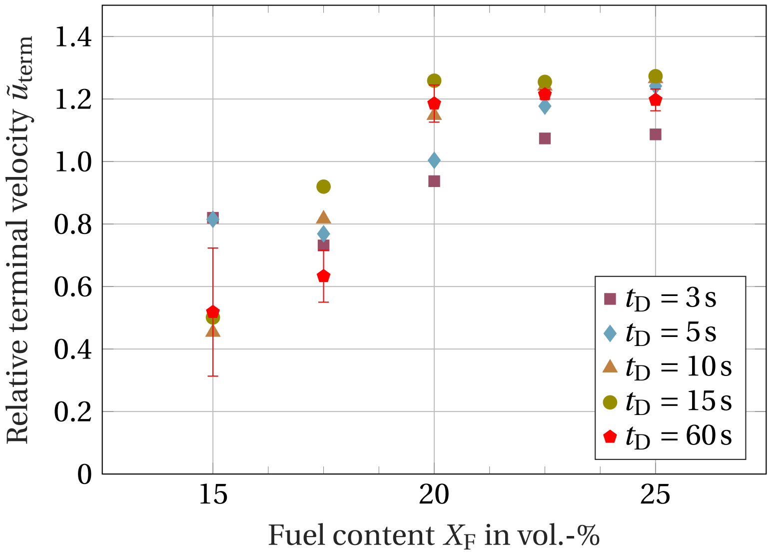

Figure 4.34: Relative terminal velocity $\tilde{u}_{term}$ over fuel content X_F at BR30S100 for inhomogeneous mixtures of 50/50 H_2/CO.

In Fig. 4.35, the impact of transverse concentration gradients on $\tilde{u}_{term}$ at the configuration BR30S300 is shown for 75/25 (left) and 50/50 H_2/CO (right). Similar to BR30S100, an increase in $\tilde{u}_{term}$ for steep gradients is depicted at a fuel content of 15 vol.-%. As soon as the fuel content is increased to 17.5 vol.-%, $\tilde{u}_{term}$ for inhomogeneous and homogeneous mixtures are similar. A decrease in $\tilde{u}_{term}$ for steep gradients is observed at 75/25 H_2/CO for 3 s at 17.5-20 vol.-%. However, the results are within the standard deviation of $\tilde{u}_{term}$ at 75/25 H_2/CO. Differences in $\tilde{u}_{term}$ are smaller at 50/50 than at 75/25 H_2/CO for fuel contents of 20 vol.-% and more.

Since the results obtained at BR60S300 are very similar, a detailed discussion is not presented in this section. The results on $\tilde{u}_{\mathrm{term}}$ for inhomogeneous mixtures at BR60S300 can be found in Appendix F.

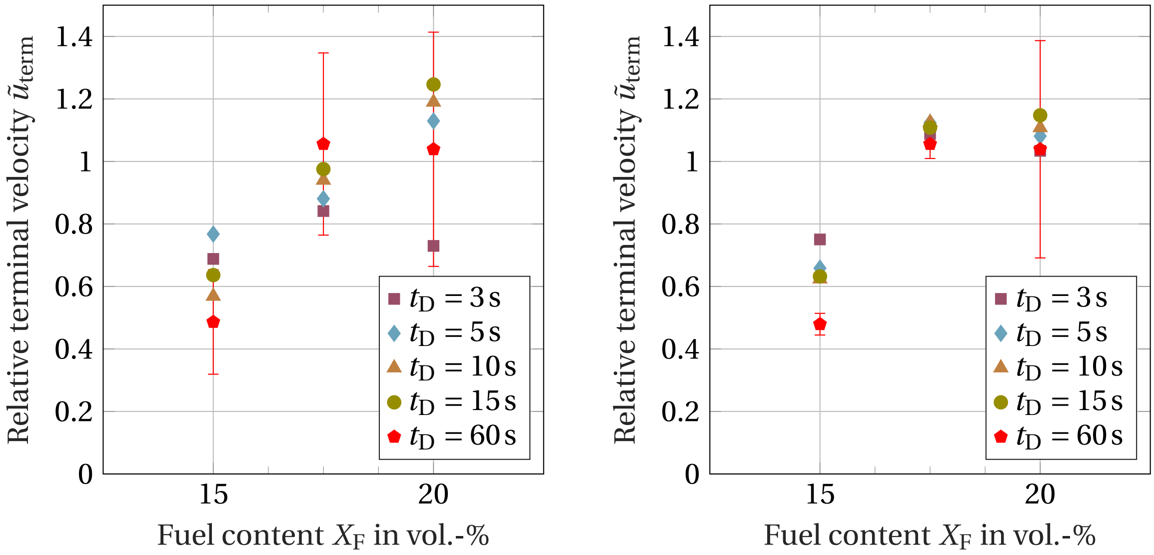

Figure 4.35: Relative terminal velocity $\tilde{u}_{\mathrm{term}}$ over fuel content X_F at BR30S300 for inhomogeneous mixtures of 75/25 (left) and 50/50 H_2/CO (right).

As shown in [16], transverse concentration gradients in 100/0 H_2/CO do not lead to an earlier onset of detonation, although the run-up distances were considerably shorter than for homogeneous mixtures. Optical investigations showed that the flame mainly propagates in regions of high fuel contents close to the channel ceiling. A shock reflection originating from an obstacle is needed for the onset of detonation. As the second explosion limit (see Sec. 2.3) is independent of the fuel content, the temperature required for autoignition is very similar for all fuel contents investigated. In order to trigger autoignition, a shock traveling at a critical Mach number is needed. However, the local speed of sound increases with an increasing H_2 content. Hence, an overall higher shock speed is required. Higher shock speeds require longer run-up distances. Therefore, the onset of detonation was observed at leaner fuel contents than in the homogeneous case.

In the case of H_2/CO mixtures, the local sound speed dependency on the fuel content is weaker than in 100/0 H_2/CO mixtures (see Fig. 3.8). Furthermore, as the ignition mechanism is still triggered by the H_2-O_2-mechanism, localized explosions in H_2-CO-air mixtures due to shock reflection originating from an obstacle occur at similar temperatures and pressures as in H_2-air mixtures (see Sec. 4.2.3). A longer flame propagation distance is hence not required to generate shocks of sufficient strength to trigger the onset of detonation.

In summary, the following can be concluded:

- Concentration gradients can lead to higher terminal velocities in the case of mixtures of a global fuel content of 15 vol.-%. Concentration gradients do not trigger a change in the flame propagation regime. An onset of detonation in leaner mixtures due to concentration gradients was not observed. The impact of concentration gradients is weaker than the impact due to a change in obstacle configuration.
- For higher global fuel contents, terminal velocities in the case of steep concentration gradients are lower than for homogeneous mixtures at the same global fuel content. This effect is stronger in the case of 75/25 than at 50/50 H_2/CO.

4.3.3 Detonations in the unobstructed channel

In Fig. 4.36 $\tilde{u}_{\mathrm{term}}$ is plotted over the fuel content for 75/25 H_2/CO at BR00. In contrast to the partially obstructed configurations, the impact of transverse concentration gradients is stronger. Steep concentration gradients at almost all fuel contents lead to a higher relative terminal velocity. The accelerating effect is evident at low fuel contents of 17.5 and 20 vol.-%. While the homogeneous mixtures are in the slow flame regime at flame speeds below a_{re}, diffusion times of 5 s lead to an increase in $\tilde{u}_{\mathrm{term}}$ up to a_{pr}. For $t_{\mathrm{D}} = 3\,\mathrm{s}$, terminal velocities above the speed of sound of the products a_{pr} are observed. Within the range of 22.5-30 vol.-%, fast flames were observed for homogeneous mixtures for 75/25 H_2/CO. Localized explosions were found at the end of the channel. In the case of concentration gradients, higher relative terminal velocities for short diffusion times of 3-5 s are obtained. This might be related to an onset of detonation further upstream in the channel. For diffusion times longer than 5 s, $\tilde{u}_{\text{term}}$ is similar to the homogeneous cases. At a fuel content of 35 vol.-%, short diffusion times still lead to a higher relative terminal velocity. However, the results are close to the homogeneous case for fuel contents of 22.5-30 vol.-%. Localized detonations might occur at the rear part of the channel due to an interaction of the shock and the end plate.

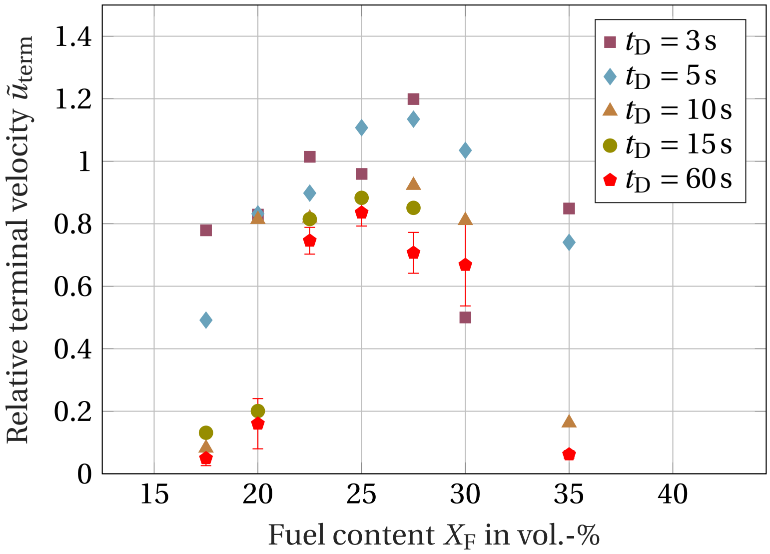

Figure 4.36: Relative terminal velocity $\tilde{u}_{\text{term}}$ over fuel content X_F at BR00 for inhomogeneous mixtures of 75/25 H_2/CO.

The conclusion of the onset of detonation at lower global fuel contents for inhomogeneous mixtures is further supported by the data provided by the dynamic pressure sensors in the rear section of the channel. As shown in Sec. 4.2.3, the onset of detonation for the homogeneous case at $X_F = 22.5$ vol.-% can be explained by an interaction between the leading shock and the endplate. The onset of detonation resulted in high peak pressures at the end plate. The maximum pressure exceeded that of a corresponding detonation in the case of the obstructed channel. In the case of an inhomogeneous mixture at a global fuel content of $X_F = 22.5$ vol.-%, the dynamic pressure profile differs from the profile obtained for the homogeneous case. In Fig. 4.37 the profile of the dynamic pressure p_{dyn} for pressure sensors PDyn7 at $x = 5.4$ m and PDyn8 at $x = 6$ m is plotted over the time t. In contrast to the homogeneous mixture at Fig. 4.17, the increase in p_{dyn} of the leading shock at $t = 39.1$ ms is steeper. The maximum pressure of 1.92 MPa matches the dynamic pressure measured for detonations in the unobstructed section at BR30S300 (see Fig. 4.20). Furthermore, the pressure profile of PDyn 8 shows a single spike. No secondary pressure increase is obtained. The pressure level is close to that of the detonations in 100/0 H_2/CO at BR00 (see Fig. 4.19). Calculation of the Mach number based on the pressure peaks in Fig. 4.42 reveals that the Mach number corresponding to the two pressure peaks is 4.7. This result is similar to the Mach numbers obtained for detonations in 100/0 H_2/CO at BR00.

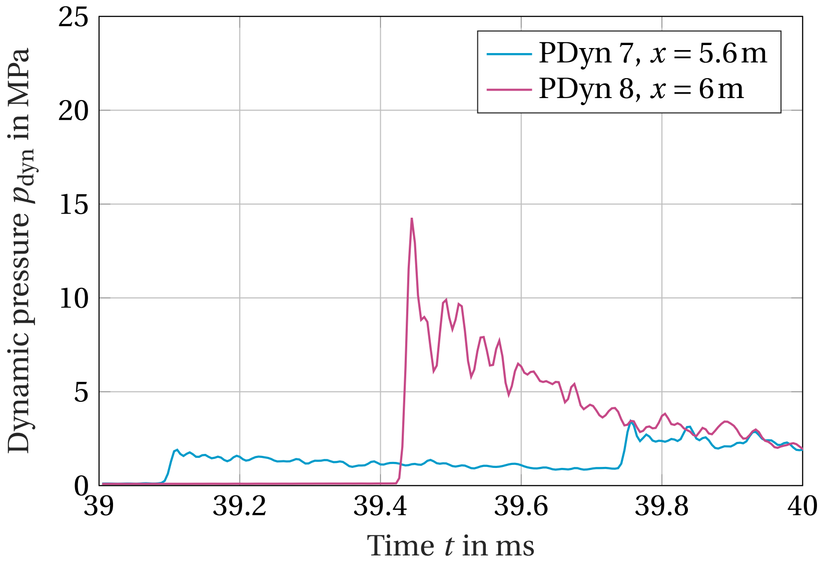

Figure 4.37: Dynamic presssure p_{dyn} at $x = 5.6$ m and $x = 6$ m over time t for 75/25 H_2/CO and $X_F = 22.5$ vol.-% for $t_D = 3$ s at BR00.

In contrast to 75/25, the impact of transverse concentration gradients in the unobstructed channel is weaker for 50/50 H_2/CO. As shown in Fig. 4.38, the influence is visible only at fuel contents of 20 and 22.5 vol.-%. In these cases, concentration gradients lead to a higher relative terminal velocity. The impact of diffusion times longer than 5 s is not visible and, therefore, is not included in the discussion of the results. For 20 vol.-%, the relative terminal velocity is more than doubled in case of short diffusion times of 3 s with respect to homogeneous mixtures. However, a slight increase to $t_D \geq 5$ s leads to relative velocities similar to the homogeneous case. If the fuel content increases to 22.5 vol.-%, the difference in $\tilde{u}_{term}$ between inhomogeneous and homogeneous mixtures becomes larger. Flames at $t_D = 3$ s reach the fast flame regime at $\tilde{u}_{\mathrm{term}} \approx 0.4$. While flames in homogeneous fuel-air mixtures propagate in the slow flame regime, strong concentration gradients can result in fast flames of $u_F > a_{Re}$. Very short diffusion times lead to a change in the flame propagation regime. For $t_D = 5\,\mathrm{s}$, $\tilde{u}_{\mathrm{term}}$ is 0.24, which refers to a flame speed close to the speed of sound of the reactants. If the fuel content is further increased, the difference between inhomogeneous and homogeneous cases diminishes. Higher relative terminal velocities are observed at $X_F = 25$-$30\,\mathrm{vol.\text{-}\%}$. However, the increase due to concentration gradients is in order of the homogeneous case's standard deviation of $\tilde{u}_{\mathrm{term}}$. The trend of $\tilde{u}_{\mathrm{term}}$ for the inhomogeneous mixtures closely follows that of the homogeneous mixtures. A change in the flame propagation regime is not observed, especially an earlier onset of detonation, as observed for 75/25 H_2/CO.

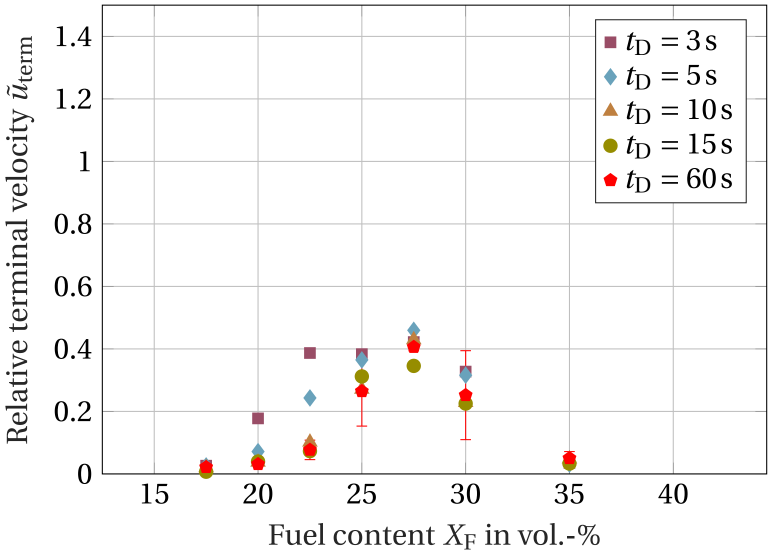

Figure 4.38: Relative terminal velocity $\tilde{u}_{\mathrm{term}}$ over fuel content X_F at BR00 for inhomogeneous mixtures of 50/50 H_2/CO.

In H_2-air mixtures, the onset of detonation in the unobstructed channel was effectively promoted by the presence of concentration gradients [16]. Boeck concluded that the approach of considering the maximum reactivity for the prediction of DDT in the case of the unobstructed channel is conservative. This conclusion can be extended to 75/25 and 50/50 H_2/CO. The criterion of maximum reactivity correctly predicts the earlier transition to the fast flame regime.

The terminal velocities in the range of 22.5-30 vol.-% can only be attributed to the onset of detonation without a reflection at the end plate. The terminal velocities are comparable to 100/0 H_2/CO in the range of 22.5-27.5 vol.-% at BR00.

In summary, the following can be concluded:

- In contrast to the partially obstructed configurations, concentration gradients in BR00 lead to an earlier change in the flame propagation regime. The transition from slow to fast flames and the onset of detonation is reached at lower global fuel contents in the case of inhomogeneous mixtures. The increase in $\tilde{u}_{\text{term}}$ is most evident for steep concentration gradients.
- In 75/25 H_2/CO $\tilde{u}_{\text{term}}$ is higher for inhomogeneous mixtures than for homogeneous mixtures for all fuel contents investigated. The onset of detonation is observed further upstream in the channel than for homogeneous mixtures. An increase in $\tilde{u}_{\text{term}}$ is found for diffusion times in the range from 3-10 s.
- For 50/50 H_2/CO concentration gradients do not lead to higher terminal velocities in all fuel contents investigated. The propagation regime changes from the slow to the fast flame regime at 22.5 vol.-% and a diffusion time of 3 s. Overall, no considerable impact of longer diffusion times on $\tilde{u}_{\text{term}}$ is observed.

4.3.4 Peak pressure evolution

The following section discusses the impact of concentration gradients on the peak pressure $p_{\text{dyn,max}}$ in the obstructed and unobstructed configurations. In Fig. 4.39, $p_{\text{dyn,max}}$ is plotted over the fuel content for 75/25 H_2/CO at BR30S100. The peak pressure closely follows the trend obtained in the homogeneous mixtures. Shorter run-up distance x_{apr} and higher relative terminal velocities are found in the case of concentration gradients at $X_F = 15$ vol.-%. However, a direct impact on $p_{\text{dyn,max}}$ is not observed. The peak pressures obtained in the case of concentration gradients are lower or very similar to $p_{\mathrm{dyn,max}}$ of the homogeneous mixtures. An increase in $p_{\mathrm{dyn,max}}$ is obtained only at X_F = 17.5 vol.-% for diffusion times of 10 s and 15 s. Since $\tilde{u}_{\mathrm{term}}$ is lower than at the homogeneous mixtures at this fuel content, the increase does not result from a change of the flame propagation regime. An evaluation of the standard deviation of $p_{\mathrm{dyn,max}}$ at X_F = 17.5 vol.-% reveals that localized explosions at diffusion times of 10 s and 15 s lead to a high standard deviation and a higher average peak pressure. The terminal velocity is lower for short diffusion times at fuel contents between 20-22.5 vol.-%. A reduction in $p_{\mathrm{dyn,max}}$ at the respective fuel contents is weaker. Therefore, it can be concluded that the flame propagation regime is the same for homogeneous and inhomogeneous mixtures.

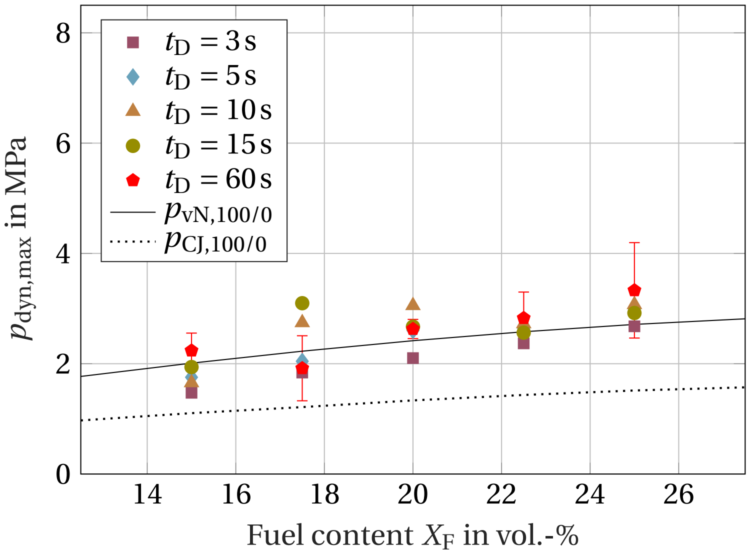

Figure 4.39: Maximum dynamic pressure $p_{\mathrm{dyn,max}}$ over fuel content X_F at BR30S100 for inhomogeneous mixtures of 75/25 H_2/CO.

For 50/50 H_2/CO, the peak pressure $p_{\mathrm{dyn,max}}$ in the case of inhomogeneous mixtures is plotted over the fuel content X_F in Fig. 4.40. Similar to 75/25 H_2/CO, the peak pressure $p_{\mathrm{dyn,max}}$ closely follows the trend of the homogeneous mixtures over the fuel content. Larger deviations are obtained only for t_D = 3 s for fuel contents of 17.5-25 vol.-%. The differences in the peak pressure obtained at the same fuel contents for homogeneous mixtures are small. No trend is evident for t_D > 3 s. With the exception at 25 vol.-%, $p_{\mathrm{dyn,max}}$ are found within the homogeneous mixture's standard deviation of $p_{\mathrm{dyn,max}}$.

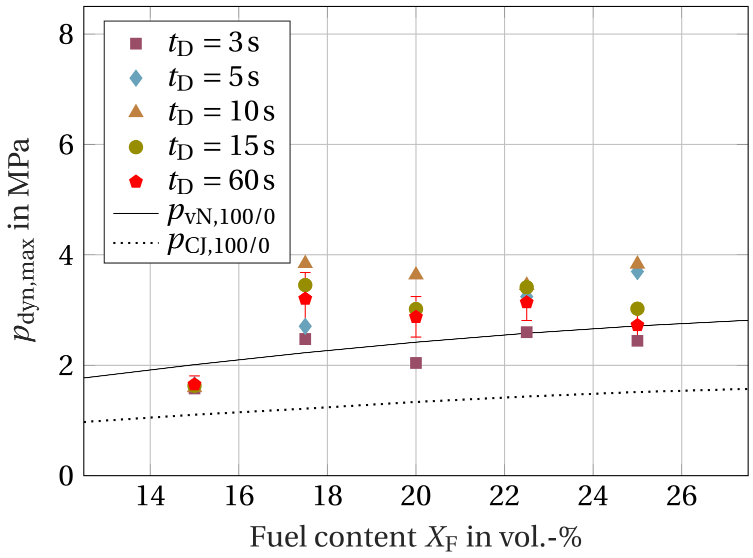

Figure 4.40: Maximum dynamic pressure $p_{dyn,max}$ over fuel content X_F at BR30S100 for inhomogeneous mixtures of 50/50 H_2/CO.

In Fig. 4.41, peak pressures $p_{dyn,max}$ are plotted over the fuel content X_F for BR30S300. The evolution of $p_{dyn,max}$ is similar for both fuel compositions. At 15 vol.-%, $p_{dyn,max}$ is similar for homogeneous and inhomogeneous mixtures of all diffusion times. If the fuel content is increased to 20 vol.-%, $p_{dyn,max}$ increases for all diffusion times except of 3 s. For $t_D = 3$ s, $\tilde{u}_{term}$ is 0.7-0.81 for all fuel contents investigated in BR30S300 in the case of inhomogeneous mixtures. Compared to longer diffusion times and homogeneous mixtures, $\tilde{u}_{term}$ is lowest for $t_D = 3$ s. This is also reflected in the peak pressures. However, it should be mentioned that the peak pressure obtained is within the standard deviation of $p_{dyn,max}$ of the homogeneous mixture at 17.5 vol.-%. For 50/50 H_2/CO, the relative terminal velocity is unity for all diffusion times at fuel contents higher than 15 vol.-%. The differences between mixtures of different diffusion times are small. This is also reflected in $p_{dyn,max}$. A considerable decrease or increase with respect to the homogeneous mixtures is not observed. Since the results for BR60S300 do not show any different behavior, a discussion is not included in this section. The influence of concentration gradients on the peak pressures for BR60S300 can be found in Appendix F.

For the unobstructed channel, the impact of concentration gradients on run-up distances x_{apr} and the terminal velocity $\tilde{u}_{term}$ is stronger than for obstructed

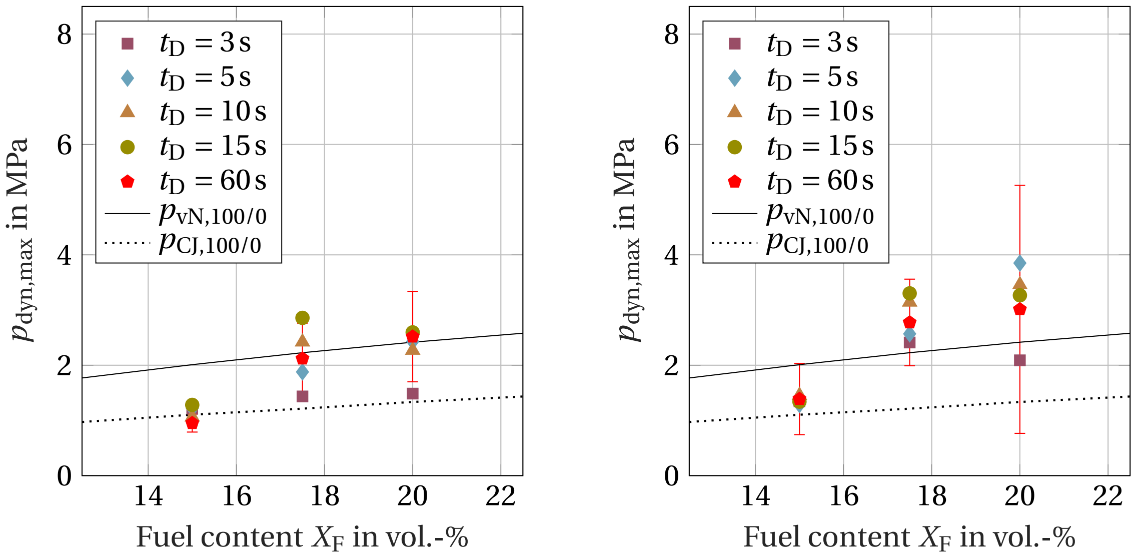

Figure 4.41: Maximum dynamic pressure $p_{\mathrm{dyn,max}}$ over fuel content X_F at BR30S300 for inhomogeneous mixtures of 75/25 (left) and 50/50 H_2/CO (right).

configurations for a fuel composition of 75/25 H_2/CO. The range of fuel contents in which flame speeds exceed the speed of sound of the combustion products is extended by concentration gradients. Higher terminal velocities are observed for all fuel contents for inhomogeneous mixtures. The behavior is reflected in $p_{\mathrm{dyn,max}}$, as shown in Fig. 4.42. For all fuel contents up to 25 vol.-%, an increase in $p_{\mathrm{dyn,max}}$ for inhomogeneous mixtures is observed. At 15 vol.-% diffusion times of 3 and 5 s lead to an increase in $p_{\mathrm{dyn,max}}$. No increase in $p_{\mathrm{dyn,max}}$ with respect to the homogeneous mixtures is observed for longer diffusion times. At 20 vol.-% higher peak pressures are also observed for $t_D = 10\,\mathrm{s}$. The relative terminal velocity for diffusion times of 3-10 s is similar to $\tilde{u}_{\mathrm{term}}$ at 22.5 vol.-% for homogeneous mixtures.

The accelerating effect of concentration gradients also leads to an increase in $p_{\mathrm{dyn,max}}$. The peak pressure obtained is similar to that of homogeneous mixtures at 20 vol.-%. For a diffusion time of 15 s, the increase in $p_{\mathrm{dyn,max}}$ with respect to the homogeneous case is small. If the fuel content is further increased, $p_{\mathrm{dyn,max}}$ is considerably higher for short diffusion times than in homogeneous mixtures. This is according to the increase in $\tilde{u}_{\mathrm{term}}$. The behavior is most evident at 22.5-27.5 vol.-%. The peak pressures reached at diffusion times of 3 s and 5 s are comparable to $p_{\text{dyn,max}}$ obtained in homogeneous mixtures of 100/0 H_2/CO at 25 vol.-%. Therefore, it can be concluded that the onset of detonation happens in the vicinity of the turbulent flame brush without interaction of the leading shock with the end plate. For longer diffusion times, an increase in $p_{\text{dyn,max}}$ in this range is only observed at 25 vol.-% for $t_D = 10$ s. If the fuel content increases to 30 vol.-%, $p_{\text{dyn,max}}$ is similar for inhomogeneous and homogeneous mixtures. An increase in $p_{\text{dyn,max}}$ with respect to homogeneous mixtures is further observed at a fuel content of 35 vol.-%. The pressure level for inhomogeneous mixtures is similar to 17.5 vol.-%.

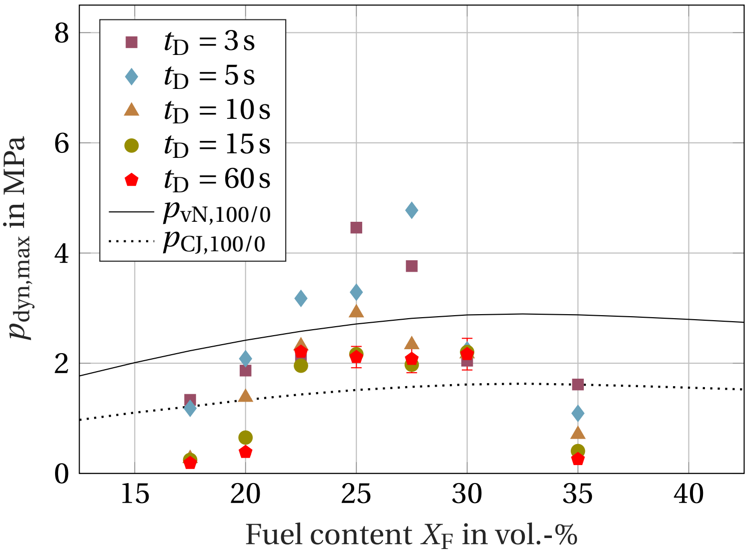

Figure 4.42: Maximum dynamic pressure $p_{\text{dyn,max}}$ over fuel content X_F at BR00 for inhomogeneous mixtures of 75/25 H_2/CO.

For 50/50, the accelerating effect of concentration gradients in the unobstructed channel is weaker than for 75/25 H_2/CO. This effect is observed for the run-up distance x_{apr} and the terminal velocity $\tilde{u}_{\text{term}}$ and is also visible in the peak pressure as shown in Fig. 4.43. A considerable increase in $p_{\text{dyn,max}}$ with respect to the homogeneous mixtures is observed only at 22.5 vol.-%. The relative terminal velocity for a diffusion time of 3 s at a fuel content of 22.5 vol.-% leads to the change in the flame propagation regime from a slow flame to a fast flame. Accordingly, the peak pressure increases. The pressure level is comparable to a homogeneous mixture at 25 vol.-%. For $t_D = 5$ s an increase in $p_{\text{dyn,max}}$ is observed, too. However, the increase is smaller than for

3 s. As concentration gradients do not change the flame propagation regime for higher fuel contents, small variations in $p_{\mathrm{dyn,max}}$ are observed.

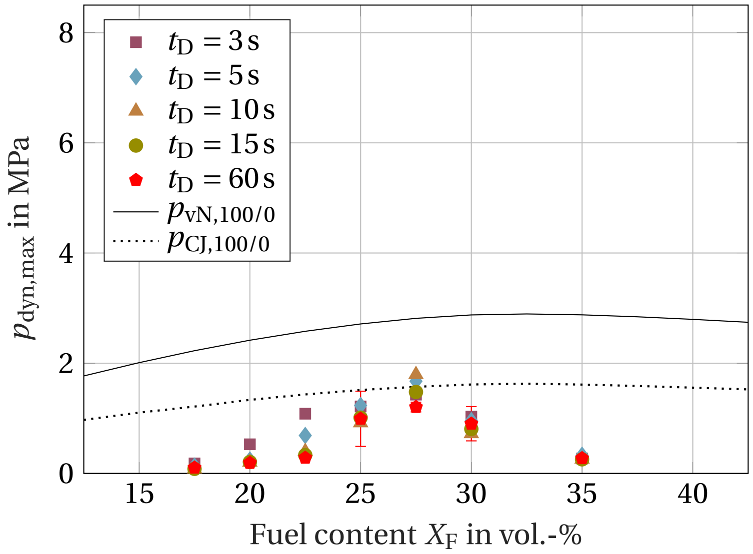

Figure 4.43: Maximum dynamic pressure $p_{\mathrm{dyn,max}}$ over fuel content X_F at BR00 for inhomogeneous mixtures of 50/50 H_2/CO.

In summary, the following can be concluded:

- The peak pressures in obstructed configurations in the case of concentration gradients are not considerably higher than for homogeneous mixtures. For BR30S100, strong concentration gradients lead to slightly lower peak pressure than homogeneous mixtures. For a larger spacing at BR30S300, the peak pressures are found within the standard deviation of the homogeneous mixtures. The impact of the fuel composition is of minor importance. Assuming similar peak pressures in homogeneous and inhomogeneous mixtures for the investigated obstructed configurations seems reasonable.

- For BR00 a considerable difference is observed for 75/25 and 50/50 H_2/CO. The accelerating effect of concentration gradients observed in 75/25 H_2/CO leads to peak pressures considerably higher than for homogeneous mixtures. This is most evident at short diffusion times. Due to the onset of detonation without interaction of the leading shock and the endplate, the level of $p_{\mathrm{dyn,max}}$ is not reached by any homogeneous mixtures of 75/25 H_2/CO at the fuel contents investigated. Therefore, a comparison based on the maximum reactivity criterion is not possible. Similar levels in $p_{\mathrm{dyn,max}}$ are reached in BR00 by 100/0 H_2/CO.

- Similar to x_{apr} and $\tilde{u}_{\mathrm{term}}$, the impact of concentration gradients decreases for $p_{\mathrm{dyn,max}}$ for 50/50 H_2/CO. Increased $p_{\mathrm{dyn,max}}$ is observed only at 22.5 vol.-%. For other fuel contents, $p_{\mathrm{dyn,max}}$ in inhomogeneous mixtures is similar to homogeneous mixtures. The influence of the diffusion time at a given fuel content is weak. By using the criterion of maximum reactivity, a comparison with homogeneous mixtures leads to a conservative estimation of the peak pressure.

5 Conclusion

This work investigated the influence of obstacle configuration, fuel composition, and fuel content on flame acceleration and the transition from deflagration to detonation in H_2-CO-air mixtures. The work provides fundamental insights into the flame dynamics in H_2-CO-air mixtures. Based on experiments in a small-scale, 6 m-long test rig of rectangular cross-section, fuels of 100/0, 75/25, and 50/50 H_2/CO were investigated. Fuel content was varied from 15 to 40 vol.-% in air. Flame velocities and peak pressure data were obtained. The influence of CO in the fuel was investigated in four obstacle configurations and one unobstructed channel configuration. The obstructed configuration featured an unobstructed part in the rear section of the channel. Since concentration gradients are often present in the fuel in real accident scenarios, the influence of concentration gradients was investigated in the final step. With respect to flame acceleration, the following can be concluded:

- In the case of partially obstructed channels, flame acceleration in H_2-CO-air mixtures behaves similarly to H_2-air mixtures. Run-up distances to the fast flame regime were found to be very similar. The influence of the obstacle configuration dominates over the lower effective burning velocity of the fuels investigated. Shorter run-up distances are found at higher obstructions. This development applies to all fuels investigated.

- In the unobstructed channel fuel dependent effects dominate. Higher fuel contents are needed to reach the fast flame regime in case of higher CO levels in the fuel. The main reason for the delayed acceleration is given by the lower effective burning velocity σS_L.

For the onset of detonation, the results can be summarized as follows:

- The onset of detonations was observed at the same fuel content in all fuel compositions investigated, depending on the obstacle configurations. In the case of fuel-rich mixtures, a decrease in terminal velocities in 100/0 H_2/CO is found at lower fuel contents than in the case of 75/25 and 50/50 H_2/CO. At high blockage ratios and small spacings, no detonations were observed. The pressure obtained during detonation propagation is higher in CO-containing mixtures than in 100/0 H_2/CO.

- In the case of the unobstructed channels, detonations were observed for 100/0 and 75/25 H_2/CO fuels. For 100/0 H_2/CO, the onset of detonation can occur without the interaction of shock waves from the rear end of the channel in the vicinity of the flame. For 75/25 H_2/CO, detonations were observed due to shock reflections at the end plate of the channel. Autoignition was triggered by shock reflection at the end plate in preconditioned gas between the flame and the end plate. The shock Mach number for 75/25 is similar to the required shock Mach number to trigger the onset of detonation after shock reflection for 100/0 H_2/CO. For 50/50 H_2/CO, the shocks generated by flame acceleration are insufficient to trigger an onset of detonation.

- The 7λ-criterion can be applied for all fuels investigated. As calculations showed, the change in detonation cell size is small in the case of CO contents below 80 % in the fuel. However, measurements of λ for H_2-CO-air mixtures are still unavailable. In contrast to the prediction by the criteria, no detonations were observed in the case of the highest obstruction and small spacing.

Transverse concentration gradients impact flame acceleration and the onset of detonation in H_2-CO-air mixtures. For H_2-air mixtures, transverse concentration gradients greatly influence the effective burning rate over the channel height. In the case of the obstructed configurations, a tipping point was reached at a global fuel content of 24 vol.-%. For fuel contents below 24 vol.-%, concentration gradients amplify flame acceleration, while gradients in higher fuel contents lead to lower acceleration. However, in contrast to H_2-air mixtures, the impact is different:

- For H_2-CO-air mixtures, the increase in the effective burning rate by concentration gradients is less pronounced than for H_2-air mixtures. Therefore, an enhanced acceleration in the case of obstructed configuration is found only for very lean mixtures in the case of low blockage ratios. With higher fuel contents, the run-up distance to the speed of sound of the isobaric combustion products is longer than in homogeneous mixtures. For higher blockage ratios, the effect of concentration gradients on the run-up distance can be neglected.

- For the unobstructed configuration, an enhanced flame acceleration is observed. In inhomogeneous mixtures, lower fuel contents are needed to reach flame speeds above the speed of sound of the products. Due to missing obstacles, flame elongation may cause a significant increase in overall consumption triggering stronger flame acceleration. The effects observed by Boeck for 100/0 and for 75/25 H_2/CO are very similar. For higher CO-contents in the fuel, the effect becomes weaker.

- The onset of detonation in inhomogeneous mixtures of 75/25 H_2/CO is reached at lower fuel contents for 75/25 H_2/CO. For 50/50 H_2/CO, the onset of detonation in the case of inhomogeneous mixtures was not observed. The impact of concentration gradients on the terminal flame velocity is lower than for 75/25 H_2/CO.

The influence of CO content on flame dynamics should be treated with great care during risk assessment of flame acceleration and deflagration to detonation transition in case of accident scenarios, as the impact of CO is multidimensional. In order to increase the understanding of CO, a detailed study of the flame dynamics in the early stages of flame propagation is needed. This includes the necessity of optical investigations and the influence of intrinsic flame instabilities on flame acceleration. Furthermore, a detailed study of the chemical kinetics leading to the stronger coupling of shock and flame front in fuel-rich H_2-CO-air detonations would be a valuable contribution. Measurements of the detonation cell size for H_2-CO-air mixtures at atmospheric pressure are crucial to further validate the reaction mechanisms and models used to determine λ.

Bibliography

[1] S. Hitz and J. Smith. Estimating global impacts from climate change. *Global Environmental Change*, 14:201–218, 2004.

[2] European comission. The european green deal, 2019.

[3] S. R. Foit, I. C. Vinke, L. G. J. de Haart, and R.-A. Eichel. Power-to-syngas - eine Schlüsseltechnologie für die Umstellung des Energiesystems? *Angewandte Chemie*, 129:5488–5498, 2017.

[4] T. Lieuwen, V. Yang, and R. Yetter. *Synthesis gas combustion: fundamentals and applications.* CRC press, 2009.

[5] G. Maschio, A. Lucchesi, and G. Stoppato. Production of syngas from biomass. *Bioresource Technology*, 48:119–126, 1994.

[6] Sergey M. Frolov. Organic waste gasification: a selective review. *Fuels*, 2:556–651, 2021.

[7] K. Stolecka and A. Rusin. Analysis of hazards related to syngas production and transport. *Renewable Energy*, 146:2535–2555, 2020.

[8] R. K. Kumar, G. W. Koroll, M. Heitsch, and E. Studer. Carbon monoxide-hydrogen combustion characteristics in severe accident containment conditions. *NEA/CSNI/R*, 2000.

[9] R. O. Gauntt, D. A. Kalinich, J. N. Cardoni, J. Phillips, A. S. Goldmann, S. Y. Pickering, M. Francis, K. Robb, L. J. Ott, and D. Wang. Fukushima Daiichi accident study: status as of april 2012, 2012.

[10] Y.-H. Koo, Y.-S. Yang, and K.-W. Song. Radioactivity release from the Fukushima accident and its consequences: A review. *Progress in Nuclear Energy*, 74:61–70, 2014.

[11] J. Yanez, M. S. Kuznetsov, and A. Souto-Iglesias. An analysis of the hydrogen explosion in the Fukushima-Daiichi accident. *International Journal of Hydrogen Energy*, 40:8261–8280, 2015.

[12] M. Klauck, E.-A. Reinecke, S. Kelm, N. Meynet, A. Bentaïb, and H.-J. Allelein. Passive auto-catalytic recombiners operation in the presence of hydrogen and carbon monoxide: Experimental study and model development. *Nuclear Engineering and Design*, 266:137–147, 2014.

[13] M. Andreani. Simulation of gas stratification build-up in the containment under severe accident conditions. In *International Conference on Nuclear Engineering*. American Society of Mechanical Engineers, 2014.

[14] D. Bjerketvedt, J. R. Bakke, and K. van Wingerden. Gas explosion handbook. *Journal of Hazardous Materials*, 52:1–150, 1997.

[15] G. Ciccarelli and S. B. Dorofeev. Flame acceleration and transition to detonation in ducts. *Progress in energy and combustion science*, 34:499–550, 2008.

[16] L. R. Boeck. Deflagration-to-detonation transition and detonation propagation in H_2-air mixtures with transverse concentration gradients. PhD-thesis, Chair of Thermodynamics, Technical University of Munich, Munich, 2015.

[17] E. S. Oran and V. N. Gamezo. Origins of the deflagration-to-detonation transition in gas-phase combustion. *Combustion and Flame*, 148:4–47, 2007.

[18] J. Hasslberger. Numerical simulation of deflagration-to-detonation transition on industry scale. PhD-thesis, Chair of Thermodynamics, Technical University of Munich, Munich, 2017.

[19] C. Barfuss, D. Heilbronn, and T. Sattelmayer. Simulation of deflagration-to-detonation transition of lean H_2-CO-air mixtures in obstructed channels. In *8th International Conference on Hydrogen Safety (ICHS) 2019*. Hydrogen Knowledge Centre, 2019.

[20] J. Hasslberger, P. Katzy, T. Sattelmayer, and L. R. Boeck. Massively parallelized simulation of deflagration-to-detonation transition in a konvoi-type pressurized water reactor. In *Proceedings of the 2016 24th International Conference on Nuclear Engineering. Volume 5: Student Paper Competition.*, 2016.

[21] K. G. Vollmer, F. A. Ettner, and T. Sattelmayer. Influence of concentration gradients on flame acceleration in tubes. *Science and Technology of Energetic Materials*, 72:74–77, 2011.

[22] K. G. Vollmer, F. A. Ettner, and T. Sattelmayer. Deflagration-to-detonation transition in hydrogen/air mixtures with a concentration gradient. *Combustion Science and Technology*, 184:1903–1915, 2012.

[23] K. G. Vollmer. Einfluss von Mischungsgradienten auf die Flammenbeschleunigung und die Detonation in Kanälen. PhD-thesis, Chair of Thermodynamics, Technical University of Munich, Munich, 2015.

[24] L. R. Boeck, F. M. Berger, J. Hasslberger, F. A. Ettner, and T. Sattelmayer. Macroscopic structure of fast deflagrations and detonations in hydrogen-air mixtures with concentration gradients. In *24th International Colloquium on the Dynamics of Explosions and Reactive Systems*, 2013.

[25] L. R. Boeck, J. Hasslberger, and T. Sattelmayer. Explosive combustion of homogeneous and inhomogeneous hydrogen-air mixtures - experimental observations and conclusions for safety applications. In *3rd Colloquium of the Munich School of Engineering*, 2013.

[26] L. R. Boeck, J. Hasslberger, F. A. Ettner, and T. Sattelmayer. Investigation of peak pressures during explosive combustion of inhomogeneous hydrogen-air mixtures. In *Proceedings of the 7th International Seminar on Fire and Explosion Hazards*, 2013.

[27] L. R. Boeck, J. Hasslberger, F. A. Ettner, and T. Sattelmayer. Flame acceleration in hydrogen-air mixtures with concentration gradients. In *24th International Colloquium on the Dynamics of Explosions and Reactive Systems, Taipei, Taiwan*, 2013.

[28] L. R. Boeck, J. Hasslberger, and T. Sattelmayer. Flame acceleration in hydrogen/air mixtures with concentration gradients. *Combustion Science and Technology*, 186:1650–1661, 2014.

[29] L. R. Boeck, J. Hasslberger, and T. Sattelmayer. Transition to detonation in non-uniform H_2-air: chemical kinetics of shock-induced strong ignition. In *25th International Colloquium on the Dynamics of Explosions and Reactive Systems, Leeds, UK*, 2015.

[30] H. Cheikhravat, M. Yahyaoui, A. Barret, N. Chaumeix, and C. E. Paillard. Influence of hydrogen distribution on flame propagation. *21st International Colloquium on the Dynamics of Explosions and Reactive Systems, Poitiers, France*, 2007.

[31] J. Daubech, I. Sochet, and Ch. Proust. Highlights of the flame acceleration in a confined nonuniform $H_2/O_2/N_2$ mixture. *Process Safety Progress*, 29:224–230, 2010.

[32] I. Sochet, F. Guelon, and P. Gillard. Deflagrations of non-uniform mixtures: A first experimental approach. *Journal de Physique IV (Proceedings)*, 12:273–279, 2002.

[33] I. Sochet, P. Gillard, and F. Guélon. Effect of the concentration distribution on the gaseous deflagration propagation in the case of H_2/O_2 mixture. *Journal of Loss Prevention in the Process Industries*, 19:250–262, 2006.

[34] D. R. Whitehouse, D. R. Greig, and G. W. Koroll. Combustion of stratified hydrogen-air mixtures in the $10.7\,\mathrm{m}^3$ combustion test facility cylinder. *Nuclear Engineering and Design*, 166:453–462, 1996.

[35] S. K. Willacy, H. N. Phylaktou, G. E. Andrews, and G. Ferrara. Stratified propane-air explosions in a duct vented geometry. *Process Safety and Environmental Protection*, 85:153–161, 2007.

[36] A. Veser, G. Stern, J. Grune, W. Breitung, and B. Burgeht. CO-H_2-air combustion tests the FZK-7m-tube, 2002.

[37] M. S. Kuznetsov, A. Friedrich, G. Necker, A. Veser, and W. Breitung. An analysis of combustion regimes for hydrogen/CO/air mixtures in different geometries, 2022.

[38] J. Kim, S.-W. Hong, S.-B. Kim, and H.-D. Kim. Three-dimensional behaviors of the H_2 and steam in the APR 1400 containment during a hypothetical loss of feed water accident. *Annals of Nuclear Energy*, 34:992–1001, 2007.

[39] A. Eder. Brennverhalten schallnaher und überschall-schneller Wasserstoff-Luft Flammen. PhD-thesis, Chair of Thermodynamics, Technical University of Munich, Munich, 2001.

[40] C. H. Wieland. Efficient simulation of flame acceleration and deflagration-to-detonation transition in smooth geometries. PhD-thesis, Chair of Thermodynamics, Technical University of Munich, Munich, 2022.

[41] F. Bartlmä. *Gasdynamik der Verbrennung*. Springer-Verlag, 2013.

[42] J. H. S. Lee. *The detonation phenomenon*. Cambridge University Press, 2008.

[43] S. R. Turns. *Introduction to combustion*. McGraw-Hill Companies New York, NY, USA, 2nd edition edition, 2000.

[44] C. Olm, I. G. Zsély, T. Varga, H. J. Curran, and T. Turányi. Comparison of the performance of several recent syngas combustion mechanisms. *Combustion and Flame*, 162:1793–1812, 2015.

[45] M. Chaos and F. L. Dryer. Syngas combustion kinetics and applications. *Combustion Science and Technology*, 180:1053–1096, 2008.

[46] S. G. Davis, A. V. Joshi, H. Wang, and F. Egolfopoulos. An optimized kinetic model of H_2/CO combustion. *Proceedings of the Combustion Institute*, 30:1283–1292, 2005.

[47] G. Mittal, C.-J. Sung, and R. A. Yetter. Autoignition of H_2/CO at elevated pressures in a rapid compression machine. *International Journal of Chemical Kinetics*, 38:516–529, 2006.

[48] D. M. Kalitan, J. D. Mertens, M. W. Crofton, and E. L. Petersen. Ignition and oxidation of lean CO/H_2 fuel blends in air. *Journal of Propulsion and Power*, 23:1291–1301, 2007.

[49] M. C. Krejci, O. Mathieu, A. J. Vissotski, S. Ravi, T. G. Sikes, E. L. Petersen, A. Kérmonès, W. Metcalfe, and H. J. Curran. Laminar flame speed and ignition delay time data for the kinetic modeling of hydrogen and syngas fuel blends. *Journal of Engineering for Gas Turbines and Power*, 135, 2013.

[50] L. D. Thi, Y. Zhang, and Z. Huang. Shock tube study on ignition delay of multi-component syngas mixtures - effect of equivalence ratio. *International Journal of Hydrogen Energy*, 39:6034–6043, 2014.

[51] W.-Q. Wang and Z.-Y. Sun. Experimental studies on explosive limits and minimum ignition energy of syngas: A comparative review. *International Journal of Hydrogen Energy*, 44:5640–5649, 2019.

[52] W. Liang, J. Liu, and C. K. Law. On explosion limits of H_2/CO/O_2 mixtures. *Combustion and Flame*, 179:130–137, 2017.

[53] A. Kéromnès, W. K. Metcalfe, K. A. Heufer, N. Donohoe, A. K. Das, C.-J. Sung, J. Herzler, C. Naumann, P. Griebel, O. Mathieu, M. C. Krejci, E. L. Petersen, W. J. Pitz, and H. J. Curran. An experimental and detailed chemical kinetic modeling study of hydrogen and syngas mixture oxidation at elevated pressures. *Combustion and Flame*, 160:995–1011, 2013.

[54] H.C. Lee, L.Y. Jiang, and A.A. Mohamad. A review on the laminar flame speed and ignition delay time of syngas mixtures. *International Journal of Hydrogen Energy*, 39:1105–1121, 2014.

[55] Y. Zhang, W. Shen, M. Fan, H. Zhang, and S. Li. Laminar flame speed studies of lean premixed H_2/CO/air flames. *Combustion and Flame*, 161:2492–2495, 2014.

[56] A. Friedrich, G. Necker, A. Veser, J. Grune, M. S. Kuznetsov, and T. Jordan. Experiments on the combustion behaviour of hydrogen-carbon monoxide-air mixtures. In *8th International Conference on Hydrogen Safety (ICHS) 2019*. Hydrogen Knowledge Centre, 2019.

[57] K.T. Aung, M.I. Hassan, and G.M. Faeth. Flame stretch interactions of laminar premixed hydrogen/air flames at normal temperature and pressure. *Combustion and Flame*, 109:1–24, 1997.

[58] N. Bouvet, F. Halter, C. Chauveau, and Y. Yoon. On the effective Lewis number formulations for lean hydrogen/hydrocarbon/air mixtures. *International Journal of Hydrogen Energy*, 38:5949–5960, 2013.

[59] C. Dong, Q. Zhou, Q. Zhao, Y. Zhang, T. Xu, and S. Hui. Experimental study on the laminar flame speed of hydrogen/carbon monoxide/air mixtures. *Fuel*, 88:1858–1863, 2009.

[60] M. I. Hassan, K. T. Aung, and G. M. Faeth. Properties of laminar premixed CO/H/air flames at various pressures. *Journal of Propulsion and Power*, 13:239–245, 1997.

[61] O. C. Kwon and G. M. Faeth. Flame/stretch interactions of premixed hydrogen-fueled flames: measurements and predictions. *Combustion and Flame*, 124:590–610, 2001.

[62] H.-M. Li, G.-X. Li, Z.-Y. Sun, Y. Zhai, and Z.-H. Zhou. Measurement of the laminar burning velocities and markstein lengths of lean and stoichiometric syngas premixed flames under various H_2 fractions. *International Journal of Hydrogen Energy*, 39:17371–17380, 2014.

[63] I. C. McLean, D. B. Smith, and S. C. Taylor. The use of carbon monoxide/hydrogen burning velocities to examine the rate of the CO+OH reaction. *Symposium (International) on Combustion*, 25:749–757, 1994.

[64] J. Natarajan, S. Nandula, T. Lieuwen, and J. Seitzman. Laminar flame speeds of synthetic gas fuel mixtures. In *Turbo Expo: Power for Land, Sea, and Air*, pages 677–686. ASMEDC, 2005.

[65] C. Prathap, A. Ray, and M.R. Ravi. Effects of dilution with carbon dioxide on the laminar burning velocity and flame stability of H_2-CO mixtures at atmospheric condition. *Combustion and Flame*, 159:482–492, 2012.

[66] H. Sun, S. I. Yang, G. Jomaas, and C. K. Law. High-pressure laminar flame speeds and kinetic modeling of carbon monoxide/hydrogen combustion. *Proceedings of the Combustion Institute*, 31:439–446, 2007.

[67] S. D. Tse, D. L. Zhu, and C. K. Law. Morphology and burning rates of expanding spherical flames in H_2/O_2/inert mixtures up to 60 atmospheres. *Proceedings of the Combustion Institute*, 28:1793–1800, 2000.

[68] C. M. Vagelopoulos and F. Egolfopoulos. Laminar flame speeds and extinction strain rates of mixtures of carbon monoxide with hydrogen, methane, and air. *Symposium (International) on Combustion*, 25:1317–1323, 1994.

[69] C. Barfuss, D. Heilbronn, and T. Sattelmayer. Verbundvorhaben: Entwicklung von Verbrennungsmodellen und Kriterien für H_2-CO-Luft-Schichten bei partiellem Einschluss Teilvorhaben: Experimentelle Untersuchungen auf Laborskala sowie Entwicklung komplementärer CFD-Verfahren, 2022.

[70] D. Goodwin, R. Speth, H. Moffat, and B. Weber. Cantera: an object-oriented software toolkit for chemical kinetics, thermodynamics and transport processes, 2021.

[71] S. Chandrasekhar. *Hydrodynamic and hydromagnetic stability*. Courier Corporation, 2013.

[72] E. S. Oran. Stochasticity and dynamics of high-speed reactive flows. In *AIP Conference Proceedings*, volume 1376, pages 38–44, 2011.

[73] R. D. Richtmyer. Taylor instability in shock acceleration of compressible fluids, 1954.

[74] E. E. Meshkov. Instability of the interface of two gases accelerated by a shock wave. *Fluid Dynamics*, 4:101–104, 1969.

[75] G. H. Markstein. *Nonsteady flame propagation.* Elsevier, 2014.

[76] P. Katzy. Combustion model for the computation of flame propagation in lean H_2-air mixtures at low turbulence. PhD-thesis, Chair of Thermodynamics, Technical University of Munich, Munich, 2020.

[77] X. Yang, M. Yu, K. Zheng, P. Luan, and S. Han. An experimental study on premixed syngas/air flame propagating across an obstacle in closed duct. *Fuel*, 267:117200, 2020.

[78] S. B. Pope. *Turbulent flows.* Cambridge University Press, 2000.

[79] A. N. Kolmogorov. A refinement of previous hypotheses concerning the local structure of turbulence in a viscous incompressible fluid at high reynolds number. *Journal of Fluid Mechanics*, 13:82–85, 1962.

[80] A. N. Kolmogorov. Local structure of turbulence in an incompressible viscous fluid at very high reynolds numbers. *Soviet Physics Uspekhi*, 10:734, 1968.

[81] R. Borghi. On the structure and morphology of turbulent premixed flames, 1985.

[82] N. Peters. The turbulent burning velocity for large-scale and small-scale turbulence. *Journal of Fluid mechanics*, 384:107–132, 1999.

[83] A. C. Mclntosh. Influence of pressure waves on the initial development of an explosion kernel. *AIAA journal*, 33:1651–1658, 1995.

[84] G. D. Salamandra, T. V. Bazhenova, and I. M. Naboko. Formation of detonation wave during combustion of gas in combustion tube. *Symposium (International) on Combustion*, 7:851–855, 1958.

[85] N. Brehm and F. Mayinger. *Ein Beitrag zum Phänomen des Überganges Deflagration-Detonation.* VDI-Verlag, 1989.

[86] C. Johansen and G. Ciccarelli. Visualization of the unburned gas flow field ahead of an accelerating flame in an obstructed square channel. *Combustion and Flame*, 156:405–416, 2009.

[87] S. B. Dorofeev, M.S. Kuznetsov, V.I. Alekseev, A.A. Efimenko, and W. Breitung. Evaluation of limits for effective flame acceleration in hydrogen mixtures. *Journal of Loss Prevention in the Process Industries*, 14:583–589, 2001.

[88] N. Donato and E. Petersen. Simplified correlation models for CO/H_2 chemical reaction times. *International Journal of Hydrogen Energy*, 33:7565–7579, 2008.

[89] M. J. Brown, I. C. McLean, D. B. Smith, and S. C. Taylor. Markstein lengths of CO/H_2/air flames, using expanding spherical flames. *Symposium (International) on Combustion*, 26:875–881, 1996.

[90] N. Bouvet, C. Chauveau, I. Gökalp, and F. Halter. Experimental studies of the fundamental flame speeds of syngas (H_2/CO)/air mixtures. *Proceedings of the Combustion Institute*, 33:913–920, 2011.

[91] G. Dixon-Lewis. Kinetic mechanism, structure and properties of premixed flames in hydrogen-oxygen-nitrogen mixtures. *Philosophical Transactions of the Royal Society of London. Series A, Mathematical and Physical Sciences*, 292:45–99, 1979.

[92] P. A. Urtiew and A. K. Oppenheim. Experimental observations of the transition to detonation in an explosive gas. *Proceedings of the Royal Society of London. Series A. Mathematical and Physical Sciences*, 295:13–28, 1966.

[93] S. B. Dorofeev, V. P. Sidorov, M. S. Kuznetsov, I. D. Matsukov, and V. I. Alekseev. Effect of scale on the onset of detonations. *Shock Waves*, 10:137–149, 2000.

[94] J. H. S. Lee, R. Knystautas, and N. Yoshikawa. Photochemical initiation of gaseous detonations, 1980.

[95] D. L. Chapman. On the rate of explosion in gases. *The London, Edinburgh, and Dublin Philosophical Magazine and Journal of Science*, 47:90–104, 1899.

[96] E. Jouguet. Sur la propagation des rèactions chimiques dans les gaz. *Journal mathematiques pures et appliquees Maths.*, 2:5–86, 1905.

[97] Y. B. Zeldovich. On the theory of the propagation of detonation in gaseous systems, 1950.

[98] J. Von Neuman. Theory of detonation waves, 1942.

[99] W. Döring. Über den Detonationsvorgang in Gasen. *Annalen der Physik*, 435:421–436, 1943.

[100] W. Fickett and W. C. Davis. *Detonation: theory and experiment*. Courier Corporation, 2000.

[101] EXPLOSION DYNAMICS LABORATORY. Shock and detonation toolbox, 2021.

[102] J. J. Erpenbeck. Stability of steady-state equilibrium detonations. *Physics of Fluids*, 5:604, 1962.

[103] V. N. Gamezo, D. Desbordes, and E. S. Oran. Formation and evolution of two-dimensional cellular detonations. *Combustion and Flame*, 116:154–165, 1998.

[104] A. I. Gavrikov, A. A. Efimenko, and S. B. Dorofeev. A model for detonation cell size prediction from chemical kinetics. *Combustion and Flame*, 120:19–33, 1999.

[105] H. D. Ng and J. H.S. Lee. Comments on explosion problems for hydrogen safety. *Journal of Loss Prevention in the Process Industries*, 21:136–146, 2008.

[106] J. Herzler and C. Naumann. Shock tube study of the ignition of lean CO/H_2 fuel blends at intermediate temperatures and high pressure. *Combustion Science and Technology*, 180:2015–2028, 2008.

[107] D. He, Y. Ding, X. Xiong, S. Shi, Y. Du, Zhimin Peng, and Weiping Yan. Shock tube study of ignition-delay measurements and kinetic mechanism research for syngas. *Journal of Propulsion and Power*, 34:836–843, 2018.

[108] J. M. Austin and J. E. Shepherd. Carbon monoxide detonations. In *Proceedings 17th International Colloquium on the Dynamics of Explosions and Reactive Systems*, pages 25–30, 1999.

[109] A. A. Vasil'ev. Ignition delay in multifuel mixtures. *Combustion, Explosion, and Shock Waves*, 43:282–285, 2007.

[110] A. V. Trotsyuk and P. A. Fomin. Modeling of an irregular cellular structure of the detonation wave in a two-fuel mixture. *Combustion, Explosion, and Shock Waves*, 55:384–389, 2019.

[111] L.-Q. Wang, H.-H. Ma, Z.-W. Shen, Y.-F. Cheng, and D.-G. Chen. Detonation behaviors of syngas-oxygen in round and square tubes. *International Journal of Hydrogen Energy*, 43:14775–14786, 2018.

[112] M. Kaneshige and J.E. Sheperd. Detonation database, 1997.

[113] M. Yu, X. Yang, K. Zheng, L. Zheng, and X. Wen. Experimental study of premixed syngas/air flame deflagration in a closed duct. *International Journal of Hydrogen Energy*, 43:13676–13686, 2018.

[114] X. Yang, M. Yu, K. Zheng, P. Luan, and S. Han. On the propagation dynamics of lean H_2/CO/air premixed flame. *International Journal of Hydrogen Energy*, 45:7210–7222, 2020.

[115] S. Han, M. Yu, X. Yang, and X. Wang. Effects of obstacle position and hydrogen volume fraction on premixed syngas-air flame acceleration. *International Journal of Hydrogen Energy*, 45:29518–29532, 2020.

[116] V. Bychkov, D. Valiev, and L.-E. Eriksson. Physical mechanism of ultrafast flame acceleration. *Physical Review Letters*, 101:164501, 2008.

[117] Y. Chen, B. Liu, Y. P. Zhang, D. L. Zhang, S. T. Revankar, W. X. Tian, S. Z. Qiu, and G. H. Su. Effects of nitrogen and carbon monoxide on the detonation of hydrogen-air gaseous mixtures. *Nuclear Engineering and Design*, 343:1–10, 2019.

[118] H. Schön. *Handbuch der reinsten Gase.* Springer-Verlag, 2006.

[119] R. K. Tepe, D. Vassallo, T. Jacksier, and R. M Barnes. Iron pentacarbonyl determination in carbon monoxide. *Spectrochimica Acta Part B: Atomic Spectroscopy*, 54:1861–1868, 1999.

[120] M. D. Rumminger and G. T. Linteris. Inhibition of premixed carbon monoxide-hydrogen-oxygen-nitrogen flames by iron pentacarbonyl. *Combustion and Flame*, 120:451–464, 2000.

[121] T. Zinner. Meteorologisches Institut Garching Oskar von Miller Turm, 2011.

[122] F. A. Ettner. Effiziente numerische Simulation des Deflagrations-Detonations-Übergangs. PhD-thesis, Chair of Thermodynamics, Technical University of Munich, Munich, 2013.

[123] E. Cussler. *Diffusion: mass transfer in fluid systems.* Cambridge University Press, 3rd edition, 2009.

[124] T. Krause, M. Meier, and J. Brunzendorf. Influence of thermal shock of piezoelectric pressure sensors on the measurement of explosion pressures. *Journal of Loss Prevention in the Process Industries*, 71:104523, 2021.

[125] A. Veser, W. Breitung, and S. B. Dorofeev. Run-up distances to supersonic flames in obstacle-laden tubes. *Journal de Physique IV (Proceedings)*, 12:333–340, 2002.

[126] M. S. Kuznetsov, V. I. Alekseev, Y. Yankin, and S. B. Dorofeev. Slow and fast deflagrations in hydrocarbon-air mixtures. *Combustion Science and Technology*, 174:157–172, 2002.

[127] M. S. Kuznetsov, V. I. Alekseev, A. Bezmelnitsyn, W. Breitung, S. B. Dorofeev, I. Matsukov, A. Veser, and Y. Yankin. *Effect of obstacle geometry on behaviour of turbulent flames.* Forschungszentrum Karlsruhe, 1999.

[128] R. Beauvais, F. Mayinger, and G. Strube. Turbulent flame acceleration-mechanisms and significance for safety considerations. *International Journal of Hydrogen Energy*, 19:701–708, 1994.

[129] O. J. Ugarte, V. Bychkov, J. Sadek, D. Valiev, and V. Akkerman. Critical role of blockage ratio for flame acceleration in channels with tightly spaced obstacles. *Physics of Fluids*, 28:093602, 2016.

[130] C. Barfuss, D. Heilbronn, and T. Sattelmayer. Impact of local flame quenching on the flame acceleration in H_2-CO-air mixtures in obstructed channels. *Journal of Loss Prevention in the Process Industries*, 71:104491, 2021.

[131] A. Teodorczyk, J.H.S. Lee, and R. Knystautas. Propagation mechanism of quasi-detonations. *Symposium (International) on Combustion*, 22:1723–1731, 1989.

[132] W. Breitung, C. K. Chan, S. B. Dorofeev, A. Eder, B. Gelfand, M. Heitsch, R. Klein, A. Malliakos, E. Shepherd, and E. Studer. Flame acceleration and deflagration-to-detonation transition in nuclear safety. *NEA/CSNI*, 2000.

[133] J. Grune, K. Sempert, H. Haberstroh, M. S. Kuznetsov, and T. Jordan. Experimental investigation of hydrogen-air deflagrations and detonations in semi-confined flat layers. *Journal of Loss Prevention in the Process Industries*, 26:317–323, 2013.

[134] J. Spurk and N. Aksel. *Strömungslehre*. Springer Berlin Heidelberg, 2010.

A Experimental investigation of fuel gas distribution for inhomogeneous mixtures

A model of the test rig was used for experimental validation. The model corresponds in height and width to the dimensions of the explosion channel. The internal geometry of the 300 mm long model corresponds to the BR60S100 configuration of the explosion channel. The model is supplied with fuel via the gas supply system used for the explosion channel. The experimental procedure of fuel injection and the determination of the fuel content is carried out in the same way as in the explosion channel (see Sec. 3.2). Gas samples are taken via access holes at various heights on one side of the model. A total of six evacuated gas probes, each with a volume of $V = 50\,\mathrm{cm}^3$, can be connected to the access holes of the model via thin tubes ($D = 3\,\mathrm{mm}$). The length of the tubes was chosen to allow sampling at the center of the model ($y = 150\,\mathrm{mm}$). Sampling is accomplished by synchronized opening of all gas probes for 0.5 s. The opening duration of the gas probes is chosen so that enough gas flows into the gas probe while the assumption of a local sample remains largely guaranteed. After sampling, the gas probes are filled with argon to a pressure of about 2.5 bar. The samples obtained this way were then analyzed in an Agilent 490 gas chromatograph. Based on the pressure before sampling and the pressure after filling with argon, and the H_2 and CO-content, the fuel distribution over the height of the channel was determined.

Since the collection and analysis of the gas mixture in the samples represent a considerable effort, and a suitable gas chromatograph was only available externally, the number of measurement points was reduced in advance to a fuel concentration of $X_\mathrm{F} = 29.6$ vol.-% and $X_\mathrm{F} = 14.8$ vol.-%. In each case, samples were taken simultaneously at all six sampling points at times of $t_\mathrm{W} = 3, 5, 10, 15, 30$, and 60 s. Since the injection into the model is analogous to the injection into the GraVent system, it is not possible to adjust the fuel con-

Table A.1: Measured fuel distribution in the model.

Case nr.	Injection pressure p_{inj}	H_2/CO	Fuel content $\overline{X}_F$	Injection time t_{inj}
113	0.6 MPa	50/50	27.1 vol.-%	0.89 s
118	0.6 MPa	75/25	28.3 vol.-%	0.73 s
163	0.6 MPa	50/50	13.4 vol.-%	0.54 s

tent accurately (see Sec. 3.2). In order to obtain a comparable fuel content for each measurement, the injection time was kept constant. Finally, the fuel content was determined for each measurement using the partial pressure method and averaged over all measurements of the respective case. The measurement matrix is summarised in table A.1.

As shown in Fig. A.1 to A.3, fuel gradients are generated across the height of the channel. A gradient is visible in the concentration curves of H_2 and those of CO. For short diffusion times up to $t_D = 10$ s, segregation of H_2 and CO is evident. The segregation decreases with increasing waiting time.

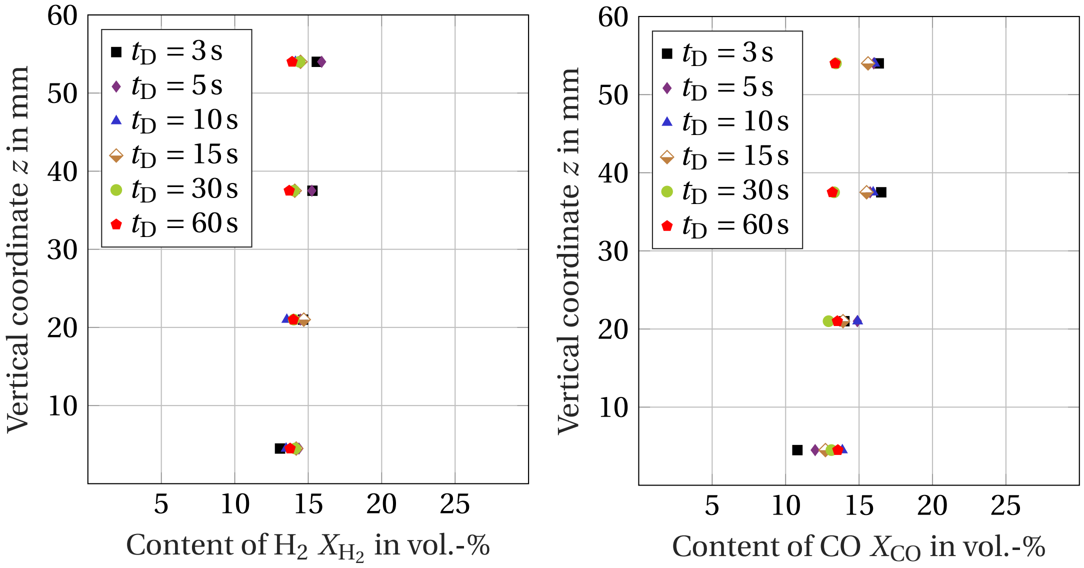

Figure A.1: Measured gas distribution of H_2 (left) and CO (right) over vertical coordinate z for 50/50 H_2/CO and $X_F = 27.1$ vol.-% (case 113).

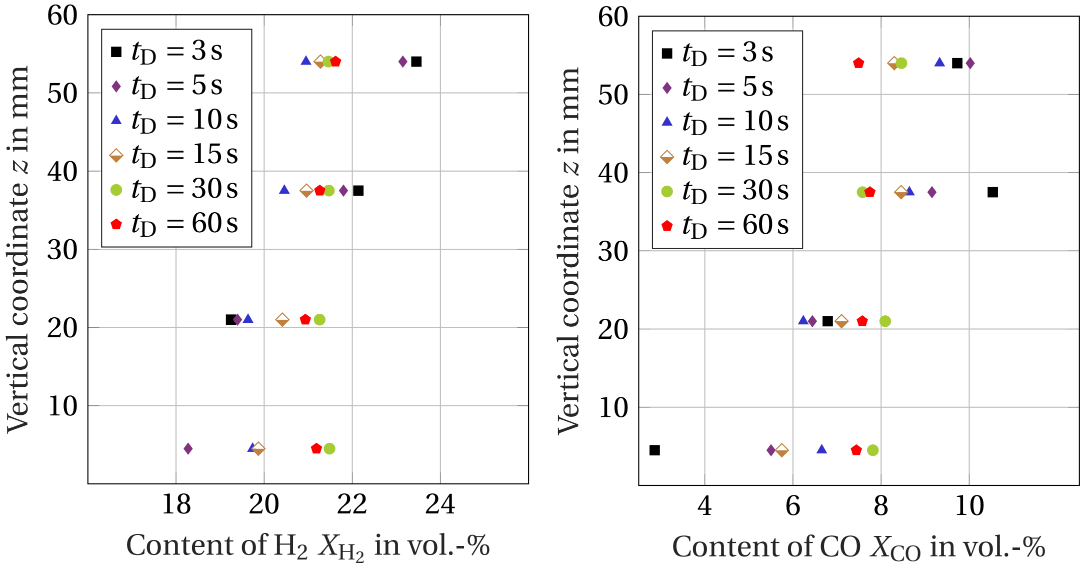

Figure A.2: Measured gas distribution of H_2 (left) and CO (right) over vertical coordinate z for 75/25 H_2/CO and $X_F = 28.3$ vol.-% (case 118).

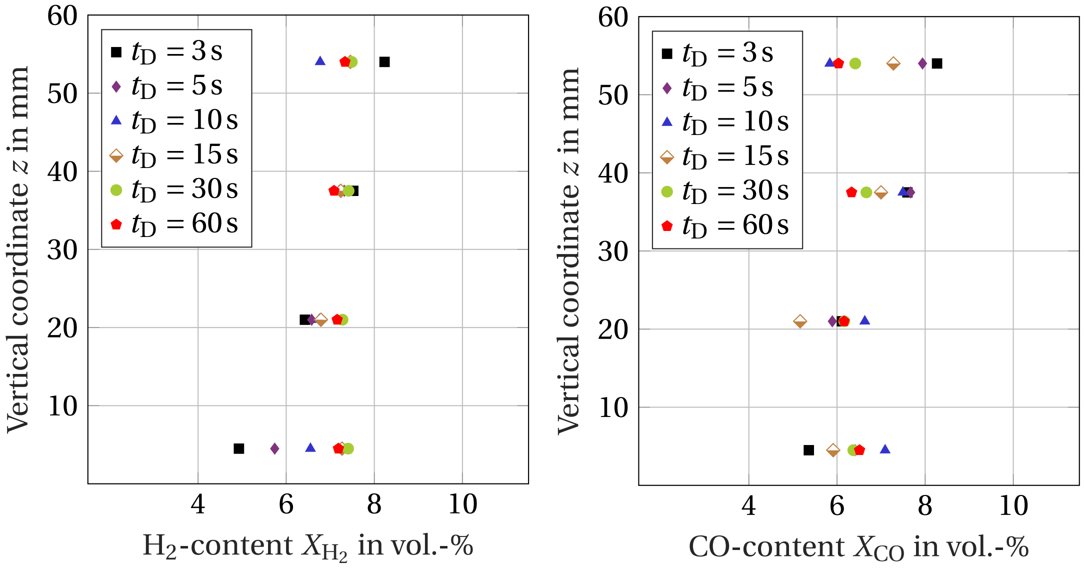

Figure A.3: Measured gas distribution of H_2 (left) and CO (right) over vertical coordinate z for 50/50 H_2/CO and $X_F = 13.4$ vol.-% (case 163).

B Estimation of injection times

The injection time t_{inj} can be estimated by

$$t_{\mathrm{inj}} = \frac{X_{\mathrm{F}} V_{\mathrm{GraV}} \rho_{\mathrm{F}}}{\dot{m}_{\mathrm{inj}}}. \tag{B.1}$$

In Eqn. B.1 V_{GraV} is the volume of the explosion channel, ρ_{F} is the density of the injected fuel (assumed at ambient conditions) and $\dot{m}_{\mathrm{inj}}$ is the mass flow rate of the fuel injected into the test rig. The mass flow rate $\dot{m}_{\mathrm{inj}}$ can be calculated if one assumes an isentropic flow through a choked nozzle [134] and is given by

$$\dot{m}_{\mathrm{inj}} = A \sqrt{\gamma \rho_{\mathrm{F}} p_{\mathrm{s}} \left(\frac{2}{\gamma + 1} \right)^{\frac{\gamma+1}{\gamma-1}}}. \tag{B.2}$$

In Eqn. B.2 A is the area of the nozzle and p_{s} the total pressure of the fuel, which is assumed to be the pressure in the fuel supply system. The total nozzle area can be calculated by the number of nozzles at the test rig and the respective diameter. By evaluation of Eqn. B.2 and B.1, the impact of the different gas properties due to the changing gas composition and the variation in the supply pressure p_{s} on the injected mass flow $\dot{m}_{\mathrm{inj}}$ and injection time t_{inj} can be evaluated. In Fig. B.1, the mass flow rate $\dot{m}_{\mathrm{inj}}$ is plotted over the pressure in the fuel supply system when considering all nozzles mounted at the test rig. As shown in Fig. B.1, the mass flow rate increases with increasing CO content in the fuel and increasing supply pressure. Maintaining the same mass flow rate for CO containing fuels as for 100/0 H_2/CO at $p_{\mathrm{s}} = 0.8\,\mathrm{MPa}$ can only be achieved by a drastic reduction in p_{s}. For 75/25 H_2/CO, a corresponding reduction in p_{s} can be achieved while a choked flow through the nozzles is maintained. For 50/50 H_2/CO, this is not possible. Furthermore, the simple approach to calculate $\dot{m}_{\mathrm{in}}$ assumes a constant supply pressure p_{s}. However, a choked flow is maintained only if the pressure ratio across the nozzle is above the critical pressure ratio. As experiments showed, the pressure in the supply system p_{s} can not be maintained above the critical pressure ratio if the supply pressure is less than 0.6 MPa.

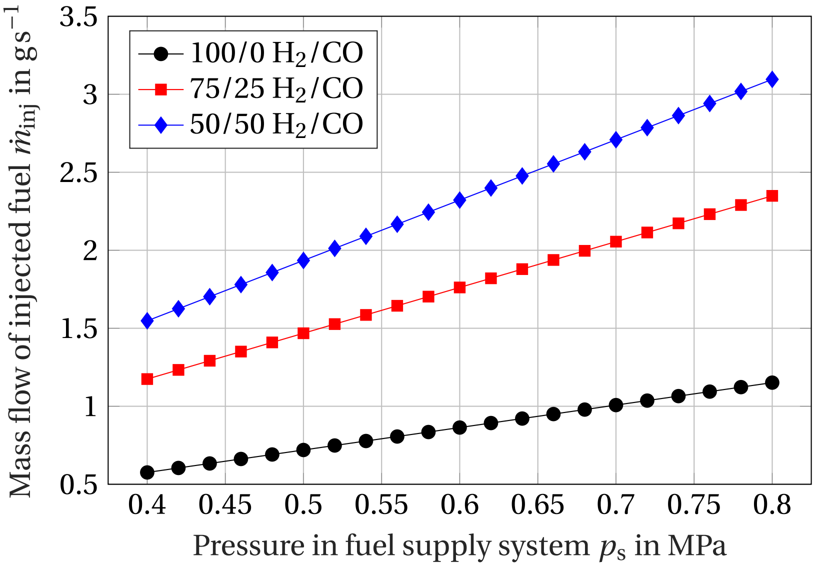

Figure B.1: Mass flow of injected fuel $\dot{m}_{\mathrm{inj}}$ over supply pressure p_{s} for 100/0, 75/25 and 50/50 H_2/CO.

In Fig. B.2, the injection time t_{inj} based on Eqn. B.1 and Eqn. B.2 is plotted over the fuel content for investigated fuels. For the calculation, the supply pressure was adjusted to $p_{\mathrm{s}} = 0.6$ MPa. As shown in Fig. B.2, the injection increases with the fuel content in the explosion channel X_{F} as well as with the CO content in the fuel.

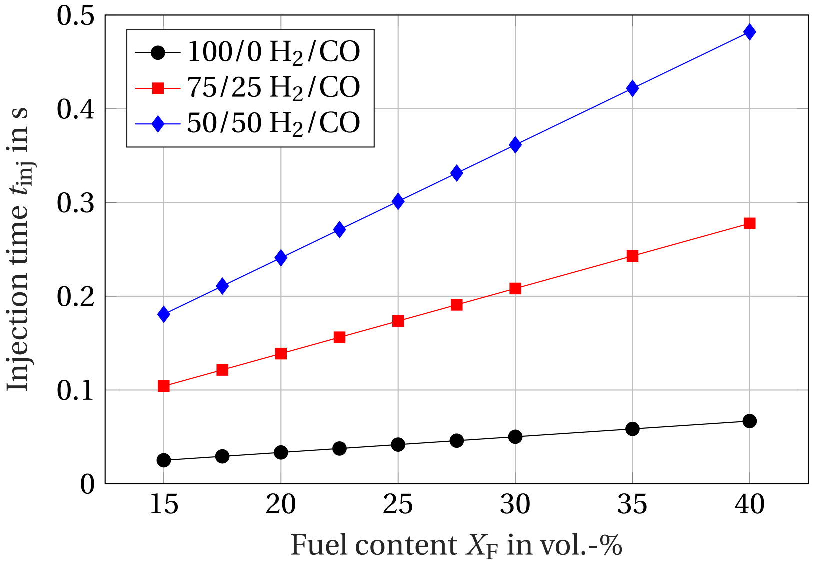

Figure B.2: Injection times t_{inj} over fuel content X_{F} for 100/0, 75/25 and 50/50 H_2/CO at a supply pressure of $p_{\mathrm{s}} = 0.6\,\mathrm{MPa}$.

C Mixture properties

Table C.1: Properties for the investigated fuel compositions and fuel contents: CJ velocity D_CJ, flow velocity downstream of the CJ-state u_CJ, speed of sound of the reactants a_Re, speed of sound of the products of isobaric, adiabatic combustion a_Pr, pressure of the CJ-state p_CJ, von Neumann pressure p_vN, adiabatic, isochoric combustion pressure p_AICC, expansion ratio σ, and laminar flame speed s_L.

X_F	H_2/CO	D_CJ in $\mathrm{m\,s^{-1}}$	u_CJ in $\mathrm{m\,s^{-1}}$	a_Re in $\mathrm{m\,s^{-1}}$	a_Pr in $\mathrm{m\,s^{-1}}$	p_CJ in MPa	p_vN in MPa	p_AICC in MPa	σ	s_l in $\mathrm{m\,s^{-1}}$
15	100/0	1523.1	633.5	370.6	766.4	1.10	2.01	0.57	4.64	0.43
15	75/25	1507.2	628.7	363.5	757.8	1.12	2.05	0.58	4.73	0.31
15	50/50	1492.1	624.5	356.8	749.6	1.14	2.09	0.59	4.82	0.19
17.5	100/0	1623.2	681.6	375.8	814.8	1.22	2.23	0.63	5.14	0.67
17.5	75/25	1598.4	672.9	367.2	802.2	1.24	2.26	0.64	5.24	0.44
17.5	50/50	1575.1	664.5	359.2	790.4	1.26	2.30	0.65	5.34	0.31
20	100/0	1713.8	724.1	381.1	860.7	1.33	2.42	0.69	5.62	0.94
20	75/25	1678.0	710.1	370.9	843.6	1.36	2.45	0.70	5.72	0.65
20	50/50	1644.6	697.2	361.6	827.8	1.38	2.48	0.71	5.82	0.46
22.5	100/0	1794.8	762.1	386.7	904.1	1.43	2.58	0.74	6.06	1.25
22.5	75/25	1745.0	742.6	374.8	881.7	1.43	2.60	0.74	6.16	0.80
22.5	50/50	1699.7	725.6	364.0	861.2	1.42	2.61	0.75	6.26	0.61
25	100/0	1867.7	798.5	392.6	944.8	1.47	2.71	0.78	6.47	1.56
25	75/25	1801.4	767.8	378.8	916.0	1.52	2.71	0.78	6.55	1.06
25	50/50	1743.6	743.6	366.5	889.7	1.53	2.71	0.78	6.62	0.78
27.5	100/0	1931.1	825.0	398.7	982.0	1.58	2.81	0.81	6.81	1.85
27.5	75/25	1847.9	792.6	383.0	944.7	1.52	2.79	0.81	6.84	1.19
27.5	50/50	1778.0	763.0	369.0	911.8	1.51	2.79	0.81	6.88	0.95
30	100/0	1983.7	848.8	405.1	1011.8	1.62	2.88	0.83	7.02	2.12
30	75/25	1886.4	806.8	387.3	966.4	1.61	2.85	0.82	7.02	1.48
30	50/50	1805.5	772.5	371.6	927.6	1.60	2.83	0.83	7.04	1.12
35	100/0	2052.2	878.6	418.9	1037.0	1.61	2.88	0.83	6.88	2.53
35	75/25	1938.7	830.0	396.2	983.4	1.61	2.87	0.83	6.93	1.86
35	50/50	1842.3	792.2	376.9	939.0	1.56	2.87	0.83	7.00	1.43
40	100/0	2097.9	896.1	434.2	1054.2	1.56	2.80	0.80	6.58	2.73
40	75/25	1963.6	839.4	405.9	987.3	1.56	2.81	0.80	6.62	2.13
40	50/50	1855.2	794.0	382.5	934.4	1.58	2.82	0.81	6.70	1.67

All properties are calculated using CANTERA [70], and the Davis reaction mechanism [46]. The initial conditions are set to $T_\mathrm{init} = 293\,\mathrm{K}$ and $p_\mathrm{init} = 0.101\,325\,\mathrm{MPa}$. The calculation of the laminar flame speed s_L is based on the tabulation provided by Barfuss et al. [69].

D Gas distribution for inhomogeneous mixtures of 75/25 H_2/CO

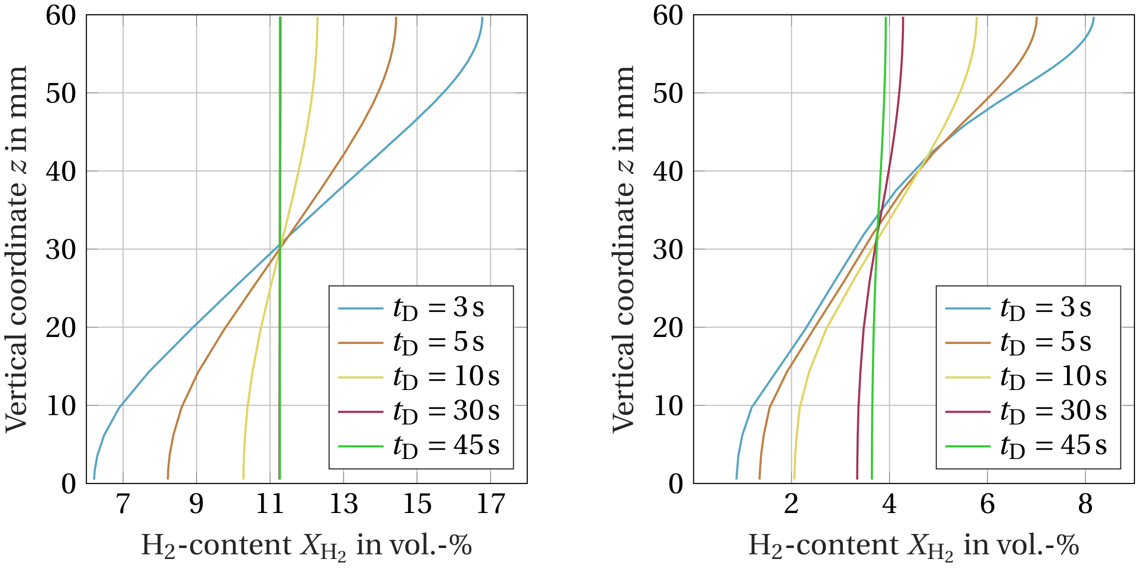

Figure D.1: H_2-distribution X_{H_2} (left) and CO-distribution X_{CO} (right) over vertical coordinate z for 50/50 H_2/CO and $X_F = 15$ vol.-%.

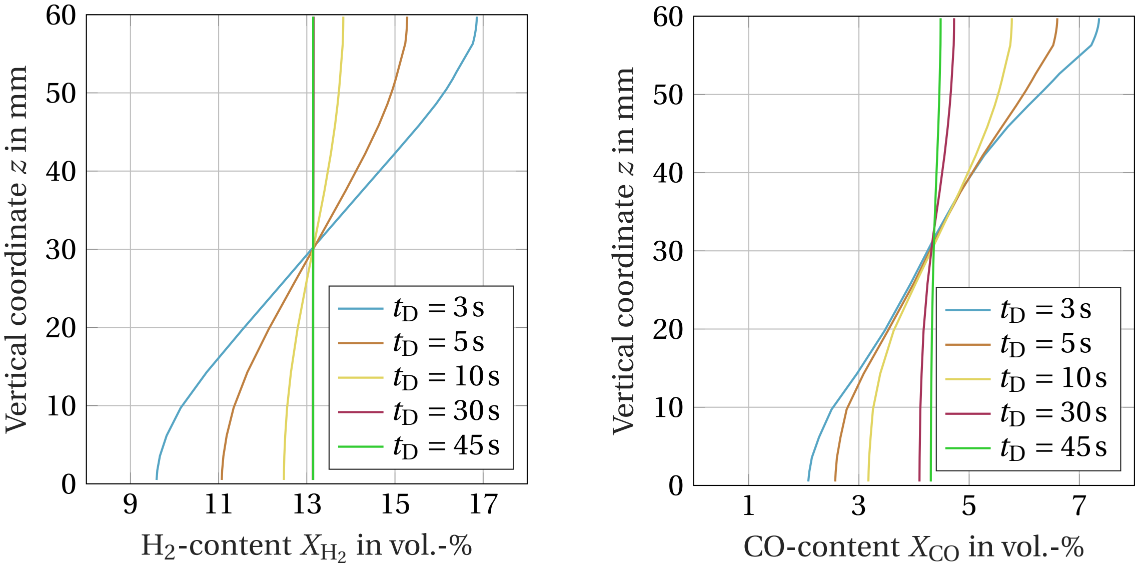

Figure D.2: H_2-distribution X_{H_2} (left) and CO-distribution X_{CO} (right) over vertical coordinate z for 75/25 H_2/CO and $X_F = 17.5$ vol.-%.

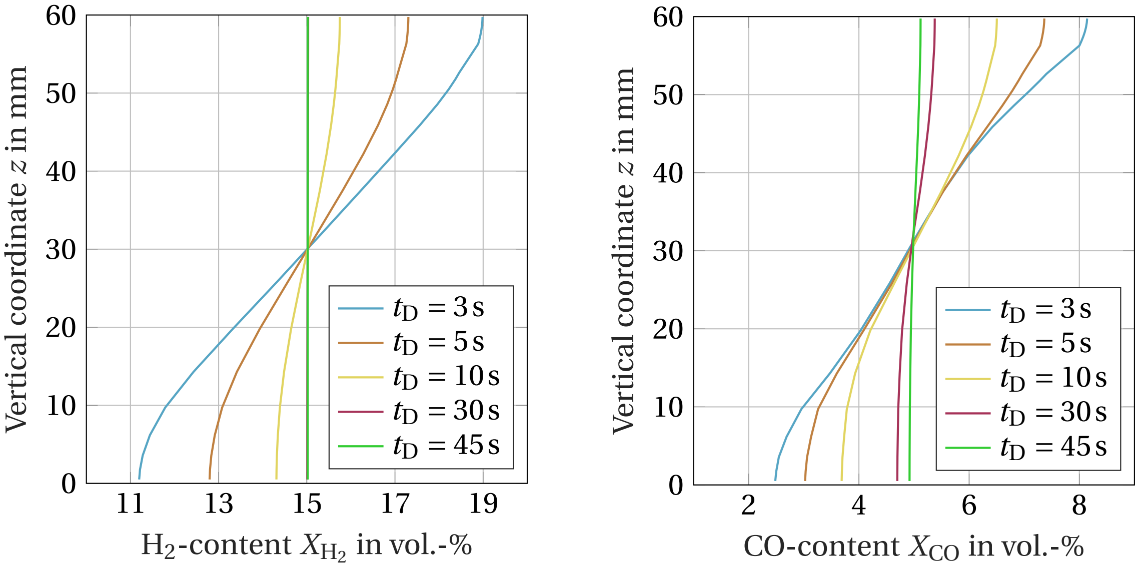

Figure D.3: H_2-distribution X_{H_2} (left) and CO-distribution X_{CO} (right) over vertical coordinate z for 75/25 H_2/CO and $X_F = 20$ vol.-%.

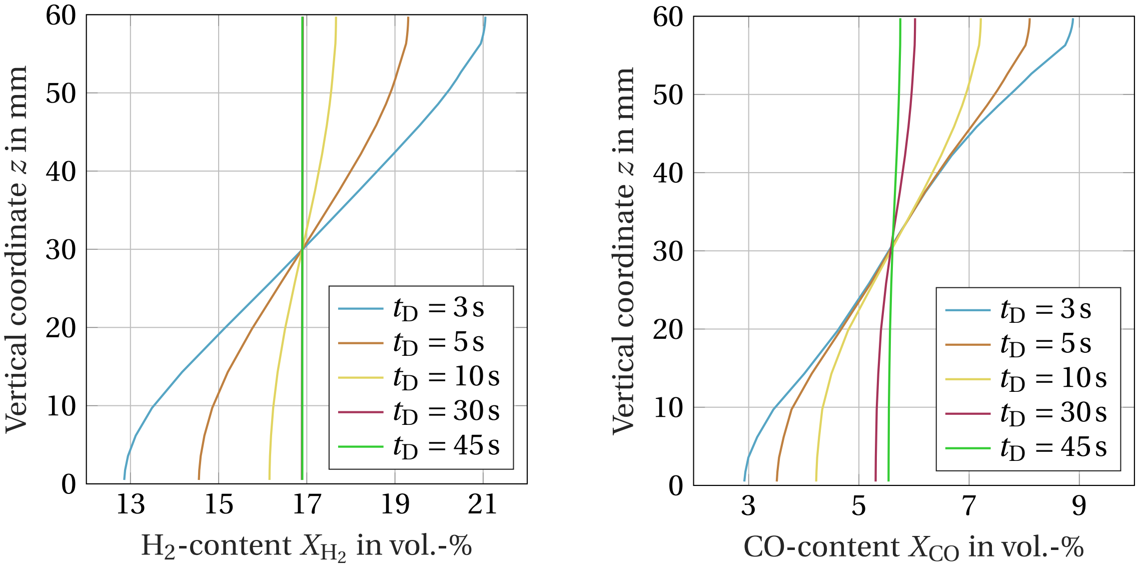

Figure D.4: H_2-distribution X_{H_2} (left) and CO-distribution X_{CO} (right) over vertical coordinate z for 75/25 H_2/CO and $X_F = 22.5$ vol.-%.

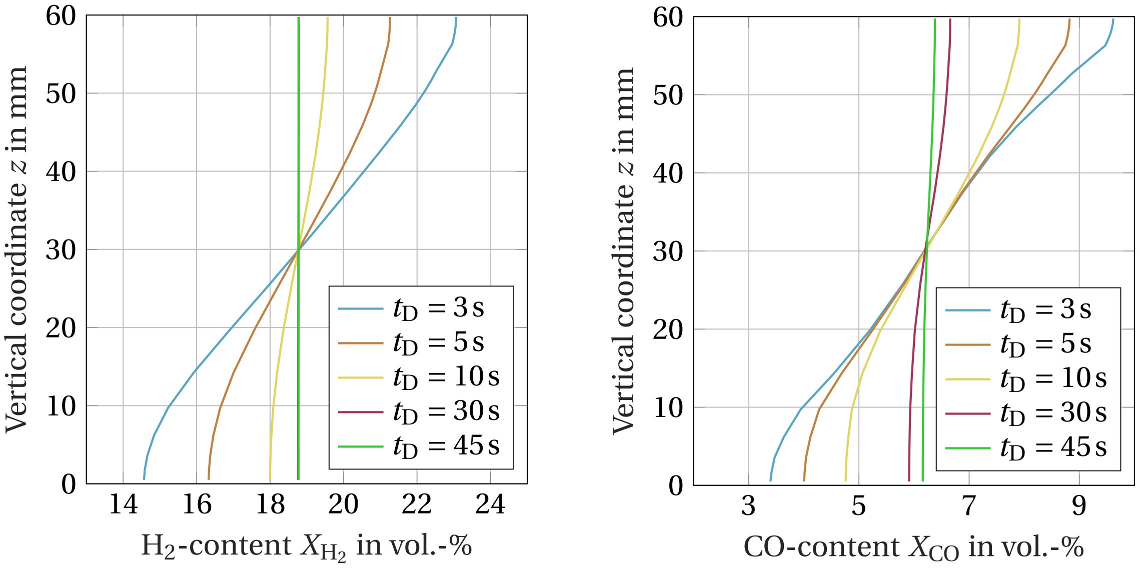

Figure D.5: H_2-distribution X_{H_2} (left) and CO-distribution X_{CO} (right) over vertical coordinate z for 75/25 H_2/CO and $X_F = 25$ vol.-%.

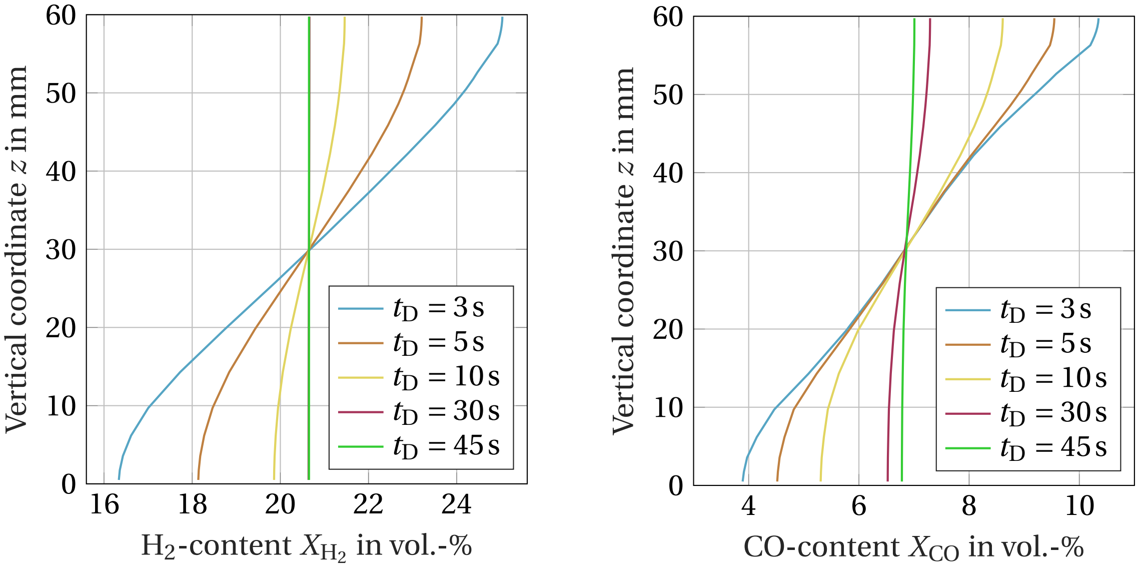

Figure D.6: H_2-distribution X_{H_2} (left) and CO-distribution X_{CO} (right) over vertical coordinate z for 75/25 H_2/CO and $X_F = 27.5$ vol.-%.

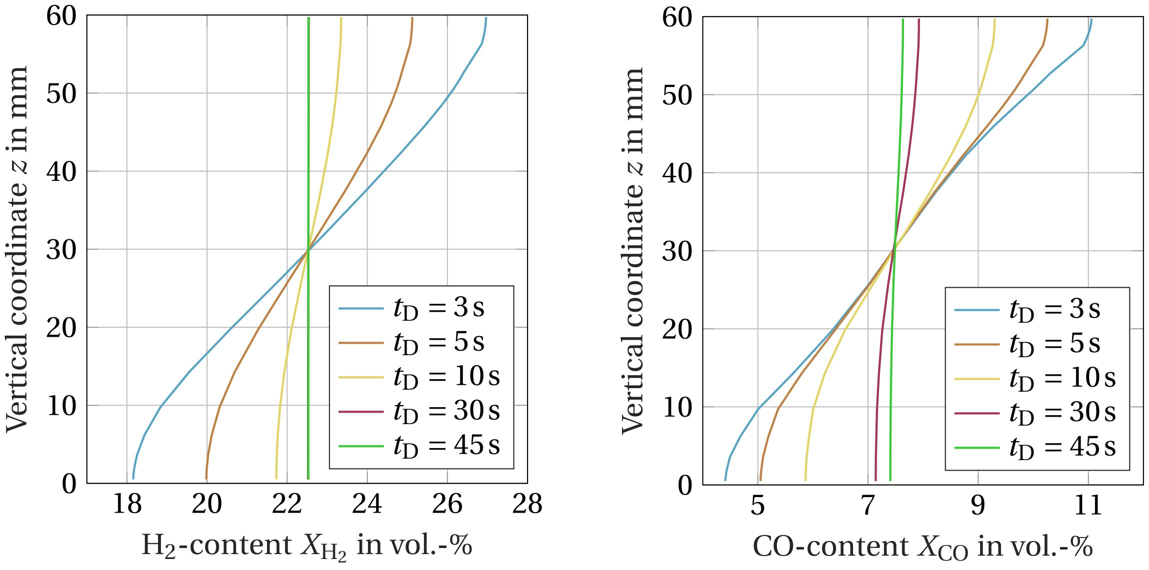

Figure D.7: H_2-distribution X_{H_2} (left) and CO-distribution X_{CO} (right) over vertical coordinate z for 75/25 H_2/CO and $X_F = 30$ vol.-%.

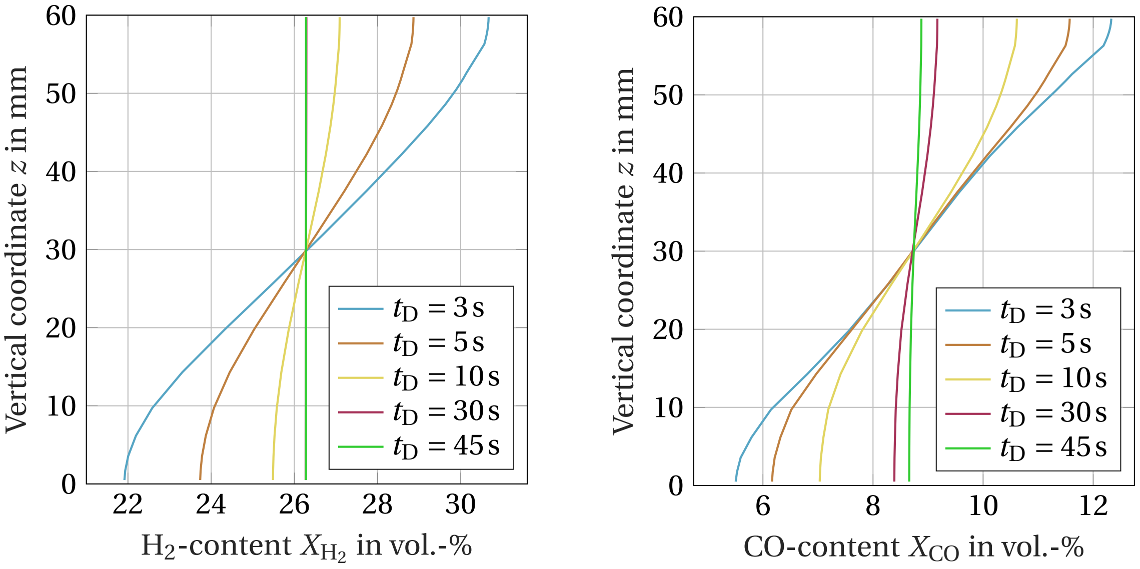

Figure D.8: H_2-distribution X_{H_2} (left) and CO-distribution X_{CO} (right) over vertical coordinate z for 75/25 H_2/CO and $X_F = 35$ vol.-%.

E Gas distribution for inhomogeneous mixtures of 50/50 H_2/CO

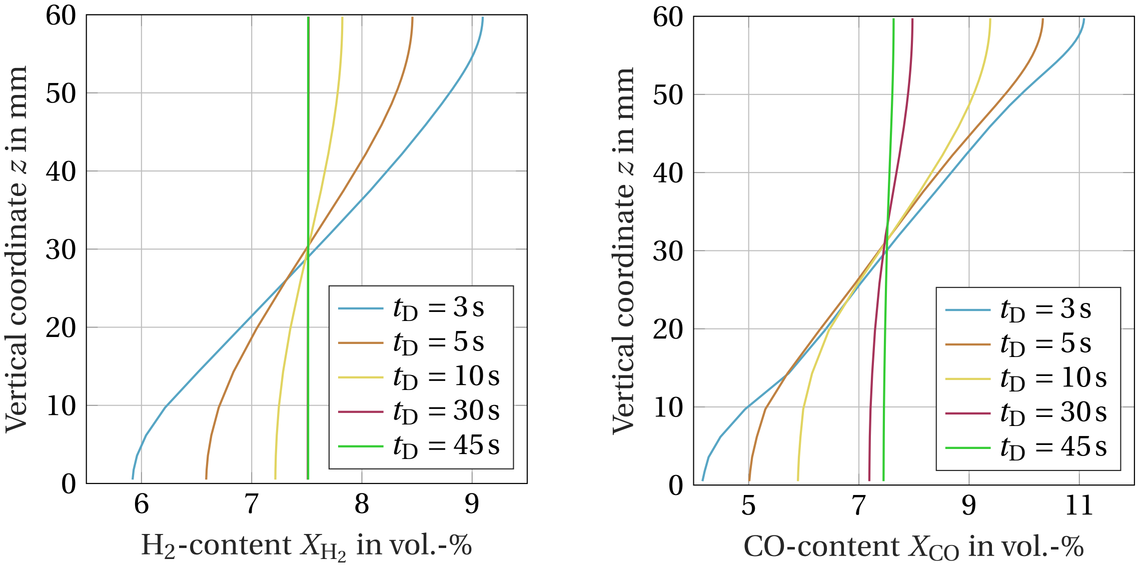

Figure E.1: H_2-distribution X_{H_2} (left) and CO-distribution X_{CO} (right) over vertical coordinate z for 50/50 H_2/CO and $X_F = 15$ vol.-%.

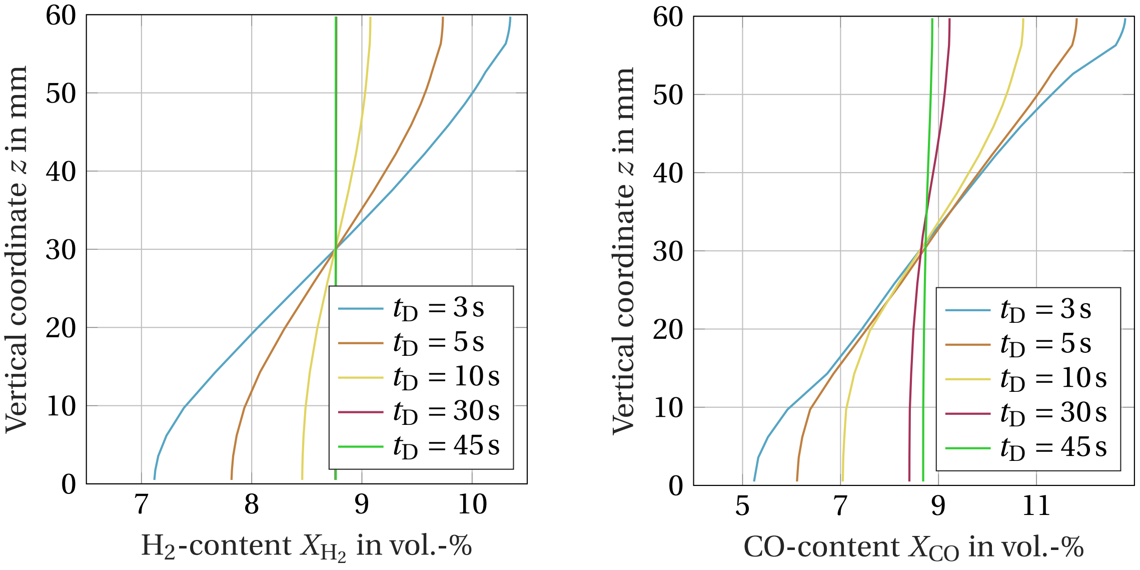

Figure E.2: H_2-distribution X_{H_2} (left) and CO-distribution X_{CO} (right) over vertical coordinate z for 50/50 H_2/CO and $X_F = 17.5$ vol.-%.

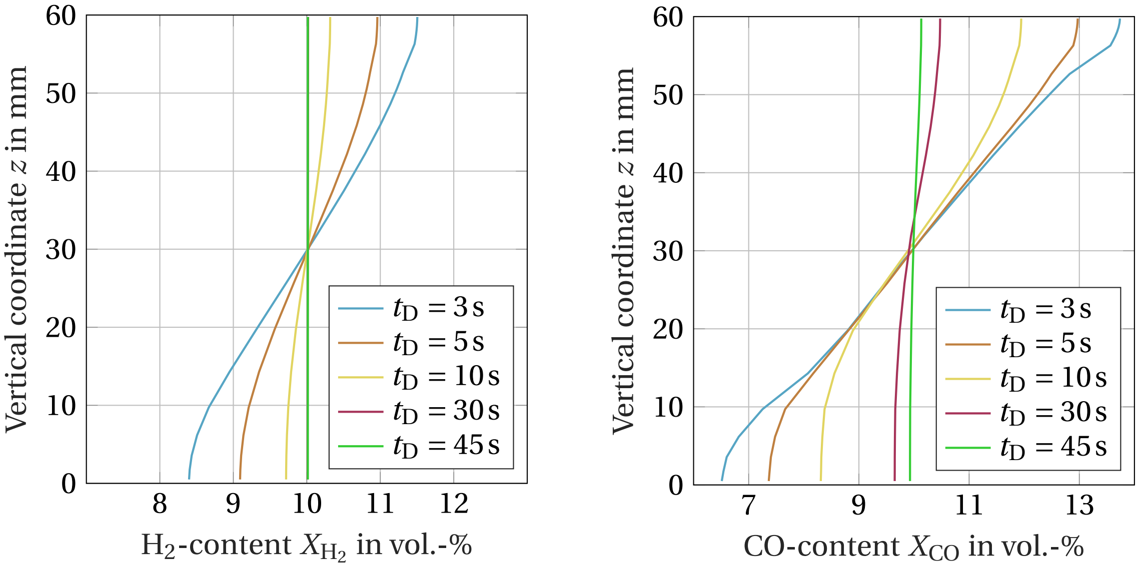

Figure E.3: H_2-distribution X_{H_2} (left) and CO-distribution X_{CO} (right) over vertical coordinate z for 50/50 H_2/CO and $X_F = 20$ vol.-%.

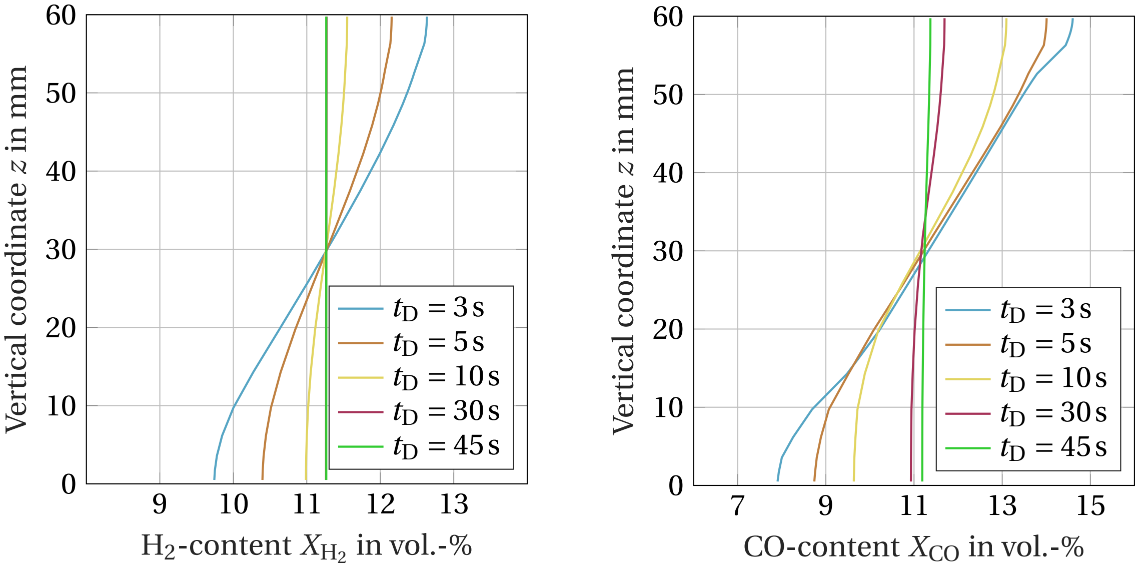

Figure E.4: H_2-distribution X_{H_2} (left) and CO-distribution X_{CO} (right) over vertical coordinate z for 50/50 H_2/CO and $X_F = 22.5$ vol.-%.

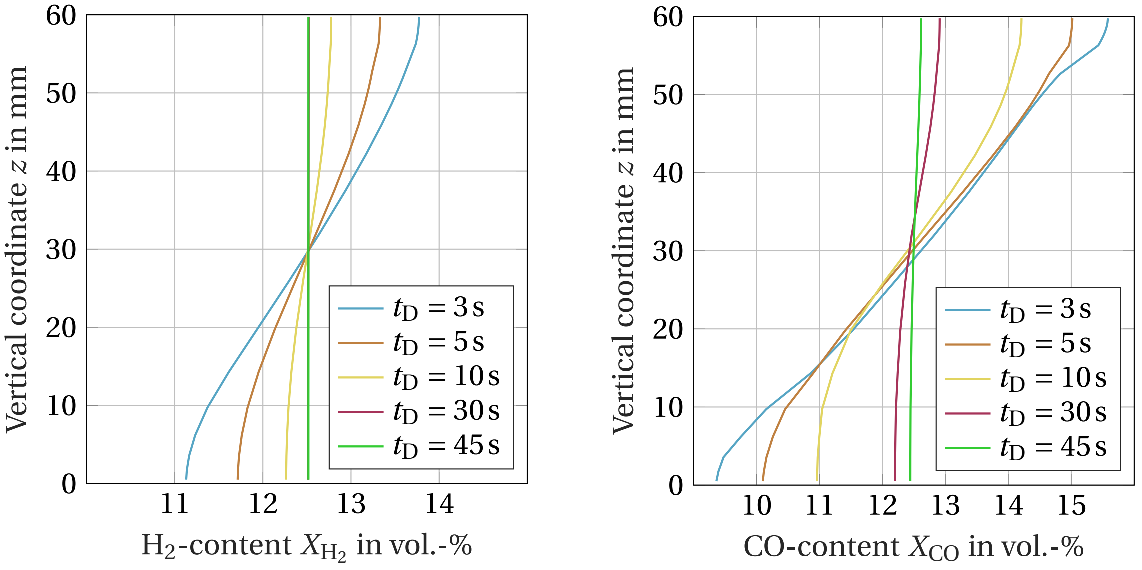

Figure E.5: H_2-distribution X_{H_2} (left) and CO-distribution X_{CO} (right) over vertical coordinate z for 50/50 H_2/CO and $X_F = 25$ vol.-%.

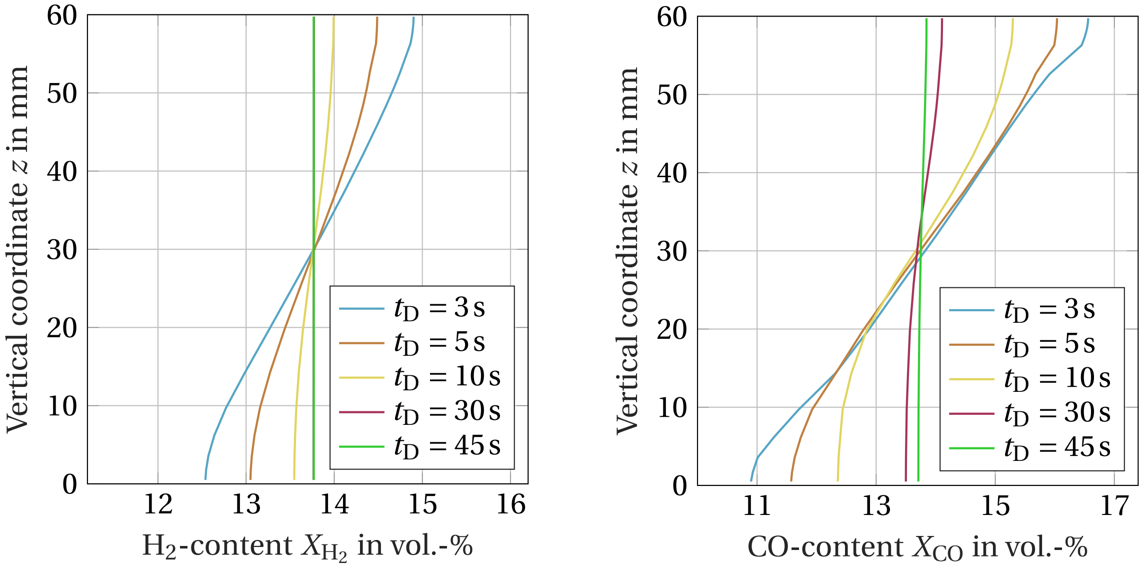

Figure E.6: H_2-distribution X_{H_2} (left) and CO-distribution X_{CO} (right) over vertical coordinate z for 50/50 H_2/CO and $X_F = 27.5$ vol.-%.

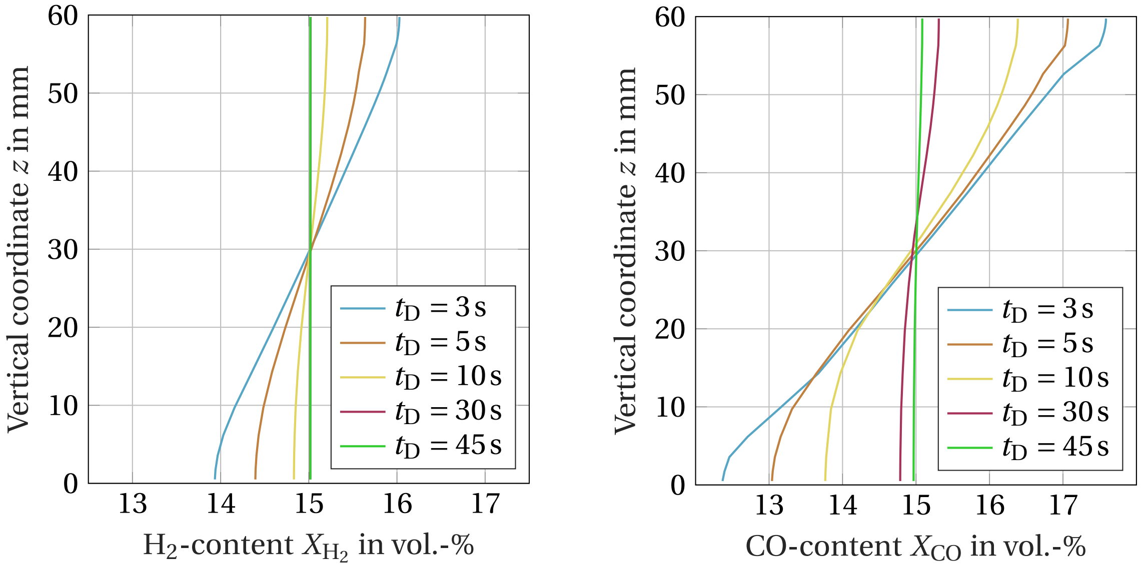

Figure E.7: H_2-distribution X_{H_2} (left) and CO-distribution X_{CO} (right) over vertical coordinate z for 50/50 H_2/CO and $X_F = 30$ vol.-%.

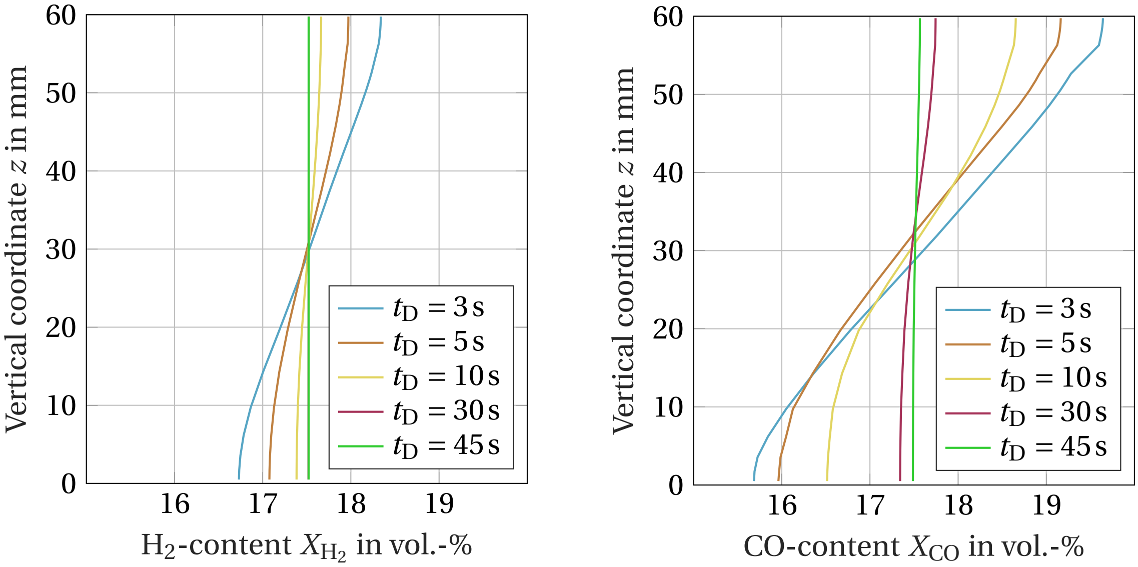

Figure E.8: H_2-distribution X_{H_2} (left) and CO-distribution X_{CO} (right) over vertical coordinate z for 50/50 H_2/CO and $X_F = 35\,\text{vol.-\%}$.

F Impact of transverse concentration gradients on the flame propagation at BR60S300

Since the results obtained at BR60S300 for inhomogeneous mixture do not show a different behavior than those for BR30S300, the results are not discussed in detail in Sec. 4.3. The plots of the run-up distance to the speed of sound of the isobaric products x_{apr}, the terminal velocity $\tilde{u}_{\mathrm{term}}$ and the peak dynamic pressure $p_{\mathrm{dyn,max}}$ over the fuel content X_{F} are shown below.

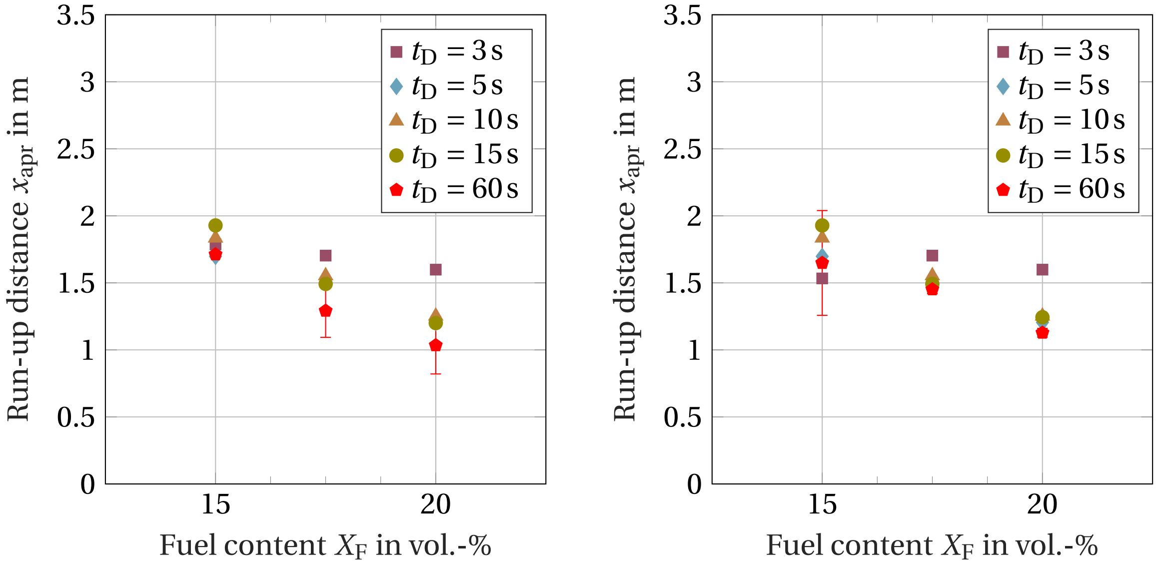

Figure F.1: Run-up distance to the speed of sound of the isobaric products x_{apr} over fuel content X_{F} at BR60S300 for inhomogeneous mixtures of 75/25 (left) and 50/50 H_2/CO (right).

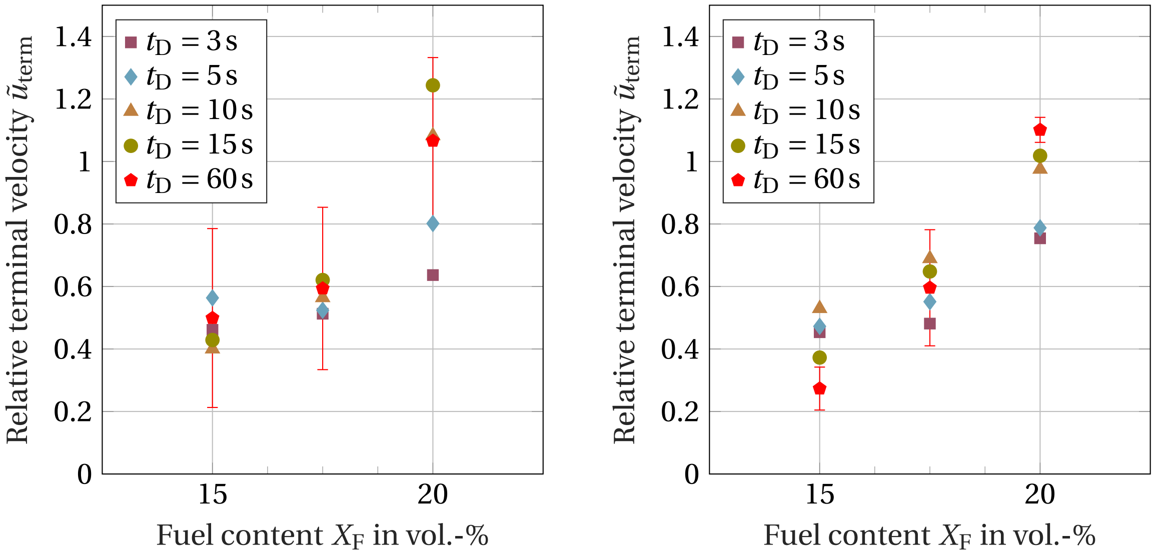

Figure F.2: Relative terminal velocity $\tilde{u}_{\mathrm{term}}$ over fuel content X_F at BR60S300 for inhomogeneous mixtures of 75/25 (left) and 50/50 H_2/CO (right).

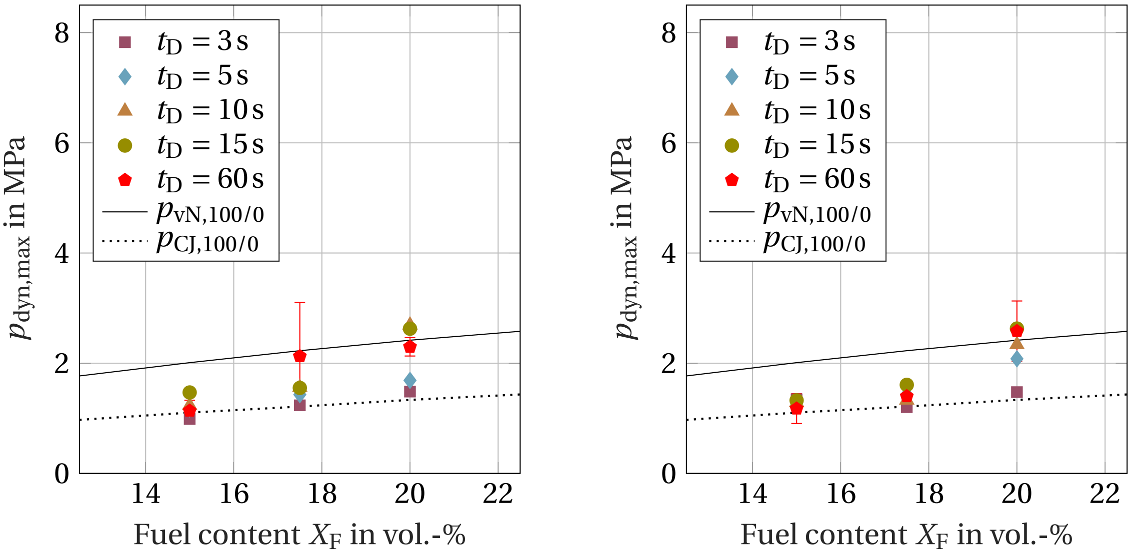

Figure F.3: Maximum dynamic pressure $p_{\mathrm{dyn,max}}$ over fuel content X_F at BR60S300 for inhomogeneous mixtures of 75/25 (left) and 50/50 H_2/CO (right).

G Supervised student thesis and projects

Associated with this dissertation, a number of student theses were supervised by the author of the present work. These theses were prepared at the chair of thermodynamics at the Technical University of Munich in the years 2017 to 2022 under the close supervision of the present author. Parts of these supervised theses may be incorporated into the present thesis. The author would like to express his sincere gratitude to all formerly supervised students for their commitment and support of this research project.

Author	Title, thesis/project type, submission date
Nur Humaira Binte Azhari	Commissioning and testing of a model for the investigation of stratified Syngas-Air-Mixtures at the GraVent-test rig, Bachelors thesis, 26.03.2018
Andreas Glatz	Inbetriebnahme der GraVent-Anlage, Bachelors thesis, 31.10.2018
Nicolas Wein	Parameterstudie zur Erzeugung geschichteter H2-CO-Luftgemische in der GraVent-Anlage, Bachelors thesis, 18.04.2019
Dariush Hosseini	Untersuchung der Flammendynamik von H2-CO-Luft-Gemischen, Bachelors thesis, 20.12.2019
Kajetan Planötscher	Optical Investigation of the Deflagration-to-Detonation-Transition in H2-CO-Air Mixtures, Research project, 09.12.2020
Dariush Hosseini	Prediction of DDT Based on Neural Network, Research internship, 09.03.2022

H Previous publications

Parts of this Ph.D. thesis have been published by the author beforehand in a journal paper or as a conference contribution. All of these publications are registered according to the valid doctoral regulations and are listed below. Therefore, they are not necessarily quoted explicitly in the text.

C. Barfuss, D. Heilbronn, T. Sattelmayer. Verbundvorhaben: Entwicklung von Verbrennungsmodellen und Kriterien für H_2-CO-Luft-Schichten bei partiellem Einschluss - Teilvorhaben A: Experimentelle Untersuchungen auf Laborskala sowie Entwicklung komplementärer CFD-Verfahren. GRS - Reaktorsicherheitsforschung, 2022

D. Heilbronn, C. Barfuss, T. Sattelmayer. Deflagration-to-detonation transition in H_2-CO-Air mixtures in a partially obstructed channel. *International Journal of Hydrogen Energy 46*, Issue 23: 12372-12383, 2021,

D. Heilbronn, C. Barfuss, T. Sattelmayer. Influence of geometry on flame acceleration and DDT in H_2-CO-air mixtures in a partially obstructed channel. *Journal of Loss Prevention in the Process Industries 71*, 2021, 104493

D. Heilbronn, C. Barfuss, T. Sattelmayer. Influence of Geometry on Flame Acceleration and DDT in H_2-CO-Air Mixtures in a Partially Obstructed Channel. *13th Int. Symposium on Hazards, Prevention, and Mitigation of Industrial Explosions (ISHPMIE)*, 2020

D. Heilbronn, C. Barfuss, T. Sattelmayer. Deflagration-to Detonation Transition in H_2-CO-Air mixtures in a partially obstructed channel. *International Conference on Hydrogen Safety (ICHS)*, 2019